Lamb wave approach to identify hidden cracks in hard-to-inspect areas of metallic structures

BENJAMIN STEVEN VIEN

BEng(Mech)(Hons.)/B.Sc.(Maths)

Thesis

Submitted for the degree of

Doctor of Philosophy

Department of Mechanical & Aerospace Engineering

Monash University

November 2016

Declaration

I hereby declare that this thesis contains no material which has been accepted for award of any other degree or diploma in any university; and to the best of my knowledge and belief contains no material previously published or written by another person, except where due reference is made.

Signature of Author: Benjamin Steven Vien

November 2016

“You’re only given a little spark of madness. You mustn’t lose it”

Robin McLaurin Williams (1951-2014)

Abstract

Lamb wave approach to identify hidden cracks in hard-to-inspect areas of metallic structures

Benjamin Steven Vien

Monash University, 2016

Supervisor: Prof Wing Kong Chiu

This thesis reports the results of a study of the scattering of the Lamb wave field due to the presence of a small crack in isotropic structures. The study addressed the challenge of detecting and quantifying a small defect at a hard-to-inspect location for structural health monitoring (SHM). The need for improved aircraft performance and efficiency has made manufacturing design and technology far more complicated, and consideration of nondestructive inspection is usually not factored into these designs. Thus, conventional methods are insufficient, as they do not to account for these advances in design.

A fuel weep hole is a classical configuration in metallic aircraft structure, which is vulnerable to fatigue cracks in hard-to-inspect locations. Conventional diagnosis methods, such as the Eddy Current Technique, are not optimal for damage detection especially in such cases where built-in sensors are restricted to very limited areas. Previous studies involved using high-frequency bulk-wave wedge transducer techniques for weep hole inspection, but the difficulty of reliably detecting and quantifying the small hidden crack still remains in SHM. A reliable and novel analytical model is needed as a reference for monitoring and assessing the early development of a small crack before reaching it reaches a critical size.

This study investigated the scattered Lamb waves on the defect, which carries information such as the severity, location, and size of the crack for SHM purposes. The isotropic specimen used in this research is aluminium plates with different geometry, which depends on the specific investigation. There is significant interest in the use of Lamb waves for hidden crack detection and quantification due to their advantageous properties of rapid wide area inspection with minimal attenuation.

It is also anticipated that the point source equivalence, which consists of a particular combination of body-force doublets, applies for Lamb wave scattering. This research has demonstrated that the point source model can represent the Lamb wave mode scattering by a small crack. This research first investigated edge cracks on the straight edge of the plate, then on the hole boundary, and, lastly, on the top boundary of a rectangular slot. This approach will guide us to the next problem by using the previous study's findings to determine the later study's configuration and to compare its results. The Finite Element method and experimental method are used for this research to explore not only the common scattered Lamb waves amplitude but also the mode, pattern, and wave directivity as a conjunction for small crack detection and characterisation.

The study of the scattering of fundamental Lamb waves by a small edge crack showed a quadratic-like relationship between crack length and scattered wave amplitude and the scattered wave pattern remains independent from the crack length. Within the small crack length-to-wavelength limit, these relationships highly correlate to point source model. It is noteworthy that the dominant scattered Lamb wave modes by an edge crack are the edge-guided and SH0 waves.

The leaky circumferential edge wave is an interesting scattering phenomenon that can direct and coalesce with SH0 waves to the geometric shadow zone. The rectangular slot study has experimentally and computationally demonstrated that leaky symmetric edge-guided waves could propagate to hard-to-inspect location impinged with a hidden crack. The scattered waves are then redirected back to the location of excitation.

The findings in this thesis give a fundamental understanding of the scattering of Lamb waves by crack on boundaries and holes as well as cracks in hard-to-inspect locations. The novelty of this research, which are the scattered wave amplitude, the wave pattern, and its directivity are important measurements to locate and quantitatively evaluate small cracks, based on the point source model. Under specific conditions, edge-guided waves can propagate around a curved edge to the blindsight area and redirected back, as shown in the hole and rectangular slot studies. These findings will assist in the development of Lamb wave propagation for SHM as a damage diagnosis tool.

Acknowledgement

First, I would like to express my sincere appreciation to my supervisor, Prof. Wing Kong Chiu, for his endless support, guidance and encouragement throughout my research. His cheerful personality and trust make him an amazing mentor. I could always rely on him if I needed support or someone to consult. I am so grateful to have Prof. Chiu as my supervisor; you have definitely made my Ph.D. candidature experience enjoyable!

Second, I would like to express gratitude to Dr. L. R. Francis Rose and Dr. Nik Rajic from DSTG for their assistance. Dr. Francis Rose played a major role in this project, and without his incredible wisdom and expertise, my research work would have been a frustrating pursuit. I appreciate his vast knowledge, his assistance in academic writing reports and, in particular, his encouragement to always think *critically*. I am very thankful for the skills and experiences I have acquired and developed under Dr. Francis Rose's guidance.

Special thanks to Nithurshan Nadarajah, Nayeem and Nabil Chowdhury for their assistance and advice; you guys surely made this journey fun and memorable. I would also like to acknowledge Monash University administrative, academic, and workshop staff in the Department of Mechanical and Aerospace Engineering for their correspondence throughout my candidature.

Lastly, I am very grateful for the continuous support and encouragement from my family. I would like to thank Phung Anh Do for being a *Bede*; Victor Kwan, Sam Li, and Hong Cheng for the snow trips; and my other mates for supplying doses of healthy distractions.

Publications

B. S. Vien, N. Nadarajah, W. K. Chiu, L. R. F. Rose, Scattering of the fundamental symmetric wave mode incident at a defect on the blind side of a weep hole in an isotropic plate, Advanced Material Research, 891-892, pp. 1237-1242 (2014)

N. Nadarajah, B. S. Vien, W. K. Chiu, L. R. F. Rose, Scattering phenomena of edge guided waves at and around notches, Advanced Material Research, 891-892, pp.1249-1254 (2014)

B. S. Vien, N. Nadarajah, W. K. Chiu, L. R. Francis Rose, Scattering of the fundamental symmetrical Lamb wave mode by a small edge crack in an isotropic plate, Journal of Mechanics Engineering and Automation, Vol. 5, pp. 210-219. (2015)

N. Nadarajah, B. S. Vien, W. K. Chiu, L. R. Francis Rose, Computational Study of the A0 Scattered Field Due to an Edge Delamination, Journal of Mechanics Engineering and Automation, Vol. 5, pp. 229-236. (2015)

B. S. Vien, N. Nadarajah, L. R. Francis Rose, W. K. Chiu, Scattering of the symmetrical edge-guided wave by a small edge crack in an isotropic plate, Structural Health Monitoring 2015: System Reliability for Verification and Implementation. Vol. 2: pp. 1965-1972 (2016)

N. Nadarajah, B. S. Vien, L. R. Francis Rose, W. K. Chiu, Quantitative Characterisation of A0 Scattered Field due to Edge Delamination as a function of through thickness position, Structural Health Monitoring 2015: System Reliability for Verification and Implementation. Vol. 2: pp. 1957-1964 (2016)

B. S. Vien, L. R. F. Rose, W. K. Chiu, An experimental study on the scattering of edge guided waves by a small edge crack in an isotropic plate, 8th European Workshop On Structural Health Monitoring, Bilbao, Spain (2016)

W. K. Chiu, B. S. Vien, L. R. F. Rose, Scattering of the edge-guided wave by an edge crack at a circular hole in an isotropic plate, 6th Asia-Pacific Workshop on Structural Health Monitoring. (2016) (Pending)

Content

Declaration II

Abstract V

Acknowledgement VII

Publications VIII

Content IX

List of Figures XIII

Chapter 1

Introduction & Literature Review 1

- 1.1 Background 2
  - 1.2.1 Motivation 2
  - 1.2.2 Scope 5
- 1.2 Lamb Wave 6
- 1.3 Elastic Wave Propagation 6
- 1.4 Lamb Wave based non-destructive evaluation 7
- 1.5 Edge-guided and creeping waves 12
- 1.6 Small Crack Detection and Quantification 19
- 1.7 Point Source Equivalence 21
  - 1.7.1 Representation Theorem 22
  - 1.7.2 Green function and Representation Theorem 24
  - 1.7.3 Representation theorem for scattered field by cracks 26
  - 1.7.4 Solution for a dipole 27
- 1.8 Point Source 31
  - 1.8.1 Branch Cut selection 32
  - 1.8.2 Point source solution 35
  - 1.8.3 Application of steepest descent method 37
  - 1.8.4 Far-field wave patterns due to normal and tangential surface forces 39

1.9 Thesis Outline 44

Chapter 2

Computational & Experimental Procedures 46

2.1 Computational Considerations and Methodology: ANSYS and MATLAB 46

2.2 Experimental Considerations and Methodology 59

Chapter 3

Scattering of the fundamental S0 Lamb wave mode by a small edge crack in an isotropic plate 68

3.1 Introduction 69

3.2 Computational Set-up and Procedure 70

3.3 Computational Investigation 72

3.4 Results 74

3.4.1 Scattered field for various incident angles and various crack lengths 74

3.4.2 Generated wave patterns by tractions on crack faces 78

3.5 Discussion 79

3.6 Conclusion 81

Chapter 4

Scattering of edge-guided waves by a small edge crack in an isotropic plate 83

4.1 Scattering of incident symmetric edge guided wave 84

4.1.1 Methodology 84

4.1.2 Computational Set-up and Procedure 86

4.1.3 Results 87

4.1.4 Discussion 92

4.2 Scattering of incident antisymmetric edge-guided wave 93

4.2.1 Methodology 93

4.2.2 Computational Setup 94

4.2.3 Experimental Setup 96

4.2.4 Results 97

4.2.5 Discussion 99

4.3 Conclusion 102

Chapter 5

Scattering of the fundamental Lamb wave modes by an edge crack at a circular hole in an isotropic plate 104

- 5.1 Scattering of the fundamental symmetric wave mode incident at defect on the blind side of a weep hole in an isotropic plate 105
- 5.1.1 Elastic wave propagation 106
- 5.1.2 Computational Investigation 106
- 5.1.3 Finite Element Simulation Results 108
  - i) No notch cases 108
  - ii) With the inclusion of a 3mm notch 109
- 5.2 Scattering of fundamental Lamb waves by an edge crack at a circular hole in an isotropic plate 111
  - 5.2.1 Methodology 111
  - 5.2.2 Computational Procedure 113
  - 5.2.3 Results 115
  - 5.2.4 Discussion 119
  - 5.2.5 Antisymmetric circumferential edge wave propagation around hole 120
- 5.3 Scattering of fundamental symmetric Lamb waves by an edge crack at a circular hole in an isotropic plate: Experimental and computational studies. 121
  - 5.3.1 Methodology 121
  - 5.3.2 Computational Procedure 123
  - 5.3.3 Experimental Procedure 125
  - 5.3.4 Results and Discussion 126
- 5.4 Conclusion 130

Chapter 6

The experimental and computational study on the scattering of fundamental edge-guided wave by a hidden crack on a rectangular curved slot 132

- 6.1 Introduction 132
- 6.2 Methodology 133
- 6.3 Computational Procedure 135

6.4 Experimental Procedure 137
6.5 Results 139
6.6 Discussion 144
6.7 Conclusion 147

Chapter 7

Summary 149
7.1 Scattering of symmetric waves by edge crack in isotropic plate 150
7.2 Scattering of edge-guided waves by edge crack in isotropic plate 151
7.3 Scattering of fundamental Lamb wave mode by an edge crack at circular hole in isotropic plate 152
7.4 Scattering of edge-guided wave with a hidden crack on a rectangular curved slot in isotropic plate 153
7.5 Implication for crack detection and quantification 154
7.6 Future work 154
Bibliography 157
APPENDIX A 166
A.1 Elastic waves in infinite medium 166
A.2 Elastic waves in semi-infinite medium 169
i) Reflection of SH waves 175
ii) Reflection of longitudinal waves 177
iii) Reflection of SV waves 179
A.3 Surface waves (Rayleigh waves) 181
A.4 Wave propagation in plates 185
A.5 The Rayleigh-Lamb frequency equation for the plate 192

List of Figures

Figure 1.1: Benefits of unitised components [2]……………………………………………....................2

Figure 1.2: Schematics of fuel weep hole and location of typical cracks [10, 11]…………………..... 3

Figure 1.3: Damage detection around a through hole by Rayleigh wave generation on the accessible surface [14]……………………………………………………….................................4

Figure 1.4: A compact, permanently attached, autonomous guided wave array prototype and multiplex electronics unit on aluminium plate with circular part-through hole [37] ………………………………………... 7

Figure 1.5: Scattering features due to the incident of predominately SH0 waves impinging with a vertical crack, Rajagopal and Lowe [31] ………………………………………….......9

Figure 1.6: Diagram of the interaction of an incident wave with a defect [65]……………………...10

Figure 1.7: Snapshot of incident wave creeping around the hole [93]……………………………… 15

Figure 1.8: Diagram of the dual transducer to detect creeping wave [7]……………………………16

Figure 1.9: The experimental and computational cylindrical scattered wave field indicated a spiral-like scattering in the angular component where the origin is at the centre of the weep hole [14]…………………………………………………………………………….18

Figure 1.10: Vertical displacement of the forward and back-scattered surface wave relative to incident wave amplitude [129]……………………………………………………………… 20

Figure 1.11: Frequency and time domain of sizing sub-procedure against crack length-wavelength ratio [72]………………………………………………………………………………. 21

Figure 1.12: Equivalent body force represents acoustic emission from a sub-surface crack [141]…...22

Figure 1.13: Traction vector acting on a surface element……………………………………………..25

Figure 1.14: Elastic body with a damage defined by the surface Σ…………………………………... 26

Figure 1.15: Representation of moment tensor density by equivalent body force doublet in two dimensions………………………………………………………………………………29

Figure 1.16: Body-force equivalents for a tension and shear crack in an isotropic medium………….30

Figure 1.17: Branch points and cuts in the complex $k=a_k+b_k$ i plane for Re[ω]>0……………………33

Figure 1.18: Limiting cases of the hyperbola parts in Fig. 1.30. Branch points A and B and cuts AOE and BOF in complex k plane for real ω……………………………………………….34

Figure 1.19: Normal (P) and shear (Q) surface force diagram on semi-infinite boundary……………35

Figure 1.20: Normal surface force radiation pattern of (LEFT) u_R and (RIGHT) u_θ for Poisson's ratio v=1/3……………………………………………………………………………..43

Figure 1.21: Tangential surface force radiation pattern of (LEFT) u_R and (RIGHT) u_θ for Poisson's ratio v=1/3…………………………………………………………………………. 43

Figure 1.22: Schematic of the key investigations starting from edge crack on straight boundary, crack on a hole and hidden crack on a rectangular slot……………………………………...44

Figure 2.1: FE procedure flow chart from ANSYS simulation to MATLAB post processing……...47

Figure 2.2: Comparison of number of nodes per wavelength for S0 and SH0 wave propagation……………………………………………………………………………48

Figure 2.3: Distance versus time of 5 cycles Hann-window SH0 Wave propagation, indicated the temporal and spatial window for 2D FFT……………………………………………. 50

Figure 2.4: Baseline subtraction of a total wave field with crack and original wave field without crack to obtain the wave field due to the presence of the crack…………………………52

Figure 2.5: Method of exciting symmetric Lamb wave modes: (LEFT) In-plane line excitation on the plate boundary. (RIGHT) Pinching force on surfaces of the plate generates pure S0…..52

Figure 2.6: Diagram showing the minimum required distance of wave train to have separated S0 and SH0 wave incidents……………………………………………………………... 53

Figure 2.7: Method of modelling crack (LEFT) by removing elements; (RIGHT) by separating nodes…………………………………………………………………………………..55

Figure 2.8: Dispersion Curve of computationally generated S0 plane wave and S0 cylindrical wave, excited at a frequency of 200 kHz……………………………………………………56

Figure 2.9: Fast Fourier transformation of the associated signal……………………………………58

Figure 2.10: Laser Vibrometer, specimen with bonded PZT and retro-reflective sheet and position system for the experimental setup……………………………………………………61

Figure 2.11: (LEFT) Laser Vibrometer decoder module (RIGHT) Krohn-Hite hardware programming filter and amplifier ……………………………………………………………………62

Figure 2.12: (LEFT) Oscilloscope showing input signal to the PZT and acquired signal via laser sensor (RIGHT) National Instrument BNC 2110 block……………………………………62

Figure 2.13: Experimental setup for Laser Vibrometry……………………………………………63

Figure 2.14: MATLAB interface for Laser Vibrometry experiment……………………………….....63

Figure 2.15: (LEFT) Single PZT bonded on the plate surface (RIGHT) PZT bonded on the edge of the plate………………………………………………………………………….….. 65

Figure 2.16: (LEFT) Signal PZT method: Dispersion curve showing dominant A0 and weak S0; (RIGHT) Edge PZT method: Dispersion curve showing dominant S0 and weak A0 at the centre frequency of 220 kHz in the out-of-plane component. (GREEN) S0 and (RED) A0 …………………………………………………………………………………... 67

Figure 3.1: The scattered wave field due to the crack using baseline subtraction from Eq. (3.1)…...70

Figure 3.2: (a) Wave field as a representation of static stress approximation and (b) Scattered wave by the edge crack is equivalent to superposition of Mode I and II crack opening displacements response………………………………………………………………. 71

Figure 3.3: (a) Geometry of FE model for 800mm x 600mm x 1mm aluminium plate showing the location of the excited force relative to the crack and (b) Detail diagram showing the 2D FFT line, point of excitation and scattered wave measurement locations relative to the crack…………………………………………………………………………….. 71

Figure 3.4: (a) Dispersion curve for scattered wave field of 3mm edge crack in the radial component with dominant S0 and (b) Dispersion curve for scattered wave field of 3mm edge crack in the θ component with dominant SH0: A0(Red), SH0(Blue) and S0(Green)………… 74

Figure 3.5: Scattered wave pattern and polar plot of 3mm crack, a/λ=0.11, (LEFT) at incident 60° and (RIGHT) 30° (a) θ component and (b) radial component………….……….…..... 75

Figure 3.6: Graph of the maximum value of (a) (LEFT) SH0 and S0 scattered displacement and (b) (RIGHT) forward and back-scattered edge wave displacement with various incident angles for a/λ=0.11 and 0.23.. 75

Figure 3.7: (LEFT) Maximum forward to back-scattered displacement ratio of scattered waves at incident 45° with various a/λ (RIGHT) Graph of the maximum scattered displacement at incident 45° with various a/λ ………………………………………………………………76

Figure 3.8: [a-d] θ component a/λ = 0.11 (3 mm) crack: comparison of applied-traction to original SH0 scattered wave patterns, normalized with maximum scattered for 75°, 60°, 45° and 30° incidences, respectively…………………………………………………………….. 76

Figure 3.9: [a-d] θ component a/λ = 0.11 (3 mm) crack: comparison of applied-traction to original SH0 scattered wave patterns, normalized without edge waves for 75°, 60°, 45° and 30° incidences, respectively…………………………………………………………….....77

Figure 3.10: [a-d] Radial component a/λ = 0.11 (3 mm) crack: comparison of applied-traction to original S0 scattered wave patterns, normalized without edge waves for 75°, 60°, 45° and 30° incidences, respectively…………………………………………………………77

Figure 3.11: [a-d] θ component a/λ = 0.23 (6 mm) crack: comparison of applied-traction to original SH0 scattered wave patterns, normalized with maximum scattered for 75°, 60°, 45° and 30° incidences, respectively…………………………………………………………….. 77

Figure 3.12: [a-d] θ component a/λ = 0.23 (6 mm) crack: comparison of applied-traction to original SH0 scattered wave patterns, normalized without edge waves for 75°, 60°, 45° and 30° incidences, respectively…………………………………………………………….....77

Figure 3.13: [a-d] Radial component a/λ = 0.23 (6 mm) crack: Comparison of applied-traction to original S0 scattered wave patterns, normalized without edge waves for 75°, 60°, 45° and 30° incidences, respectively…………………………………………………………78

Figure 3.14: [a-c] Parallel and perpendicular forcing on a/λ = 0.11 (3 mm); θ component normalized with maximum scatter, θ component normalized without edge waves and radial component, respectively……………………………………………………………………78

Figure 3.15: Normalised Analytical Plane Stress and FE normal and shear stresses with depth (along the y axis)…………………………………………………………………………….. 80

Figure 4.1.1: Illustrating the procedure of obtaining the scattered wave field due to the presence of a crack by using baseline subtraction……………………………………………………...85

Figure 4.1.2: (a) (LEFT) 800x600x1mm aluminium plate FE geometry showing location of crack and (b) (RIGHT) Detail diagram portraying the 45° 2D FFT line, excitation point and scattered wave measurement…………………………………………………………..... 86

Figure 4.1.3: Dispersion curves indicate (a) Dominant S0 in the r component, (b) Dominant SH0 in the θ component and (c) Dominant Rayleigh-like edge wave along the edge of the plate. A0 (RED), Plane stress edge wave (YELLOW), SH0 (BLUE) and S0 (GREEN)……... 88

Figure 4.1.4: The scattered wave field due to the presence of a 3mm (a/λ=0.22) edge crack (a) where S0 is dominant in r component and (b) SH0 is dominant in θ component………………88

Figure 4.1.5: The normalised scattered wave polar plot of (a) SH0 mode for 0.07≤a/λ≤0.22 of amplitude u_θ (R0, θs)/$|u_\theta|$max, (b) SH0 mode for 0.29≤a/λ≤0.43 of amplitude u_θ (R0,

θs)/|u_θ|max, (c) S0 mode for 0.07≤a/λ≤0.22 of amplitude u_r (R0, θs)/|u_r|max and (d) S0 mode for 0.29≤a/λ≤0.43 of amplitude u_r (R0, θs)/|u_r|max…………………………….....89

Figure 4.1.6: The scattered wave displacement for various a/λ in (a) Forward region of SH0, (b) Backward region of SH0, (c) Forward region of S0 and (d) Backward region of S0 with respect to the incident wave maximum displacement……………………………….... 90

Figure 4.1.7: Transmitted and reflected edge wave displacements due to the presence of edge crack against a/λ with respect to the incident maximum displacement……………………….. 91

Figure 4.1.8: Baseline FE stresses compared with the analytical edge wave stresses in plane stress case, relative to the maximum stress………………………………………………..... 91

Figure 4.2.1: Illustration of baseline subtraction to obtain the scattered wave field due to the presence of a crack…………………………………………………………………………... 94

Figure 4.2.2: (a) (LEFT) 440x220x3mm aluminium plate indicating location of crack and (b) (RIGHT) Detail diagram of crack showing the 2D FFT line, excitation point and scattered wave measurements…………………………………………………………………….... 95

Figure 4.2.3: Experimental dispersion curves. (LEFT) Asymmetric edge guided wave along the edge of the plate in z component and (RIGHT) Dominant A0 Lamb wave in z component scanned along 45˚ line…………………………………………………………………... 97

Figure 4.2.4: The normalised FE scattered wave polar plots for various crack lengths: (a) (LEFT) 0.1≤a/λ≤0.25 and (b) (RIGHT) 0.3≤a/λ≤0.5 with a/λ=0.1 for comparison……………...97

Figure 4.2.5: The normalised experimental and computational scattered antisymmetric wave patterns comparison for various crack length…………………………………………….…..... 98

Figure 4.2.6: Experimental and computational comparison of normalised scattered wave displacement dependences with crack length for various angles. (a) (LEFT) Forward-scattered amplitude and (b) (RIGHT) Backward-scattered amplitudes……………………....... 99

Figure 4.2.7: Shear stresses depth variation of the incident antisymmetric edge wave relative to the maximum shear stress………………………………………………………………..100

Figure 4.2.8: Scattered wave field equivalent to force doublets due to mode III and mode II crack openings……………………………………………………………………………...100

Figure 4.2.9: Relative displacements with respect to incident wave amplitude of analytical scattered Rayleigh wave displacements obtain from Mendelsohn [129] and computational antisymmetric edge-guided wave…………………………………………………… 101

Figure 5.1.1: (a) (LEFT) Location of typical crack emanating from a fuel weep hole (b) (RIGHT) geometry of FE model for 200mmx200mmx4mm aluminium plate showing the location of the excitation force relative to the hole and notch……………………………………...106

Figure 5.1.2: Snapshot from FE simulation of the scattering in the out-of-plane (u_z) direction of an incident S0 wave, λ =27.2mm, by a circular hole of diameter (a) 10mm; (b) 30mm, and (c) 60mm [121]…………………………………………………………………………108

Figure 5.1.3: Dispersion curve for diameter (a) 10mm (left), (b) 30mm (middle) and (c) 60mm (right) with 3mm notch aluminium plate; S0 (Green), SH0 (Blue) and A0 (Red)…………….110

Figure 5.1.4: Snapshot of the time progression of scattered field θ direction of diameter:(a) 10mm (top); (b) 30mm (middle) and (c) 60mm (bottom) (a) At 30μs and 48μs the SH0 spiral is a visible aspect; at 66μs the scattered wavefront, SH0 and edge waves, radiates into the medium also SH0 source is more apparent. (b) and (c): The SH0 spiral is not evident but the SH0 source is more apparent. SH0 detaching from the surface as seen in (b) 48 μs and 72 μs and (c) 58μs and 76μs, although the edge wave still travels around the surface after SH0 detachment……………………………………………………………………….. 110

Figure 5.2.1: Illustration of the baseline subtraction procedure to obtain the scattered wave field due to the presence of a crack on hole…………………………………………………….... 112

Figure 5.2.2: (a) (LEFT) 600x600x3mm aluminium plate FE geometry showing the location of crack, 45° 2D FFT scan line, scattered wave measurement; (b) (RIGHT) Near hole diagram portraying the excitation point, crack location and origin of cylindrical coordinate system. ………………………………………………………………………………………113

Figure 5.2.3: Plots of 2D FFT amplitude and dispersion curve indicating (a) (LEFT) a dominant SH0 wave in the θ component; (b) (MIDDLE) a dominant S0 wave in the r component; (c) (RIGHT) a circumferential edge wave along the hole circumference with wave speed close to the plane stress edge wave speed…………………………………………….... 115

Figure 5.2.4: Normalised scattered wave polar plot of SH0 waves with respect to the incident wave maximum displacement. (a) 0.07≤a/λ≤0.17; (b) 0.21≤a/λ≤0.31………………………116

Figure 5.2.5: Normalised scattered wave polar plot of S0 waves with respect to the incident wave maximum displacement. (a) 0.07≤a/λ≤0.17; (b) 0.21≤a/λ≤0.31………………………116

Figure 5.2.6: The scattered SH0 wave displacement for various a/λ in (a) 0˚-180˚ region and (b) 180˚-360˚ region with respect to the incident wave maximum displacement………………. 116

Figure 5.2.7: The scattered S0 wave displacement for various a/λ in (a) 0˚-180˚ region and (b) 180˚-360˚ region with respect to the incident wave maximum displacement………………. 117

Figure 5.2.8: Relative displacements with respect to incident wave amplitude of analytical scattered Rayleigh wave displacement obtained from Mendelsohn [129], computational edge wave obtained from Vien et al [168] and computational circumferential edge wave……….. 118

Figure 5.2.9: The attenuation of incident circumferential edge wave displacement over the circumference; (DOT) FE circumferential edge wave displacements, (LINE) data interpolation……………………………………………………………………… 118

Figure 5.2.10: Time snapshot at 20μs and 40μs of edge waves propagating around the hole……… 120

Figure 5.3.1: Illustration of the baseline subtraction procedure to obtain the scattered wave field due to the presence of a crack on hole…………………………………………………... 122

Figure 5.3.2: (LEFT) 450x450x3mm aluminium plate FE geometry showing the location of the crack, 45° 2D FFT scan line, scattered wave measurement; the excitation point and excitation point (RIGHT) Near hole diagram portraying the crack location and origin of the cylindrical coordinate system at centre of the hole…………………………….... 123

Figure 5.3.3: (LEFT) Experimental setup of 3D Laser Vibrometer and specimen. (RIGHT) Close-up image of the hole with crack attached with retro-reflective film……………………… 125

Figure 5.3.4: Plots of 2D FFT FE dispersion curve indicating that (LEFT) a dominant S0 wave in the r component;(RIGHT) a dominant SH0 wave in the θ component…………………... 126

Figure 5.3.5: Normalised scattered wave polar plot of SH0 waves with respect to the incident wave maximum displacement. (a) 0.05≤a/λ≤0.11; (b) 0.14≤a/λ≤0.20……………………… 127

Figure 5.3.6: Normalised scattered wave polar plot of S0 waves with respect to the incident wave maximum displacement. (a) 0.05≤a/λ≤0.11; (b) 0.14≤a/λ≤0.20……………………… 127

Figure 5.3.7: FE and experimental results: Normalised scattered SH0 wave displacement for various a/λ in (a) 0˚-180˚ region and (b) 180˚-360˚ region with respect to the incident wave maximum displacement……………………………………………………………...127

Figure 5.3.8: FE results: Normalised scattered S0 wave displacement for various a/λ in (a) 0˚-180˚ region and (b) 180˚-360˚ region with respect to the incident wave maximum displacement……………………………………………………………………… 128

Figure 5.3.9: Snapshot of experimental scattered SH0 wave field at time 40μs for (a) a/λ≈0.14, (b) a/λ≈0.16 and (c) a/λ≈0.20………………………………………………………... 129

Figure 5.3.10: Experimental and computational comparison of the normalised scattered wave polar plot of SH0 waves with respect to the incident wave maximum displacement for (a) a/λ≈0.14, (b) a/λ≈0.16 and (c) a/λ≈0.20…………………………………………….. 129

Figure 6.1: Time snapshot of the experimental wave field in the vertical component of the edge-guided wave propagating around the rectangular curved slot at 20, 40, 60 and 80μs…………………………………………………………………………..... 133

Figure 6.2: Baseline subtraction of total wave field with crack and original wave field without crack to obtain the scattered wave field due to the presence of a hidden crack……………....134

Figure 6.3: (LEFT) Model configuration of the rectangular curved slot centre in a 450 x 450 x 3 mm aluminium plate. (RIGHT) Close-up diagram of rectangular slot showing excitation and crack location…………………………………………………………………...135

Figure 6.4: (LEFT) Laser vibrometry setup showing 450 x 450 mm aluminium plate with retroreflective sheet mounted on the positioning system (RIGHT) Close-up image of crack and PZT bonded on the rectangular slot edge……………………………………138

Figure 6.5: (a) Plots of 2D FFT FE dispersion curve indicating (a) a dominant S0 wave in the r component; (b) a dominant SH0 wave in the θ component; (c) a symmetric edge-guided wave along the straight boundary……………………………………………………139

Figure 6.6: The experimental and FE attenuation of incident circumferential edge wave displacement over the circumference. Interpolation line indicates a rate of inversely proportional to power of 0.55 over distance/wavelength……………………………… 140

Figure 6.7: FE normalised scattered wave polar plot of SH0 waves with respect to the incident wave maximum displacement. (a) 0.04≤a/λ≤0.19; (b) 0.22≤a/λ≤0.34……………………… 140

Figure 6.8: FE normalised scattered wave polar plot of S0 waves with respect to the incident wave maximum displacement. (a) 0.04≤a/λ≤0.19; (b) 0.22≤a/λ≤0.34……………………… 141

Figure 6.9: (TOP) Snapshot of experimental in the angular cylindrical component showing a dominant scattered SH0 wave field at time 70μs and (BOTTOM) Experimental and FE normalised scattered SH0 wave patterns for (a) a/λ≈0.19, (b) a/λ≈0.26 and (c) a/λ≈0.34 …………………………………………………………………………………… 142

Figure 6.10: FE and experimental results: Normalised scattered SH0 wave displacement for various a/λ and (b) FE results: Normalised scattered S0 wave displacement for various a/λ with respect to the incident wave maximum displacement………………………………… 143

Figure 6.11: Experimental and computational comparison of the normalised scattered wave displacement of the edge-guided waves with respect to the incident wave maximum displacement, compared with analytical Rayleigh wave case [129]…………………... 143

Figure 6.12: Stress variations associated with the incident edge wave, as a function of depth y from the edge………………………………………………………………………………144

Figure 6.13: Scattered wave field representation due to the contribution of force-doublets associated with the mode I and mode II crack opening displacements…………………………… 145

Figure A.1: (TOP) Longitudinal wave and (BOTTOM) Transverse wave and their particle oscillation direction……………………………………………………….…….......................... 169

Figure A.2: Reflection, transmission and mode conversion of incident longitude wave at an angle……………………………………………………………….……...................... 174

Figure A.3: Ray representation of reflection of SH-wave from a free boundary………................. 177

Figure A.4: Ray representation of the reflection of P-wave from a free boundary…………..…...... 178

Figure A.5: Amplitude ratios A2/A1 and B2/A1 for incident P wave for Poisson's ratio v=1/3…...178

Figure A.6: Ray representation of the reflection of SV-wave from a free boundary………………. 179

Figure A.7: Amplitude ratios A2/B1 and B2/B1 for incident SV wave for Poisson's ratio v=1/3… 180

Figure A.8: Rayleigh wave propagation…………………………………………………………… 181

Figure A.9: Rayleigh wave speed as a function of Poisson's Ratio using the approximation expression………………………………………………………..........................184

Figure A.10: Relative normal and shear stresses of Rayleigh wave as a function of depth/wavelength ……………………………………………………………………………………… 184

Figure A.11: Boundary conditions at y=±b on isotropic plate for Lamb wave propagation………… 185

Figure A.12: Dispersion curve for the symmetric and antisymmetric modes in a 3mm aluminium plate ……………………………………………………………………………………… 194

Figure A.13: Stress through thickness profile of mode shape (LEFT) S0 mode and (RIGHT) A0 mode in a 3mm aluminium plate at 200 kHz frequency (BLUE) in-plane stress (RED) out-of-plane stress and (GREEN) shear stress…………………………………………………194

Figure A.14: (LEFT) Dispersion curve in terms of phase velocity. (RIGHT) Dispersion curve in terms of group velocity……………………………………………………………………..195

Chapter 1

Introduction & Literature Review

This thesis reports on the potential use of scattered Lamb wave field measurements to detect and quantify small, hidden cracks, or cracks in hard-to-inspect location. This is done to address the challenges posed for structural health monitoring (SHM) techniques due to the innovation in airframe designs. The target is to establish new fundamental science to address a lack of development in diagnostic capability, which will complement the modern manufacturing design that has serious implications for the safety of future aircraft.

The investigation of the scattered wave field from a known crack dimension and location is a pre-requisite forward problem for a subsequent attempt to investigate the inverse problem of characterising the crack size based on the scattered field measurements. This chapter establishes the relevant background for understanding the use of elastic waves to detect and quantify damages in an isotropic medium for SHM. This first chapter reviews the following:

1. The necessity of novel inspection and utilisation of Lamb wave propagation for structural integrity monitoring.
2. The fundamental understanding of elastic wave and Lamb wave propagations.
3. Scattering wave modes by characteristic features for assessing and characterising defects.
4. Use of analytical representation models for scattered wave field and measurements for quantification purposes.

1.1 Background

1.2.1 Motivation

The extensive improvements of structural performances in weight reduction, fuel efficiency, affordability, and producibility have resulted in unitised components, especially for manufacturing of airframe for A380, A350 and B787. Ultimately, major aircraft manufacturers have pursued to reduce production costs by replacing multi-piece fastener assemblies with unitised components [1, 2]. Significant reduction of aluminium sheets and fasteners will result in weight saving, and will result in the improvement of fuel efficiency and reduction in greenhouse gas emission. Unitised components will help improve package payload per unit of energy and reduction of part counts that enhance transport efficiency, according to Renton [3].

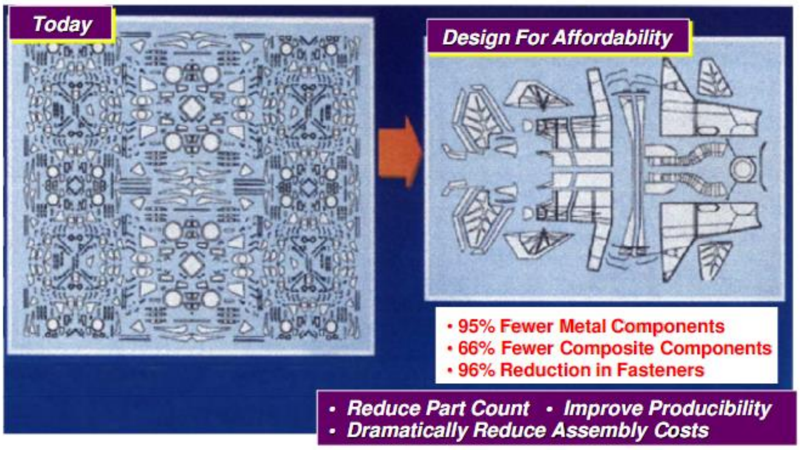

Figure 1.1: Benefits of unitised components [2]

Metallic structures are known to withstand compression loading well, exhibit high ductility, flexibility, and considered low-maintenance in manufacturing design. Hence metallic structures are widely used in the aircraft industry [1]. For example, a F-22 fighter jet has a majority structural weight distribution with 39% titanium [2], which is a superior choice for enduring both tensile and compressive loads, and is highly resistant to corrosion. The combination of composites and titanium is frequently used to achieve structural efficiency and reduce aircraft weight. However, fatigue cracking and corrosion are still common problems for metallic components.

The presence of fatigue cracks in metallic aircraft structure is a critical issue and require inspections as it can lead to failure of the structure [4]. Regular non-destructive inspection can ultimately reduce the risk of fatigue crack failures by evaluating and repairing crucial areas [5]. However, it is not feasible for unitised components to be disassembled for the current conventional non-destructive inspection, and making it difficult to detect defects [6]. A traditional approach, such as eddy current technique, would require disassembling of components. This approach is time-consuming as it is required to completely empty the fuel for the diagnosis process [7]. Other methods discussed by Ihn and Chang [8, 9], require built-in or already bonded sensors and actuators for diagnostics, which are unlikely to be reliable in detecting hidden defects. Also, modern improvements in aircraft components design do not usually account for inspection or maintenance. This gives rise to a hard-to-inspect region, which requires different inspection methods than the conventional inspection to complement the advanced technologies and improvements. For a successful implementation of unitised component in the next few decades, research on an innovative structural inspection procedure is required.

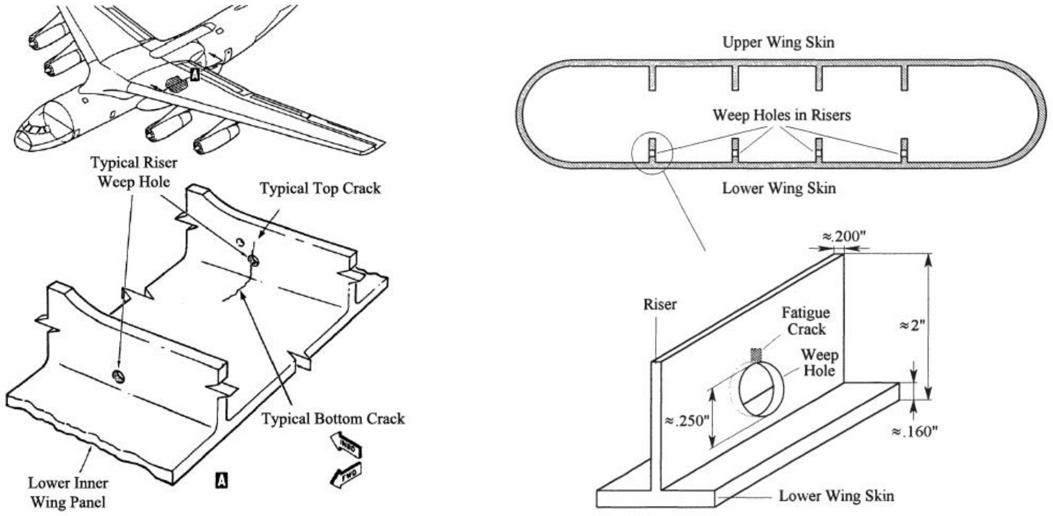

Figure 1.2: Schematics of fuel weep hole and location of typical cracks [10, 11]

A specific example of a hard-to-inspect region is the fuel weep hole (Refer to Fig 1.2). The configuration is common in current metallic aircraft components, including primary or flight critical structure and therefore poses a significant challenge [4, 10]. The fuel vent hole in the riser acts as a stress concentration location. Thus, it is vulnerable to fatigue cracking and due to the presence of flammable fuel inside the wing, restricts electrically powered diagnostic sensor to the locations external to the wing. Traditional ultrasound method can be used for inspection if fatigue crack initiates from the bottom of the hole, given the accessible region is on the lower inner wing panel.

Previous studies have found that if the fatigue crack initiates from the bottom of the hole, the conventional ultrasonic method can be used for inspection [12]. However, if the fatigue cracks initiate from the top, the crack becomes hidden in the geometrical shadow zone of the incident ultrasonic wave. Thus, the conventional wave based in-situ structural health monitoring methodologies will not be able to detect the crack. Previous studies [7] have tackled this problem by using conventional wedge-transducers and circumferential creeping waves propagating around the hole boundary to detect cracks in the shadow zone. More recent experimental and computational studies [13-15] have indicated the possibility that the scattering phenomenon due to the defect can be utilised to characterise the damage for the hard-to-inspect fuel vent hole in the wing spar of an ageing aircraft.

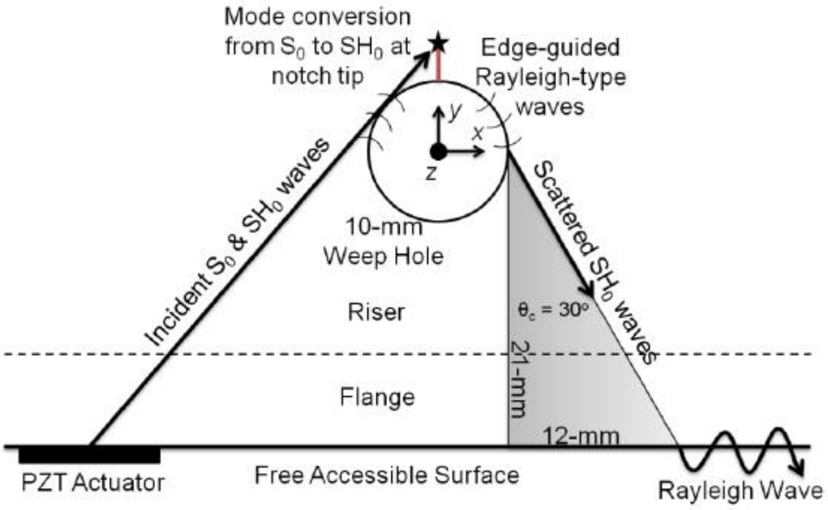

Figure 1.3: Damage detection around a through hole by Rayleigh wave generation on the accessible surface [14]

Doherty and Chiu [13] suggested that the scattering at the defect tip can be attributed to the presence of fundamental shear horizontal (SH0) wave mode in the riser section. The scattered SH0 wave field from the defect is subsequently shredded from the defect onto the external wing-skin, as shown in Fig. 1.3. Further research is required to understand this interesting spiralling phenomenon and scattered wave field measurement to optimise the detectability and potential quantification of defects on the blind side.

1.2.2 Scope

The key purpose for structure health monitoring is to locate a crack before it reaches a critical size, which may result in catastrophic failure. Lamb waves normally operate in the low frequency range of 50-300 kHz, compared to ultrasonic wave diagnostic methods which exceed 4 MHz. This means the Lamb wave scatter investigation is at the long wavelength limit, where damage dimension is smaller than the incident wavelength. The thesis explores the scattered wave by small defect behaviour in the long wavelength limit and models it as a simple source.

This research objective is to determine useful scattered wave measurements due to the presence of a small crack in a hard-to-inspect location of isotropic material. The behaviour of the scattered wave field is modelled corresponding to point source equivalence. The study first investigates a simple edge crack problem on a plate before introducing a complex geometry. For each stage, the previous findings will guide the following configuration and study setup.

The scope of this thesis is outlined by reviewing on:

- Whether the small crack can be equivalent to a point source model and, if so, under what limitations.
- The relationship with scattered wave measurements and crack length and can it be used for small crack diagnosis.
- What conditions must be satisfied to direct edge-guided waves around a curved boundary to a hidden location?
- To demonstrate whether the previous findings are still applicable in a hard-to-inspect rectangular slot problem.

1.2 Lamb Wave

Lamb waves are elastic thin-plate waves propagation discovered by Horace Lamb [16] and Worlton introduced Lamb waves for damage detection in 1957 [17]. After the discovery of Lamb waves, many published papers emphasised the development and usage of Lamb wave for applications in aerospace and civil industries. The fundamental theory for elastic waves is extensively discussed and derived in the literature by Graff [18], Achenbach [19] and Auld [20].

Lamb waves have been considered for non-destructive evaluation because of their desirable properties [21], such as long distance propagation and sensitivity to defect detection. Lamb wave has advantageous qualities for structural health monitoring, as it is far more efficient when used for non-destructive inspection compared to other conventional methods. Such methods are limited to localised scanning, and requires components to be disassembled making them time-consuming. Furthermore, recent works that indicate the field of research in Lamb wave non-destructive evaluation is currently very active [22-26]. However, there is no analytical solution for challenging application such as complex structure and composite materials.

1.3 Elastic Wave Propagation

Early elastic wave propagation literature had studied on seismology [27]. In the past few decades, elastic wave for structural health monitoring has been studied extensively and has become an active field of research.

The derivation of elastic wave and applications can be found in Graff [18] and Achenbach [19]. In elastodynamics, the equation of equilibrium for the elastic displacement (static elasticity) is formed through definitions of infinitesimal strain, stress and the constitutive relation of strain and stress. The derivation of elastic wave and Rayleigh-Lamb waves can be found in APPENDIX A1-A5.

1.4 Lamb Wave based non-destructive evaluation

In the past decade, many studies focused on the scattering field of a defect in a plate at low frequency [13, 28-32]. At low frequency, the symmetric Lamb wave stresses along the thickness of the plate are simple and almost uniform. Therefore, the defect sensitivity for detection does not depend on thickness. Low frequencies wave propagations have become desirable in non-destructive evaluation due to the low dispersion (group velocity does not change significantly with frequency) and low leakage of energy if immersed in liquids. At higher frequency-thickness product, multiple modes will exist, and the signal will be difficult to interpret. Hence, it is more desirable to have single modes, and this can be done by exciting waves at low frequency. Lamb waves in plates at low frequency; SH1 cut-off of approximately 1.53 MHz-mm [33] for aluminium, comprise of at most three fundamental modes: antisymmetrical (A0) mode, symmetrical (S0) mode, and shear horizontal (SH0) mode. It is known that symmetric waves are more sensitive to through-thickness defect, and antisymmetric waves are sensitive to in-plane defect due to their thickness stress profile [34]. Hence, A0 is used more in recent research for applicable detection of composite delamination [35, 36].

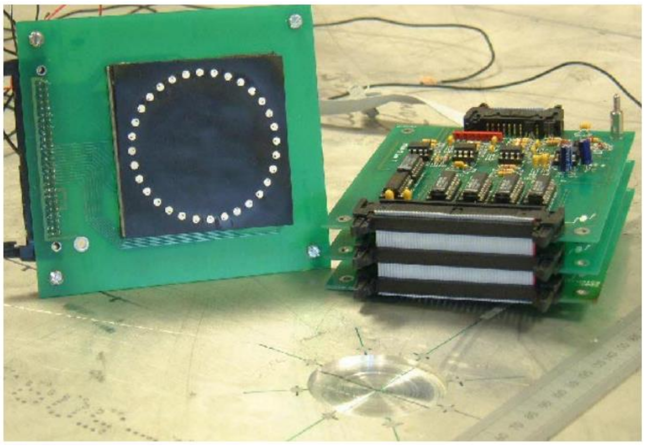

Figure. 1.4: A compact, permanently attached, autonomous guided wave array prototype and multiplex electronics unit on aluminium plate with circular part-through hole [37].

Arrays or arrangement of built-in electric sensors is a standard technique for Lamb wave based damage identification as shown in Fig. 1.4. Many researchers [8, 24, 38-41] used embedded piezoelectric transducers to monitor fatigue crack and probabilistic methods to locate and characterise crack in plate-like structures. These SHM techniques involve using comparative baseline data, which originally requires the structure to be without damage. It is highly impractical to obtain an initial set of data in operational conditions. To overcome these complications, researchers have proposed baseline-free methods [42-44]. Furthermore, time reversal method approach became a recognisable technique among researchers in the field of Lamb wave to perform SHM without the need for baseline data [45-49]. However, a complex structure such as the fuel weep hole restricts the number and arrangement of transducers to a limited region, which makes the use of multiple sensors no longer optimal, thus give rise to a hard-to-inspect problem [4, 13-15]. A novel form of diagnostic by integrating active smart patch was studied by Rajic et al. [50]. Due to the size of these patches, they can impact on the structural integrity of the component due to the discontinuity in elastic modulus. Once embedded into a structure they become inaccessible for maintenance. Doherty and Chiu [13-15] experimental and computational studies showed elastic waves could impinge with a hidden crack, however, did not explore further in depth on the significant of scattered wave measurements for quantitative crack characterisation. This will be useful to study and to understand more information on this scattering.

Low frequency symmetric and shear horizontal Lamb wave modes are an attractive option for long range non-destructive evaluation due to its non-dispersive nature and uniform stress thickness profile. Diligent and Lowe [28-30, 51-53] have published a considerable amount of work on the fundamental Lamb wave modes interaction and collaborated with other researchers. In an particular S0 interaction study, Lowe and Diligent [29, 30] used reflection characterisation for a notch in a plate and showed good agreement with the theoretical result at low-frequency Lamb wave mode. They also stated that quasistatic approximation could be used to identify open cracks up to approximately the quarter of the plate thickness, whereas higher frequency is not as easily modelled due to the dispersive wave nature which other researchers have done the same [23, 54-57]. The difficulty in generating only S0 in their experimental investigation has been discussed. A conventional method to excite S0 Lamb waves is aligning a plane transducer at an angle to the surface. This can be done by a wedge transducer or coupling through a local fluid bath. An alternative method is to use two PZT applying symmetrical loading to generate S0 waves [28, 58]. To ensure an S0 wave, the transducer must be symmetric at the centre line of the plate to avoid the unwanted A0 mode. Regardless, A0 can still be easily generated even using the wedge, fluid bath or symmetrical two PZT techniques.

Some studies have focused on shear horizontal waves in the zeroth order, SH0. These waves exhibit non-dispersive quality throughout all frequency, negligible attenuation and no change in signal shape changing and are sensitive to the crack oriented along the propagation direction. Studies such as Rajagopal and Lowe [31] and Ratassepp et al. [32] investigated notches and defects due to SH0 attractive qualities. They also measured the reflection behaviour influenced by the distance of the source. This is done by exciting SH0 dominating in the direction to the defect, while S0 propagates perpendicularly away such that maximum amplitude of SH0 impinges with the crack and minimal S0 waves interacts with the crack, refer to Fig. 1.5. Although a large specimen is required, this is a simple technique to ensure the appropriate wave mode interacts with the defect. Recent studies have investigated shear PZT sensors to excited SH0 waves [60-63]. A study by Seung et al. [64] has investigated on a newly development omnidirectional shear-horizontal guided wave EMAT without exciting other modes.

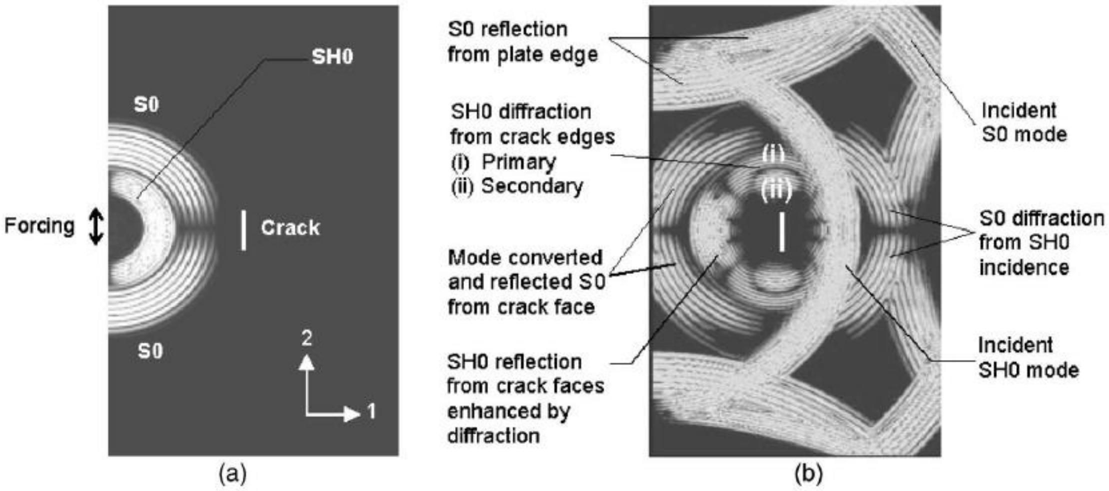

Figure 1.5: Scattering features due to the incident of predominately SH0 waves impinging with a vertical crack, Rajagopal and Lowe [31]

Furthermore, in the near field, scattering is affected by the diffraction phenomena. Rajagopal and Lowe [31] and Ratassepp et al. [32] stated that the scattering field is the interference between the primary diffraction from the crack tip and secondary diffraction, Rayleigh-like waves travel along the crack and radiate from the crack tip. The waves travelling along the crack face are surface waves, which are closely related to Rayleigh waves. It is observed that the leaky surface waves interact with the body waves and the undulation in the reflection signals as also observed by Diligent et al. [28] as well, although in a different geometry.

Many previous mentioned Lamb wave studies focused on the analysis of wave interaction with large crack length relative to incident wavelength [30, 51, 58]. There is a lack of Lamb wave investigation on early development crack; small crack (relative to incident wavelength), and techniques for quantifiable diagnosis. It is particularly difficult to detect scattered Lamb wave at low frequency due to the size of the defect, where high frequency are often used because of smaller wavelength [21].

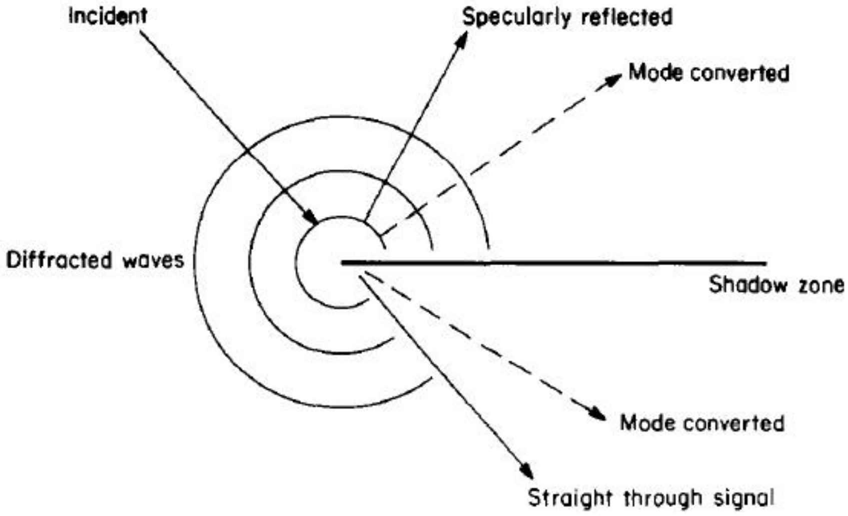

Figure 1.6: Diagram of the interaction of an incident wave with a defect [65]

For nondestructive testing, Ogilvy and Temple [65] and Scruby et al. [66] assumed plane-strain, and discussed diffraction of elastic waves and used the time-of-flight method. When an impinging wave is in the same order as the defect and interacts with the crack, three possible outcomes are noted: (i) Specular reflection from the crack face, (ii) Rayleigh waves travelling along the crack surface, and (iii) Radiating energy when reaching the crack tip, and diffraction or scattered cylindrical waves originating from the crack tip, refer to Fig. 1.6. Ogilvy and Temple [65] indicated that an optimal angle incident would provide a maximum scattering to incident amplitude ratio. In such a case, the far-field approximation for the results is equivalent to theoretical results.

Unfortunately, since Lamb waves are dispersive in nature, group velocity changes significantly with frequency. This means waves excited at different frequency components of the wave will travel at different speeds and the pulse shape will change as it travels along the distance. Thus, long-range inspection is rather difficult. A study to predict the linear spreading of wave dispersion and attempt to limit the excited bandwidth such that little dispersion occurs was reported by Wilcox et al. [68].

It has been reported that scattered wave measurements carry essential information to characterise the crack. The scattered amplitude is a common quantity to evaluate the crack size, in contrast to scattered wave mode and pattern. The majority of researchers only reported on scattering wave amplitude at fixed locations and some studies [28, 54-56, 67] provided the radiation patterns due to the defect to show the relationship between relative amplitude and angular dependence. The scattered wave mode is an effective quantity for potential crack characterisation especially for application with non-symmetrical defect or geometry. In a symmetrical geometrical problem, an incident symmetric Lamb wave mode will only reflect or scatter symmetric Lamb wave mode, vice versa with antisymmetric Lamb wave modes. On the other hand, non-symmetrical applications such as partial through-thickness featured studied by Diligent et al. [53] and Grahn [56], an incident Lamb wave mode can mode convert to the anti-symmetric and symmetric wave modes.

To acquire the scattered wave pattern, a common and simple technique is to use circular array around a defect [37, 55]. The disadvantage of this technique is that the incident and scattered waves will interact with the multiple sensors. Thus, the detected signal will involve scattered by the defect and sensor. Another method is to use Laser Vibrometry to scan and produce a 2D wave field [6, 24, 57, 74-76]. The Laser Vibrometry eliminates embedment of multiple sensors on a test specimen, which makes them highly advantageous choice to observe wave propagation. However, only a few researchers have access this expensive equipment and it has been currently used for research in the field of Lamb wave propagation since it is impractical to be installed on real structures, unlike PZT. The Laser Vibrometry and PZT are further discussed in Chapter 2.

A recent comprehensive review by Mitra and Gopalakirshnan [69] covered the last decade and discussed on current and possible future areas of research in guided waves based SHM. It has been reviewed that a majority of researcher still use time and frequency analysis in Lamb wave investigation to analysis and characterise damage in plate [70-73]. A popular modal content analysis involving 2D Fourier Transformation is commonly used among researchers to post-process wave amplitude and frequency. More details on post-processing analysis are discussed in Chapter 2.

1.5 Edge-guided and creeping waves

In a plate, two edge waves exist: the symmetric edge-guided wave (plane-stress analogue of Rayleigh waves [77]) and anti-symmetric edge-guided waves, which also decays exponentially with distance from the free edge. These Rayleigh-like waves propagation are described as the superposition of the antisymmetric and symmetric Lamb wave modes [78]. The existence of edge-guided Rayleigh-like waves was first demonstrated by Viktorov [78] and later the first dispersive edge wave was derived by using the classical theory of plate bending in Konenkov [79]. The approach to finding the solution and dispersion relation involve the same methodology as Rayleigh wave in APPENDIX A.5, however, requires implementation of approximate theories, such as classical Kirchhoff plate theory to reduce to the Poisson plate theory for antisymmetric waves and Mindlin plate theory reduce to Poisson plate theory for symmetric waves. These theories are considered to solve edge wave solutions at very low frequency in isotropic plates [80-82]. For higher frequency range, an asymptotic expansion technique is used to determine the high-order dispersion relation [83]. Thurston and McKenna [82] used the classical theory of thin plates, and Norris [81] approximated the solution for anisotropic plates in thin shells. Galinde et al. [84] used semi-analytical and finite element approach to approximate a solution for edge waves in anisotropic silicon and mode shape for symmetric and antisymmetric edge waves.

These previous findings on the approximate solution of the elastic equation for edge-guided waves, which are also verified experimentally and computationally, are consistent among researchers.

Krushynaska [85] was one of the studies to provide a complete analytical study using superposition method to solve low frequency edge wave speed, which is essentially independent of Poison's ratio and similar to Rayleigh wave speed. The study was in good agreement with the experimental edge wave study by Lagasses and Oliner [86]. Furthermore, extensive work by Zernov [87] investigated symmetric edge guided waves speed and dispersion with different boundary conditions. At the low frequency-thickness limit, the edge wave mode is almost uniform across the plate thickness and remains essentially non-dispersive, which is ideal for through-crack detection. Whereas, at high frequency, the edge wave energy localised at the plate edge, rapidly decays along the plate height and are dispersive. Further edge wave analysis at high frequency requires approximate approach are derived by Zakharov [83] to take account for in and out-of-plane motions.

Theoretical work by Rulf [88], as well as literature from Graff [18], Ewing et al. [89] and Viktorov [78] derived the elastic wave propagation in the cylindrical core. Given that condition of the hole surface is a stress-free boundary, in cylindrical coordinates with the z-axis along the axis of the cavity, such that the boundary conditions are $\sigma_{r\theta} = 0$ and $\sigma_{rr} = 0$, when $r = a$. Considering plane strain conditions, there is no z-axis displacement or variation along that direction i.e. $\frac{d}{dz} = 0$. Studies relating to the Lamb wave scattering of the hole were investigated by McKeon and Hinders [67], Chang and Mal [54], and Fromme and Sayir [55], developed analytical approaches, by using Kane-Mindlin higher order and other plate theories. As a result with analytical benchmarks, many researchers had investigated scattering Lamb by a hole computationally and experimentally as well [28, 37, 55, 56, 67, 90, 91]. Furthermore, partial through-thickness hole is also studied to approximate corrosion and other composite defects [53, 56].

The traction-free and plane strain conditions are considered into the stress equations in cylindrical coordinates to solve for the elastic wave propagating around the hole circumference. Analytical derivation and analysis of Rayleigh wave propagating around the hole has been discussed [78, 88, 89].

The nontrivial solution of edge wave propagating around a cylindrical surface [78] can be approached by setting its determinant of coefficients to zero. This will lead to complex roots, which associate to the property of amplitude decay with propagating distance. However, edge-guided waves on the hole circumference are not yet analytically solved and will require approximate theories, similar to the scattering of the hole [67].

Approximation attempted for Rayleigh wave on curved surface implies that the decay is a function of diameter to wavelength ratio [78, 88, 92]. On the other hand, surface waves propagating on a straight boundary have no geometrical decay with propagating distance. Their investigations developed a fundamental framework on wave propagating on the circumference of the hole. This is done by taking the characteristic length wavelength to diameter ratio, λ/d, and deriving the equation of motion in cylindrical coordinates. Furthermore, an equation is established and shows a dispersion function of a ratio of the wavelength to the diameter of the bore. At the asymptotic limit, the surface wave wavelength is equivalent to Rayleigh wave wavelength at a plane boundary. This argument does reduce the surface wave propagating on the curved surface equation to Rayleigh wave at a plane boundary equation. The features of the equation indicate that the phase velocity increases when wavelength increases. However over a critical wavelength, due to the increasing phase velocity with wavelength, these edge waves cannot propagate around the circumference without attenuation [88]. The effect is explained by the fact that over the cut-off wavelength will cause shear waves to radiate and the energy of the surface wave to dissipate. The cut-off wavelength highly suggested this scenario when the diameter is smaller than the wavelength. This had raised questions on wave propagating curved surfaces as well as visualising the effect caused by these surface waves which led to further studies to investigate this matter.

Scattering of bulk waves by cylindrical cavity was first discussed and visualised using photoelasticity by Ying et al. [93] in the context of plane-strain scattering from circular holes, refer to Fig. 1.7. The incident wave is shown to creep around the hole into the shadow zone and circulates for almost the entire circle. This led to the first visualisation of creeping waves and featured its unique ability to circulate the circumference and researchers started exploring possible applications [7, 11, 94, 95]. It is valid to note that creeping wave coherently exists with the propagating surface wave on the circumference of the hole and that Rulf's theoretical work [88] closely relates to the existence of creeping waves.

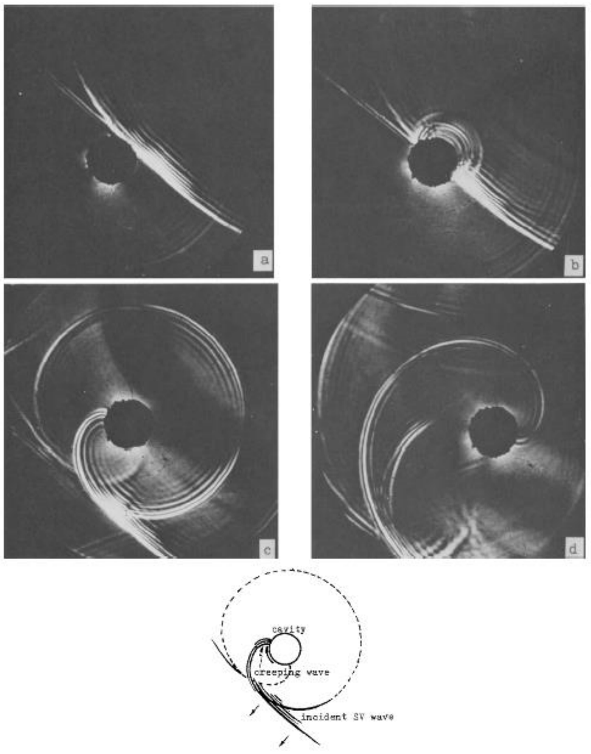

Figure 1.7: Snapshot of incident wave creeping around the hole [93]

Hurst and Temple [94] investigated the velocity of the creeping waves and their applications to non-destructive testing. They used time-of-flight method, which is the time difference between the arrivals of the signals from the upper surface of the hole to the nearest receiver, to determine the speed as well as the size of a defect, if present. The speed of the creeping wave is a function of parameter *ka*; where *k* is wave number, and *a* is the radius of the cavity and is not necessary the same as a bulk wave speed. Hurst and Temple [94] studied *ka* ranging from 0 to 20. Small *ka* values showed that the creeping wave velocity of compression wave is only 85% of the bulk velocity. At larger *ka* value of 300, the creeping wave is 98% of the bulk wave velocity for compression waves. They indicated a practical sense to determine defects by using creeping waves and time-of-flight method.

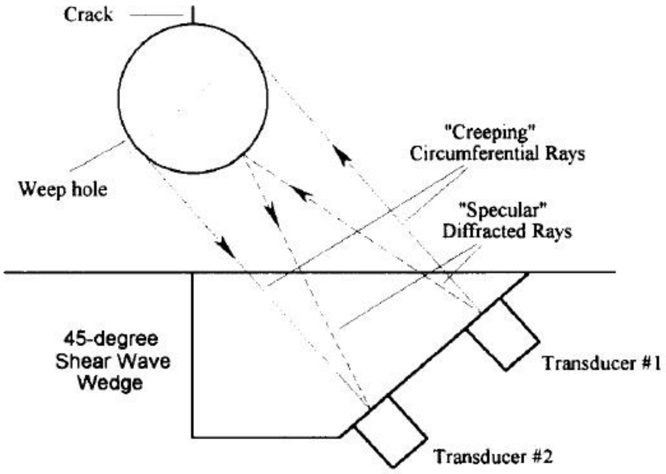

Figure 1.8: Diagram of the dual transducer to detect creeping wave [7]

Nagy et al. [7] was the first study to proposed the use of the circumferential creeping waves propagating around the hole boundary to detect cracks in the optical shadow zone. Conventional ultrasonic techniques often have difficulties to detect the creeping waves signal, which disappears from the specular reflection signals. Rather than using the conventional ultrasonic inspection technique, Nagy et al. [7] implemented two small-diameter transducers on the same wedge in either pulse/echo or pitch/catch mode for detection sensitivity and comparison, as shown in Fig. 1.8. This technique eliminates the detection of backscattering reflection from the weeping hole surface and increases creeping wave signal. The detectability of the weeping hole crack greatly depends on the crack size. However, the diameter and uneven chamfer increases the noise signal. Hence it becomes difficult to inspect. The depth of the crack has to be in similar order as the wavelength, and preferable be open to cause scattering than ensuring transmission. The effect of crack depth with uneven thickness is an adverse effect on the detectability of the flaw. The energy of creeping wave is concentrated near the surface region, and a through-thickness crack produces the strongest scattering. Due to the phase velocity difference of the leaky and Rayleigh wave, the surface wave attenuates by leaking energy into the surrounding material. The leakage significantly decreases with increasing frequency, and the attenuation becomes a problem if the frequency is too low, while higher frequency cannot effectively excite creeping waves.

Further studies by Aldrin and Achenbach [96] and Hassan and Nagy [95, 97] have expanded on the research of Nagy et al. [7] and led to further investigations on circumferential creeping waves, fluid-filled holes and time-of-flight method to determine arrival times for leaky Rayleigh waves.

Diligent et al. [28, 53] has worked on the 2D plane strain problem which represents a 3D shape in a low frequency of excitation to predict the reflection and scattering field. This is done while varying diameter, frequency and detection distance away from the hole. They found that the reflection exhibit an undulation effect. This is considered as a secondary reflection, which consists of reflected SH0 waves, and creeping waves which travel around the circumference of the hole. However, the creeping waves were only briefly mentioned, and no additional investigation was conducted to discuss the attenuation and properties of the creeping wave. Diligent et al. [28] provided extensive knowledge in regards to scattering and reflection of S0 mode from a hole, experimentally, analytically and computationally. They were able to conclude that the normalisation of the distance and hole diameter at a frequency of 100 kHz is a common trend, in which computational and experimental analysis agrees well with the analytical results.

It was not until a more recent study by Doherty and Chiu [13-15] took advantage of the creeping waves and continued the fuel weep hole problem. Doherty and Chiu reported both experimentally and computationally, a distinctive spiralling phenomenon due to scattering at the defect, as shown in Fig. 1.9. They showed the SH0 scattering phenomenon can be used to monitor the growth of the fatigue crack in the shadow zone of a hole although no quantitative measurement was demonstrated to assess the fatigue crack. Furthermore, they found that the scattered SH0 mode from the defect is subsequently converted to a Rayleigh-type wave on the free surface of the flange. They suggested that the magnitude of this Rayleigh wave mode can be used to characterise the fatigue crack on the open hole within the structure, thereby providing a novel and effective inspection technique for this hard-to-inspect location. Crack development in hard-to-inspect areas and blind areas which may require the use of scattering phenomena and other measurements beside amplitude to monitor these cracks.

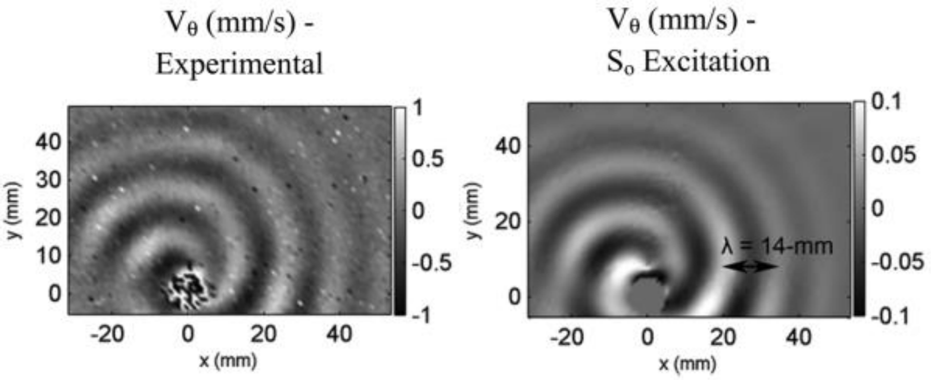

Figure 1.9: The experimental and computational cylindrical scattered wave field indicated a spiral-like scattering in the angular component where the origin is at the centre of the weep hole [14]

Their results indicate that for both A0 and S0 input the θ direction scattered field are of similar magnitude for both inputs. The dominant wavelengths of these scattered fields are the same, suggesting that they are attributable to the SH0 mode. In their experimental results, the A0 component scattering appears more intense than the S0 component even though the incident wave has a higher S0 content. In their study, it is unsure whether A0, the antisymmetric edge-guided-wave or the combination of these two waves interacted with the crack. Furthermore, this is particularly unusual because it contradicts previous studies and theory where symmetric waves should be more sensitive to through-thickness crack. There is a need for investigations on this phenomenon and to address this unusual dominant scattering A0 mode. In addition to previous work [54, 56, 67], further investigation on the A0 and S0 scattering wave patterns and directivity due to the crack on holes with varying hole diameter size is also essential to understand this spiralling phenomenon.

Doherty and Chiu stated that A0 mode is more amenable to the scattering process and possibly that A0 mode being able to mode convert to a surface wave that travels around the open hole and interacts with the defect. Elastic waves travelling around the open hole is anticipated to attenuate similar to the leaky Rayleigh wave.

According to the Doherty and Chiu experimental and computational results, the spiralling scattered wave field can be seen to leak SH0 wave tangentially to the open hole. Chang and Mal [54] have already investigated the cracks on the hole using two receivers and their results were verified with the theoretical model of the hole which acts as a source [98]. The scattered phenomena found in Doherty and Chiu work is most likely to be an SH0 source creeping around the hole boundary. There is a lack of a complete; analytical, FE and experimental, study on edge waves circulating a curve boundary.

Studies by Nagy [7, 97], Hurst and Temple [94], and Doherty and Chui [14] provided the knowledge of surface wave propagating on the cylindrical circumferences and its possible application. Additional investigations are needed to determine the scattering amplitude signal and scattering pattern of a defect with varying incident angle in a plane stress case. These are worth investigating specifically on creeping wave and its interaction with the hole to promote and advance detection for hidden cracks in complex metallic structures.

1.6 Small Crack Detection and Quantification

Over the past decades, methods of detection have been studied to detect fatigue crack in metallic structures. Time-of-flight method is a well-known technique to determine flaws in structures based on the travel of arrival and reflection of waves [65, 99]. Amplitude and energy spectrum parameters have shown to be a method of analysis for crack detection with Rayleigh wave incident [99, 100].

Reviews [101-103] discussed further on the theories of scattering of elastic waves by different idealised crack behaviours in media and suggested particular characteristic length for crack quantification. Previous studies [104-106] have provided analytical solutions to the plane strain diffraction of an elastic wave by crack. A significant contribution in the field of elastic wave interaction with several crack types by Mal [107-110] led forward further research in analytical and computational studies at that time.

There are many works done on crack characterisation methods, such as inverse scattering [111, 112] and time-domain ray tracing method [113, 114]. A particular area of interest for crack characterisation was under the quasi-static approximation of wave interaction. A quasi-static approximation of wave interaction with a finite crack was analytical approached by Sih and Loeber

[115, 116] and Teitel [117]. Rose and Krumhansl [118] and Resch and Nelson [119] reported on the relationship of crack size and amplitude of the scattered wave for crack monitoring and characterisation under the long-wavelength condition. Under this condition, the scattered wave strength is proportional to the integral of the crack opening displacement [119, 120]. The use of elastic wave on small fatigue surface-breaking in the long wavelength limit was also a popular study [121-126]. In plane strain case, scattering by Rayleigh wave was highly considered for surface-breaking, due to the absence of geometrical decay with propagating distance. Detection of small surface-breaking cracks has been investigated with the target of characterising the crack as a function of crack length [127, 128].

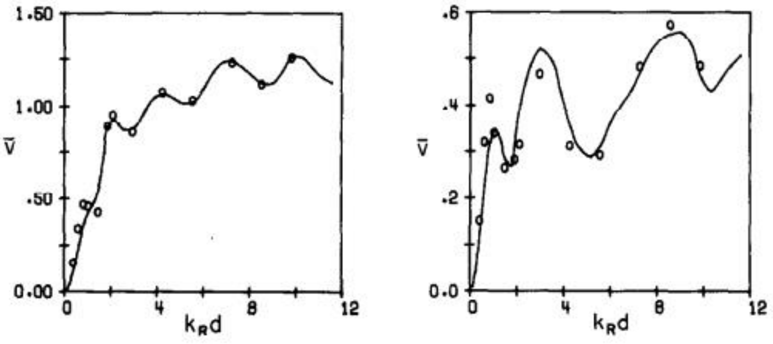

Figure 1.10: Vertical displacement of the (LEFT) forward and (RIGHT) back-scattered surface wave relative to incident wave amplitude [129]

The solution of the time harmonic elastic wave at a surface crack in plane strain has been solved analytically and numerically by Mendelsohn et al. [129] and Achenbach et al. [130, 131] refer to Fig. 1.10. Later many computational studies [132-134] of surface-breaking crack have compared their results to Mendelsohn and Achenbach theoretical solutions [129, 131, 135]. A particular study by Masserey and Mazza [72] analysed the near-field scattering at a surface crack using Laser Interferometer. It was not until their work that was able to experimentally quantify crack size from of crack length to Rayleigh wavelength ratio of 0.15 by using the combination of time and frequency domain as a method to quantify a surface crack in near field analysis for an entire range of crack length to Rayleigh wavelength, refer to Fig. 1.11.

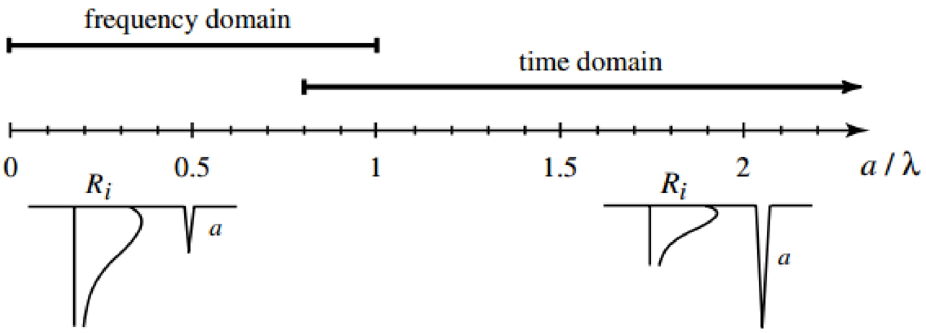

Figure 1.11: Frequency and time domain of sizing sub-procedure against crack length-wavelength ratio [72]

Analytical solution of wave scattering by a finite crack with an incident SH0 for high frequency has been attempted [136]. The solution to the plane wave reflection at a free edge for the incident S0 case has been recently solved by Gunawan and Hirose [137]. Their approach is to represent the scattered field as a sum of the guided wave modes including the non-propagating modes. Below the SH1 cut-off (1.53Mhz-mm), the reflection and mode conversion coefficient turn out to be very well approximated by plane stress theory. However, to obtain the representation of the field close to the edge, one has to use normal mode expansion. This can be done by determining the unknown coefficients in this expansion to satisfy the boundary conditions.

1.7 Point Source Equivalence

It is said that the crack can be represented by equivalent body force doublets. When these force doublets are applied in the absence of the crack, the same scattered wave field will be produced. This equivalent body-force has been well derived in seismology by Aki and Richards [27] and Burridge [138]. The equivalent body force for scattering due to a crack has been represented in previous studies [139-141]. More recently, Zhang and Achenbach [141] use this equivalent to a crack. However no study have utilised this point source equivalence for Lamb wave scattering by crack, refer to Fig. 1.12.

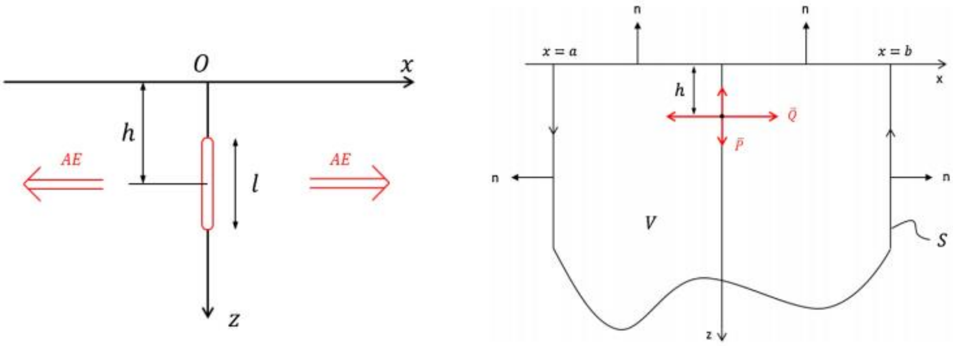

Figure 1.12: Equivalent body force represents acoustic emission from a sub-surface crack [141]

Consider an incident Lamb wave at an edge crack problem. For near-normal incidence, the solution of plane strain can be easily converted into plane stress. However, for a near-edge incident, the field that is generated when viewed along the y-axis includes a major component from an edge-wave in the addition of the plane wave at near-normal incidence. An approach is to analytically derive the stresses along the y-axis for a plane-wave incidence and the stresses for a point source. Based on the principle of superposition [20], the scattered wave field is equivalent to applying equal and opposite baseline stresses on the crack face that cancels those produced by the incident wave. This meets the condition of a stress-free crack. In the case of bulk waves [27], given the crack is sufficiently small, the summation of baseline stresses can be equivalent to the point source consisting of body-force doublets. The source term is caused by the crack displacement opening over length. It can be anticipated that a similar equivalence still holds for Lamb wave scattering.

1.7.1 Representation Theorem

Consider the equation of motion, recall from Eqn (A1.1) and rearranged such in vector and Cartesian tensor notation:

$$\nabla.\boldsymbol{\sigma} - \rho\ddot{\boldsymbol{u}} = -\boldsymbol{f}$$

$$\sigma_{ji,j} - \rho\ddot{u}_i = -f_i \tag{1.6.1}$$

Note that the symmetries of stiffness matrix c_{ijkl}

$$c_{ijkl} = c_{jikl} \text{ because } \sigma_{ij} = \sigma_{ji}$$

$$c_{ijkl} = c_{ijlk} \text{ because } \epsilon_{kl} = \epsilon_{lk}$$

$$c_{ijkl} = c_{klij} \text{ because } \frac{\partial W}{\partial \epsilon_{ij}} = \sigma_{ij} = c_{ijkl}\epsilon_{kl} \text{ hence } \frac{\partial^2 W}{\partial \epsilon_{kl}\partial \epsilon_{ij}} = \frac{\partial^2 W}{\partial \epsilon_{ij}\partial \epsilon_{kl}} \qquad (1.6.2)$$

For an isotropic material, we recall from Eqn. (A.1.3)

$$c_{ijkl} = \lambda\delta_{ij}\delta_{kl} + \mu(\delta_{ik}\delta_{jl} + \delta_{il}\delta_{jk})$$

And strain-displacement relations, constitutive equation from Eqn. (A1.4).

For Betti-Rayleigh Reciprocal Relation, consider the general time dependent case. Here, restrict attention to the time-harmonic field

$$\boldsymbol{u}(\boldsymbol{x},t) = \widehat{\boldsymbol{u}}(\boldsymbol{x},\omega)e^{-i\omega t} \; and \; \boldsymbol{\sigma}(x,t) = \widehat{\boldsymbol{\sigma}}(\boldsymbol{x},\omega)e^{-i\omega t} \qquad (1.6.3)$$

Consider two elastic states (identified by superscripts A and B), for the same body V, bounded by a surface S, and the same frequency ω, so that

$$\nabla.\widehat{\boldsymbol{\sigma}}^{\boldsymbol{A}} + \rho\omega^2\widehat{\boldsymbol{u}}^{\boldsymbol{A}} = -\boldsymbol{f}^{\boldsymbol{A}} \qquad (1.6.4)$$

Take the scalar product with $\widehat{\boldsymbol{u}}^{\boldsymbol{B}}$

$$\nabla.\widehat{\boldsymbol{\sigma}}^{\boldsymbol{A}}.\widehat{\boldsymbol{u}}^{\boldsymbol{B}} + \rho\omega^2\widehat{\boldsymbol{u}}^{\boldsymbol{A}}.\widehat{\boldsymbol{u}}^{\boldsymbol{B}} = -\boldsymbol{f}^{\boldsymbol{A}}.\widehat{\boldsymbol{u}}^{\boldsymbol{B}} \qquad (1.6.5)$$

Interchange A and B and subtract the resulting equation to obtain,

$$\nabla.\boldsymbol{\hat{\sigma}^A}.\boldsymbol{\hat{u}^B} - \nabla.\boldsymbol{\hat{\sigma}^B}.\boldsymbol{\hat{u}^A} = \boldsymbol{f^B}.\boldsymbol{\hat{u}^A} - \boldsymbol{f^A}.\boldsymbol{\hat{u}^B}$$

Using the vector identity,

$$\left(\sigma_{ji}u_i\right)_{,j} = \sigma_{ji,j}u_i + \sigma_{ij}\epsilon_{ij} \tag{1.6.6}$$

And where $\sigma_{ij}^A\epsilon_{ij}^B = \sigma_{ij}^B\epsilon_{ij}^A$

So that,

$$\nabla.(\boldsymbol{\hat{\sigma}^A}.\boldsymbol{\hat{u}^B} - \boldsymbol{\hat{\sigma}^B}.\boldsymbol{\hat{u}^A}) = \boldsymbol{f^B}.\boldsymbol{\hat{u}^A} - \boldsymbol{f^A}.\boldsymbol{\hat{u}^B} \tag{1.6.7}$$

This statement of the reciprocal relation holds point wise within V. It is usual to integrate the above over V using Gauss's Theorem to convert the LHS to a surface integral over S.

$$\oiint_S\left(\boldsymbol{\hat{\sigma}^A}.\boldsymbol{\hat{u}^B} - \boldsymbol{\hat{\sigma}^B}.\boldsymbol{\hat{u}^A}\right).\boldsymbol{n}\,dS = \int_V(\boldsymbol{f^B}.\boldsymbol{\hat{u}^A} - \boldsymbol{f^A}.\boldsymbol{\hat{u}^B})\ dV \tag{1.6.8}$$

Where $\boldsymbol{n}$ = unit outward normal.

This form of the reciprocal relations is used to derive a representation theorem involving the Green function. Note that the two elastic stats A and B do not necessary satisfy the same boundary conditions.

1.7.2 Green function and Representation Theorem

Let $G_{in}(\boldsymbol{x},\boldsymbol{\xi})$ denote the i^{th} component of displacement at point $\boldsymbol{x}$ due to a unit point force acting in the n^{th} direction at point $\boldsymbol{\xi}$

Consider the body force $\boldsymbol{f}$,

$$\boldsymbol{f} = \delta_{in}\delta(\boldsymbol{x}-\boldsymbol{\xi})\delta(t) \tag{1.6.9}$$

We omitted the time dependence, so

$$\left(c_{ijkl}G_{kn,l}\right)_{,j} + \rho\omega^2 G_{in} = -\delta_{in}\delta(\boldsymbol{x} - \boldsymbol{\xi}) \tag{1.6.10}$$

And represents an outgoing wave at infinity, if V is infinite.

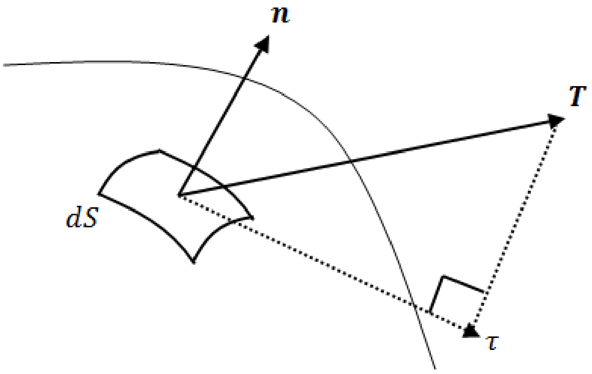

Figure 1.13: Traction vector acting on a surface element

Using G_{in} as state B with $-\boldsymbol{f^B}$ leads to the following integral representation for state A; with the superscript A omitted i.e. $\boldsymbol{f^B} = \boldsymbol{f} = f_i$.

$$\hat{u}_n(\xi) = \int_V f_i(\boldsymbol{x})G_{in}(\boldsymbol{x},\boldsymbol{\xi})dV + \oiint_S G_{in}(\boldsymbol{x},\boldsymbol{\xi})T_i[\widehat{\boldsymbol{u}}(\boldsymbol{x})] - u_i(\boldsymbol{x})(c_{ijkl}G_{kn,l}(\boldsymbol{x},\boldsymbol{\xi}))dS \tag{1.6.11}$$

Where, $T_i = \tau_{ij}.n_j$ is traction on S, refer to Fig 1.13. So $T_i[\widehat{\boldsymbol{u}}(\boldsymbol{x})]$ denotes the traction vector associate with $\widehat{\boldsymbol{u}}$**.** If G satisfies homogeneous boundary condition on S, i.e. traction of the displacement is prescribed to be zero at every point on S, then G satisfies the reciprocal relation

$$\boldsymbol{G}(\boldsymbol{x},\boldsymbol{\xi}) = \boldsymbol{G}(\boldsymbol{\xi},\boldsymbol{x}) \; hence \; G_{in} = G_{ni} \tag{1.6.12}$$

Interchanging the $\boldsymbol{x}$ and $\boldsymbol{\xi}$ leads to the representation theorem.

$$\hat{u}_n(x) = \int_V f_i(\xi)G_{ni}(\boldsymbol{x},\boldsymbol{\xi})dV + \oiint_S G_{ni}(\boldsymbol{x},\boldsymbol{\xi})T_i[\hat{\boldsymbol{u}}(\boldsymbol{x})] - u_i(\xi)(c_{ijkl}\frac{\partial G_{kn}(\boldsymbol{x},\boldsymbol{\xi})}{\partial \xi_l})dS$$

(1.6.13)

Note that for the application of the reciprocal relation, $\hat{\boldsymbol{u}}$ and $\boldsymbol{G}$ do not need to satisfy the same boundary condition. However, the final form here of the presentation theorem requires that $\boldsymbol{G}$ satisfies homogeneous boundary condition.

1.7.3 Representation theorem for scattered field by cracks

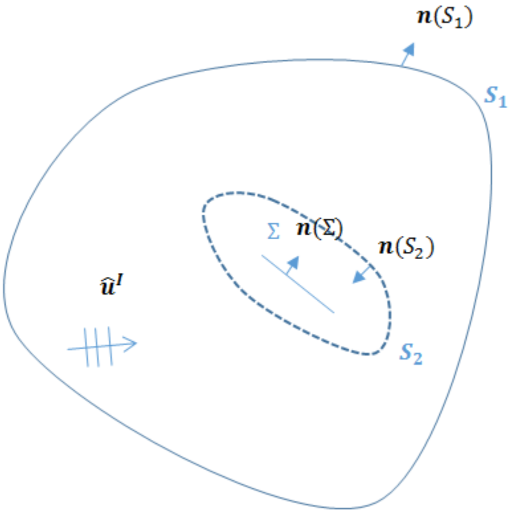

Figure 1.14: Elastic body with a damage defined by the surface Σ

The total field can be regarded as the superposition of the incident field $\hat{\boldsymbol{u}}^{\boldsymbol{I}}$ that would prevail in an uncracked body, and a scattered field $\hat{\boldsymbol{u}}^{\boldsymbol{S}}$ due to the presence of a crack indicated by the surface Σ. The displacement is discontinuous, but the associated tractions are continuous across Σ.

Using the previous equation for the scattered field and considering that since $S_1 \to \infty$, so its contribution can be ignored. S_2 can be collapsed on to Σ, noting that $\boldsymbol{n}(S_2)$ on the upper side of Σ is equal to -$\boldsymbol{n}(\Sigma)$**,** as indicated in Fig. 1.14, leading to,

$$\hat{u}_n(x) = \int_{\Sigma} \Delta\hat{u}_i(\xi) \left(c_{ijkl} \frac{\partial G_{nk}(x,\xi)}{\partial \xi_l} \right) n_j d\, \Sigma(\xi) \tag{1.6.14}$$

Where, $\Delta\hat{u}_i(\xi) = \hat{u}_i^+(\xi) - \hat{u}_i^-(\xi)$, and $\hat{u}_i^\pm$ denotes u on the top and bottom faces of Σ respectively.

This representation is in accord with Aki and Richards [27]. For the case of a shear crack on the plane ξ_3 with $\Delta\hat{u}_1$ as the only non-zero displacement discontinuity and an isotropic body, the following equation reduces to:

$$\hat{u}_n(x) = \int_{\Sigma} \mu\Delta\hat{u}_1(\xi) \left\{ \frac{\partial G_{n1}}{\partial \xi_3} + \frac{\partial G_{n3}}{\partial \xi_1} \right\} d\Sigma(\xi) \tag{1.6.15}$$

1.7.4 Solution for a dipole

Start with the solution for a point force at the origin of an anti-plane problem.

$$\mu(\nabla^2 W + k^2 w) = -\delta(\boldsymbol{x}) = -\delta(x)\delta(y) \tag{1.6.16}$$

Thus the solution is, using $e^{-i\omega t}$,

$$G(x,y) = \frac{i}{4} H_0^1(kr) \tag{1.6.17}$$

Consider a pair of forces and its limiting process starting from a doublet with strength $\frac{1}{\Delta y}$.

To generate a doublet, we take the limit such that, $\Delta y \to 0$.

Take,

$$G_{dipole} = \lim_{\Delta y \to 0} \frac{1}{\Delta y} \{ G(x, y - \Delta y) - G(x,y) \}$$

$$= \lim_{\Delta y \to 0} \frac{1}{\Delta y} \left\{ G(x,y) - \Delta y \frac{\partial G(x,y)}{\partial y} + \cdots - G(x,y) \right\}$$

$$= -\frac{\partial G(x,y)}{\partial y} \tag{1.6.18}$$

For a homogeneous and unbound space, the Green function depends only on the relative location of the receiver with respect to the source.

Hence, a doublet can also be expressed as,

$$\frac{\partial G}{\partial \xi_i}(\boldsymbol{x}, \boldsymbol{\xi}) = -\frac{\partial G}{\partial x_i}(\boldsymbol{x}, \boldsymbol{\xi}) \tag{1.6.19}$$

For force doublets in 2D, we can obtain 2 types of doublets,

$$G_{doublet} = -\frac{\partial G(x,y)}{\partial y} \tag{1.6.20}$$

$$G_{doublet} = -\frac{\partial G(x,y)}{\partial x} \tag{1.6.21}$$

So the doublet becomes,

$$\frac{\partial G_{n1}}{\partial \xi_3}(\boldsymbol{x}, \boldsymbol{\xi}) = -\frac{\partial G_{n1}}{\partial x_3}(\boldsymbol{x}, \boldsymbol{\xi}) \tag{1.6.22}$$

It is the field due to the force doublets, as shown in Fig. 1.15, and similarly for $\frac{\partial G_{n3}}{\partial \xi_1}$so that the kernel in shear crack equation (1.97) represents the field of a so-called ‘double couple’.

Aki and Richards [27] notes that this source has no net force and no net moment. They have indicated that the body force equivalent for a displacement discontinuity is not unique. The double couple is the standard representation for a mode II crack element. The body force equivalent for a mode I crack element is as follows.

The general analysis of discontinuous displacement across an internal surface is done by first considering the convolution symbol so that,

$$\hat{u}_n(x) = \int_{\Sigma} \Delta\hat{u}_i(\xi) * \left(c_{ijkl}\frac{\partial G_{nk}(x,\xi)}{\partial \xi_l}\right) n_j d\,\Sigma(\xi) \tag{1.6.23}$$

Here we introduce a moment, *M*, and moment density tensor , *m*,

$$m_{pq} = \Delta\hat{u}_i c_{ijpq} n_j \qquad \text{and} \qquad M_{pq} = \iint_{\Sigma} m_{pq}\, d\Sigma \tag{1.6.24}$$

Where this quantity depends on the source strength and orientation. We consider a long wavelength compared to the dimension of Σ. Thus, the source now is effectively a point source.

Hence

$$\hat{u}_n(x) = \int_{\Sigma} m_{pq} * G_{np,q}\, d\Sigma(\xi) \tag{1.6.25}$$

Such that for an isotropic body using (1.3),

$$m_{pq} = \lambda n_k[\Delta\hat{u}_i(\xi)]\delta_{pq} + \mu\left(n_p\Delta\hat{u}_q(\xi) + n_q\Delta\hat{u}_p(\xi)\right) \tag{1.6.26}$$

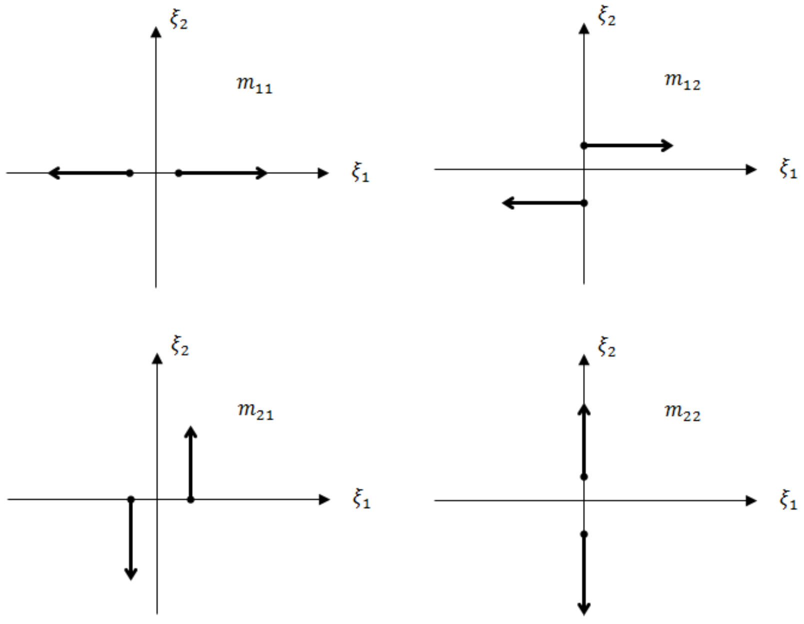

Figure 1.15: Representation of moment tensor density by equivalent body force doublet in two dimensions

Furthermore, in the case of discontinuity in the $\xi_2 = 0$ plane with $\Delta\hat{u}_1$ as the only non-zero displacement, similarly to the shear crack before,

$$\boldsymbol{m} = \begin{pmatrix} 0 & \mu\Delta\hat{u}_1(\xi) \\ \mu\Delta\hat{u}_1(\xi) & 0 \end{pmatrix} \tag{1.6.27}$$

In a case of a tension cracking, the $\xi_2 = 0$ plane with $\Delta\hat{u}_2$ as the only non-zero displacement, thus the moment density tensor is

$$\boldsymbol{m} = \begin{pmatrix} \lambda\Delta\hat{u}_2(\xi) & 0 \\ 0 & (\lambda+2\mu)\Delta\hat{u}_2(\xi) \end{pmatrix} \tag{1.6.28}$$

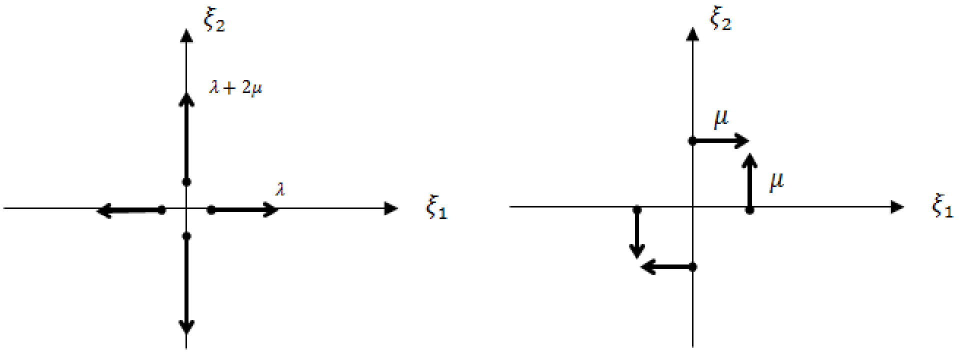

Figure 1.16: Body-force equivalents for a tension and shear crack in an isotropic medium

This represents a tension crack equivalent to two dipoles with magnitudes λ and $(\lambda + 2\mu)$ body forces equivalent to point source. For shear crack, it can be shown to be equivalent to two dipoles with magnitude μ body forces, as illustrated in Fig. 1.16.

In a sense, a centre of dilation produces only S0 waves where the ψ potential is zero and for a centre of shear the contribution of φ potential is zero and only pure SH0 wave. The attempt is to adopt the reasoning to get the plane stress of crack openings; Mode I and Mode II, to a body force equivalent.

1.8 Point Source

The solution of a point source on a semi-infinite medium has been investigated by Lamb [16]. One can simply convert from a plane strain to a plane stress application by changing the elastic constant λ and v, to $\overline{\lambda}$ and $\overline{v}$ in order to satisfy the plane stress conditions.

$$\overline{\lambda} = \frac{2\mu\lambda}{\lambda+2\mu} \; and \; \overline{v} = \frac{v}{1+v} \tag{1.7.1}$$

Consider the equation of motion of an isotropic elastic solid in two-dimensions (x, y) from Eqn. (A1.1.5).

$$(\lambda + \mu)\nabla\nabla.\boldsymbol{u} + \mu\nabla^2\boldsymbol{u} - \rho\ddot{\boldsymbol{u}} = \rho\boldsymbol{f} \tag{1.7.2}$$

Where, $\boldsymbol{u}$ is a displacement vector and u and v are the component displacements.

The displacement is expressed into scalar ϕ and vector $\boldsymbol{\varphi}$ potentials.

$$\boldsymbol{u} = \nabla.\phi + \nabla \times \boldsymbol{\psi} \tag{1.7.3}$$

So the component displacement can be expressed as,

$$u = \frac{\partial\phi}{\partial x} + \frac{\partial\boldsymbol{\psi}}{\partial y} \; and \; \; v = \frac{\partial\phi}{\partial y} - \frac{\partial\boldsymbol{\psi}}{\partial x} \tag{1.7.4}$$

The potentials satisfy

$$\nabla^2\phi - \frac{1}{c_L^2}\frac{\partial^2\phi}{\partial t^2} = 0 \; and \; \nabla^2\varphi - \frac{1}{c_T^2}\frac{\partial^2\boldsymbol{\psi}}{\partial t^2} = 0 \tag{1.7.5}$$

Where, $c_L^2 = \frac{\lambda+2\mu}{\rho} \; and \; c_T^2 = \frac{\mu}{\rho}$

Assume steady-state solution, the potentials can be expressed in this form,

$$\phi(x,y,t) = \bar{\phi}(x,y)e^{-i\omega t} \; and \; \psi(x,y,t) = \bar{\psi}(x,y)e^{-i\omega t} \quad (1.7.6)$$

Therefore the potentials satisfy the equations,

$$\nabla^2\phi + k_L^2\phi = 0 \; and \; \nabla^2\psi + k_T^2\psi = 0 \quad (1.7.7)$$

Where, $k_L = \frac{\omega}{c_L} \; and \; k_T = \frac{\omega}{c_T}$

Now taking the Fourier transform over x domain

$$\Phi(k,y) = \int \bar{\phi}(x,y,\omega)\, e^{-ikx}\, dx \;\; and \; \Psi(k,y) = \int \bar{\psi}(x,y,\omega)\, e^{-ikx}\, dx \quad (1.7.8)$$

Then from (5a, b), we get,

$$\nabla^2\Phi - \alpha^2\Phi = 0 \; and \; \nabla^2\Psi - \beta^2\Psi = 0 \quad (1.7.9)$$

where $\alpha = \sqrt{k^2 - k_L^2} \;\; and \; \beta = \sqrt{k^2 - k_T^2}$. The positive radicals $\alpha \; and \; \beta$ are chosen by the condition, where $Re[\alpha] \geq 0, \;\; Re[\beta] \geq 0$.

1.8.1 Branch Cut selection

The radical $\alpha = \pm\sqrt{k^2 - k_L^2}$ and $\beta = \pm\sqrt{k^2 - k_T^2}$ are chosen by the condition where $Re[\alpha] \geq 0$, and $Re[\beta] \geq 0$. Consider the branch points $\pm k_L \; and \pm k_T$; since the branch points are located on the real axis, the complex value of ω must be considered. Therefore, first take the cuts for complex $k_L = \frac{\omega}{c_L}$ and $k_T = \frac{\omega}{c_T}$. The radical has four combinations as there are four sheets of α and β, the permissible sheet must satisfy the condition for $Re[\alpha] \geq 0 \; and \;\; Re[\beta] \geq 0$.

Therefore, the cuts will be given by $Re[\alpha] = 0$ and $Re[\beta] = 0$. Given, the complex $\omega = a_\omega + b_\omega i$ and $k = a_k + b_k i$.

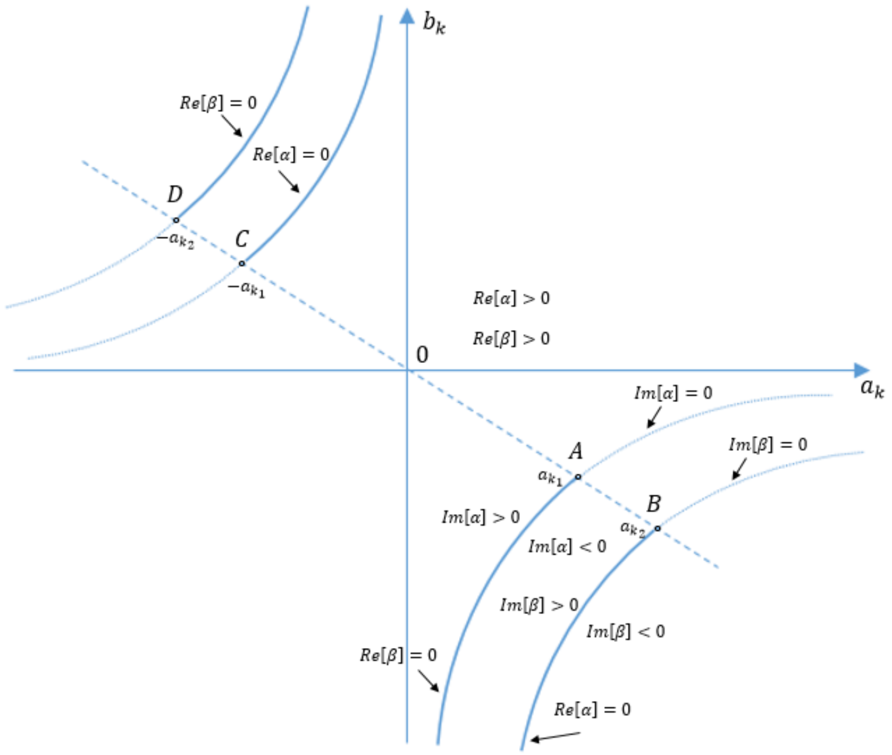

Figure 1.17: Branch points and cuts in the complex $k = a_k + b_k i$ plane for $Re[\omega] > 0$

For $Re[\alpha] = 0$, then $Re[\alpha^2] \leq 0$. So,

$$\alpha^2 = k^2 - k_L^2 = \left(a_k^2 - b_k^2 - \frac{a_\omega^2}{c_L} + \frac{b_\omega^2}{c_L}\right) + \left(2a_k b_k + \frac{2a_\omega b_\omega}{c_L}\right) i \tag{1.7.10}$$

Therefore,

$$a_k^2 - b_k^2 < \frac{a_\omega^2}{c_L} - \frac{b_\omega^2}{c_L} \text{ and } a_k b_k = -\frac{2a_\omega b_\omega}{c_L} \text{ for real and negative} \tag{1.7.11}$$

For ω to be real then,

$$a_k^2 - b_k^2 < \frac{a_\omega^2}{c_L} \text{ and } a_k b_k = 0 \tag{1.7.12}$$

Either,

$$a_k = 0 \ and \ -b_k^2 < \frac{a_\omega^2}{c_L} \qquad \text{or} \qquad b_k = 0 \ and \ a_k^2 < \frac{a_\omega^2}{c_L} \tag{1.7.13}$$

The condition $Re[\alpha] \geq 0$ restricts the choice of a cut. When $b_k = 0$ from Eqn. 1.7.13, a part of the real axis between the branch points at A and C, as shown in Fig. 1.18. The imaginary axis determined by condition $a_k = 0$ from Eqn. 1.7.13 is not an independent cut, since it does no pass through a branch point. However, the imaginary axis can be used by combining with that part of the real axis to form AOE and BOL cuts as shown in Fig. 1.18. For real ω, the $Re[\alpha]$ does not change sign in the right half plane except for $a_k > a_{k_1}$, which is on A, refer to Fig. 1.18. Therefore, for any permissible path in the right half plane, $Im[\alpha]$ can change sign only on crossing A.

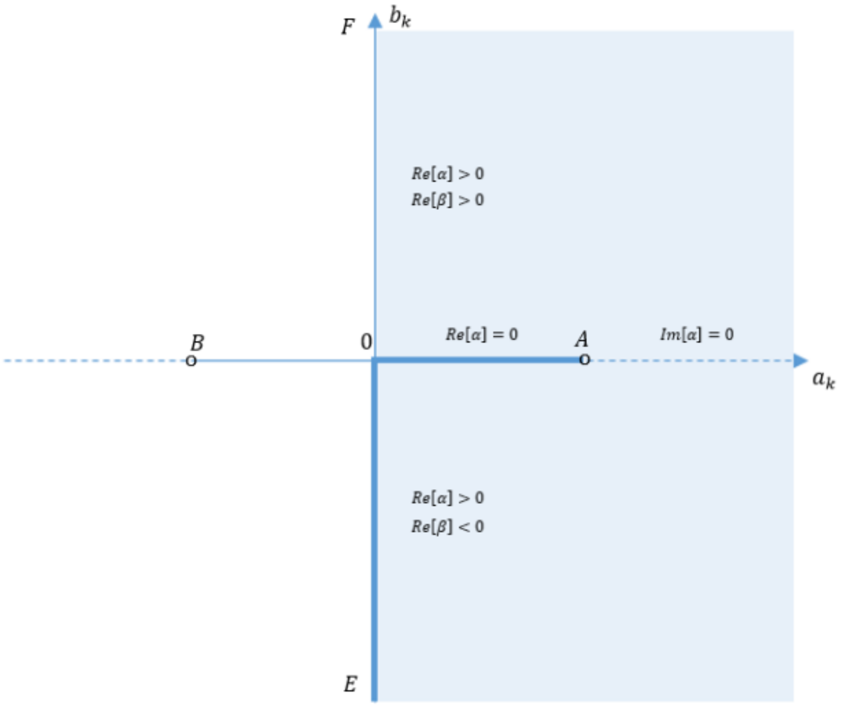

Figure 1.18: Limiting cases of the hyperbola parts in Fig. 1.17. Branch points A and B and cuts AOE and BOF in complex k plane for real ω

1.8.2 Point source solution

Then, for a bounded response for $y \to \infty$

$$\Phi(k, y) = A(k)e^{-\alpha y} \text{ and } \Psi(k, y) = B(k)e^{-\beta y} \tag{1.7.14}$$

Therefore, the solution to the region $y > 0$

$$\phi^I(x, y) = A(k)e^{-\alpha y}e^{ikx} \; and \; \psi^I(x, y) = B(k)e^{-\beta y}e^{ikx} \tag{1.7.15}$$

Consider the stresses in terms of potentials,

$$\sigma_{xx} = \lambda\left(\frac{\partial^2\phi}{\partial x^2} + \frac{\partial^2\phi}{\partial y^2}\right) + 2\mu\left(\frac{\partial^2\phi}{\partial x^2} + \frac{\partial^2\psi}{\partial x\partial y}\right) = -\mu k_T^2\phi - 2\mu\frac{\partial^2\phi}{\partial y^2} + 2\mu\frac{\partial^2\psi}{\partial x\partial y} \tag{1.7.16}$$

$$\sigma_{yy} = \lambda\left(\frac{\partial^2\phi}{\partial x^2} + \frac{\partial^2\phi}{\partial y^2}\right) + 2\mu\left(\frac{\partial^2\phi}{\partial y^2} - \frac{\partial^2\psi}{\partial x\partial y}\right) = -\mu k_T^2\phi - 2\mu\frac{\partial^2\phi}{\partial x^2} - 2\mu\frac{\partial^2\psi}{\partial x\partial y} \tag{1.7.17}$$

$$\sigma_{xy} = \mu\left(2\frac{\partial^2\phi}{\partial x\partial y} - \frac{\partial^2\psi}{\partial x^2} + \frac{\partial^2\psi}{\partial y^2}\right) = 2\mu\frac{\partial^2\phi}{\partial x\partial y} - \mu k_T^2\psi - 2\mu\frac{\partial^2\psi}{\partial x^2} \tag{1.7.18}$$

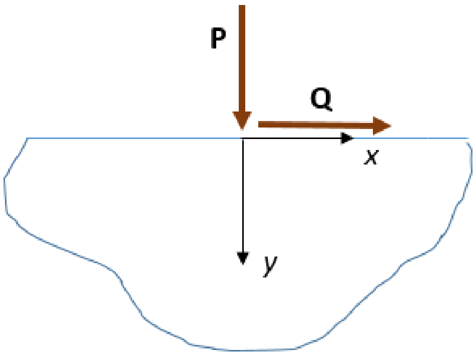

Figure 1.19: Normal (P) and shear (Q) surface force diagram on semi-infinite boundary

Consider only a normal force at the surface, $y = 0$ such that (as shown in Fig. 1.19),

$$\sigma_{yy} = -P\delta(x)$$

$$\sigma_{xy} = 0$$

(1.7.19)

Using Eqn. (1.7.17) and (1.7.18), then

$$A_1^s(k) = \frac{k_T^2 - 2k^2}{\mu((2k^2 - k_T^2)^2 - 4\alpha\beta k^2)} P$$

$$B_1^S(k) = \frac{-2\alpha k}{\mu((2k^2 - k_T^2)^2 - 4\alpha\beta k^2)} Pi$$

(1.7.20)

Consider a shear force at the surface, $y = 0$ such that,

$$\sigma_{yy} = 0$$

$$\sigma_{xy} = -Q\delta(x)$$

(1.7.21)

Using Eqn. (1.7.17) and (1.7.18), then,

$$A_2^s(k) = \frac{2\beta k}{\mu((2k^2 - k_T^2)^2 - 4\alpha\beta k^2)} Qi$$

$$B_2^s(k) = \frac{k_T^2 - 2k^2}{\mu((2k^2 - k_T^2)^2 - 4\alpha\beta k^2)} Q$$

(1.7.22)

1.8.3 Application of steepest descent method

In order to determine the far-field wave pattern due to the normal and tangential surface forces, the steepest-descent method is used to determine the field at infinity.

First, consider the integrals have the general form of,

$$I = \int_{-\infty}^{\infty} \chi(k) e^{ikx-\sqrt{k^2-m^2}y}\, dk \tag{1.7.23}$$

The polar coordinates are introduced such that $x = r sin\theta$ and $y = r cos\theta$ where θ is measured from the y axis. So,

$$I = \int_{-\infty}^{\infty} \chi(k) e^{rf(k)}\, dk \tag{1.7.24}$$

Where, $f(k) = ik sin\theta - \sqrt{k^2 - m^2} cos\theta$

The saddle points of $Re[f(k)]$ is determined from $\frac{df(k)}{dk} = 0$. We obtain,

$$i sin\theta = \frac{k cos\theta}{\sqrt{k^2-m^2}} \text{ so } k_0 = \pm m sin\theta \tag{1.7.25}$$

Consider point $k_0 = -m sin\theta,$ whereas the point at $+$ version would be used for consideration on the negative real axis $-m \leq k_0 \leq 0$.

At the saddle point $f(k_0) = -im$ and $f''(k_0) = \frac{i}{m\cos^2\theta}$. The contour of integration is now deformed so it passes through the saddle point along the steepest descent path. Near the saddle,

$$f(k) - f(k_0) = \frac{1}{2}(k - k_0)^2 f''(k_0)$$

$$f(k) - f(k_0) = -u^2 \tag{1.7.26}$$

Let $k - k_0 = r\, e^{i\theta}$

So it can be expressed as,

$$u^2 = -r^2\, f''(k_0) e^{2i\theta} \tag{1.7.27}$$

We write,

$$f''(k_0) = |f''(k_0)| e^{i\theta_b} \tag{1.7.28}$$

Therefore,

$$u^2 = -r^2 |f''(k_0)| e^{i(\theta_b + 2\theta)} \tag{1.7.29}$$

For u^2 to be positive and real, $e^{i(\theta_b+2\theta)}$ must be real and negative. Hence, fix $\theta_b + 2\theta = \pm\pi$, Then

$$u^2 = -r^2 |f''(k_0)| e^{\frac{i(\theta_b+2\theta)}{2}} e^{\frac{i\pi}{2}} \tag{1.7.30}$$

So that, $u = \pm r |f''(k_0)|^{\frac{1}{2}}$

Then we obtain,

$$u = \pm (k - k_0) |f''(k_0)|^{\frac{1}{2}}\, e^{-i\theta} \tag{1.7.31}$$

Therefore,

$$-u^2 = \frac{1}{2} (k - k_0)^2 \frac{i}{m \cos^2 \theta} \tag{1.7.32}$$

$$k - k_0 = \pm 2\sqrt{m} u\, cos\theta\, e^{\frac{i\pi}{4}} \tag{1.7.33}$$

$$\arg\left[\frac{1}{2} f''(k_0) e^{2i\theta}\right] = 0 \tag{1.7.34}$$

We approximate for large value of r,

$$I \sim \sqrt{\frac{2\pi}{r}} \frac{\chi(k_0)}{|f''(k_0)|^{\frac{1}{2}}}\ e^{rf(k_0)+\frac{i\pi}{4}} \tag{1.7.35}$$

$$I \sim \sqrt{\frac{2\pi m}{r}} \chi(k_0) cos\theta\ e^{rf(k_0)+\frac{i\pi}{4}} \tag{1.7.36}$$

1.8.4 Far-field wave patterns due to normal and tangential surface forces

Consider normal surface force from Eqn. (1.7.15); where,

$$\phi^I(x,y) = A(k)e^{-\alpha y}e^{ikx}\ and\ \psi^I(x,y) = B(k)e^{-\beta y}e^{ikx} \tag{1.7.37}$$

Now recall,

$$u = \frac{\partial\phi}{\partial x} + \frac{\partial\boldsymbol{\psi}}{\partial y} = ik\phi^I(x,y) - \beta\psi^I(x,y)\ and\ \ v = \frac{\partial\phi}{\partial y} - \frac{\partial\boldsymbol{\psi}}{\partial x} = -\alpha\phi^I(x,y) - ik\psi^I(x,y) \tag{1.7.38}$$

Also, from Eqn. (1.7.20)

$$A_1^S(k) = \frac{k_T^2 - 2k^2}{F(k)} \frac{P}{\mu}\ \ and\ \ B_1^S(k) = \frac{-2\alpha k}{F(k)} \frac{Pi}{\mu}$$

where, $F(k) = (2k^2 - k_T^2)^2 - 4\alpha\beta k^2 = (2k^2 - k_T^2)^2 - 4(k^2 - k_L^2)^{\frac{1}{2}}(k^2 - k_T^2)^{\frac{1}{2}}k^2$

The displacements from Eqn. (1.7.38) can be expressed as,

$$u = (I_{uL} + I_{uT})\frac{P}{\mu} \tag{1.7.39}$$

$$v = (I_{vL} + I_{vT})\frac{P}{\mu} \tag{1.7.40}$$

Using the displacement form Eqn. (1.7.39) and (1.7.40) and by substituting (1.7.20), we obtain the integrals

$$I_{uL} = \frac{i}{2\pi}\int_{-\infty}^{\infty} \frac{-k\left(2k^2-k_T^2\right)}{F(k)} e^{ikx-\sqrt{k^2-k_L^2}y}\ dk \tag{1.7.41}$$

$$I_{uT} = \frac{i}{\pi}\int_{-\infty}^{\infty} \frac{k\left(k^2-k_T^2\right)^{\frac{1}{2}}\left(k^2-k_L^2\right)^{\frac{1}{2}}}{F(k)} e^{ikx-\sqrt{k^2-k_T^2}\,y}\ dk \tag{1.7.42}$$

$$I_{vL} = \frac{1}{2\pi}\int_{-\infty}^{\infty} \frac{\left(k^2-k_L^2\right)^{\frac{1}{2}}\left(2k^2-k_T^2\right)}{F(k)} e^{ikx-\sqrt{k^2-k_L^2}y}\ dk \tag{1.7.43}$$

$$I_{vT} = -\frac{1}{2\pi}\int_{-\infty}^{\infty} \frac{k^2\left(k^2-k_L^2\right)^{\frac{1}{2}}}{F(k)} e^{ikx-\sqrt{k^2-k_T^2}y}\ dk \tag{1.7.44}$$

Now using the approximation from (1.7.36) and the above Eqn. (1.7.41-44), for u displacement.

$$I_{uL} \sim i\sqrt{\frac{1}{2\pi r}}\frac{k_L^{\frac{3}{2}} sin\theta(2k_L^2\sin^2\theta - k_T^2)}{F(-k_L sin\theta)} cos\theta\ e^{-ik_L r+\frac{i\pi}{4}}$$

$$I_{uT} \sim \sqrt{\frac{2}{\pi r}}\frac{-k_T^{\frac{5}{2}}\frac{1}{2} sin2\theta(k_T^2\sin^2\theta - k_L^2)^{\frac{1}{2}}}{F(-k_T sin\theta)} cos\theta e^{-ik_T r+\frac{i\pi}{4}}$$

$$u = \left(i\frac{k_L^{\frac{3}{2}} sin\theta(2k_L^2\sin^2\theta - k_T^2)}{F(-k_L sin\theta)} e^{-ik_L r} + \frac{k_T^{5/2} sin2\theta(k_T^2\sin^2\theta - k_L^2)^{\frac{1}{2}}}{F(-k_T sin\theta)} e^{-ik_T r} \right)\sqrt{\frac{2}{\pi r}}\frac{P}{\mu} e^{\frac{i\pi}{4}} cos\theta$$

(1.7.45)

And, for v displacement,

$$I_{vL} \sim i\sqrt{\frac{1}{2\pi r}}\frac{k_L^{\frac{3}{2}} cos\,(2k_L^2\sin^2\theta - k_T^2)}{F(-k_L sin\theta)} cos\theta\; e^{-ik_L r+\frac{i\pi}{4}}$$

$$I_{vT} \sim -\sqrt{\frac{1}{2\pi r}}\frac{k_T^{5/2}\sin^2\theta\,(k_T^2\sin^2\theta - k_L^2)^{\frac{1}{2}}}{F(-k_T sin\theta)} cos\theta e^{-ik_T r+\frac{i\pi}{4}}$$

$$v = \left(i\frac{k_L^{\frac{3}{2}}\cos\theta\,(2k_L^2\sin^2\theta - k_T^2)}{F(-k_L sin\theta)} e^{-ik_L r} - \frac{2k_T^{5/2}\sin^2\theta\,(k_T^2\sin^2\theta - k_L^2)^{\frac{1}{2}}}{F(-k_T sin\theta)} e^{-ik_T r} \right)\sqrt{\frac{2}{\pi r}}\frac{P}{\mu} e^{\frac{i\pi}{4}} cos\theta$$

(1.7.46)

Consider tangential surface force, recall from (1.7.22),

$$A_2^s(k) = \frac{2\beta k}{F(k)}\frac{Qi}{\mu} \quad and \quad B_2^s(k) = \frac{k_T^2 - 2k^2}{F(k)}\frac{Q}{\mu}$$

Using the displacement form Eqn. (1.7.39) and (1.7.40) and by substituting (1.7.22), we obtain the integrals

$$I_{uL} = \frac{-1}{\pi}\int_{-\infty}^{\infty}\frac{k^2\left(k^2 - k_T^2\right)^{\frac{1}{2}}}{F(k)} e^{ikx - \sqrt{k^2 - k_L^2}y}\; dk \tag{1.7.47}$$

$$I_{uT} = \frac{1}{2\pi}\int_{-\infty}^{\infty}\frac{\left(k^2 - k_T^2\right)^{\frac{1}{2}}\left(2k^2 - k_T^2\right)}{F(k)} e^{ikx - \sqrt{k^2 - k_T^2}y}\; dk \tag{1.7.48}$$

$$I_{vL} = \frac{-i}{\pi}\int_{-\infty}^{\infty}\frac{k\left(k^2 - k_T^2\right)^{\frac{1}{2}}\left(k^2 - k_L^2\right)^{\frac{1}{2}}}{F(k)} e^{ikx - \sqrt{k^2 - k_L^2}\,y}\; dk \tag{1.7.49}$$

$$I_{vT} = \frac{i}{2\pi}\int_{-\infty}^{\infty}\frac{k\left(2k^2 - k_T^2\right)}{F(k)} e^{ikx - \sqrt{k^2 - k_T^2}y}\; dk \tag{1.7.50}$$

Now using the approximation from (1.7.36), and the above Eqn. (1.7.47-50) for u displacement,

$$I_{uL} \sim -\sqrt{\frac{2}{\pi r}} \frac{k_L^{5/2} \sin^2\theta \, (k_L^2 \sin^2\theta - k_T^2)^{\frac{1}{2}}}{F(-k_L sin\theta)} cos\theta \; e^{-ik_L r + \frac{i\pi}{4}}$$

$$I_{uT} \sim -i\sqrt{\frac{1}{2\pi r}} \frac{k_T^{7/2} \, cos\,\theta \, cos\,2\theta}{F(-k_T sin\theta)} cos\theta \; e^{-ik_T r + \frac{i\pi}{4}}$$

$$u = \left(-\frac{k_L^{\frac{5}{2}} \sin^2\theta \, (k_L^2 \sin^2\theta - k_T^2)^{\frac{1}{2}}}{F(-k_L sin\theta)} e^{-ik_L r} - i\frac{1}{2}\frac{k_T^{7/2} \, cos\,\theta \, cos\,2\theta}{F(-k_T sin\theta)} e^{-ik_T r} \right) \sqrt{\frac{2}{\pi r}} \frac{Q}{\mu} e^{\frac{i\pi}{4}} cos\theta$$

(1.7.51)

And, for v displacement,

$$I_{vL} \sim \sqrt{\frac{1}{2\pi r}} \frac{-k_L^{\frac{5}{2}} sin2\theta (k_L^2 \sin^2\theta - k_T^2)^{\frac{1}{2}}}{F(-k_L sin\theta)} \; cos\theta \; e^{-ik_L r + \frac{i\pi}{4}}$$

$$I_{vT} \sim i\sqrt{\frac{1}{2\pi r}} \frac{k_T^{7/2} sin\theta \, cos\,2\theta}{F(-k_T sin\theta)} \; cos\theta \; e^{-ik_T r + \frac{i\pi}{4}}$$

$$v = \left(\frac{1}{2}\frac{-k_L^{\frac{5}{2}} sin2\theta (k_L^2 \sin^2\theta - k_T^2)^{\frac{1}{2}}}{F(-k_L sin\theta)} e^{-ik_L r} + i\frac{1}{2}\frac{k_T^{7/2} sin\theta \, cos\,2\theta}{F(-k_T sin\theta)} e^{-ik_T r} \right) \sqrt{\frac{2}{\pi r}} \frac{Q}{\mu} e^{\frac{i\pi}{4}} cos\theta$$

(1.7.52)

The far-field u and v displacements obtained from using the steepest-descent method for normal and tangential surface forces can be plotted into radial and tangential components of the field by using the following relations:

$$u_R = u_y \cos\theta + u_x \sin\theta$$

$$u_\theta = u_x \cos\theta - u_y \sin\theta \tag{1.7.53}$$

Hence, the resulting displacement field u_R and u_θ are shown as a function of θ in Fig. 1.20 and 1.21.

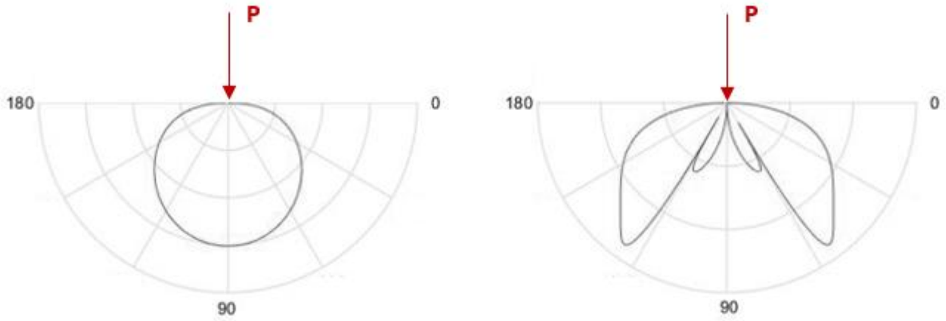

Figure 1.20: Normal surface force radiation pattern of (LEFT) u_R *and (RIGHT)* u_θ *for Poisson's ratio* $v = \frac{1}{3}$

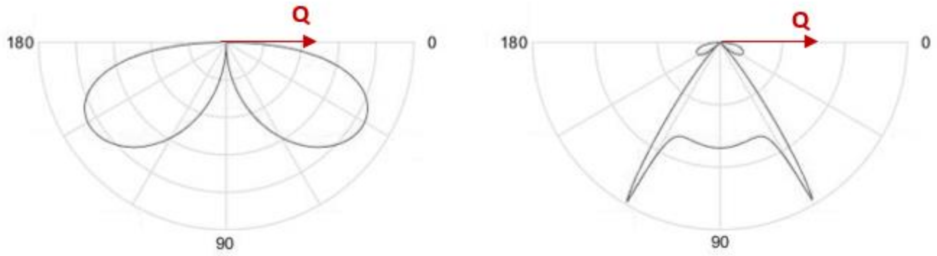

Figure 1.21: Tangential surface force radiation pattern of (LEFT) u_R *and (RIGHT)* u_θ *for Poisson's ratio* $v = \frac{1}{3}$

1.9 Thesis Outline

The proposed research aims to meet the challenge of identifying cracks at hard-to-inspect location by investigating scattered wave field due to a small crack on different geometries. The thesis objective is to find key scattering measurements to potentially enable ultrasonic-based SHM techniques to be successfully applied to unitised and complex metallic components. The novelty of the work involves using point source model to represent the Lamb wave scattering by an early stage; small, crack and using the proposed measurements to detect and determine the crack length. This will address the absence of hidden crack study which has not been investigated in complex and hard-to-inspect location. This research attempts to determine whether a novel inspection can be implemented to detect blind side cracks using the corresponding scattering signature.

Firstly, by investigating the two basic subcategorised problems; small crack defect and a hole, this study provides fundamental knowledge to understand the scattering phenomena due to the defect and the hole, individually, before tackling a hidden crack problem. The thesis will report on the edge crack problem, hole problem, and lastly the hidden crack (on the rectangular slot) problem. The schematic of systematic approach is shown in Fig. 1.22.

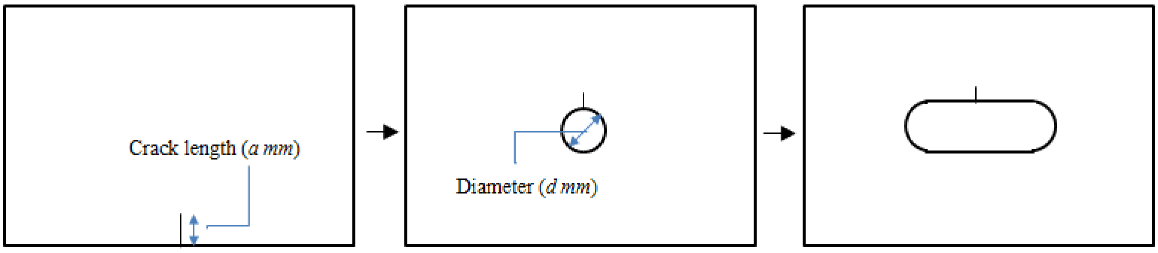

Figure 1.22: Schematic of the key investigations starting from edge crack on straight boundary, crack on a hole and hidden crack on a rectangular slot

The first main topic will investigate the interaction of Lamb waves with a small (relative to incident wavelength) edge crack at a straight boundary in an isotropic plate. The edge crack problem is viewed as a crack on the hole by taking the limit such that radius is approaching infinite. The first configuration is to minimise the numbers of characteristic length to achieve a fully defined simple problem. This will give comprehensive scattering results due to the presence of only an edge crack, before introducing the effect due to the radius.

The next topic is the small crack on a hole, and a particular focus of this thesis. Here, we introduce characteristic length of radius-to-wavelength ratio to explore the additional scattering effect of a radius. The final main topic is the establishment of a hidden crack by introducing another characteristic length so that the geometry is a rectangular slot with a hidden crack. The findings from previous chapters are used to tackle this hidden crack problem.

This study will also provide a fundamental knowledge of scattering Lamb waves to tackle and further knowledge on the different investigation methods for hidden defects in innovative and complex structures. Hence, the understanding and investigation on the forward scatter problem of a known defect and unknown scattering phenomena establish the inverse problem of detecting the hidden defects and characterising it from the scattering wave amplitude and pattern.

The next chapter will explore the computational and experimental considerations and methodologies to setup the studies for the scattered wave field from cracks. Furthermore, the post-processing and techniques to analyse the scattered wave field are reported.

Chapter 2

Computational & Experimental Procedures

In this chapter, the experimental and computational FE methodology for the study of scattered Lamb wave due to a presence of a crack is discussed. The Laser Vibrometer is used to measure the velocity wave field at the surface of the specimen, and the excited signals are generated by PZT actuators bonded onto the specimen. The 2D Fast Fourier transformation (2D FFT) has been used extensively in recent research for determination of Lamb wave velocity and mode. A 2D FFT was performed to identify the centre frequency and wavenumber of the wave field in both experimental and computational study.

ANSYS 15.0 is used as a Finite Element computational analysis tool to study the scattering of Lamb waves. Finite Element Analysis (FEA) provides an effective and necessary tool for analysing the solution for elastic wave propagation. Pre-requisite computational studies such as mesh configuration and Lamb wave modelling are investigated to determine the optimal computational setup for this research.

2.1 Computational Considerations and Methodology: ANSYS and MATLAB

Many studies have explored different methods of wave propagation simulation such as Finite Element [15, 28, 30-32, 53] and LISA/SIM method [23, 142]. These are effective numerical tools for solving wave propagation problem. In the context of SHM, FE simulation and modelling for guided waves is most common modelling technique to compare and assist experimental studies [23, 142, 143]. For this research, ANSYS 15.0 Explicit Dynamic is used for Finite Element Analysis of wave propagation and interaction. It is a particular highly advantageous to use Explicit Solver since the explicit increment is approximately to the simulated model size. Thus, it requires much less memory than Implicit Solver whereas the cost of the implicit procedure increases exponentially. Implicit Solver requires significant smaller time step and has difficulty converging thus resulting in large number of iteration than Explicit Solvers. Explicit procedure acquires solution without iterating by advancing from the previous increment with the expense of a large number of small time increments. Hence, the solution of individual time increment are inexpensive and fine resolution solution of wave propagating problem can be obtained at a relatively low cost of memory.

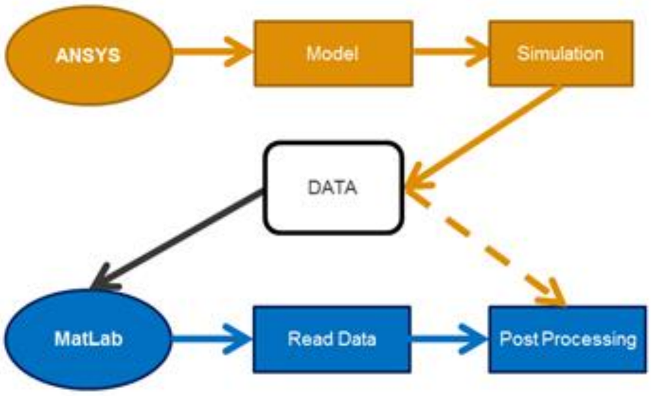

Figure 2.1: FE procedure flow chart from ANSYS simulation to MATLAB post processing

For the post-processing, MATLAB was used for further analysis, computational coding and generation of the function for analysis. The ANSYS data files can be significantly compressed into .mat files, which reduces memory usage by at least three times. MATLAB scripts and functions coded in the preliminary research are data conversion files from ANSYS to MATLAB, 2D Fast Fourier transformation to dispersion curve, scattering field, baseline subtraction and scattered polar plots.

For specimen mesh discretisation, many authors use a different number of nodes per wavelength such that the error is relatively acceptable. The level of acceptability is different from case to case. The fundamental sampling theorem states at least two points per wavelength are necessary to detect the frequency. However, this does not retain the overall wave propagation shape. When a wave travels along the distance, the error will accumulate and the numerical solution becomes more inaccurate. Although, there is no prescribed method in detail, it is advised at least 6 to 10 nodes per wavelength is necessary for achieving the required accuracy of the mode shape [144]. Mace and Manconi [145] noted the criterion of at least 6 elements per wavelength is acceptable, given the aspect ratio is approximately unity. Depending on the studies integration scheme, some studies implemented over 20 elements per wavelength for implicit method approach due to the complex geometry of the structure [146]. Thus, a mesh study is required to ensure that the mesh size is optimal for the specific study.

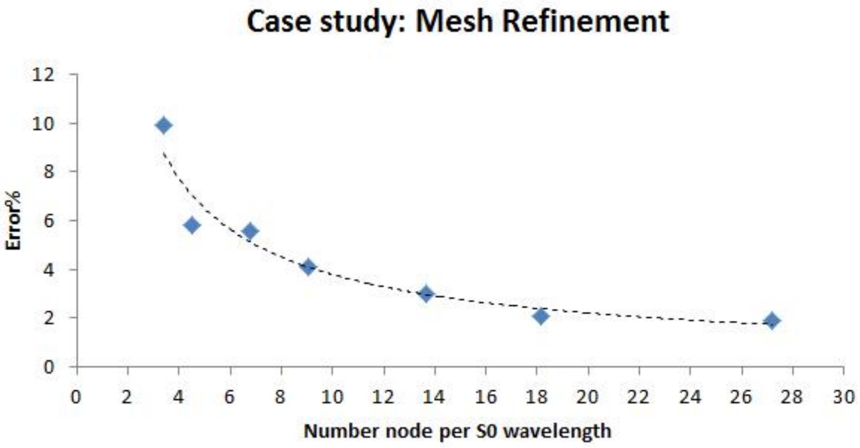

Figure 2.2: Comparison of a number of nodes per wavelength for S0 and SH0 wave propagation

A mesh convergence study has been conducted of mesh size 1mm to 8mm. A simple 3D aluminium specimen has been modelled to investigate the effect of mesh size with wavelength. We aim to use this study to determine a point of compromise where we get sufficient accuracy while keeping computational work to an acceptable standard. A planar wave is excited by using an edge forcing with symmetrical boundary conditions. Three criterions were investigated; the amplitude decay, wave profile and centre frequency and the wavenumber maximum deviations are specified as relative errors [147]. It is found that at least 10 nodes per wavelength retain both wave profile and centre frequency and are in good agreement with DISPERSE [33] with less than 3% error. In Fig. 2.2 shows a graphical comparison of a number of nodes per S0 wavelength.

The most common meshes are square or hexagonal elements for the computational analysis of propagating waves. However, some studies have used tetrahedron elements to better capture their complex shape and problem. In the first hole study, it was later found there was no difference between the set of results between using tetrahedron and hexagonal elements. Although, The advantage of hexagonal elements is that the computational work is reduced significantly, especially for low-frequency fundamental wave propagation. Additionally, Diligent et al. [28] considered membrane mesh and produced acceptable solutions as well. Although for small defects and complex shapes, it is recommended to have smaller elements refined, such as applying adaptive refinement near the defect or sharp edges to capture the near-field effect. For low-frequency wave propagation, hexagonal elements are preferred due to the reduced degree of freedom for efficiency in computational work. This will ultimately prevent the need for interpolation of data which may accumulate error when post-processing results.

Explicit Time Integration was used in the studies. The maximum allowable time step criterion is L/C as stability limit for Explicit Time Integration [148] where factor 0.8 is considered is used as the safety factor for most studies, although can differ between users depending on the application, to ensure model simulation stability and optimal computational run time. For wave propagation in 3D-continuum, the critical time time-step is the same as time step criterion in LS DYNA support ANSYS manual [149]. Further studies and literature [148, 150, 151] have discussed the critical time step in detail for different applications.

There are many techniques to extract and identify the wave speed and mode. One may plot the wave field in the distance-time curve to determine the group velocity, which will require a Hilbert transformation or Fourier transform to obtain the maximum amplitude at the centre frequency[152] from the dispersion curve. An effective method to determine the wave modes and velocity is performing a 2D Fast Fourier transformation (2D FFT) on the signal [147]. The Fourier transformations of signals are represented as a superposition of plane waves. Each wave has a definite phase velocity, in the sense of harmonic components of plane waves. The application for 2D FFT requires the number of spatial and temporal points as 2^n, where n is a positive integer. Furthermore, there is a Nyquist sampling rate requirement which determines the maximum frequency and wavenumber content given by the time and spatial signal. Previous studies [13-15, 147, 153] have used 2D FFT method to determine the wave velocity, amplitude, wave number and mode of the wave propagating in the plate. The investigations of Alleyne and Cawley [147] have significantly shown 0.5% error while compared to the theoretical solution to the maximum peak value in the dispersion curve. For 2D FFT it is ideal to capture the entire wave train within the spatial window for all time frames. However, it is also ideal to capture entire signal in the temporal window for all spatial frames as well. Since the entire signal cannot be contained in both spatial and temporal window, a compromise must be made, refer to Fig. 2.3.

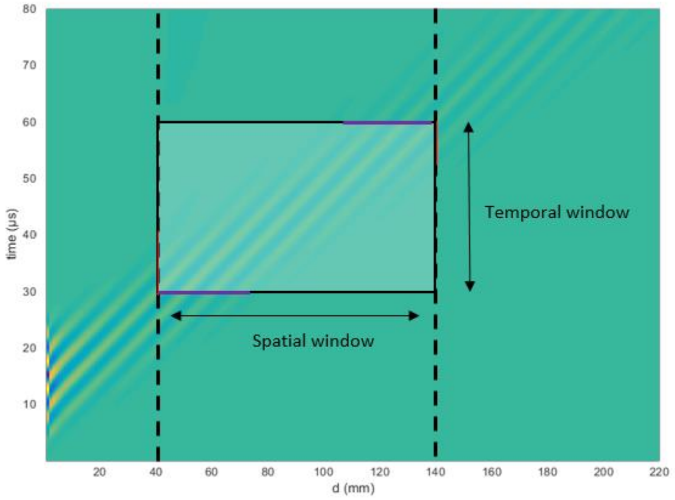

Figure 2.3: Distance versus time of 5 cycles Hann-window SH0 Wave propagation, indicated the temporal and spatial window for 2D FFT

The compromise may induce a discontinuity of the signal. Thus, a slow decay in the discrete frequency spectrum, much like an inverse proportionality of sample size may occur. One may consider an apodisation, a convolution to prevent discontinuity. The amplitude of the wave signal can be obtained through Fourier transformation. However, if the wave signal is windowed or apodisation is used, a correction factor is needed since window reduces the power of the signal. For Hann-window, amplitude correction factor is 2. An effective alternative is taking the maximum peak of Hilbert Transformation over the signal to obtain the maximum amplitude. Since 2D FFT accurately identifies the centre frequency and wave number, the compromise can be made by capturing the entire signal in the temporal window instead. 2D FFT can compare the data from experimental and the computational simulation dispersion curve solution from ‘DISPERSE’ [33]. It is convenient to arrange the 2D FFT spatial scan line perpendicularly to the wavefronts to determine the correct wave number; hence a radial line from the origin of the source is considered. Otherwise, two spatial scan lines are required to determine the horizontal and vertical components of the wave number to resolve for the correct wave number. Time gating the signal is required to avoid reflected wave from the adjacent boundaries. It may be required to scan at least 2.5 wavelengths away from the boundary since the effect of non-propagating Lamb wave modes is negligible [98].

The experimental and computational 2D FFT line scans are performed in MATLAB with the inbuilt multidimensional Fast Fourier transform function *fftn*. The 2D FFT results are used to create the dispersion curves to identify the dominant Lamb wave modes in different cylindrical coordinate components from ’DISPERSE’ [33].

In order to investigate the scattered wave field, a baseline subtraction is employed to separate the scattered wave displacement field, $u_{scatter}$ associated with the defect.

$$u_{scatter}(r,\theta,t) = u_{total}(r,\theta,t) - u_{baseline}(r,\theta,t) \tag{2.1}$$

where, u_{total} denotes the response of the damaged structure and $u_{baseline}$ denotes the baseline field that is generated by the same excitation in the absence of a defect.

The baseline subtraction is particularly simple to perform for FE simulations as illustrated in Fig. 2.4. However, for experimental scans, a correction is needed to artificially adjust measured wave field to obtain the scattered wave field. This is done by selecting a time where the subtraction of the total and baseline field is expected to be zero; before any scattering occurs. The two scanned fields are incrementally displaced, vertically and horizontally, until the baseline subtraction field is minimal. The experimental wave fields cannot be perfectly subtracted. So, the experimental scattered field will have weak signals of the incident waves.

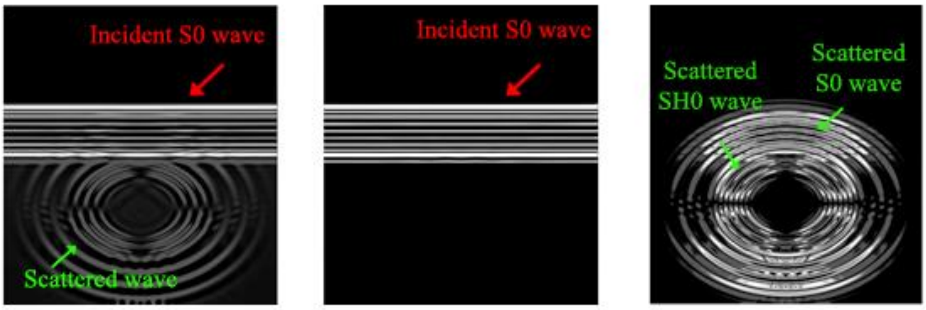

Total wave field (With defect)

Baseline wave field (No defect)

Scattered wave field due to defect

Figure 2.4: Baseline subtraction of a total wave field with crack and original wave field without crack to obtain the wave field due to the presence of the crack

Lamb wave modes such as A0, S0 and SH0 were produced with different techniques such as symmetrical forcing, edge forcing as well as the traditional single point forcing. Although a transducer can be modelled in FE using an Implicit Solver [154, 155], the force excitation method significantly reduces computational work but does not give the voltage from the piezoelectric transducer. Hence it is efficient since it can produce similar wavefront and pure fundamental Lamb modes. In this research, the forcing excitation is regarded to isolate and avoid multimode and investigate the interaction of specific wave mode with a defect. Different methods to excite Lamb waves were investigated.

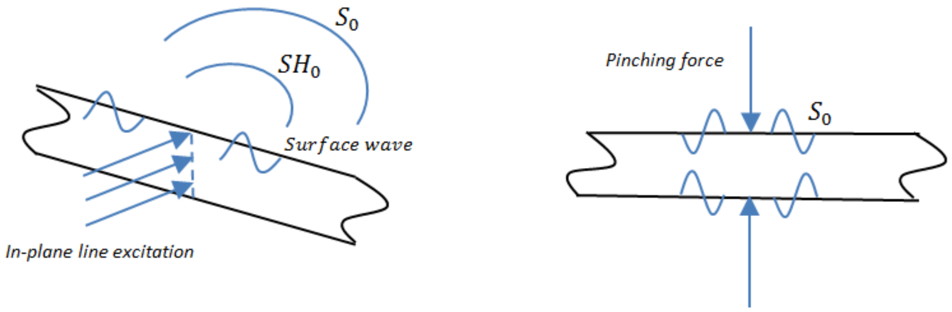

Figure 2.5: Method of exciting symmetric Lamb wave modes: (LEFT) In-plane line excitation on the plate boundary. (RIGHT) Pinching force on surfaces of the plate generates pure S0

Conclusively, the traditional single point forcing on the surface of the plate was not a desirable method to purely excite one Lamb wave modes. There are two acceptable methods to excite S0 waves as illustrated in Fig. 2.5. First, an edge forcing, where S0 and SH0 are excited. It is best to align the line of direction of wave propagation to the defect for maximum S0 interaction and SH0 minimum interaction, or vice versa if SH0 is desirable. The second method only excites S0 and this is done by symmetrically forcing both plates surface about the mid-plane. This force configuration is also known as a pitching force. However, this technique is very difficult to adopt experimentally with transducers. If multimode are excited it is preferable to ensure the individual modes incident with the defect at a different time such that the incident waves do not overlap, refer to Fig. 2.6. For the symmetric wave modes, the distance between the defect and excitation point must be at least the same number of the wave train such that the head of the SH0 wave train touches the tail of the S0 wave train. This is particularly useful when analysing the scattered wave field experimentally.

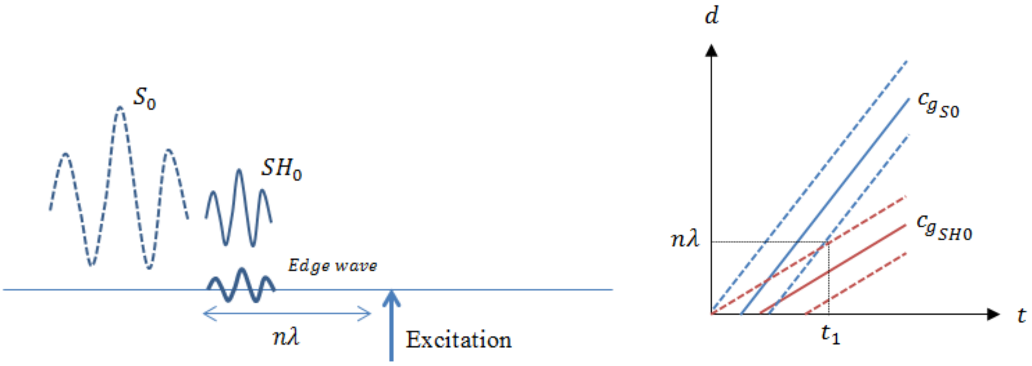

Figure 2.6: Diagram showing the minimum required distance of wave train to have separated S0 and SH0 wave incidents

Consider the planar wave approximation investigation. It is difficult to produce plane waves computationally, however over a certain distance, an incident cylindrical wave can be equivalent to planar wave. The distance from the source to the impinging point such as a defect, ensure the curvature wavefront is reasonable planar. A strategy is set up that the wavefront through the point of interest error must be significantly smaller than the wavelength. Furthermore, the exciting signal will influence this certain for planar wave approximation. The exciting signal is Hann-window to minimise the dispersive nature of the wave as well as reduce spectral leakage [22]. Theoretically, a greater number of the Hann-windowed cycle is preferable, but they are limited due to the plate dimension. Studies have been done using 3-10 cycles Hann-window. Additional half cycles were considered as well, such that the maximum of the signal is also the peak of the envelope window. However, it is required to have the full incident wave train for analysis such that the distance should be slightly more than the incident wave train. For example, for a 5.5 cycle Hann-window signal, a distance of more than 5.5 wavelengths is required. In this research, each study will have a different number of cycles and are chosen depending on factors which include plate geometry, incident wave speed, scanning locations of scattered waves, and the number of modes. Effectively, the number of cycles is optimised to separate wave modes and also to significantly reduce computational time.

The plate size for wave propagation problem depends on the signal and the defect location. The dimension is strictly optimised to avoid or to minimise reflection and mode conversion from the boundary, which overlaps and interfere with the scattered wave. Techniques to model an infinite plate include infinite boundaries and absorbing boundaries, which Moreau and Castaings [156] states can be conducted at approximately 2.5 wavelengths thick to avoid larger plate sizes, and symmetrical boundaries for plane wave solution. Rajagopal et al. [31] further developed layer methods for frequency and time domain to mimic an unbound isotopic media using commercially available finite element packages. Studies such as Diligent et al. [28] used 600mm x 1200mm long plate to avoid unwanted edge reflection. Using a simple large plate is sufficient, easiest to use and can avoid complex functions to mimic infinite boundaries, where it is impossible to do so in experimental work.

The number of mesh through the thickness depends on Lamb wave mode. For symmetrical wave modes, the profile is simple and uniform given at the frequency-thickness product is less than 1.53 MHz-mm [33, 157]. Thus the smallest possible thickness may be used as the element size. The antisymmetric wave mode thickness profile is complex and requires more elements through the thickness. One may use the global mesh condition and a thicker specimen to ensure the wave thickness profile is also captured.

The crack can be modelled by using removal of elements to match the nodes for baseline subtraction, or by separation of nodes, as illustrated in Fig. 2.7. A notch is considered equivalent to a V-tip crack, since the notch width is significantly smaller than the wavelength and notch length [51, 52]. The results of the V-tip crack and notch are consistent with the findings of Owen and Fawke [158]. Although shape stress field results in the near-field of the notch roots have inaccuracies, they exhibit the accurate global behaviour. Further investigation by Ratassepp et al. [32] concluded that the near-field of the defect of zero width, notch and V-tip crack are similar. Other considerations of near-field accurate modelling crack are using quarter point crack tip and local mesh refinement as discussed in Aliabadi and Rooke [159]. The notch representation of the defect resembles the artificial crack created in the experimental study of this research. Whereas, in the computational study the V-tip crack representation is considered. It is worthwhile to note that further mesh refinement may decrease the time step to satisfy the criterion, hence increasing computational work.

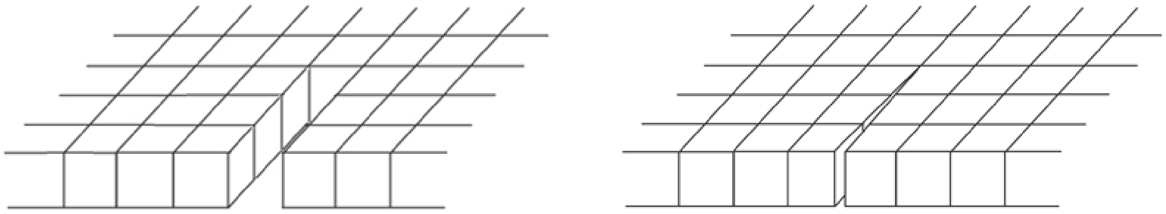

Removal of elements

Separation of nodes

Figure 2.7: Method of modelling crack (LEFT) by removing elements; (RIGHT) by separating nodes

ANSYS 15.0 Explicit Dynamic was used as an *Analysis System* to compute wave propagation in a specimen model. At first, the material properties; Young's Modulus, Poisson's Ratio and density are defined in *Engineering Data*. The model was dimensioned in *Geometry* using rectangular sectioning to ensure uniform element during meshing operation. In '*Mechanical model'*, the geometry model parts are grouped to form the specimen plate. An additional coordinate system can be usually created at the centre of a hole or crack tip for later analysis. Furthermore, absorbing boundaries and symmetrical boundaries, under *Symmetry* and *Symmetry Region* can be used to approximate the specimen plate as an infinite medium as discussed previously. The mesh is limited to specific global element size using the *Mapped Face Meshing Control* for uniformity, with no triangular elements to minimise the total number of nodes. *Named selections* can be used to investigate localised area of interest and grouping nodes, edges and bodies with the same functionality. In the Explicit Dynamics section *Analysis Settings*, end time was set between 150 μs to 200 μs with initial, minimum and maximum time step to a fixed value. In *Output controls*, the results are saved at equally spaced points.

'*Forcing*' is inserted intentionally at a vertex of the rectangular body. The magnitude of the forces was tabulated with inputs time and force. The runtime of the simulation strictly depends on the number of nodes, hence plate size. Usually, for a simple 2D plate simulation, this is roughly 1 to 2 hours. However, for a more complex shape with irregular features, the runtime can exceed 48 hours.

In solution, *Directional deformations* were used to visualise the elastic wave propagation. In directional deformation, the coordinate system is set under specific orientation, and the results are sorted by timeframes. The data displacement and coordinates are exported into a .txt file and are extracted to MATLAB for post-processing.

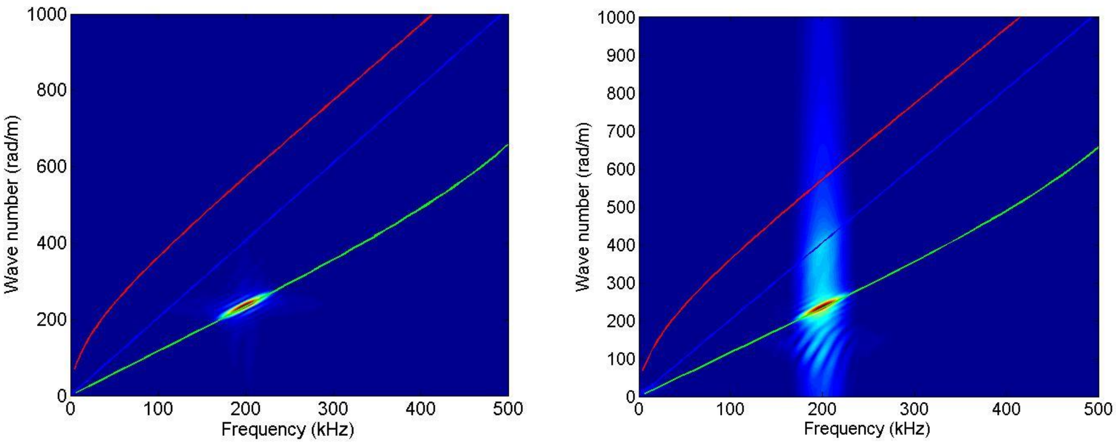

Figure 2.8: Dispersion Curve of computationally generated S0 plane wave and S0 cylindrical wave, excited at a frequency of 200 kHz

DISPERSE [33] was used as the analytical benchmark to compare with the computational work from plane waves and cylindrical waves in the study of errors associated with computational simulations. The maximum peak solution in the dispersion curve of computational cylindrical wave and plane wave is compared with DISPERSE. Both the computationally generated plane waves indicated that the frequency was 198.97 kHz and wave number of 234.18 rad/s throughout all distance, compared to the expected value of 200 kHz and 233.31 rad/s. The computational cylindrical wave results show reasonable solution compared to the solution for the computational plane wave, with a maximum deviation of 1.65%. Despite the agreements to cylindrical waves as regarded as plane waves, the spread is far greater in the cylindrical wave in the dispersion curve, refer to Fig. 2.8.

In order to compare results, normalisation is required since the scattered wave field is not planar wave. The field is that of a point source, in which cylindrical waves decay with propagating distance, R, where,

$$amplitude \propto \frac{1}{\sqrt{R}} \tag{2.2}$$

By virtue of energy conversation in two dimensions, the decay is inversely proportional to R^2. Hence, it is required to factor off this cylindrical decay to obtain measurements of the scattered wave amplitude that only depends on the scattered wave and not on the propagating distance.

The strategy first assumes that the propagating wave is expressed as,

$$u(x,t) = \hat{u}(x,w)e^{-iwt} \tag{2.3}$$

where $\hat{u}(x,w)$ represents the complex amplitude, single frequency; harmonic time dependence.

A point source at the origin will now generate a field,

$$\hat{u}(x,w) = G(\boldsymbol{x},o,w) = \frac{i}{4}H_0^1(|k(\boldsymbol{x})|) \tag{2.4}$$

For a point source; Greens function for an observation point at source **o**.

$$G \cong \sqrt{\frac{i}{8\pi kr}}e^{ikr} \; for \; kr \gg 1 \; (far \; field) \tag{2.5}$$

Thus that dependence is factored out of $\hat{u}^s(x,w)$ to define the scattering amplitude.

$$\hat{u}^s(x,w) \cong \sqrt{\frac{i}{8\pi kr}}e^{ikr} \times A(\boldsymbol{k^s},\boldsymbol{k^I}) \tag{2.5}$$

This is the FT of time domain scattered field.

Hence,

$$\frac{\hat{u}^S(x,w)}{\left\{const\sqrt{\frac{1}{kr}}e^{ikr}\right\}} \tag{2.6}$$

is the first normalisation factor.

The constant can be obtained by taking points away from the defect by FE.

This then defines

$$G(r,w) = \frac{\widehat{w}(r,w)}{\hat{p}(w)} \tag{2.7}$$

Where $\hat{p}(w)$ is the input. Then, FFT the associated signal, refer to Fig. 2.9.

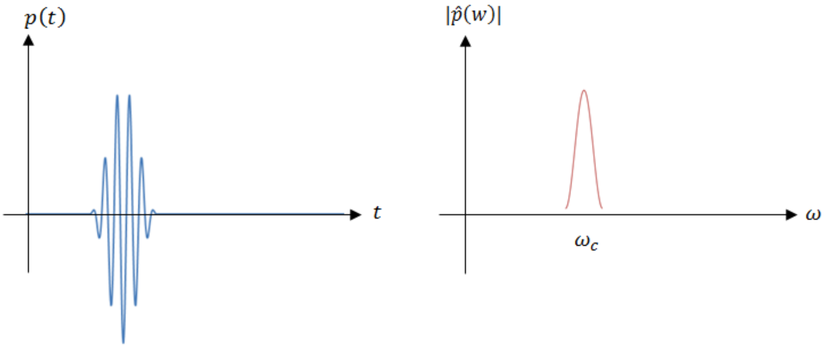

Figure 2.9: Fast Fourier transformation of the associated signal

Note, a correction factor is required for the maximum $|\hat{p}(w)|$ due to the windowing of the signal.

Alternatively, one can also perform a Hilbert transformation and trace the maximum peak displacement value over distance, then linearise data such that,

$$Y = MX + C \tag{2.8}$$

$$X = \frac{1}{\sqrt{R}} \; and \; M = const$$

However, if the incident wave is not planar, a second normalisation is required to account for a point source tone burst.

Therefore, the incident field is like a plane wave $e^{i\boldsymbol{k^I x}}$ but modified by point source decay so

$$\hat{u}^I(\boldsymbol{x}, w_c) \cong const \sqrt{\frac{1}{kR_1}} e^{ikR_1} \times e^{ik^I x} \tag{2.9}$$

where R_1 is the propagating distance due to the incident wave and superscript I denotes the incident wave.

Hence, the normalisation is as follows,

$$\hat{u}_z^s[(R_0, \theta^S), w\colon \theta^I] \cong \left\{\sqrt{\frac{1}{kR_1}} e^{ikR_1}\right\}\left\{\sqrt{\frac{1}{kR_0}} e^{ikR_0}\right\} \times A(\boldsymbol{k^s}, \boldsymbol{k^I}) \tag{2.10}$$

where R_0 is the propagating distance due to the scattered wave and superscript s denotes the scattered wave.

The first term of Eqn. (2.10) is the normalisation for input in order to make the input like a plane wave and the second term is the scattered field normalisation. The last term is the normalised scattering amplitude.

Hence, upshot is to obtain and plot $\left|A\left(\boldsymbol{k^s}, \boldsymbol{k^I}\right)\right| vs\ \theta^S$. In general,

$$A\left(\boldsymbol{k^s}, \boldsymbol{k^I}\right) = \frac{\hat{u}_z^s[Q, w; P]}{\sqrt{\frac{1}{k_{in}R_1}} e^{ik_{in}R_1} \sqrt{\frac{1}{k_{out}R_0}} e^{ik_{out}R_0}} \tag{2.11}$$

2.2 Experimental Considerations and Methodology

In this chapter, the considerations and methodology of the experimental laser vibrometry rig for non-contact guided wave field measurements, PZT actuator and specimen are discussed.

There are many commercially available products to detect Lamb waves. Recently, the Laser Vibrometry has become an important tool to record low-frequency wave propagation in velocity components. Studies [24, 57, 75, 76] have reported that the experimental results from scanning Laser Vibrometry were in good agreement with the classical piezoceramic-based sensing technique, and were also comparable with the numerical simulations. The key advantage is its non-contact high-resolution technique to obtain 2D velocity wave field over a time domain. However, a particular large scan will exceed more than 24 hours. The Laser Vibrometry requires high precision setup, regular maintenance and additional equipment to operate which can be very costly. Furthermore, due to the sensitivity of the laser, there is a material limitation. The surface of the material must be smooth and sufficiently reflective otherwise, a retro-reflective film or spray is required. In the field of Lamb wave propagation on plate-like structures, the general purpose of Laser Vibrometry has only been used for research and not practical for SHM, unlike the PZT.

The Laser Vibrometer utilise the Doppler Effect caused by the frequency shift due to the incident and reflected beam. Thus the measured frequency is related to the surface velocity, and the wavelength of the incident laser beam is given by:

$$f = \frac{2v}{\lambda} \tag{2.12}$$

In this experimental setup, the POLYTEC CLV 3D sensor head is fixed and the specimen is mounted onto a Parker Automation 404XE XY positioning system. Previous experimental studies often fix their specimen, whereas their sensor head follows an inputted scanned path. However, the complication of this technique is that during the scanning process the beam angles are constantly changing, and resolving the individual motion components become necessary. Thus it is advantageous for a stationary laser head to be used with integrated left, right and top beams for three components of velocity.

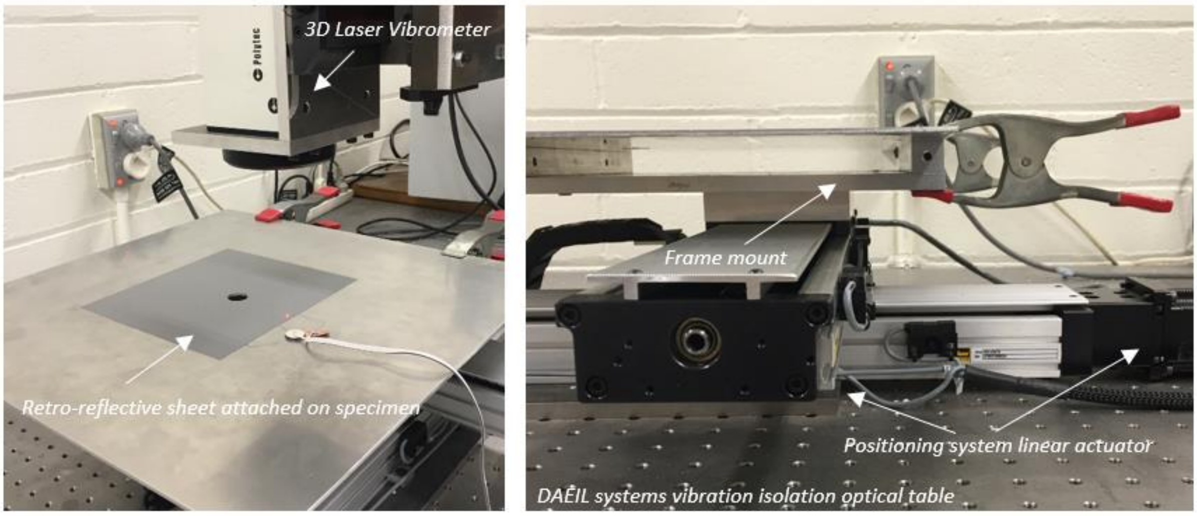

Figure 2.10: Laser Vibrometer, specimen with bonded PZT and retro-reflective sheet and position system for the experimental setup

Two Parker Linear Positioner controls the motion in the x-y plane and the laser focal point can be adjusted. Parker stepper motor LV233 is programmed to drive the linear positioning system with acceptable step size for the resolution of the scanned path. The laser and specimen rig is mounted on a DAEIL system vibration isolation optical table to minimise vibration as shown in Fig. 2.10.

The 1.5MHz modified CLV-M030.B decoder module converts to surface velocity output, which can be set to output a voltage directly proportional to the surface velocity with a factor of 5, 25 or 125mm/s/V as shown in Fig. 2.11. Data acquisition is processed through a National Instrument PCI-6115 board and BNC-2110, to convert the measured analogue signal to digital signal as shown in Fig. 2.12. The excitation signals are filtered with a low pass filter and amplified by a Krohn-Hite Model 3944 programmable 4 channel 2Mhz filter and 7602 wideband power amplifier. The experimental rig diagram is shown in Fig. 2.13.

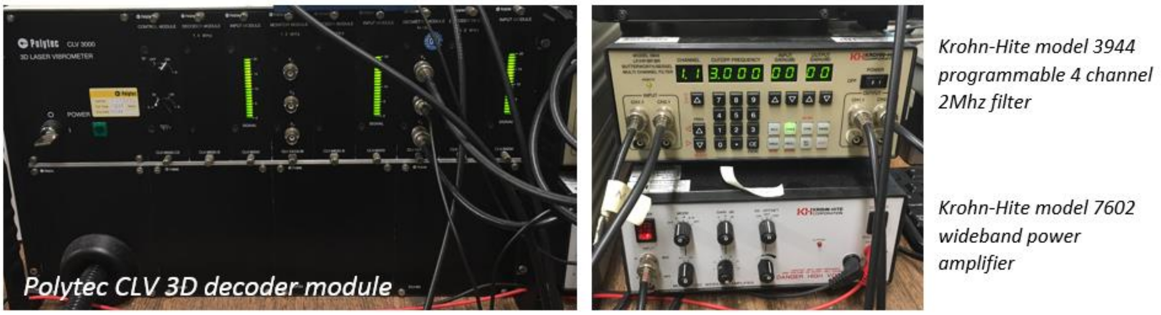

Figure 2.11: (LEFT) Laser Vibrometer decoder module (RIGHT) Krohn-Hite hardware programming filter and amplifier

Figure 2.12: (LEFT) Oscilloscope showing input signal to the PZT and acquired signal via laser sensor (RIGHT) National Instrument BNC 2110 block

The experimental velocity wave field results exhibit significant noise for the in-plane measurements due to weak reflections of laser beam back toward the sensor. In order to maximise the reflected energy back to the sensor head, Polytec high-gain retro-reflective sheet with a pressure-sensitive adhesive is attached onto the specimen. The retro-reflective sheet greatly improves the resolution of the results. ARDOX reflective spray was also tested. However, due to the sensitivity of our research, i.e. baseline subtraction, it is highly advised to use the retro-reflective sheet.

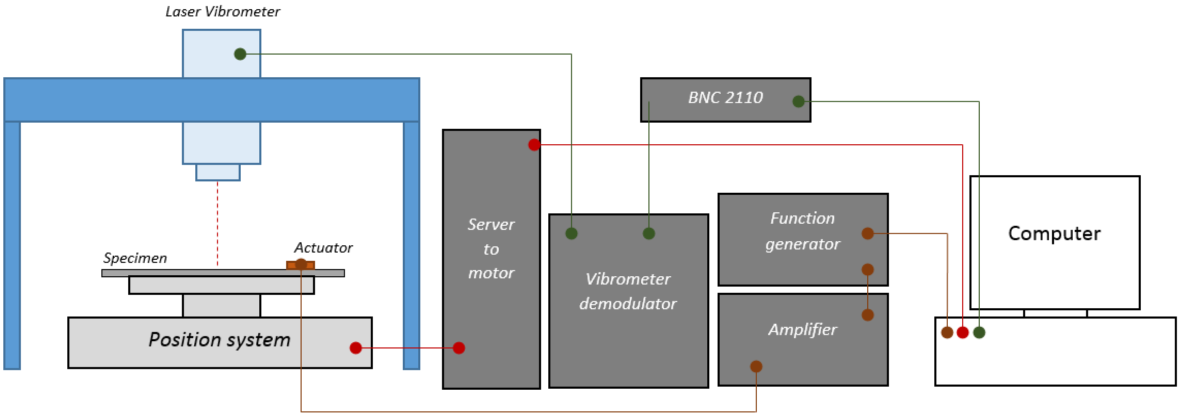

Figure 2.13: Experimental setup for Laser Vibrometry

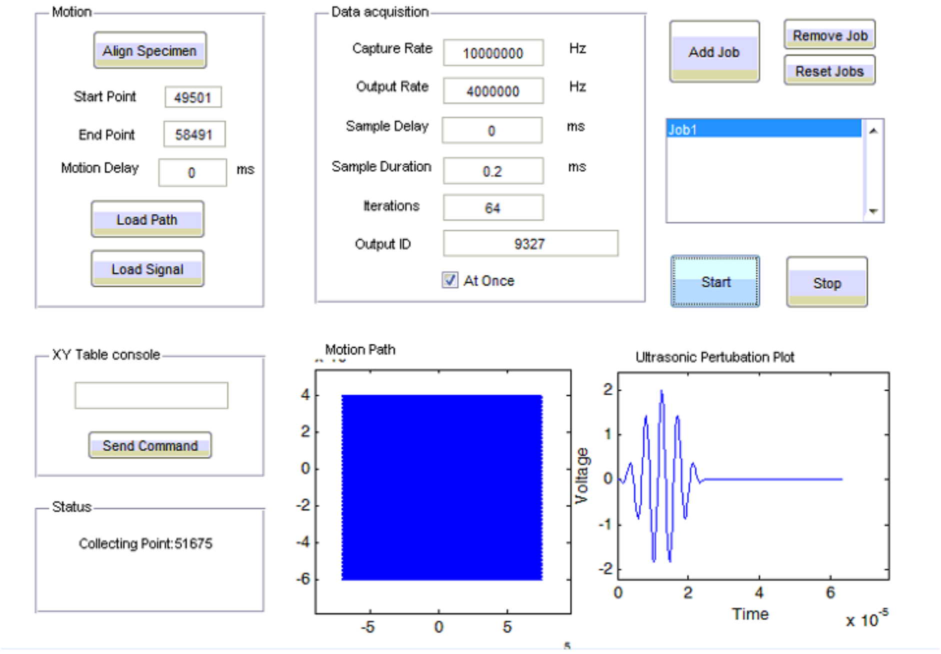

Motion

Start Point 49501

End Point 58491

Motion Delay 0 ms

Data acquisition

Capture Rate 10000000 Hz

Output Rate 4000000 Hz

Sample Delay 0 ms

Sample Duration 0.2 ms

Iterations 64

Output ID 9327

☑ At Once

Job1

Status

Collecting Point:51675

Figure 2.14: MATLAB interface for Laser Vibrometry experiment

The Laser Vibrometry is controlled by the software platform MATLAB. Operation and control are entered in a Graphical User Interface function as shown in Fig. 2.14. Motion scanned paths, voltage-time relationships can be loaded as .mat files, and are freely adjusted through the GUI. The capture rate was set at maximum 10MHz.

MATLAB simultaneously controls and positions the specimen on the XY-position system. It sends the excitation signals to the PZT and receives data from the Laser Vibrometer decoder. User specified delay for data acquisition ensures the decay of any residual vibrations from the movement. The PZT actuator is then excited and data acquisition happens at a specified temporal resolution. A second delay ensures the data acquisition is completed, and collection of averaging is performed to make sure signal to noise ratio between the XY table is moved onward to the next coordinate. This process is repeated until all specified point defined in the motion path is completed. The number of point status is updated in the GUI. This experiment normally completes within a few hours.

Once the scans are complete, the acquired data is post-processed in MATLAB for further analysis. The initial stage in post processing is the reconstruction of wave fields in either Cartesian or cylindrical components of surface velocity. Regardless, one can simply change from Cartesian to a cylindrical coordinate system by a transformation matrix.

$$\begin{bmatrix} e_r \\ e_\theta \end{bmatrix} = \begin{bmatrix} \cos\theta & \sin\theta \\ -\sin\theta & \cos\theta \end{bmatrix} \begin{bmatrix} e_x \\ e_y \end{bmatrix} \tag{2.13}$$

Both actuator and sensor are an essential part of SHM system. For piezoceramics actuator, the materials are lead zirconate titanate which consists of magnetostrictive (Terenol), electrostrictive (lead magnesium niobate), and shape memory alloys (nickle titanium alloy). The actuator converts an applied electric, magnetic or thermal field signal into a strain that is transmitted to a specimen through an adhesive layer. The choice of actuator for different application will depend on its categorised performance, which includes stiffness, bandwidth, linearity, temperature sensitivity, brittle and fracture toughness, reliability, etc [160].

The actuator in this research experimental investigation is a piezoceramic transducer which is used to generate incident Lamb wave modes. Pure fundamental modes are known to be particularly difficult to excite. For through-thickness crack detection, the symmetric Lamb wave mode is an ideal choice due to their uniform thickness profile. However, exciting symmetric Lamb wave mode is known to be difficult without exciting the anti-symmetric modes [28, 30, 53].

The literature on the solution Lamb-wave tuning with piezoelectric transducers are presented by Giurgiutiu [22] by representing the transducer as a generic shear stress distribution model. The maximum coupling between the transducer and the fundamental A0 and S0 Lamb wave mode in the plate would occur when the transducer length is an odd multiple of the half-wavelength and minima when it equals an even multiple of half-wavelength. Although different Lamb wave modes have different wavelengths, one will need to select PZT size and tune frequency into one or another Lamb wave mode. The operating frequency for the experimental study is at approximately 200 kHz and, thus, the optimal PZT diameter in accordance with the tuning curve is range 10mm-16mm to have both dominant A0 and S0 mode. It is unlikely to totally eliminate all other wave modes experimentally. Hence, it is a requirement to investigate the relative strength between the A0 and S0 wave modes. Experimental frequency sweep scans over a range of frequency is also conducted to verify that the PZT dominantly excites the specific fundamental Lamb wave mode at approximately 200 kHz. The frequency sweep scan is discussed later.

The PZT has two common modes of vibration; radial mode and thickness mode. In order to also improve the S0 to A0 signal, one should choose a PZT with a smaller thickness. However, this will consequently reduce the overall signal strength. Another technique is to bond the PZT symmetrically on edge to the midplane, refer to Fig. 2.15. Alternatively, bonding two PZTs on the opposite side can also excite predominantly S0 Lamb waves. However, any misalignment using either of those two techniques will excite a dominant A0. A simple method is a time gating the signal, such that the faster wave propagate and interact first with the defect.

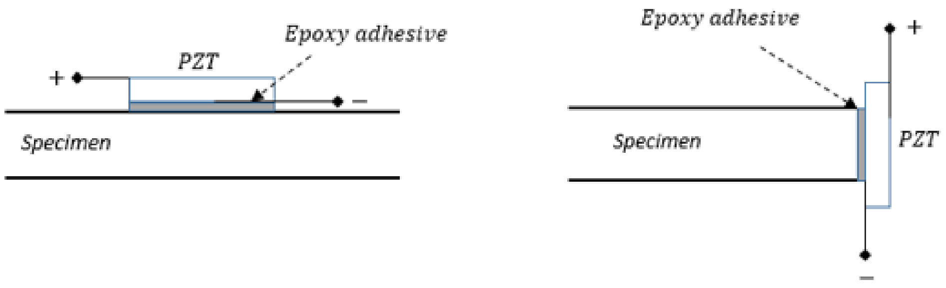

Figure 2.15: (LEFT) Single PZT bonded on the plate surface (RIGHT) PZT bonded on the edge of the plate

The bond layer between the PZT and the specimen has a major impact on the experiment. This layer dictates the strain transfer to the test specimen and applies local stress distribution. In this research, the PZT is bonded with ARALDITE epoxy adhesive and copper conducting tape was attached to the PZT surfaces. A load is applied onto the PZT for approximately 24 hours to allow the epoxy to evenly distribute, such that a uniform thickness of the epoxy adhesive is achieved. Conducting wires are soldered to the copper conducting tape.

The bond layer and piezoceramic transducer may degrade over time and possibly compromise the performance and reliability of the SHM system. Environmental temperature is one of the main factors that hinders long-term stability of embedded piezoceramic in SHM systems. A study on the effect of a debonding piezoceramic device and adhesive layer indicated significant energy loss and signal change [161]. Furthermore, the piezoelectric properties will remain consistent as long the applied strain does not exceed the static failure strain of the material, otherwise, the performances are likely to degrade [162, 163].

To determine the appropriate PZT to excite a particular frequency, a frequency sweep (excitation over a range of frequency) is applied by scanning a spatial distance over a temporal domain from the excitation source. By using the tuning curve, we were able to determine the estimated frequency where the excitation is purely a single mode. To excite S0 wave, since the S0 wavelength at 200 kHz is approximately 30mm, the PZT diameter of approximately 15mm is needed. A case study was performed and has indicated the relative modal content of the Lamb wave modes in a dispersion curve. Fig. 2.16 shows by placing the 16mm diameter PZT with a 2mm thickness on the surface and edge of the plate (refer to Fig. 2.15), and exciting Lamb waves at 220 kHz for a 3mm aluminium plate. The other advantage of using a 3D Laser Vibrometry is to determine the wave field in the in-plane directions. Symmetrics wave modes are dominant in the in-plane directions, and antisymmetric waves are dominant in the out-of-plane direction. Based on their particle motions, the SH0 and S0 wave can be separately analysed in the angular and radial cylindrical components, respectively. So, wave propagation can be analysed in their dominant direction. However, there is still traces of other wave modes, and this is because of Poisson’s ratio.

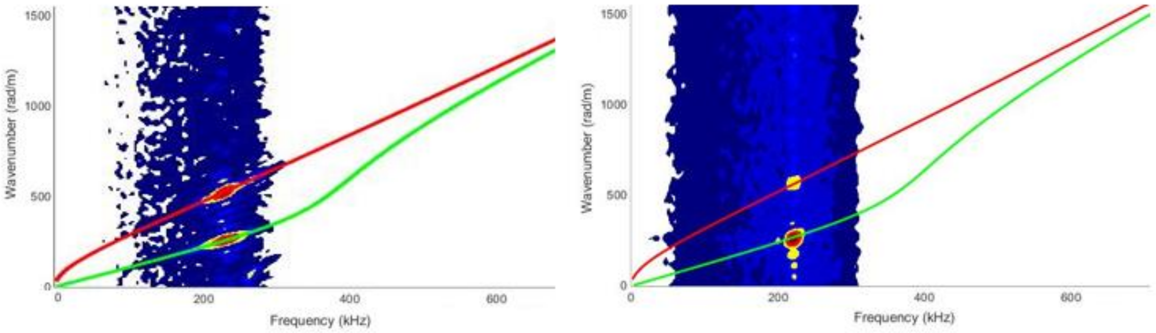

Figure 2.16: (LEFT) Signal PZT method: Dispersion curve showing dominant A0 and weak S0; (RIGHT) Edge PZT method: Dispersion curve showing dominant S0 and weak A0 at the centre frequency of 220 kHz in the out-of-plane component. (GREEN) S0 and (RED) A0

The crack is artificially created with a hacksaw having a thin blade. The achievable width of the crack is approximately 0.3 to 0.4 mm. The artificial crack closely resembles a notch. A travelling microscope is used to measure the crack dimensions to the hundredth decimal in millimetres. Although the artificial notch may not be very representative of a real crack, the research intended to investigate open simple straight crack; non-crack crack face such that wave cannot be transmitted through the crack faces. Additionally, if the crack length is much larger than the width, the effect due to the crack width is negligible. This research only focuses on linear wave propagation behaviour, so the notch-like crack is considered in the experimental studies, and whereas, a fatigue crack is a plasticity-induced crack which involves nonlinear wave propagation.

The general procedure is to scan a baseline without a crack and then introduce a small crack. Once the small crack is analysed, the crack length is increased, and this procedure is repeated. This practice uses the same plate and PZT to maintain a level of accuracy for baseline subtraction.

Chapter 3

Scattering of the fundamental S0 Lamb wave mode by a small edge crack in an isotropic plate

This chapter explores the scattering of the fundamental S0 Lamb wave mode by an edge crack in an aluminium plate. S0 is essentially non-dispersive at low frequency and symmetric to mid-plane of the plate. The edge crack is small, relative to incident wavelength. In particular, the study investigates the characteristic of S0 scattered wave field from a crack on the boundary. The fundamental S0 lamb is an advantageous wave mode to detect through-thickness crack due to its uniform mode shape thickness profile. Furthermore, S0 fast group velocity at low frequency is well suited for rapid long range inspection. The scattering from the incident S0 provide the symmetric modes; S0 and SH0, given the crack is symmetrical about the midplane of the plate.

The effect of angle of incidence and crack length are studied as a forward scattering problem, in an attempt to establish a quantitative relationship between the scattered amplitude and crack size. Frequency analysis is considered in this study to understand the scattering wave field. Additionally, the baseline stresses are applied to the crack faces to show that the scattered wave field can also be obtained by force equivalent.

The research focused on early detection such that the crack length is smaller than the incident S0 wavelength. It is understood that the scattered wave field can be reproduced by applying particular combination body forces at the location of the crack tip. This strength of these forces depends on the integral of cracking opening displacements.

3.1 Introduction

Fatigue cracks in engineering structures are a common problem and require regular inspections to detect and monitor small cracks before they reach a critical size that could result in catastrophic failure. Conventional ultrasonic techniques, such as pulse-echo and pitch-catch method [26], involve scanning over the area of interest and require local accessibility for inspections. This conventional technique is very time consuming and can be impractical for crack detection in large and complex structures. Lamb waves propagation is an alternative method which has been acknowledged by many authors for ultrasonic non-destructive damage detection due to its attractive properties for wide-area inspection with little attenuation. Lamb waves and their applications have been extensively investigated, both computationally and experimentally [7, 13, 15, 18, 19, 29-32, 52, 78, 147]. The Finite Element Method (FEM) provides a time-efficient and advantageous computational tool to analyse wave propagation in complicated structures and configurations for which the analytical solutions do not exist.

The scattered wave fields when an incident elastic wave impinges on a crack have been investigated for bulk waves [65, 129, 131], and more recently, for Lamb waves [31, 32]. It is known that an infinitesimal crack is equivalent to a point source consisting of body-force doublets with different forcing combinations that correspond to different crack opening modes [27]. This suggests that the scattered wave field due to the presence of small edge crack can be modelled as point source when the incident wavelength is much longer than the crack dimension.

The aim of this chapter is to computationally explore the interaction of low frequency zeroth order symmetrical modes with a small (compared to wavelength) edge crack. The first investigation will report on the scattered wave pattern and amplitude for various angles of incidence and various crack lengths. The second set of investigation is to simulate the scattered wave pattern by applying tractions on the crack faces to enforce a traction-free boundary condition, based on the principle of superposition. The motivation for this study is to investigate and analyse the scattered wave field from a known crack size as a pre-requisite for a subsequent attempt to investigate the inverse problem of characterizing the crack size based on the measurements of the scattered field. The nature of the wave scattered by an edge crack will be reported on.

3.2 Computational Set-up and Procedure

Lamb waves are generally dispersive and if excited at higher frequency-thickness product, multiple modes will exist and the acquired signals may be difficult to interpret. However if excited by a point source that is symmetrical with respect to the plate's midplane and at low frequency-thickness product range, below the SH1 cut-off of 1.53 MHz-mm for aluminium [33], the Lamb waves consist of only two propagating modes, viz. the fundamental symmetric wave (S0) and shear horizontal wave (SH0). In this study, only S0 Lamb wave excitation will be considered.

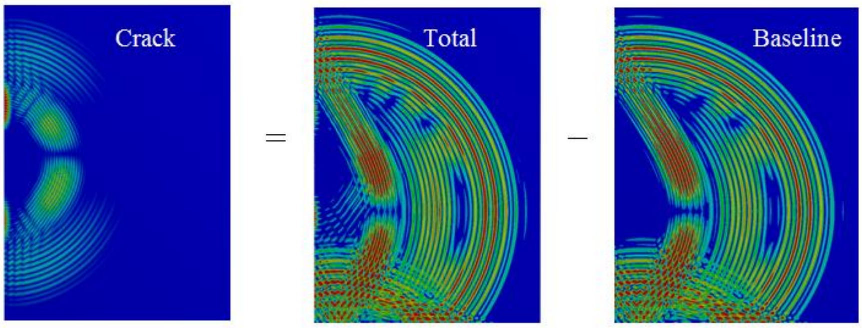

Figure 3.1: The scattered wave field due to the crack using baseline subtraction from Eq. (3.1)

A baseline subtraction is employed to separate the scattered wave displacement field, $u_{scatter}$, associated with the small edge cracks as follows (cf. Fig. 3.1):

$$u_{scatter}(r,\theta,t) = u_{total}(r,\theta,t) - u_{baseline}(r,\theta,t) \tag{3.1}$$

where u_{total} denotes the response of the cracked structure, whereas $u_{baseline}$ denotes the baseline field that is generated by the same excitation but in the absence of a defect.

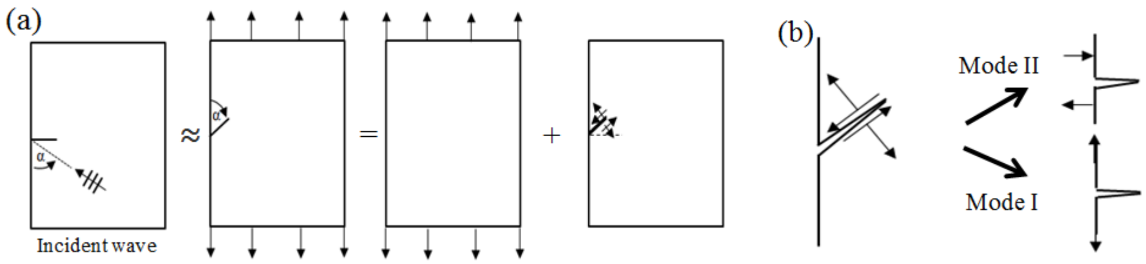

Figure 3.2: (a) Wave field as a representation of static stress approximation and (b) Scattered wave by the edge crack is equivalent to superposition of Mode I and II crack opening displacements response

The scattered field can also be obtained as the field generated by applying equal and opposite tractions on the crack faces that cancel those produced by the incident S0, in accordance with the principle of superposition [20, 29, 30], as illustrated in Fig. 3.2. This will meet the condition of a traction-free crack after the superposition of the incident and scattered field. For this purpose, only the baseline σ_{xx} and σ_{xy} stresses are required as any variant in the normal direction, z, is negligible due to the thin-plate approximation. Since the crack is sufficiently small, the stresses along the crack face are approximately constant along the crack, and hence only one of nodal stresses is required. The time sequence of each baseline stresses are then applied as tractions on the 3mm and 6mm crack faces to generate the wave fields that correspond to the scattered fields obtained from Eq. (3.1).

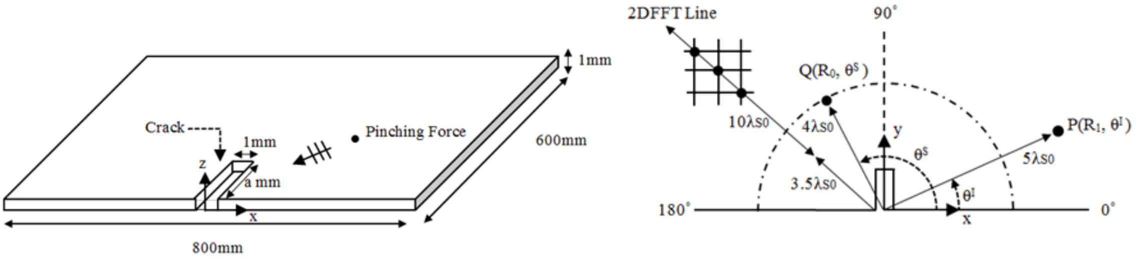

Figure 3.3: (a) Geometry of FE model for 800mm x 600mm x 1mm aluminium plate showing the location of the excited force relative to the crack and (b) Detail diagram showing the 2D FFT line, point of excitation and scattered wave measurement locations relative to the crack

3.3 Computational Investigation

ANSYS is used as the Finite Element (FE) computational analysis tool for this study. The simulation represents an aluminum test plate 800mm × 600mm × 1mm (density of 2700kg/m^3, Poisson's ratio of 0.33 and Young modulus of 69GPa) as shown in Fig. 3.3(a). The plate contains an edge crack located at the origin, as indicated in Fig. 3.3. The plate is discretised into 8-node linear cubic elements of size 1mm, and the crack is accordingly modelled as a notch of width equal to 1mm, which is much smaller than the crack length, *a*, of 3mm and 6mm for the angular dependence investigation. The maximum amplitude of the scattered S0 and SH0 wave pattern at 45° incidence is also investigated for crack lengths from 1mm to 9mm with 1mm increment, to determine the dependence of scattered amplitude with crack length.

The incident S0 mode is generated by applying equal and opposite point forces to nodes on opposite faces of the plate, with the force acting in the direction normal to surface, which can be aptly described as a *pinching force*. The pinching force excitation signal consisted of a 10-cycle Hann-window tone burst centred at frequency 200 kHz to minimise dispersion. At this centre frequency, the incident S0 mode has a wavelength $\lambda_{S0} = 26.6$ mm, and SH0 mode has a wavelength $\lambda_{SH0} = 15.3$ mm. This input excitation is applied at point P with polar coordinates (R_1, θ^I). To approximate a planar incident wave, the cylindrical excitation source is placed at $5\lambda_{S0}$ away, to ensure that the impinging wavelength at $\lambda_{S0}/2$ along the boundary from the crack base is no more than $0.05\lambda_{S0}$ in error compared with a plane wave. Polar coordinates (r, θ) with origin at the crack base and the r and θ components of the surface displacement will be used to track the scattered Lamb wave modes (cf. Fig. 3.3).

The cracks are modelled as a 1mm width notch by element removal in FE. The notch width is sufficiently large to prevent contact from the adjacent crack face and small enough to approximate to a zero-width discontinuity [52] such that reflectivity from notch width is negligible.

The FE simulation uses 1mm cubic element size, which satisfies the requirement of 10 elements per wavelength for accurate modelling [147] , and a time step of 0.1µs, which satisfies the Explicit Time Integration 0.8 L/C stability limit [148], where L is the smallest element length, C is the fastest wave speed. A 2D FFT is performed on the nodes along the line 45° from the crack base edge indicated in Fig. 3.3(b) and was used to produce the dispersion curves to identify the dominant scattered Lamb wave mode in the θ and r components from *DISPERSE* [33], as shown in Fig. 3.4(a) and (b). The 2D FFT consists of more than 400 time samples, 40μs. The 2D FFT spatial distance is taken at least $3.5\lambda_{S0}$ away from the crack base, to avoid detection of higher non-propagating Lamb wave modes [29] and over approximately 10 λ_{S0} distances with 1024 equidistant spatial samples with zero padding [147]. The scattered wave pattern is obtained by polar plotting the maximum displacement values, which is obtained by performing a Hilbert transformation over a time-domain [26], measured at point Q with polar coordinates (R_0, θ^S) at distance $R_0 \approx 4\ \lambda_{S0}$ away as shown in Fig. 3.3(b).

The scattered patterns are analysed in two sections: back-scattered displacement, u_B, measured in $0° \leq \theta < 90°$ and forward-scattered displacement, u_F, as measured in $90° \leq \theta \leq 180°$. The maximum scattered wave, u_{max}, relative to maximum input excitation displacement as the reference displacement, u_{ref}, in relation to angle dependence and crack length dependence are investigated. In order to compare the scattered wave pattern results, the scattered field maximum displacement is considered to normalize the scattered wave field in order to observe the scattered displacements relative to its maxima. The edge wave displacements are disregarded because the purpose is simply to compare the S0 and SH0 scattering patterns without considering the absolute values of amplitude. The scattered wave pattern for various crack lengths are investigated and later compared in the second investigation to the wave patterns produced by applying tractions on the crack faces. For each angle of incidence, the baseline (without crack) stresses distribution along the location crack length were applied as traction on the crack faces to produce the wave field for the second set of investigation. The angular location of the lobes was used to compare the scattered wave field due to the crack and wave field due to the traction on crack face.

3.4 Results

3.4.1 Scattered field for various incident angles and various crack lengths

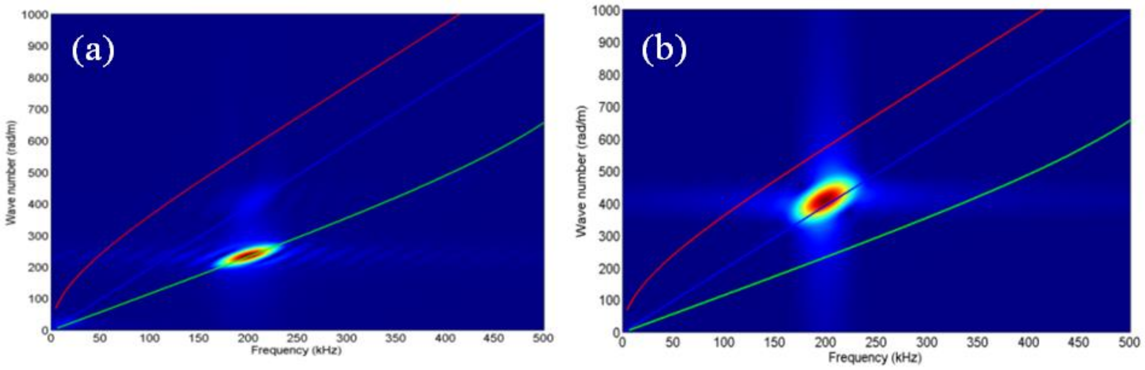

Figure 3.4: (a) Dispersion curve for scattered wave field of 3mm edge crack in the radial component with dominant S0 and (b) Dispersion curve for scattered wave field of 3mm edge crack in the θ component with dominant SH0: A0(Red), SH0(Blue) and S0(Green)

The investigation includes results of scattered wave pattern generated by an S0 Lamb wave at various incident angles to an edge crack of length 3mm (a/λ=0.11) and 6mm (a/λ=0.23). The dispersion curves have indicated predominant scattered SH0 and S0 Lamb wave in the θ and r components, respectively, refer to Fig. 3.4. The results also indicated the propagation of Rayleigh-like edge waves. In Fig. 3.5 showed scattered wave pattern dependence with angle of incidence. This is expected since the stress applied to the crack face will depend on angle of incidence. In general, the larger a/λ scattered amplitude have stronger S0, SH0 and edge wave scattered maximum displacement and the scattered SH0 waves are relatively stronger compared to the scattered S0 waves, as can be seen in Fig. 3.6. Discussion on the pattern and maximum displacements are presented in Section 3.5.

The increase of crack length has shown an increase of forward-scattered lobe and a trend of increasing maximum displacement value as shown in Fig. 3.7. It can be seen that the maximum scattered displacement is approximately proportional to a/λ until $a/\lambda \approx 0.23$, beyond which the maximum displacement values appear to plateau.

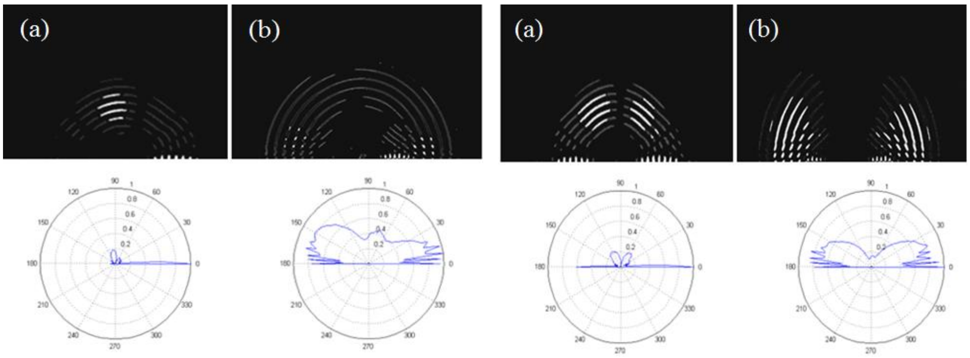

Figure 3.5: Scattered wave pattern and polar plot of 3mm crack, a/λ=0.11, at incident (LEFT) 60°and (RIGHT) 30° (a) θ component and (b) radial component

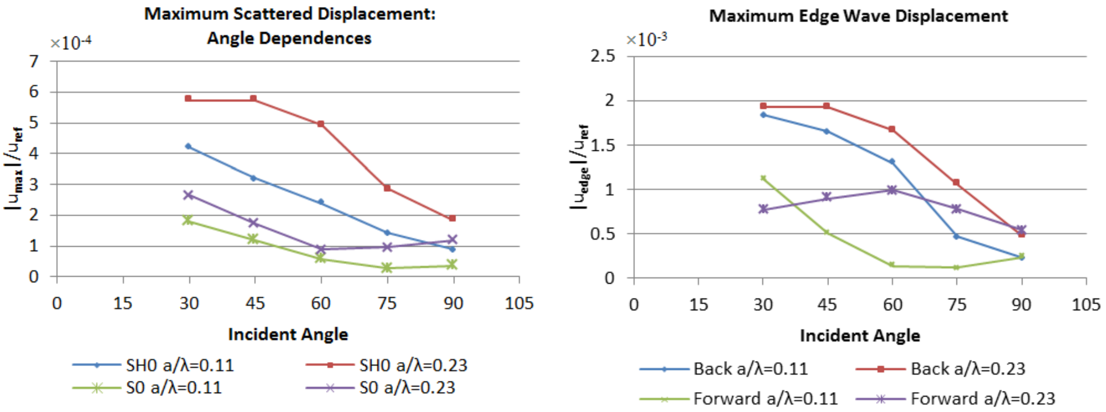

Figure 3.6: Graph of the absolute maximum value of (a) (LEFT) SH0 and S0 scattered displacement and (b) (RIGHT) forward and back-scattered edge wave maximum displacement with various incident angles for a/λ=0.11 and 0.23.

The *θ* component results of *a/λ*=0.11 and 0.23 scattered wave patterns, refer to Fig. 3.8 and Fig. 3.11, showed that as incident angle decreases or crack length increase the maximum scattered amplitude increases. However, the SH0 scattered wave patterns are distinct at different incident angles. At 75° and 60° incidences, in Fig. 3.9 and Fig. 3.12, there is a larger forward-scattered lobe which is almost symmetrical at the 90° line. The forward and back-scattered amplitude ratio approaches to unity when incident angle is small. Furthermore, the *a/λ*=0.11 and 0.23 SH0 wave pattern appears more symmetrical along the 90° line and similar to a SH0 point source for smaller angle of incidence, which can be seen in Fig. 3.9(d) and Fig. 3.12(d). The symmetrical wave pattern indicates dominant primary forcing component, either perpendicular or parallel, acting on the crack at the extreme angle of incidences being 30° and 75°. The scattering wave patterns observed at incident angles between the extremities are a combination of parallel and perpendicular forces acting on the crack face.

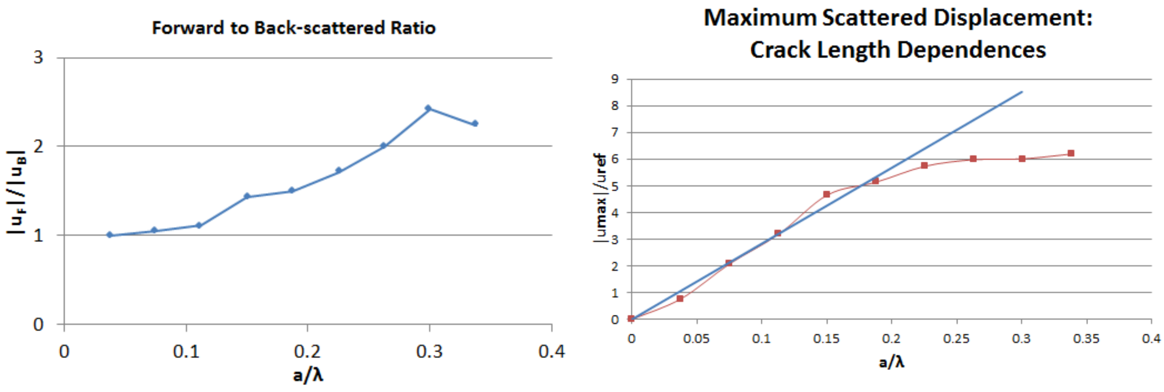

Figure 3.7: (LEFT) Maximum forward to back-scattered displacement ratio of scattered SH0 waves at incident 45° with various a/λ. (RIGHT): Graph of the maximum scattered displacement at incident 45° with various a/λ for up to a/λ=0.2 as indicated by the linear blue line.

The radial component of the *a/λ*=0.11 and 0.23 scattered wave pattern have a slightly stronger back-scatter and features of a S0 point-like source at incident angle 30°, 45° and 60° incidences as shown in Fig. 3.10 and Fig. 3.13. An interesting scattering effect is the surface wave propagating on the horizontal boundary, contrasted in Fig. 3.5. The *a/λ*=0.11 and 0.23 results showed weaker forward-scattered edge waves amplitude as shown in Fig. 3.6.

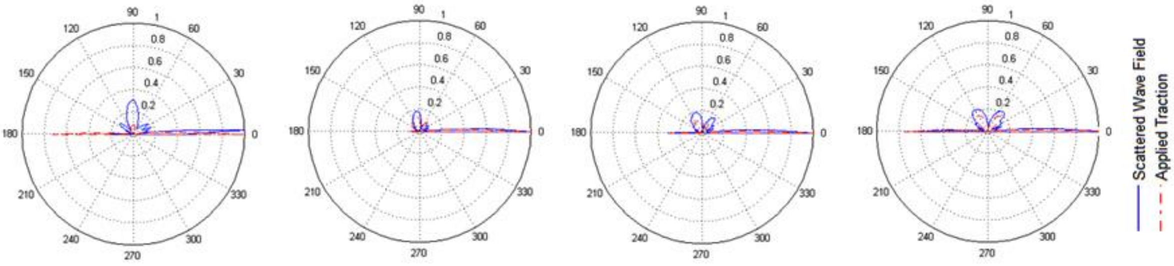

(a) *(b)* *(c)* *(d)*

Figure 3.8: [a-d] θ component a/λ = 0.11 (3 mm) crack: comparison of applied-traction to original SH0 scattered wave patterns, normalized with maximum scattered for 75°, 60°, 45° and 30° incidences, respectively.

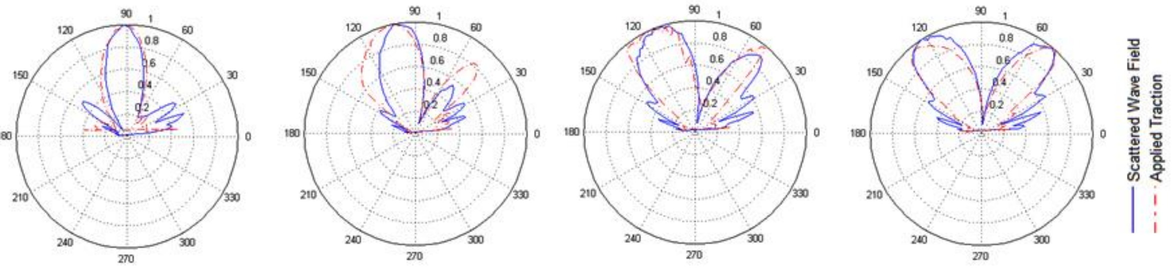

(a) *(b)* *(c)* *(d)*

Figure 3.9: [a-d] θ component a/λ = 0.11 (3 mm) crack: comparison of applied-traction to original SH0 scattered wave patterns, normalized without edge waves for 75°, 60°, 45° and 30° incidences, respectively.

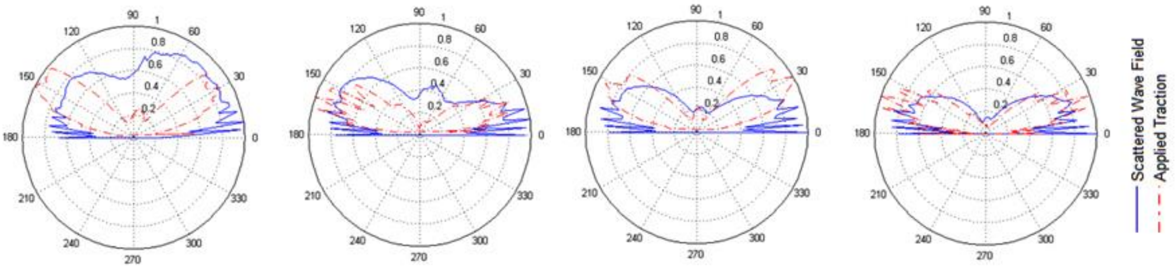

(a) *(b)* *(c)* *(d)*

Figure 3.10: [a-d] Radial component a/λ = 0.11 (3 mm) crack: comparison of applied-traction to original S0 scattered wave Patterns, normalized without edge waves for 75°, 60°, 45° and 30° incidences, respectively.

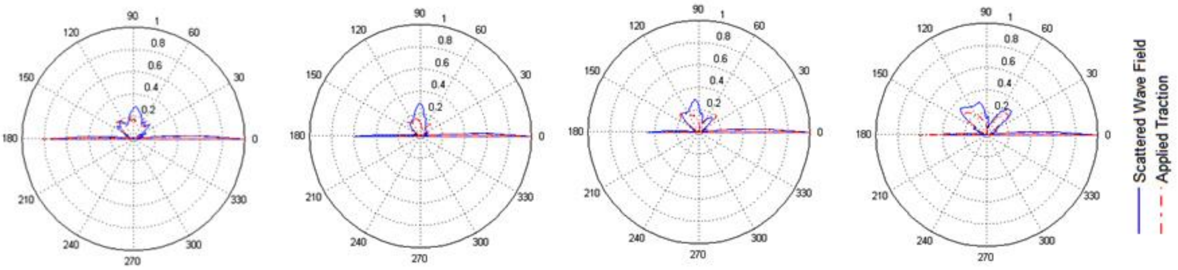

(a) *(b)* *(c)* *(d)*

Figure 3.11: [a-d] θ component a/λ = 0.23 (6 mm) crack: comparison of applied-traction to original SH0 scattered wave patterns, normalized with maximum scattered for 75°, 60°, 45° and 30° incidences, respectively.

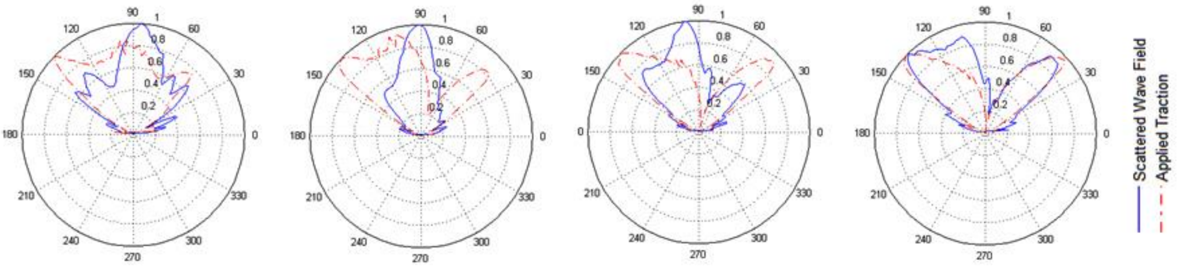

(a) *(b)* *(c)* *(d)*

Figure 3.12: [a-d] θ component a/λ = 0.23 (6 mm) crack: comparison of applied-traction to original SH0 scattered wave patterns, normalized without edge waves for 75°, 60°, 45° and 30° incidences, respectively.

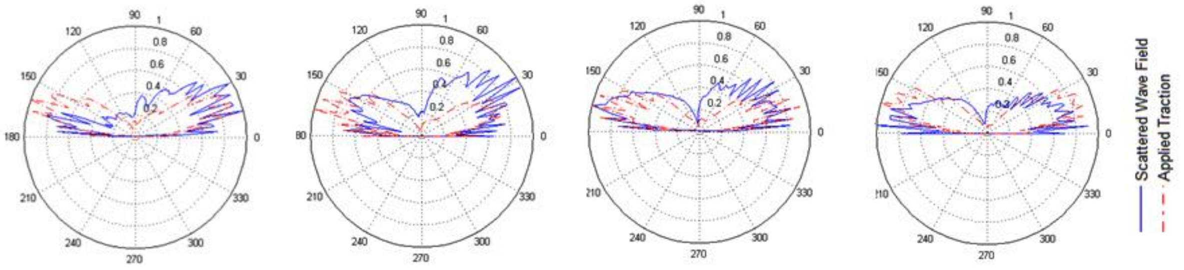

(a) (b) (c) (d)

Figure 3.13: [a-d] Radial component a/λ = 0.23 (6 mm) crack: Comparison of applied-traction to original S0 scattered wave patterns, normalized without edge waves for 75°, 60°, 45° and 30° incidences, respectively.

3.4.2 Generated wave patterns by tractions on crack faces

In general, the simulated wave pattern investigation represents much of a point-like source and as incident angle decreases the maximum wave field amplitude increases. The applied-traction on the crack face S0 and SH0 wave patterns results have shown similarity to the first investigation S0 and SH0 scattered wave pattern as shown in Fig. 3.9-13. However it did not match well in the S0 wave patterns for larger incident angles as shown in Fig. 3.10 and 3.13.

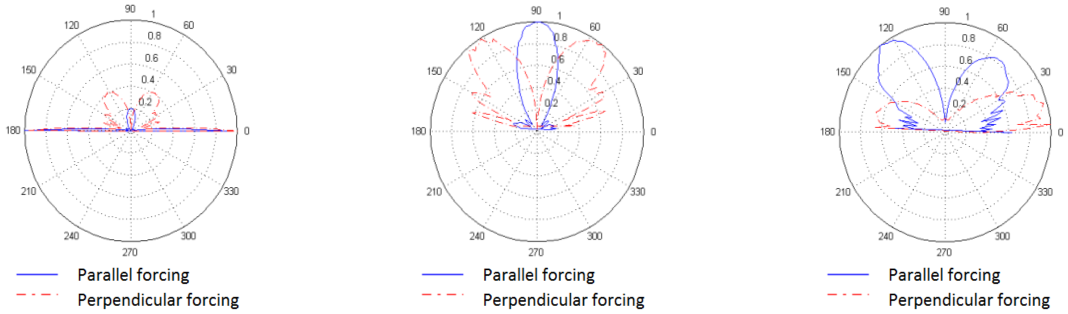

θ component *θ component* *Radial component*

Figure 3.14: [a-c] Parallel and perpendicular forcing on a/λ = 0.11 (3 mm); θ component normalized with maximum scatter, θ component normalized without edge waves and radial component, respectively.

The *a/λ*=0.11 and 0.23 simulated wave pattern reported a slightly larger forward to back-scattered edge wave ratio and the SH0 wave displacements are slightly smaller compared to the original scattered pattern as shown in Fig. 3.8 and Fig. 3.11. Furthermore, perpendicular and parallel forcing components to the 3mm crack face are investigated separately. Fig. 3.14 showed that the perpendicular forcing wave pattern appears much like a symmetrical point-like source pattern, however the parallel forcing have shown similar scattered 75° and 60° wave pattern.

3.5 Discussion

The low frequency approach (the wavelength is significant larger than plate thickness and crack dimension) makes the assumption that the problem can be analysed in plane stress condition.

One can obtain normal and shear stresses of elastic waves in a semi-infinite medium problem in plane stress conditions by using the simple change of elastic constants to convert plane strain results to plane stress, which is found in Graff [18]. In Fig. 3.15 the FE and analytical incident planar wave stresses along the y axis have similar trend. However, the difference in stresses, especially σ_{xx}, is due to the additional contribution of edge wave propagating along the plate boundary. Since the incident wave is excited as a cylindrical source, the incident wave field also includes a major component from the edge wave travelling on the boundary in addition to the incident S0 wave if excited at a smaller angle of incidence. In the next study, the scattering of edge-guided waves are studied for this problem.

For all angle of incidences, the relationship between stresses and depth to wavelength have shown linear behaviour until the depth is approximately 20% of wavelength which is shown in Fig. 3.15.

Theoretically, the simulated wave pattern will be exactly the same as the scattered wave pattern if the stresses are applied to the crack face as a function of depth. When crack length is less than 20% of wavelength, the wave pattern can simply be simulated as body-forces acting on the crack face; hence equivalent to a point-like source. Whereas theoretically, one might have expected a quadratic variation in which strength is proportional to the integral of the crack opening displacement [119]. The linear trend observed was from a limit for which the scattered wave pattern appear less likely to a point source, however, the quadratic trend may be more apparent for substantially smaller a/λ. It is also worth mentioning previous study observe an increasing trend, however for much larger crack size to wavelength ratio [58].

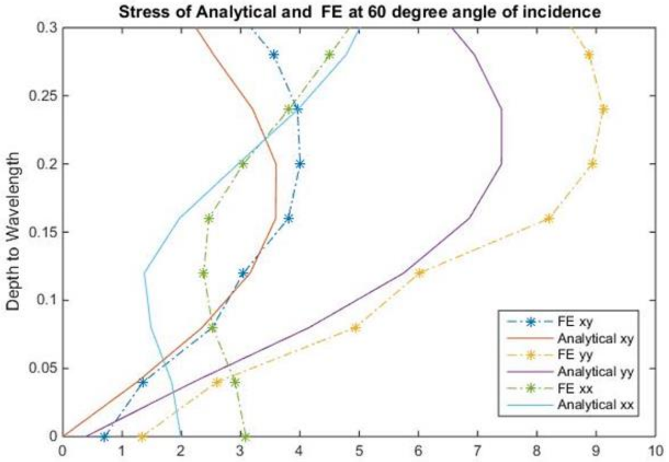

Figure 3.15: Normalised Analytical Plane Stress and FE normal and shear stresses with depth (along the y axis)

The preceding FE results show that the scattered wave pattern and amplitude due to an edge crack depend on both the crack length and the incident angle. The small cracks have S0 and SH0 point-like source scattered wave patterns which are better represented in smaller incident angles. For larger incident angles, the scattered wave patterns have a stronger forward scattered lobe. These wave patterns are expected since smaller incident angles have a stronger perpendicular force component since σ_{xx} is more dominant for smaller angle of incidences. Whereas 75° and 60° incidence have a relatively stronger parallel force component since σ_{xy} has more influence for larger angle of incidences. Thus the combination of parallel and perpendicular components on the crack face can strongly influence the wave pattern.

The normal stress σ_{xx} gives rise to a so-called mode I crack opening, whereas the shear stress σ_{xy} gives rise to a mode II crack opening. For small cracks, the mode I crack opening generates a scattered field that is the same as that of a force doublet. This field is symmetrical with respect to $\theta = 90$. Whereas the mode II crack opening generates a scattered field that is the same as that for the force doublet shown on the right. This field is asymmetric with respect to $\theta = 90$.

For small cracks, with $a/\lambda < 0.2$, the normal stress is much larger than the shear stress, and accordingly the mode I contribution dominates the scattered field. This explains why the scattering pattern is symmetrical for small cracks, but becomes increasingly asymmetrical for $a/\lambda > 0.2$.

In Fig. 3.7 the SH0 wave patterns are almost symmetrical when a/λ is small, hence under this condition the scattered wave pattern can be represented as a point-source and its amplitude is a function of a as shown in Fig. 3.7.

The S0 scattered wave patterns have shown multiple narrow side lobes near the plate boundary, which are distinguishable in Fig. 3.10. These narrow lobes are interference of head waves connecting with the S0 and SH0 as seen in radial components in Fig. 3.5(b). In Fig. 3.4(a) the dispersion curve indicated a weak SH0 signal in the radial component which also suggested the existence of head waves since head waves have similar velocity as the SH0 wave. The a/λ =0.23 polar plot showed some back-scattered multiple narrow lobes which can be seen in Fig. 3.7. The inaccuracy is due to assumption of constant stress profile for small crack and in order to simulate an accurate scattered wave pattern, the full stress profile is needed to be considered. The 75° and 60° incidences S0 scattered wave pattern results are significantly weaker and appears inaccurate in which the notch width may be a significant contributor to the scattered pattern.

At higher angle of incidence the problem here is similar to the plane strain problem however at lower angle of incidence this resembles a plane stress case with an additional, yet small, contribution of the edge wave. This explains the additional stress contribution in FE due to the edge wave as seen in Fig. 3.15 compare the analytical plane stress normal and shear stress of the S0 Lamb wave.

3.6 Conclusion

The edge crack S0 and SH0 scattered wave fields when impinged by incident S0 wave have been reported. The scattered wave amplitude for a small crack of length a, $a/\lambda<0.23$, is observed to be linearly proportional to a, although it is expected to be increase quadratically [119]. The dominant scattered wave modes are edge wave and SH0 and the weaker mode was the scattered S0 wave. The scattered wave pattern is influenced by the angle of incidence and due to the difference of normal and shear stress combination creates different wave patterns. It is shown that for small crack the scattered wave can be produced by applying traction to the crack faces and, thus, suggesting the scattered wave pattern for a small crack can be represented as a point source consisting body-forces doublets. For small cracks, the mode I crack opening generated scattered field that is the same as that of a force doublet. The result in this chapter is an essential pre-requisite approach to guide the investigation of an edge crack on a through-thickness hole. The next study attempts to determine whether the point source equivalence also applies to incident edge-guided waves.

Chapter 4

Scattering of edge-guided waves by a small edge crack in an isotropic plate

In this chapter, the scattering of the symmetric and antisymmetric edge-guided waves by a small edge crack in an aluminium plate are investigated. It is highly advantageous to use edge-guided wave due to its attractive property of no geometric decay over propagating distance on a straight boundary. Thus, this highlights edge-guide wave is a very attractive incident wave mode for SHM.

The study involves the incidence of edge-guided waves which eliminated the characteristic length of the angle of incidence. Hence, the investigations involve only the varying of crack length to determine its dependence with scattering amplitude. The incident edge waves have shown greater sensitivity to edge crack compared to the incident S0 wave mode. The edge crack scattered a dominant edge wave, SH0 and weak S0, similar to the incident S0 investigation.

Both studies of symmetric and antisymmetric wave showed scattered wave patterns and amplitude trends for small edge crack, indicating a simple point-like source representation. This configuration and scattered wave measurements can be used for the inverse problem of characterising a small edge crack from the scattered wave field.

4.1 Scattering of incident symmetric edge guided wave

This study investigates the scattered wave patterns and amplitudes generated by a small edge crack when impinged by an edge-guided wave, for quantitative inspection in structural health monitoring (SHM). Exploiting Lamb waves is an alternative method for crack detection due to its attractive properties for wide-area inspection with low attenuation [26]. However, problems involving propagating and scattering of Lamb waves are considerably more challenging to solve analytically than the corresponding problems involving bulk waves [18, 19, 78, 129, 131]. Recent papers [13, 15, 30-32, 149] have investigated the use of Lamb wave propagation to detect different type of defects in idealised and complex structures.

The aim of this study is to investigate the interaction of an incident edge-guided wave in a plate with a small edge crack (i.e. small relative to the incident wavelength). Edge-guided waves exhibit no geometrical decay with propagation distance, which is a highly advantageous property for SHM. The chapter will report on the scattered wave pattern and amplitude for various crack sizes. This study of the forward scattering problem is a desirable pre-requisite before addressing the more practically important inverse problem of characterising the crack size based on scattered wave field measurements. For the bulk wave case, it is known that scattering by a small (infinitesimal) crack is equivalent to the radiated field from a particular combination of force doublets [27]. It can be anticipated that a similar equivalence should hold for Lamb-wave scattering by small cracks. This will be investigated in the present work for the special case of an incident edge-guided wave. The more general case of oblique incidence is also being investigated and will be reported on previously.

4.1.1 Methodology

In the present work, attention is restricted to frequencies below the cut-off for the first order symmetric Lamb wave mode SH1 (1.53Mhz-mm). Thus, the only propagating symmetric modes are

S0 and SH0. The SH0 mode is non-dispersive whereas the S0 mode is also practically non-dispersive in this low-frequency regime.

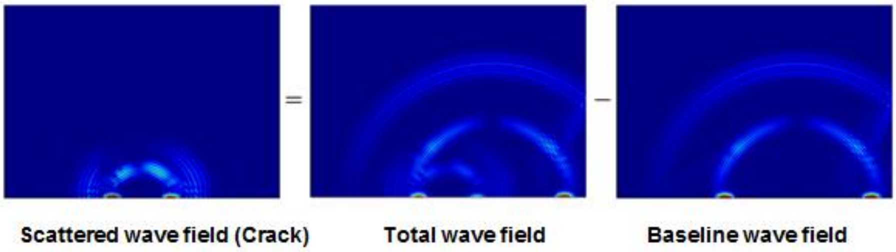

Figure 4.1.1: Illustrating the procedure of obtaining the scattered wave field due to the presence of a crack by using baseline subtraction

These symmetric modes can be generated by applied force distributions that are symmetrical with respect to the plate's mid-plane. Furthermore, a symmetric edge-guided wave can also be generated by mid-plane symmetric forces applied along a straight edge. This symmetric edge wave can be regarded as the plane stress analogue of the Rayleigh (surface) wave, and the corresponding wavespeed can therefore be obtained from the Rayleigh wavespeed by using the familiar change of elastic constants to convert plane strain results to plane stress [18].

In order to analyse the scattered wave displacement field associated with the small edge crack, a baseline subtraction is employed, as indicated in Fig. 4.1.1. Based on the principle of superposition [20], the scattered wave field is equivalent to applying equal and opposite tractions to the crack faces that cancels the stresses associated with the incident wave. The crack length a is assumed to be in the range $h<a<\lambda/2$, where h is the plate thickness and λ the wavelength of the incident wave. For this size range, the incident field can be expected to consist primarily of the edge-guided wave, with the contribution of the propagating symmetric modes along the edge being negligible. For small cracks, the scattered field can be expected to be like that of a point source located at the crack mouth (i.e. the point of intersection with the straight edge), and with the strength of the point source being proportional to some power of the crack length. This equivalence suggests that (i) the scattering pattern should be relatively independent of crack size, whereas (ii) the scattering amplitude should depend on some power of the crack length a. It will be seen that these expectations are indeed confirmed.

4.1.2 Computational Set-up and Procedure

In this study, ANSYS 15.0 is used as the Finite Element (FE) computational analysis tool to simulate wave propagation in an aluminium test plate. An aluminium plate 800mm×600mm of 1mm thickness (density of 2700kg/m^3, Poisson's ratio of 0.33 and Young modulus of 69GPa) is modelled, as shown in Figure 4.1.2(a). The edge crack is located at the origin of the plate. The plate is discretised into 1mm 8-node linear hexagonal elements which satisfy the requirement of 10 elements per λ for accurate modelling [147], and a time step of 0.1 µs, which satisfies the Explicit Time Integration stability limit of 0.8L/C, where L denotes smallest element length and C the fastest wave speed [148].

The defect is modelled as a V-tip crack with a maximum spacing of 0.2mm between the crack faces. The dependence of scattered amplitude with crack length is investigated by varying the crack size, a, from 1mm-6mm with 1mm increments. The incident edge-guided wave is generated approximately 5λ away with the line force acting direction normal to the edge surface. To minimise dispersion, the force excitation signal is chosen to be a 5-cycle Hann-windowed tone burst with centre frequency 200 kHz. At this centre frequency, the incident wavelengths of edge wave, S0 and SH0 are 13.8mm, 26.6mm and 15.3mm, respectively [33].

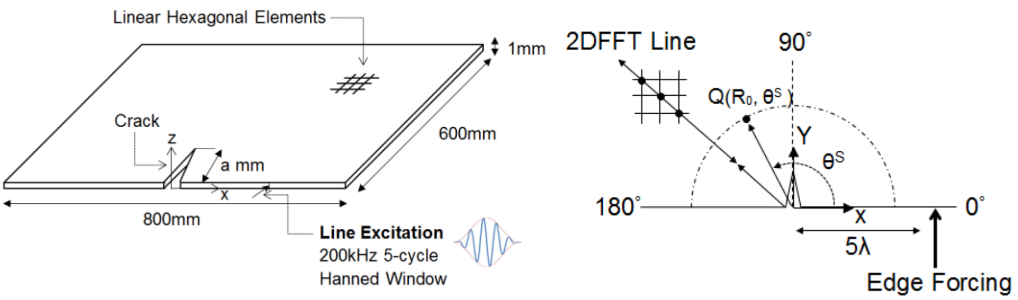

Figure 4.1.2: (a) (LEFT) 800x600x1mm aluminium plate FE geometry showing location of crack and (b) (RIGHT) Detail diagram portraying the 45° 2D FFT line, excitation point and scattered wave measurement.

2D Fast Fourier Transformation is performed on the nodes along the edge and along the line 45° from the crack base edge as indicated in Fig. 4.1.2(b). This is used to create the dispersion curve in order to identify the dominant Lamb wave mode from DISPERSE [33]. The 2D FFT spatial distance is taken at least 3.5 wavelengths away from the crack base to avoid detection of higher non-propagating Lamb waves and over approximately 10λ distances with 1024 equidistant spatial samples with zero padding [147].

The scattered wave displacement are analysed in two regions: Backward-scattered measured in $0° \leq \theta^s < 90°$ and Forward-scattered as measured in $90° \leq \theta^s \leq 180°$ with the angle θ^s as defined in Figure 2(b). Hilbert transformation was performed over the time domain signals measured at points Q at distance $R_0=4\lambda$ away from the edge crack, and for various angles θ^s, cf. Fig. 4.1.2(b). The maximum amplitude of the associated analytic signals was used as the measure of the scattered field amplitude. For both scattered SH0 and S0 modes, the backward-scattered displacements were measured at 18°, 42°, 66° and 90° and the forward-scattered were measured at 90°, 114°, 138° and 162° in radial (r) and angular (θ) components. The amplitudes of the reflected ($\theta^s = 0°$) and transmitted ($\theta^s = 180°$) edge waves were also recorded.

The scattered S0 and SH0 wave pattern results are then normalised to account for the cylindrical wave decay (at a rate inversely proportional to the square root of propagating distance), and relative to the incident edge wave displacement. In FE simulation, a ‘very low’ geometrical decay of edge waves was observed. This decay is attributed to contamination of the edge wave by contributions from the symmetric Lamb modes. However, this observed decay was taken into account to normalise the edge wave displacements and patterns.

4.1.3 Results

The Lamb-wave dispersion curves were used to identify the dominant modes in each of the displacement components. The 2D FFT scan along the 45° line indicated dominant S0 and SH0 in r

and θ components respectively, as shown in Fig. 4.1.3(a) and (b). The 2D FFT scan along the edge was performed and indicated a propagating edge wave, indicated in Fig. 4.1.3(c).

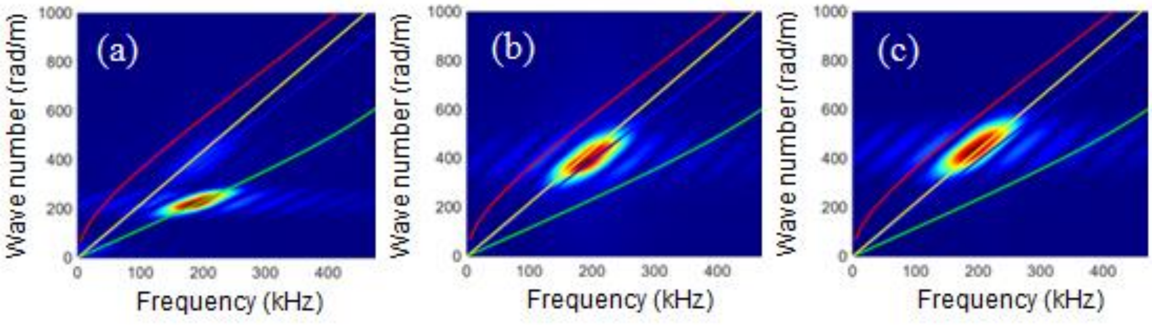

Figure 4.1.3: Dispersion curves indicate (a) Dominant S0 in the r component, (b) Dominant SH0 in the θ component and (c) Dominant Rayleigh-like edge wave along the edge of the plate. A0 (RED), Plane stress edge wave (YELLOW), SH0 (BLUE) and S0 (GREEN).

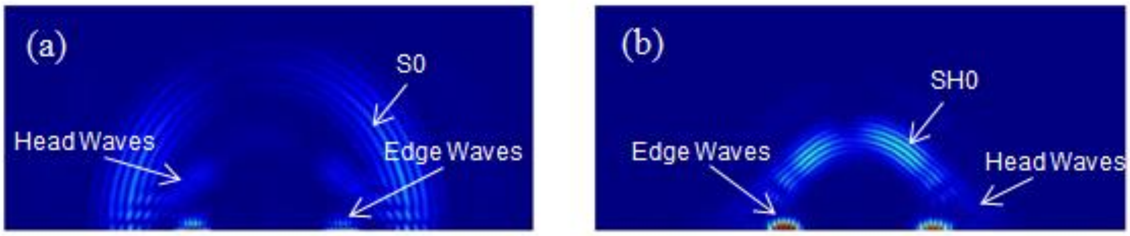

Figure 4.1.4: The scattered wave field due to the presence of a 3mm (a/λ=0.22) edge crack (a) where S0 is dominant in r component and (b) SH0 is dominant in θ component.

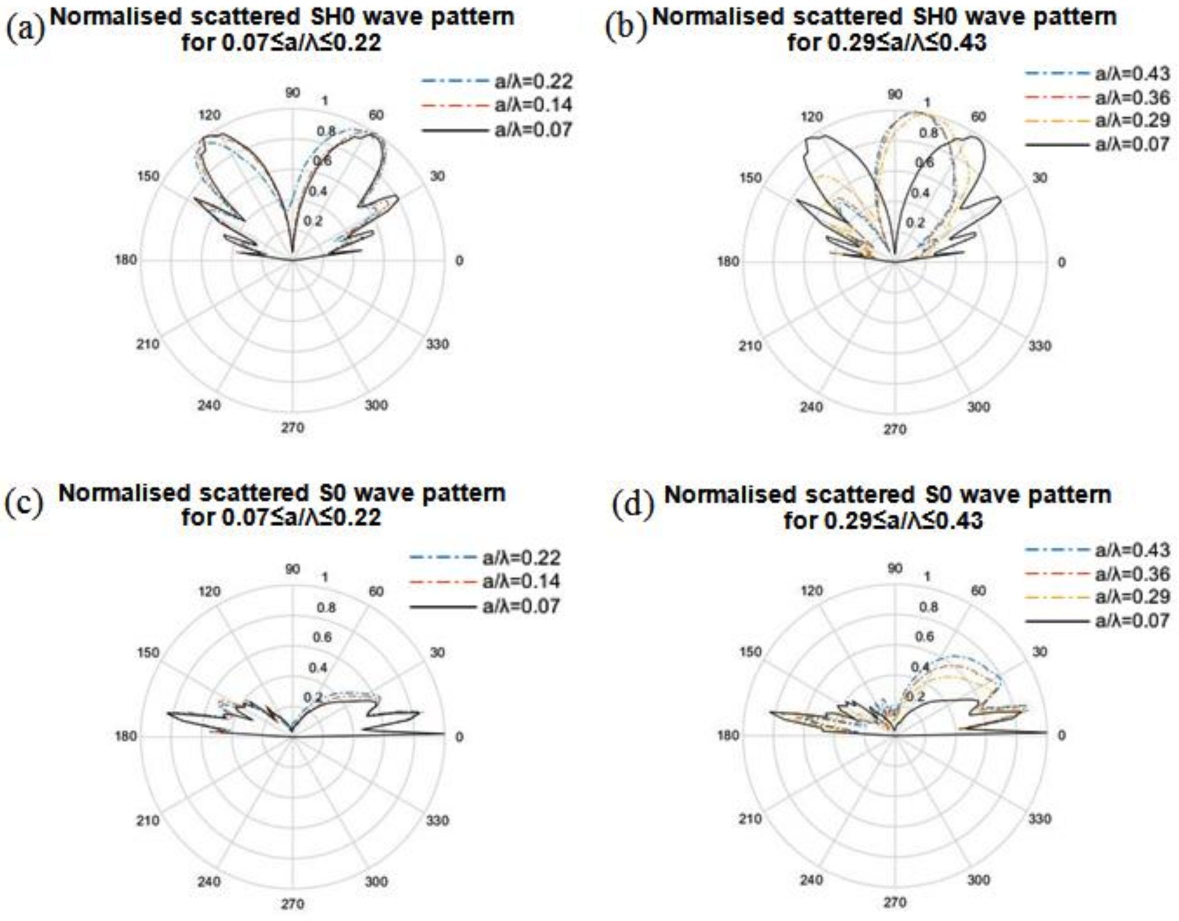

Figure 4.1.5: The normalised scattered wave polar plot of (a) SH0 mode for $0.07 \leq a/\lambda \leq 0.22$ of amplitude u_θ (R_0, θ^s)/$|u_\theta|_{max}$, (b) SH0 mode for $0.29 \leq a/\lambda \leq 0.43$ of amplitude u_θ (R_0, θ^s)/$|u_\theta|_{max}$, (c) S0 mode for $0.07 \leq a/\lambda \leq 0.22$ of amplitude u_r (R_0, θ^s)/$|u_r|_{max}$ and (d) S0 mode for $0.29 \leq a/\lambda \leq 0.43$ of amplitude u_r (R_0, θ^s)/$|u_r|_{max}$

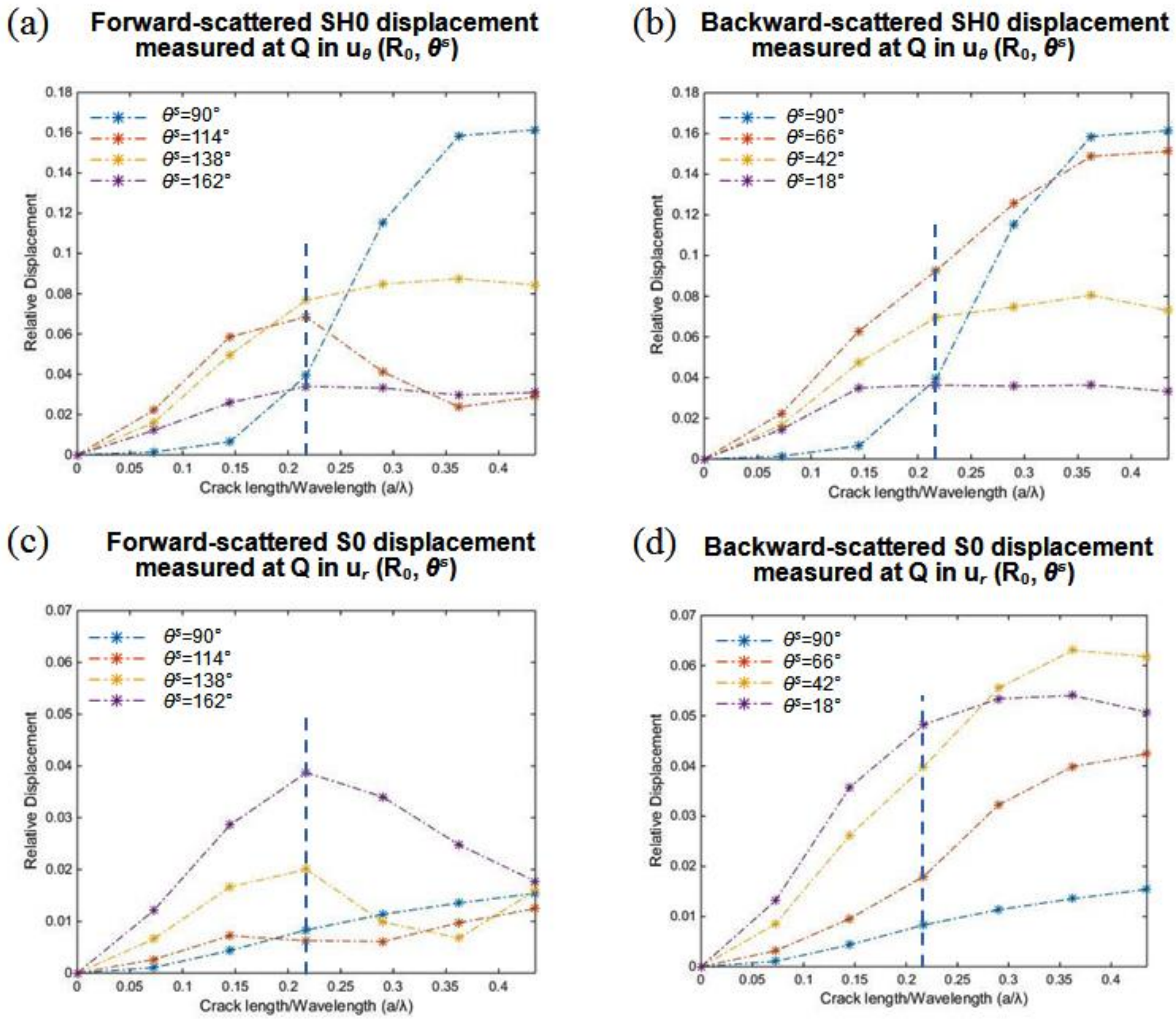

(a) Forward-scattered SH0 displacement measured at Q in u_θ (R_0, θ^s)

(b) Backward-scattered SH0 displacement measured at Q in u_θ (R_0, θ^s)

(c) Forward-scattered S0 displacement measured at Q in u_r (R_0, θ^s)

(d) Backward-scattered S0 displacement measured at Q in u_r (R_0, θ^s)

Figure 4.1.6: The scattered wave displacement for various a/λ in (a) Forward region of SH0, (b) Backward region of SH0, (c) Forward region of S0 and (d) Backward region of S0 with respect to the incident wave maximum displacement

Fig. 4.1.4 portrays the dominant scattered wave fields in cylindrical components due to presence of an edge crack. Fig. 4.1.5(a) and (b) for the SH0 mode shows the scattering pattern for the angular component of displacement u_θ, which is the dominant component for that mode, whereas Fig. 4.1.5(c) and (d) for the S0 mode shows the scattering pattern for the radial component u_r. There are head waves connecting with the S0 and SH0 as indicated in the dispersion curve, seen in Fig. 4.1.3(a), as a weak SH0 signal. The SH0 and S0 scattered wave patterns have shown symmetrical wave pattern along the 90° line when crack length is smaller than 3mm ($a/\lambda \leq 0.22$) edge cracks as shown in Fig. 4.1.5.

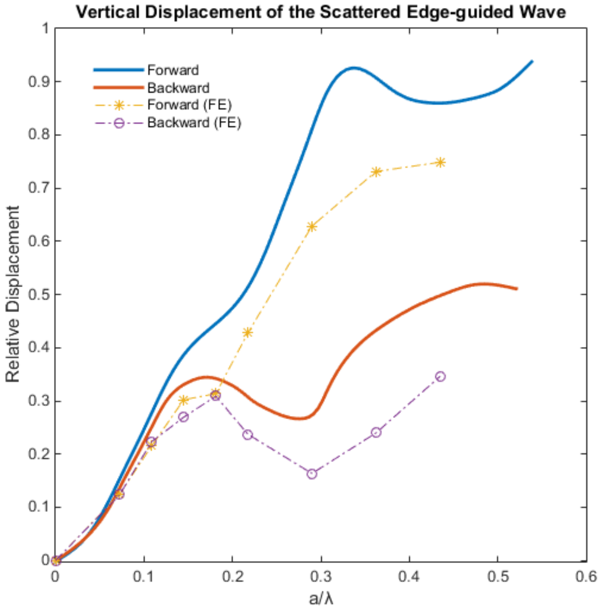

Figure 4.1.7: Forward and back-scattered edge wave displacements due to the presence of edge crack against a/λ with respect to the incident maximum displacement compared with analytical Rayleigh wave [129]

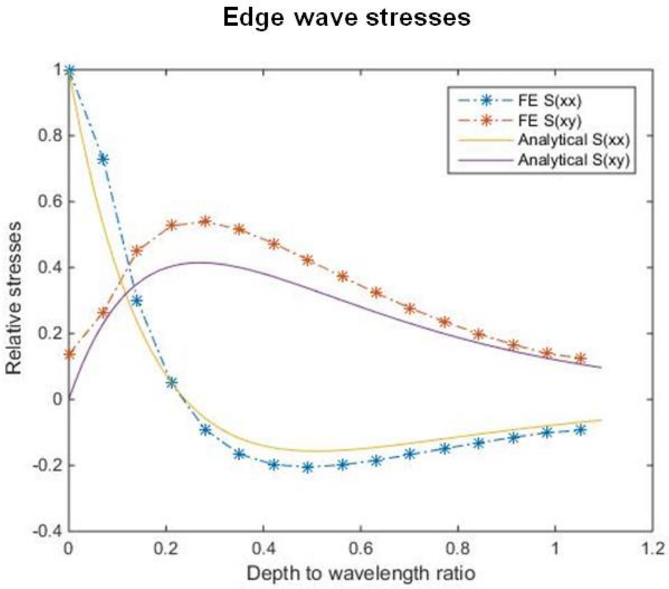

Figure 4.1.8: Baseline FE stresses compared with the analytical edge wave stresses in plane stress case, relative to the maximum stress

As the crack length increases, the scattered wave patterns no longer retain a symmetrical pattern as it develops a stronger backward-scattered lobe in both S0 and SH0 scattered wave pattern. The scattered S0 and SH0 displacements have indicated in both regions increasing linear trend with respect to crack length until $a/\lambda \approx 0.22$ as shown in Fig. 4.1.6. Beyond this limit, the S0 and SH0 backward-scattered displacements are significantly stronger than the forward-scattered displacements values and plateau as crack length increases.

The transmitted and reflected edge wave maximum displacements are in similar magnitude and also increase linearly as a function of a until $a/\lambda \approx 0.22$. However, as crack length continues to increase the transmitted edge wave becomes dominant as seen in Fig. 4.1.7.

4.1.4 Discussion

The FE results showed that, for small cracks $a/\lambda \leq 0.22$, the scattered wave pattern is independent of crack length, whereas the scattering amplitude increases linearly with a. This is particularly similar to the limit of approximately 0.2 depths to wavelength ratio where the direction of particle rotation reverses for Rayleigh waves [18], and hence also for the symmetrical edge-guided waves, as shown in Fig. 4.1.8. The scattered edge wave amplitude trends very similar to the analytical Rayleigh wave by Mendelsohn et al. [129] for small crack length. Since the analytical results only involve with a pure Rayleigh wave incidence, there is inaccuracy for larger crack length scattered wave amplitude since there is additional contribution due to incident bulk wave, refer to Fig. 4.1.7. For long wavelength limit, the edge-guided waves are similar to Rayleigh wave [87], which is shown in Fig. 4.1.7. Although the scattered amplitude is observed to increase linearly, it is expected to have a quadratic trend as shown in Fig. 4.1.7. The quadratic variation should be more obvious if the study had investigated more crack $a/\lambda < 0.7$. An approximate theory is required to obtain the analytical solution of the scattering on incident symmetric edge-guided waves by an edge crack, and to verify the point source equivalence.

This suggests, under this cut-off limit, the small edge crack is equivalent to point source. Furthermore, since the incident edge wave has a dominant σ_{xx} component, the scattered wave patterns can be simply represented by a point source only consisting of a perpendicular forcing component.

However, for larger cracks, the scattered wave pattern is best represented by applying opposite baseline stress profile as a function of depth on the crack faces. As crack size increase, the key features are strong S0 and SH0 backward-scattered lobes and forward-scattered edge-wave displacement. In particular, the scattered S0 and SH0 forward-scattered lobes maximum displacements remain the same as crack length increases. These asymmetrical features in wave pattern are caused by the significant contribution of σ_{xy} component and the non-uniformity of stresses along the crack face.

4.2 Scattering of incident antisymmetric edge-guided wave

The aim of this study is to experimentally and computationally investigate the interaction of incident antisymmetric edge guided wave in a plate with a small edge crack relative to the incident wavelength. Antisymmetric edge-guided wave they also exhibit no geometrical decay, which makes them ideal for long range inspection. Scattered wave pattern and amplitude for various crack sizes will be reported on and are demonstrated to be equivalent to the radiated field from a particular combination of force body-doublets [27].

4.2.1 Methodology

The symmetric and antisymmetric modes are uncoupled and are generated by applied force distributions that are symmetrical or antisymmetrical with respect to the plate’s mid-plane. Additionally, the antisymmetric edge-guided waves can be excited by out-of-plane forces applied on the straight edge. The antisymmetric edge-guided wave has been found to propagate at a similar speed as the fundamental A0 Lamb wave. In this study, only the antisymmetric wave modes were investigated. A baseline subtraction is employed to analyse the scattered wave displacement field associated with the small edge crack as shown in Fig. 4.2.1.

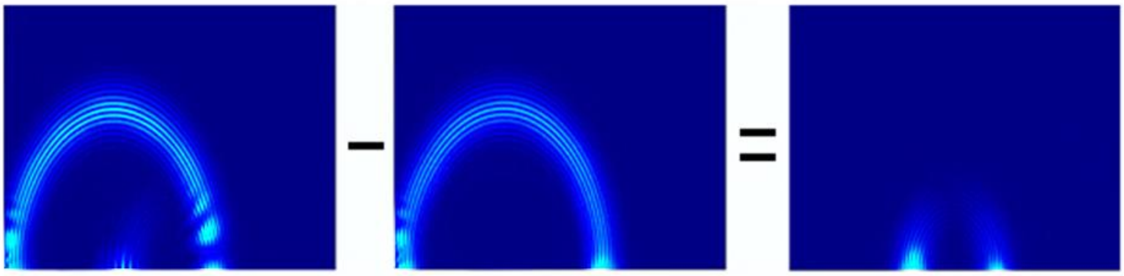

Figure 4.2.1: Illustration of baseline subtraction to obtain the scattered wave field due to the presence of a crack.

The scattered wave field is equivalent to applying equal and opposite tractions to the crack faces that cancel the stresses associated with the incident wave based on principle of superposition [20]. The crack length is in the range $a < \lambda/2$, where λ is the wavelength of the incident wave. It can be expected that the incident field consist primarily of the edge-guided wave since the contribution of the propagation antisymmetric modes along the edge is negligible.

For small crack size, the scattered wave field can be expected to be equivalent to a point source located the crack mouth. This equivalence suggests that the scattering wave pattern should be relatively independent of crack size, whereas the scattering amplitude should depend on crack length squared.

4.2.2 Computational Setup

ANSYS 15.0 is used as the Finite Element (FE) computational analysis tool to simulate wave propagation in an aluminium test plate. A plate of dimensions 440mm x 220mm of 3mm is modelled, as indicated in Fig. 4.2.2 (a) with density of 2700kg/m^3, Poisson’s ratio of 0.33 and Young modulus of 69GPa.

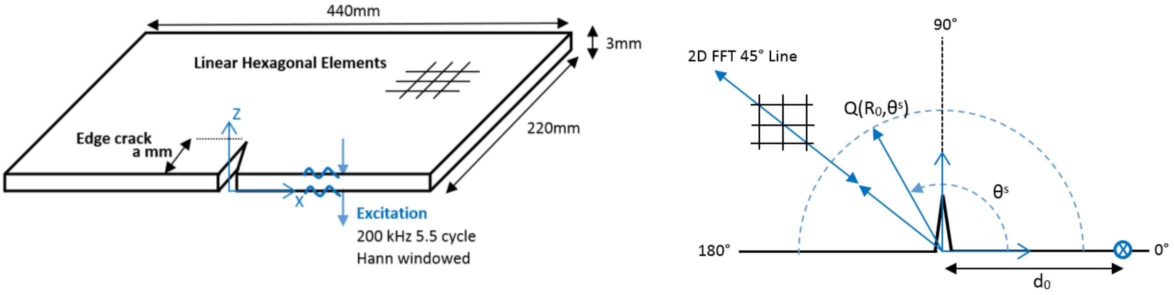

Figure 4.2.2: (a) (LEFT) 440x220x3mm aluminium plate indicating location of crack and (b) (RIGHT) Detail diagram of crack showing the 2D FFT line, excitation point and scattered wave measurements.

The edge crack is located at the origin of the plate as shown in Fig. 4.2.2. The plate is discretised into 0.5mm 8-node linear hexagonal elements which satisfy the requirement of 10 elements per wavelength for accurate modelling [147], and a time step of 0.05µs, which satisfies the Explicit Time Integration stability limit of 0.8L/C, where L denotes smallest element length and C the fastest wave speed [148]. The defect is modelled as a V-tip crack with maximum spacing of 0.2 mm between the crack faces. The dependence of scattered amplitude with crack length is investigated by varying crack size from 1mm to 5mm. The computational investigation relies on applying an out-of-plane force along the edge, at a distance of $d_0 \approx 7\lambda$ from the crack, as indicated in Fig. 4.2.2 (b). This loading configuration ensures that the dominant part of the incident wave at the crack location is an antisymmetric edge-guided wave mode [84]. To minimise dispersion, the excitation signal is chosen to be a 5.5-cycle Hann-windowed tone burst with centre frequency 200kHz. At this centre frequency, the A0 wavelength is 9.9mm [33].

2D Fast Fourier Transformation is performed on the nodes along the edge and along a line at 45° degrees from the crack base, as indicated in Fig. 4.2.2(b). This is used to create the dispersion curve in order to identify the dominant Lamb wave mode from DISPERSE [33]. The 2D FFT spatial distance is taken at least 3.5λ away from the crack base to avoid detection of higher non-propagating Lamb waves and over approximately 10λ distance with zero padding [147].

4.2.3 Experimental Setup

A 5005H34 aluminium alloy plate with the same dimensions as for the computational model is considered. Polytec CLV 3D automated laser vibrometry is used to record the in-plane and out-of-plane velocity components of the propagating Lamb waves. A Polytec retro-reflective sheet is attached to the plate to significantly improve the data quality. PZ26 transducer of diameter 10mm and thickness 2mm was bonded on the edge to excite edge-guided waves. It was found that although the transducer is nominally placed symmetrically with respect to the plate's midplane, in an attempt to generate only the symmetric modes, it seems difficult in practice to avoid some asymmetry, which results in the generation of antisymmetric modes as well. However, because the crack geometry is symmetrical with respect to the plate's midplane, there is no mode coupling due to the scattering process, i.e. an incident antisymmetric wave generates only antisymmetric scattered modes and similarly an incident symmetric wave generates only symmetric scattered modes.

In the experimental investigation, the defect is a notch which is artificially created to prevent the surfaces of crack from contact; hence no waves can transmit through the crack surfaces. The notch has a width of 0.3 mm and lengths 1.11, 1.76, 2.21, 2.66, 3.15, 3.48 and 4.59mm to determine the crack length dependence. Similarly to the computational investigation, the post-processing of data are the same.

The scattered wave displacement are analysed in two regions: Backward-scattered measured in $0 \leq \theta^s < 90$ and Forward-scattered as measured in $90 \leq \theta^s \leq 180$ with the angle define in Fig. 4.2.2(b). Hilbert transformation was performed over the time domain signals measured at points at distance 4λ away from the edge crack, and for various angles. The scattered wave amplitudes were measured where antisymmetric modes are the greatest; near and along the plate's edge. Thus, the backward-scattered amplitudes were measured at 0˚, 10˚, 20˚ and 30˚ and the forward-scattered were measured at 150˚, 160˚, 170˚ and 180˚. The amplitude at 0˚ and 180˚ are reflected and transmitted edge waves, respectively. The scattered antisymmetric wave pattern results are normalised to account for the cylindrical wave decay and relative to the incident edge wave displacement. For the purpose of analysing the wave pattern dependence with crack size, the amplitude is normalised relative to the scattered wave field maximum amplitude.

4.2.4 Results

A 2D FFT processing in conjunction with Lamb-wave dispersion curves was used to identify the modes, as illustrated in Fig. 4.2.3. The scan along the 45˚ line indicated a dominant A0 in the out-of-plane component, whereas the scan along the edge indicated a propagating antisymmetric edge-guided wave whose wave speed is very close to the A0 Lamb wave. Fig. 4.2.3 shows the experimental dispersion curve. The computational dispersion curve showed the same dispersion curve with the absence of symmetrical Lamb wave modes. For this study, we will be analysing the scattered wave field in the z components where the antisymmetric modes are dominant.

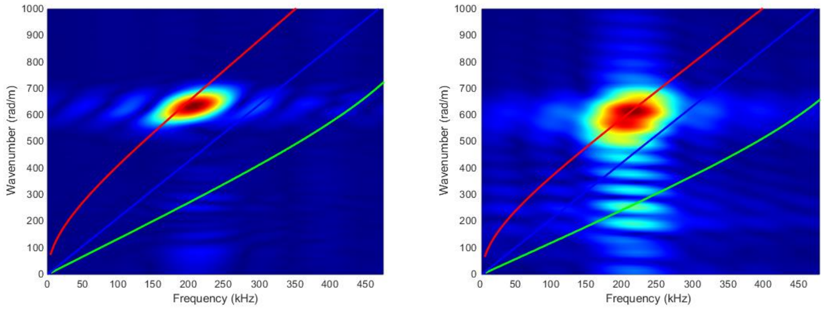

Figure 4.2.3: Experimental dispersion curves. (LEFT) Asymmetric edge guided wave along the edge of the plate in z component and (RIGHT) Dominant A0 Lamb wave in z component scanned along 45˚ line.

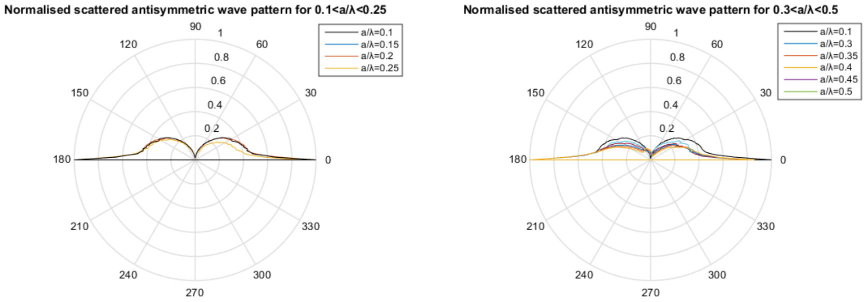

Figure 4.2.4: The normalised FE scattered wave polar plots for various crack lengths: (a) (LEFT) 0.1≤a/λ≤0.25 and (b) (RIGHT) 0.3≤a/λ≤0.5 with a/λ=0.1 for comparison.

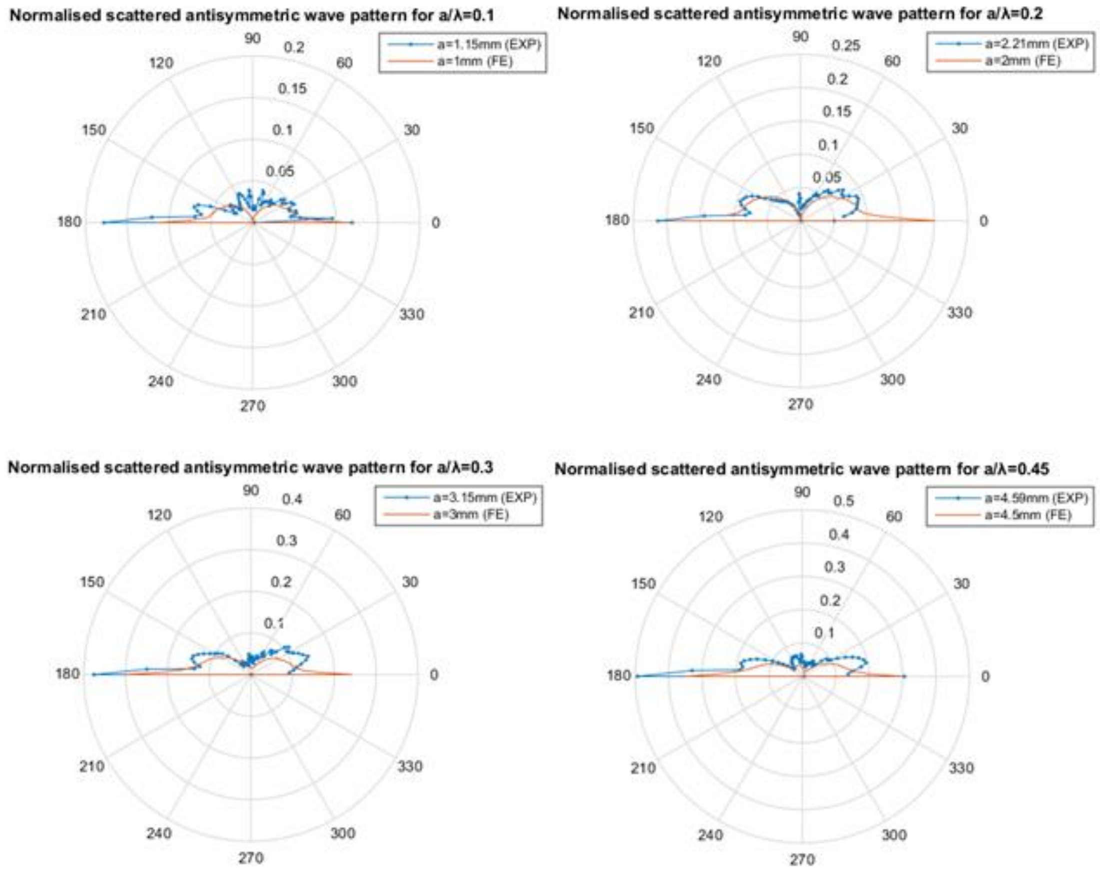
Normalised scattered antisymmetric wave pattern for a/λ=0.1

Normalised scattered antisymmetric wave pattern for a/λ=0.2

Normalised scattered antisymmetric wave pattern for a/λ=0.3

Normalised scattered antisymmetric wave pattern for a/λ=0.45

Figure 4.2.5: The normalised experimental and computational scattered antisymmetric wave patterns comparison for various crack length

It can be seen from Fig 4.2.4 (a) that the scattered wave patterns are unchanged for crack length less than 2mm, i.e. for $a/\lambda<0.2$, whereas for larger crack, there is a minor difference in the symmetrical lobes relative amplitude compared to the smaller crack length, as shown in Fig. 4.2.4(b). The antisymmetric scattered wave patterns in both experimental and computational investigations are symmetrical along the 90˚ line as shown in Fig. 4.2.5. Both have same features of two symmetrical lobes in the forward and backward-scattered regions and their maximum amplitude is along the edge of the plate. Overall, the experimental results have shown good agreement with the computational results.

Fig. 4.2.6 show that the amplitude of the scattered A0 and the antisymmetric edge waves initially increases quadratically with crack length until $a/\lambda<0.2$, but thereafter, the amplitude increases at a reduced rate, which appears to plateau for the backward scattered (reflected) wave, whereas the forward scattered (transmitted) edge wave continues to increase and becomes more dominant.

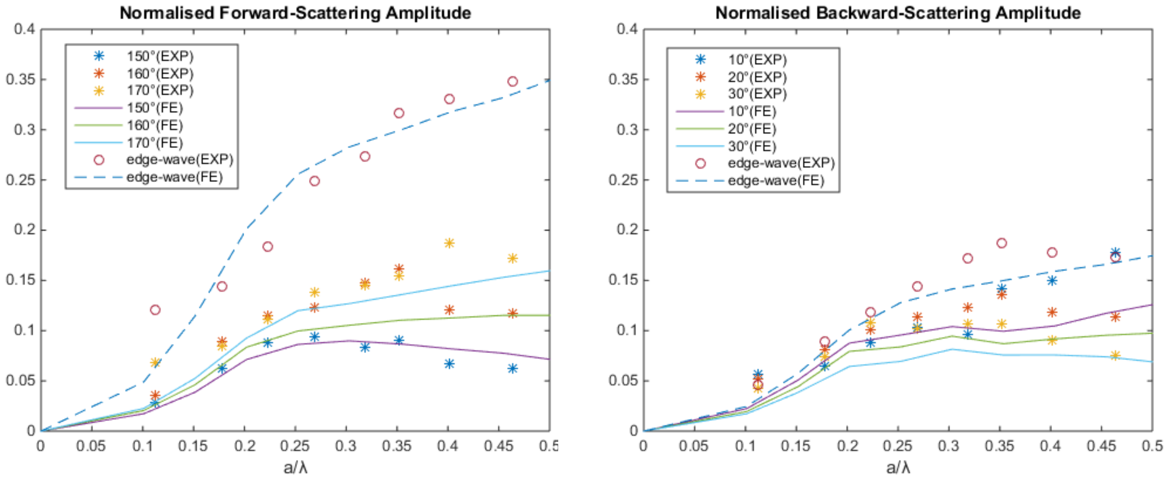

Figure 4.2.6: Experimental and computational comparison of normalised scattered wave displacement dependences with crack length for various angles. (a)(LEFT) Forward-scattered amplitude and (b)(RIGHT) Backward-scattered amplitudes

4.2.5 Discussion

Both experimental and computational results showed that for small edge crack $a/\lambda<0.2$, the scattered wave pattern is independent of crack length and the scattering amplitude increases as a function of a^2. This trend is consistent with the observation that the shear stress distributions along the crack length are approximately constant for $y/\lambda<0.2$ as shown in Fig. 4.2.7. For $a/\lambda<0.2$, a small edge crack is equivalent to point source whose strength is proportional to the integral of the crack opening displacement [119], and thus proportional to a^2. This point source consists of a particular combination of body-force doublets where the σ_{xy} gives rise to mode II crack opening and σ_{xz} gives rise to mode III crack opening as portrayed in Fig. 4.2.8.

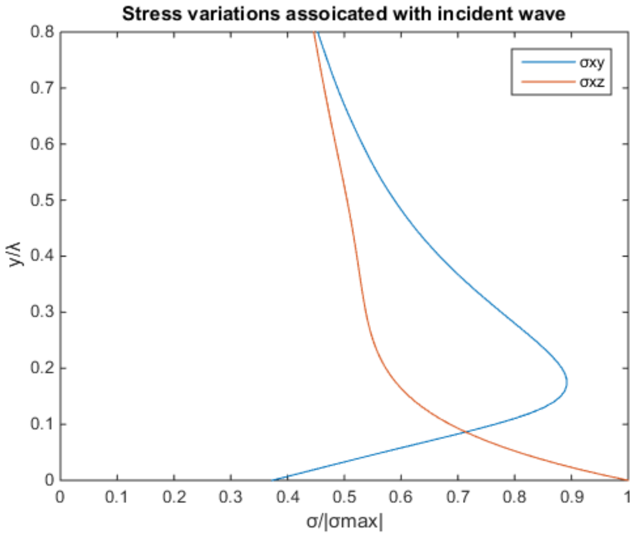

Figure 4.2.7: Shear stresses depth variation of the incident antisymmetric edge wave relative to the maximum shear stress.

However, as the crack size increases, the stress distribution in Fig. 4.2.7 show marked variation, and a quasistatic approximation becomes less accurate, so that the strength of the equivalent source does not continue to increase as a^2.

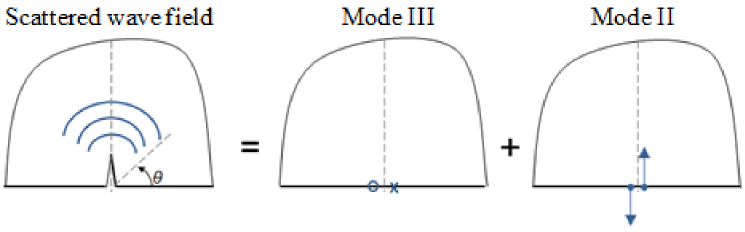

Figure 4.2.8: Scattered wave field equivalent to force doublets due to mode III and mode II crack openings.

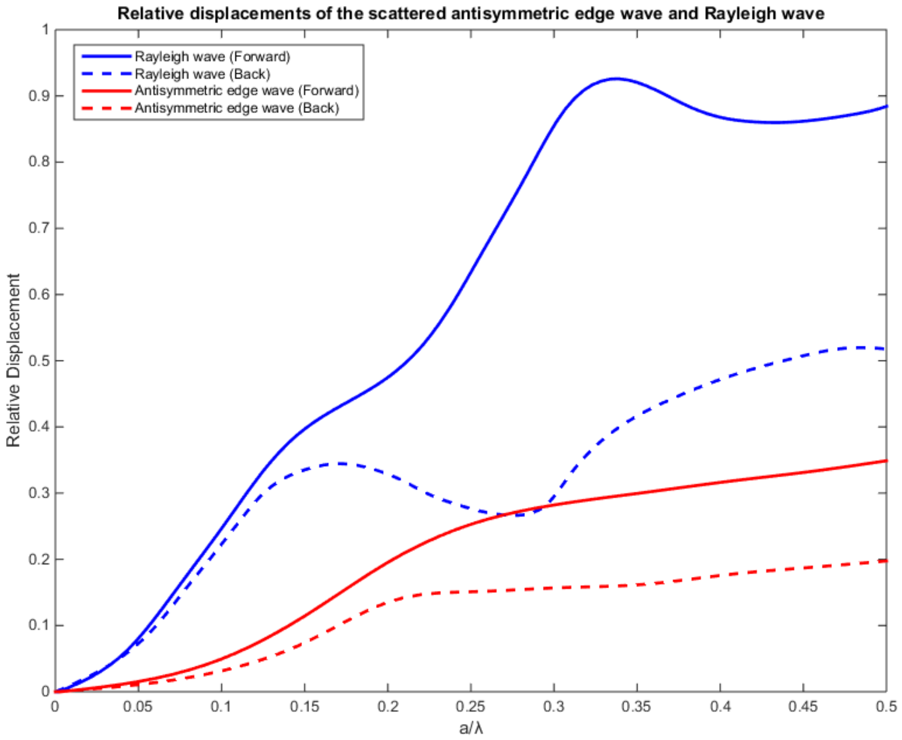

Figure 4.2.9: Relative displacements with respect to incident wave amplitude of analytical scattered Rayleigh wave displacements obtain from Mendelsohn [129] and computational antisymmetric edge-guided wave.

Nevertheless, the scattering pattern remained similar, with only a slight change in relative amplitude as crack length increases beyond $a/\lambda \approx 0.2$, as shown in Fig. 4.2.4(b). It is noteworthy that a very similar behaviour has been reported both theoretically and experimentally for the scattering of Rayleigh waves by small surface-breaking cracks [6, 20], as indicated in Fig. 4.2.9. For small crack length to incident wavelength ratio, the antisymmetric edge-guided waves should be similar to Rayleigh wave [83, 85, 87], which is indicated in Fig. 4.2.9. Beyond the small crack limit, the stress distributions and particle motion of the antisymmetric edge-guided and Rayleigh waves are significantly different and hence the scattered displacement is no longer similar. This will require an approximate theory to analytically solve the far-field scattering of antisymmetric edge-guided wave and to verify if the force doublet method approximates to the scattering at long wavelength limit.

In previous study [164], it was reported that the scattering amplitude for an incident symmetric edge-guided wave appears to increase linearly with crack length for small crack size, whereas theoretically one might have expected a quadratic variation. However, the same apparent linear trend can also be observed for the Rayleigh wave scattering in Fig. 4.2.9, with closer inspection revealing an initial quadratic variation. This quadratic trend is more obvious in the present study of scattering of an antisymmetric edge-guided wave, as can been seen in Fig. 4.2.9.

4.3 Conclusion

The scattered wave field of a low frequency edge wave with a small edge crack in an isotropic plate has been reported. It was shown that, for small crack lengths $a/\lambda \leq 0.22$, the angular variation of the scattering pattern is independent of crack length, which is consistent with modelling the scattered field as being due to a point source (a force doublet) at the location of the crack mouth. Furthermore, the scattering amplitude for the scattered wave into the plate, as well as the reflected and transmitted amplitudes for the edge guided wave, are proportional to crack length a.

The scattered wave field of a low frequency antisymmetric edge-guided wave with a small edge crack in an isotropic plate has been reported. It has been shown that experimental and computational results are in close agreement, of both the scattering pattern and for variation of scattering amplitude with crack size. For small crack length $a/\lambda<0.2$, the scattering pattern is independent of the crack length and the amplitude of the scattered A0 Lamb wave and antisymmetric edge waves is proportional to a^2, which is consistent with modelling the scattered wave field as being due to a point source at the location of the crack mouth equivalent to a combination of force doublets. These experimental and computational results for the forward scattering problem constitute a valuable finding and have shown scattering of incident edge-guided waves by a small crack can be represented by a point source model. Further studies are required to determine the analytical solutions using the approximate theories to obtain the scattering of symmetric and antisymmetric edge-guided waves by an edge crack.

The analytical solutions will verify whether the scattering by an edge crack can also be approximated as a point source representation at the long wavelength limit.

These results for the scattering problem provide a useful framework for addressing a small edge cracks on a through-thickness hole by using an incident edge-guided wave. The previous works are extended the analysis to radial cracks at circular holes, which is more representative of typical occurrences of cracking in practice.

Chapter 5

Scattering of the fundamental Lamb wave modes by an edge crack at a circular hole in an isotropic plate

In this chapter, an additional feature of through-thickness hole is introduced. Fuel weep holes are prone to develop fatigue crack and these structure components are required to be disassembled for damage diagnosis. This process is time-consuming. The current state-of-the-art method is inefficient and outdated and requires reliable and innovative diagnosis methods to regularly monitor and assess the crack size for structural integrity monitoring purposes. This hole investigation explores the effect of crack length on a hole to determine a quantitative relationship between the scattered amplitude and crack size for early damage detection.

The dependence of hole diameter is first investigated to understand the basic scattering phenomenon due to this hole feature. It is later observed that the symmetric edge-waves propagating on the circumference of a hole completely attenuate into the medium below a critical d/λ. By constraining $d/\lambda > 1$, this allows the incident circumferential edge-guided wave to propagate around the hole boundary and impinge with the defect. For $d/\lambda < 1$, only fundamental symmetric wave mode can impinge with the defect. Furthermore, the scattering by the fundamental symmetric wave mode and edge-guided wave by an edge crack at a circular hole are investigated under these two conditions. These hole studies are the extension to the edge crack boundary problem. It is also anticipated that the scattered wave field can be represented as a point source located on the hole boundary.

Many studies [28, 37, 54-56, 67] have investigated the scattering effect of the hole and provided scattered wave patterns. Significant investigations have been done on the scattering by part through-thickness of the hole. Previous researchers [7, 14] have used a creeping wave and was used by the means of hidden crack detection. This study attempts to determine the conditions for creeping edge-waves to circulate around the hole.

The scattering of S0 from a rivet hole with a crack has been studied [54] however, the scattered Lamb wave modes and patterns by the small edge crack on a hole have not been reported and modelled for small crack characterisation. Furthermore, no previous study has excited edge-guided waves on a hole boundary and investigated the interaction with a propagating leaky circumferential edge-guided wave and a hidden crack.

5.1 Scattering of the fundamental symmetric wave mode incident at defect on the blind side of a weep hole in an isotropic plate

The aim of this study is to explore computationally the interaction of low frequency zeroth order symmetrical modes with a through-thickness crack emanating from a circular hole, with the crack being modelled by a notch as indicated in Fig. 5.1.1. The interaction of an incident wave with an open hole is presented first. This helps to identify the boundary conditions that exist when a notch is included on the open hole to simulate a defect located on the blind side of the incident wave. The nature of the wave scattered by this hidden defect will be reported on, and its relevance for the detection and quantification of this defect will be discussed. The nature of scattered wave passing the notch is studied in terms of the following length-scales: diameter of the open hole and defect length. The incident wave frequency is kept constant. The scattering phenomena at the notch on the hole that is located on the blind side of the incident Lamb wave will be presented.

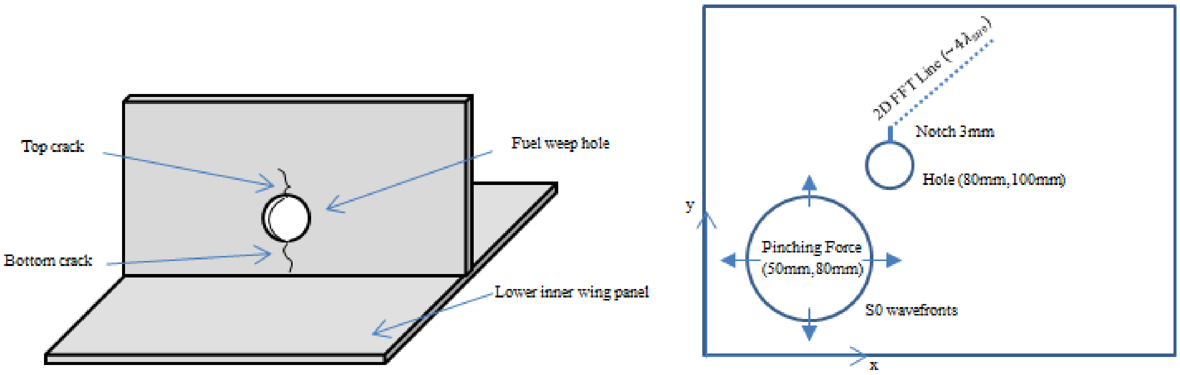

Figure 5.1.1: (a) (LEFT) Location of typical crack emanating from a fuel weep hole (b) (RIGHT) geometry of FE model for 200mmx200mmx4mm aluminium plate showing the location of the excitation force relative to the hole and notch.

5.1.1 Elastic wave propagation

At low frequency, only the lowest order Lamb-wave modes (A0, S0 and SH0) are propagating modes. SH0 is non-dispersive shear wave propagating in the plate polarised in a direction parallel to the plate surface. S0 is considered non-dispersive at low frequency and has constant amplitude through the plate thickness, with its particle vibration predominantly parallel to the direction of propagation. The A0 mode will not be encountered in the present work due to the symmetry of the plate and loading configuration relative to the mid-plane. In this work, an incident S0 mode will be used.

5.1.2 Computational Investigation

ANSYS is used as the computational analysis tool for this study. The simulation represents an aluminium test plate 200mm×200mm×4mm (density of 2770kg/m^3, Poisson’s ratio of 0.33 and Young modulus of 71GPa). The plate contains a circular hole centred at (80mm, 100mm), and whose diameter is varied from 10mm, 30mm and 60mm. One set of computations involves only the hole as scatterer, whereas for a second set of computations, a fatigue crack is simulated by a notch 3mm in length and 0.5mm width, located directly on top of the hole, as shown in Fig. 5.1.1(b). For the purposes of generating only the S0 mode, equal and opposite point forces are applied to nodes on opposite faces of the plate, with the forces acting in the direction normal to the plate surface. This disposition of forces can be referred to as a *pinching force*, which is located at coordinates (50mm, 80mm), cf. Fig. 5.1.1(b). The pinching force excitation signal consists of a 5-cycle Hanning windowed tone burst centred at frequency 200 kHz to minimise dispersion. At this centre frequency, the incident S0 mode has a wavelength of 27.2 mm, and it is tracked in the FE model through the associated out-of-plane displacement u_z on the plate's surface. By contrast, the scattered wave, which will be shown to be predominantly SH0, has no out-of-plane component, and it must therefore be tracked by the in-plane displacement. Here we shall use polar coordinates (r, θ) with origin at the centre of the hole, and the θ component of the surface displacement will be used for tracking the scattered SH0 mode, whose wavelength λ_{SH0} is 14.9 mm.

The through-thickness *small crack* investigation is considered in the FE simulation. The FE simulation uses 1mm tetrahedron element size, which satisfies the requirement of 10 elements per wavelength for accurate modelling [21, 31], and a time step of 0.2 μs, which satisfies the Explicit Time Integration stability limit [148]. The intention for this study was to use tetrahedron elements to accurately model the hole geometry. However, it was later investigated that the linear cubic elements provided the identical results and solved sufficiently faster. Thereby, all other hole or complex geometry studies continued to use linear cubic element instead.

A 2D Fast Fourier Transform (2D FFT) is taken along the line indicated in Fig. 5.1.1 (b) was used to produce the dispersion curves, as shown later in Fig. 5.1.3, and hence identify the modes. The 2D FFT consists of more than 100 time samples, $20\mu s$; the spatial distance is approximately $4\lambda_{SH0}$ originating from the notch tip with 1024 equidistant spatial samples and zero padding.

5.1.3 Finite Element Simulation Results

i) No notch cases

The FE simulation of scattering by a hole without a notch indicated a noteworthy effect. For the 10mm diameter hole, the incident S0 wave passed through with little perceptible effect (Fig. 5.1.2(a)), whereas the 30mm and 60mm diameter holes showed clear evidence of creeping waves, indicated by curling S0 wavefronts hugging the surface of the hole (Fig. 5.1.2(b) and (c)). This suggests that the effective length scales for creeping waves are when the impinging wavelength is smaller than the hole diameter $\lambda < d$. Previous studies [7, 93, 94] also conducted their investigations on creeping waves under this length scale condition.

The creeping wave is leaky edge-guided wave, which has similar speed to a Rayleigh wave [7, 93]. As with Rayleigh waves, these edge waves arise from the requirement to ensure stress-free boundary conditions at a free surface. These Rayleigh-type edge waves are leaky [7] which can be regarded to be a consequence of a weak scattering perturbation caused by the cylindrical surface.

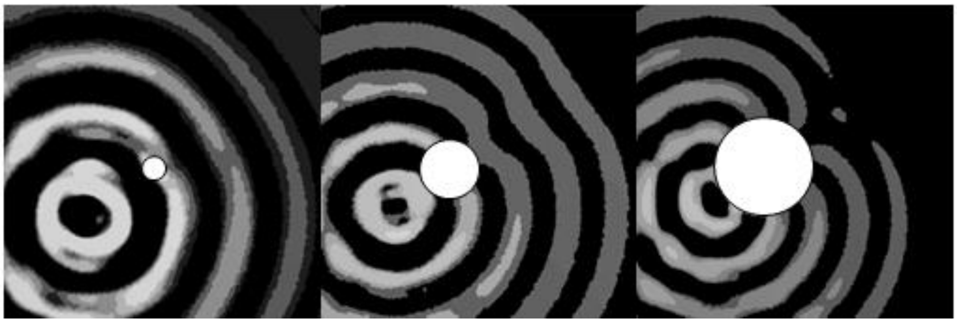

Figure 5.1.2: Snapshot from FE simulation of the scattering in the out-of-plane (u_z) direction of an incident S0 wave, λ =27.2mm, by a circular hole of diameter (a) 10mm; (b) 30mm, and (c) 60mm [165]

ii) With the inclusion of a 3mm notch

For the simulations involving a notch, a baseline subtraction is used for the purpose of isolating the scattered wave field associated with the presence of the notch.

The FE notch investigation showed SH0 source-like mode conversion at the notch tip. A 2D FFT of the scattered field indicated a dominant contribution corresponding to the wavelength of the SH0 mode, as indicated in Fig. 5.1.3. Since only incident S0 wave was propagated, the scattered field suggested SH0 wave originated from the notch tip. The SH0 wave propagating from the notch tip is strongly affected by the hole diameter, as can be seen in Fig. 5.1.4. Recall that Fig. 5.1.2 showed the S0 wave is *held up* more visibly at larger hole diameters. It seems plausible that the same would happen for the SH0 scattered wave from the notch tip. The FE notch simulation showed that SH0 wave originating from the notch tip generated a leaky edge wave when impinging with the hole. This edge wave turns more sharply in a small diameter hole relative to large diameter holes.

In Fig. 5.1.4(a), the scattered SH0 waves appears to remain attached to the hole surface, which evidently is SH0 combined with leaky edge wave. At time 66μs, in Fig. 5.1.4(a), the leaky edge waves radiates into the medium. For larger diameter holes, as can be seen in Fig. 5.1.4(b) and (c), this wave coalescing phenomena is also observable, but when the SH0 waves detaches from the surface, the edge wave continues to travel along the surface. This wave detachment from the surface is more noticeable for larger diameter holes, as can be seen in Fig 5.1.4(c) at 58 μs and 76 μs.

The coalescing of SH0 wavefront from the notch tip and the leaky edge wave is what results in the appearance of the spiralling SH0 wave observed in Doherty and Chiu [13]. It can be seen from the later snapshots in Fig. 5.1.4(a) at 48 μs and 66 μs that the subsequent evolution of the SH0 wavefront resembles the pattern that would be expected for a point source of SH0 waves located at the notch tip. This SH0 virtual source is more noticeable than the SH0 spiral for larger diameter holes, cf. Fig. 5.1.4(b) and (c). This suggests that the appearance of SH0 spiralling effect depends sensitively on the ratio of notch length to wavelength, and is only observed in a limited range of that ratio.

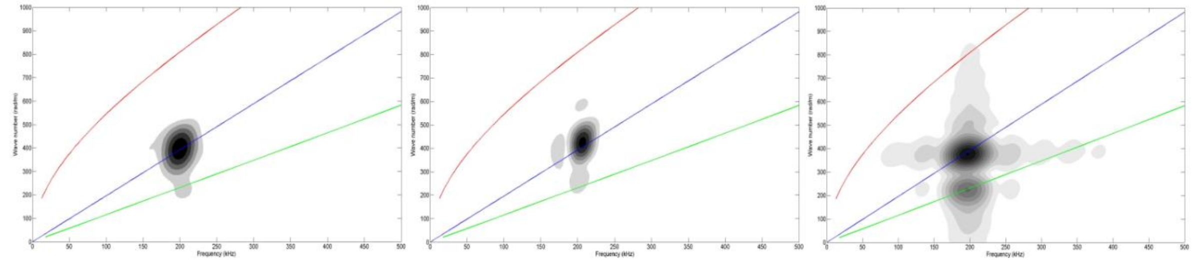

Figure 5.1.3: Dispersion curve for diameter (a) 10mm (left), (b) 30mm (middle) and (c) 60mm (right) with 3mm notch aluminium plate; S0 (Green), SH0 (Blue) and A0 (Red)

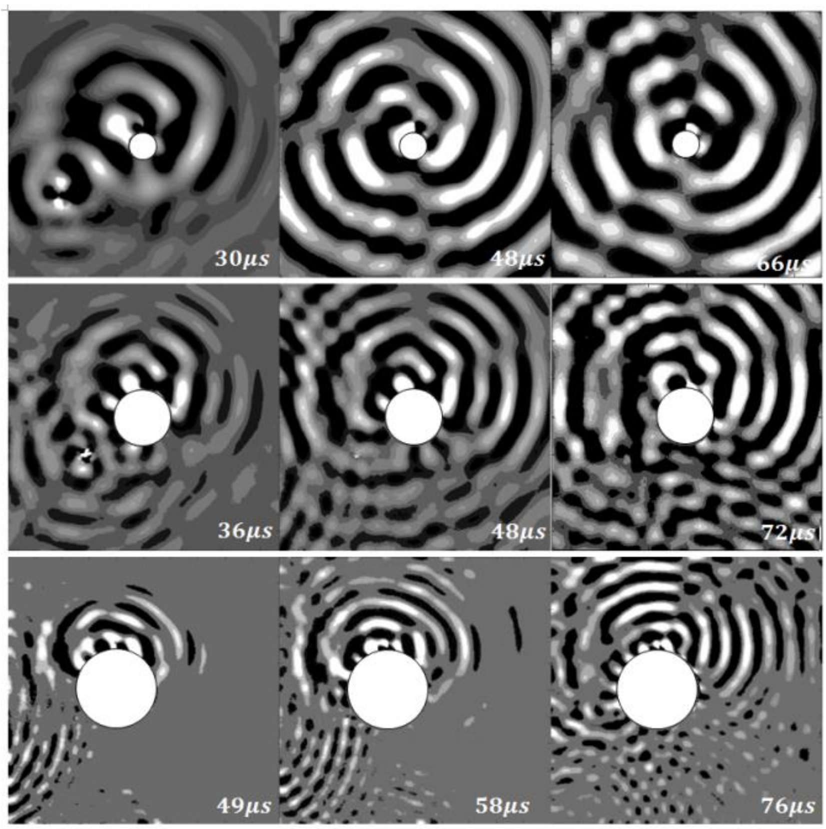

Figure 5.1.4: Snapshot of the time progression of scattered field θ direction of diameter:(a) 10mm (top); (b) 30mm (middle) and (c) 60mm (bottom) (a) At 30μs and 48μs the SH0 spiral is a visible aspect; at 66μs the scattered wavefront, SH0 and edge waves, radiates into the medium also SH0 source is more apparent. (b) and (c): The SH0 spiral is not evident but the SH0 source is more apparent. SH0 detaching from the surface as seen in (b) 48 μs and 72 μsand (c) 58μs and 76μs, although the edge wave still travels around the surface after SH0 detachment.

5.2 Scattering of fundamental Lamb waves by an edge crack at a circular hole in an isotropic plate

The scattered wave field when an incident elastic wave impinges on a crack have been investigated for both bulk waves [129, 131] and Lamb waves [31, 32, 164, 166, 167]. It is known that a scattering by an infinitesimal crack is equivalent to the radiate field from a particular combination of force doublets for bulk waves [27]. An extension of this idea to Lamb-wave scattering has been investigated in our previous work for edge crack along a straight edge [164, 166, 167]. For small cracks, the scattered field can be expected to be like that of a point source located at the crack mouth and with strength proportional to some power of the crack length relative to wavelength a/λ. This point source equivalence also suggested that the scattering pattern should be relatively independent of crack size. It can be expected that an emanating crack on the hole can be represented as a point source as well.

This study computationally investigates the interaction of a symmetric edge-guided wave with a through-thickness crack emanating from a circular hole. The amplitude and scattered wave patterns due to the presence of emanating crack are reported. It is expected that the scattered wave amplitude should increase as a power function of a/λ similarly to the edge crack on a straight boundary case [164].

5.2.1 Methodology

In this investigation, the frequency is restricted below the cut-off for the first order symmetric Lamb wave mode SH1 (1.53Mhz-mm). In this low frequency-regime the SH0 is non-dispersive whereas the S0 mode is essentially non-dispersive as well. The scattered wave field associated with the small edge crack is obtained via a baseline subtraction. This procedure is illustrated in Fig. 5.2.1 using a visualisation of computational results.

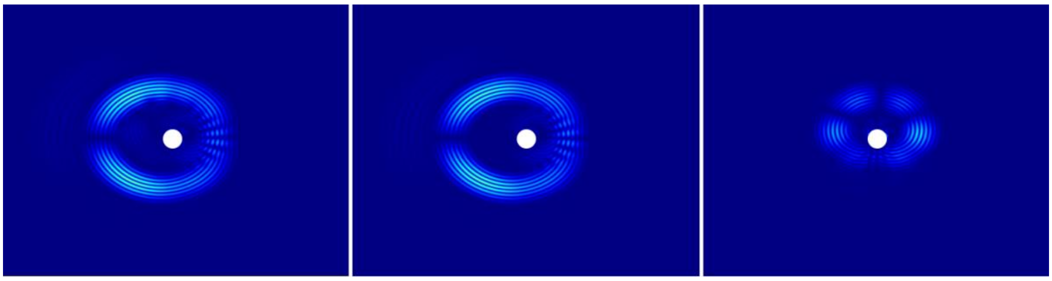

Figure 5.2.1: Illustration of the baseline subtraction procedure to obtain the scattered wave field due to the presence of a crack on hole

An applied force distribution that is symmetrical with respect to the plate's mid-plane can only generate purely symmetric modes. Furthermore, the symmetric edge-guided wave are generated by mid-plane symmetric force applied on the hole boundary. The symmetric edge wave can be regarded as a plane stress analogue of the Rayleigh wave and one can obtain its wave speed by a simple change of elastic constants to convert plane strain to plane stress [18]. Although, edge waves propagating along the curve, also known as circumferential creeping waves, are known to leak to the medium. For plane strain case, studies [88] have analytically solved and revealed conditions for Rayleigh waves propagating around curved edges. These conditions should be similar in the plane stress case, so in order for edge wave to propagating around the circumference the diameter must be larger than the incident wave length $d/\lambda>1$. For large radius, this wave should be very similar to edge wave on straight boundary. However under a critical diameter to wavelength ratio these waves attenuate to the medium and cease propagating on the curved surface.

The geometrical configuration being investigated is shown in Fig. 5.2.2. It involves a radial crack of length, a, emanating from a circular hole of diameter, d. The crack length is assumed to be small compare to the incident wavelength λ and the hole diameter, such that $a/\lambda<<1$ and $a/d<<1$. Under these conditions, for small cracks, the scattered wave field is expected to behave like a point source with strength being proportional to some power of the crack length. Additionally, this point source equivalent also suggests that the scattered pattern should be relatively independent of crack size.

It is anticipated that the scattered wave patterns should have some similar features to the edge crack on a straight boundary [164]. Furthermore, the scattered edge wave on straight boundary study investigated crack length with 1mm increment and the amplitudes were observed to increase linearly with crack length. In this study, a smaller crack size increment is used and the SH0 and S0 scattered patterns and displacement trends with crack length are reported.

5.2.2 Computational Procedure

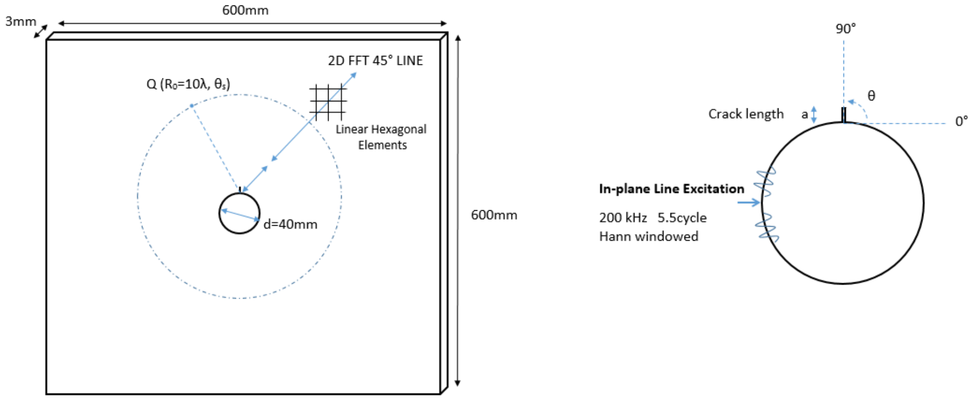

Figure 5.2.2: (a) (LEFT) 600x600x3mm aluminium plate FE geometry showing the location of crack, 45° 2D FFT scan line, scattered wave measurement; (b) (RIGHT) Near hole diagram portraying the excitation point, crack location and origin of cylindrical coordinate system.

ANSYS 15.0 is used as the Finite Element (FE) computational analysis tool to simulate wave propagation in an aluminium test specimen. An aluminium plate 600mm x 600mm of 3mm thickness (density 2700kg/m^2, Poisson ratio of 0.33 and Young modulus of 69 GPa) is modelled, refer to Fig. 5.2.2. A through-hole with 40mm diameter is located centre of the plate. The small crack modelled as a notch with width 0.5mm emanate at the 12 o'clock position of the hole with size 1mm to 4.5mm in 0.5mm increments. The plate specimen is discretised into 0.5mm 8-node linear hexagonal elements which satisfy the requirement of 10 elements per wavelength for accurate modelling [147] and time step of 0.02 µs, which satisfies the standard stability criterion for Explicit Time Integration of being less than or equal to 0.8*L/C*, where *L* denotes the smallest element length and *C* the fastest wave speed [148].

The incident edge-guided wave is generated at 9 o'clock position of the hole, which is approximately 3λ away from the edge crack as shown in Fig. 5.2.2(b). The force excitation signal is chosen to be a 5.5 cycle Hann-windowed tone burst with centre frequency 200 kHz. At this centre frequency the wavelength of circumferential edge wave, S0 and SH0 are 14.4mm, 26.6mm and 15.3mm [33]. It is noted that the circumferential edge wave wavelength is larger than the wavelength of 13.8mm for edge waves at a straight edge [164], indicating a slightly faster wave speed for the circumferential edge wave around a circular hole relative to the straight edge. This leads to a spiralling pattern scattering by a small crack as observed by Doherty and Chiu [13, 15] .The force excitation will also generate S0 and SH0 wave, however, given the small crack length range, the incident field can be expected to consist primarily circumferential edge wave where the contribution of the other symmetrical wave mode along the circumference are negligible.

2D Fast Fourier transformation is performed around the circumference and along the 45˚ line from the crack base edge as portrayed in Fig. 5.2.2(a). The 2D FFT results is used to create the dispersion curve in order to identify the dominant Lamb Wave modes from DISPERSE [33]. The 2D FFT spatial distance is taken at least 3.5λ away from the crack base over approximately 10λ distance with 1024 equidistant spatial sample with zero padding [147]. A 2D FFT scan is also perform along the hole circumference to determine the circumferential edge wave wavenumber. Hilbert transformation was performed over the time domain signals measured at point Q at distance approximately 10λ away to obtain an approximated far-field scattered wave pattern refer to Fig. 5.2.2(a). The maximum amplitude of the associated analytic signals was used as the measure of the scattered field amplitude. The scattered wave displacements are analysed in two regions: from 0˚ to 180˚ and 180˚ to 360˚ refer to Fig. 5.2.2(b) and the maximum scattered displacements were measured at 0˚, 45˚, 90˚, 180˚, 225˚ and 270˚.

The scattered wave pattern results are normalised to account for the cylindrical wave decay and relative to the incident edge wave displacement at the location of the crack. For the purpose of analysing the wave pattern dependence with crack size, the amplitude is normalised relative to the scattered wave field maximum amplitude. The back-scatter and forward-scatter circumferential edge wave displacement is measured at 9 o’clock and 3 o’clock position of hole circumference, respectively, and the results are normalised to account for the circumferential edge wave decay as well. This leaky edge wave attenuation over circumferential distance is also briefly reported for this specific hole geometry.

5.2.3 Results

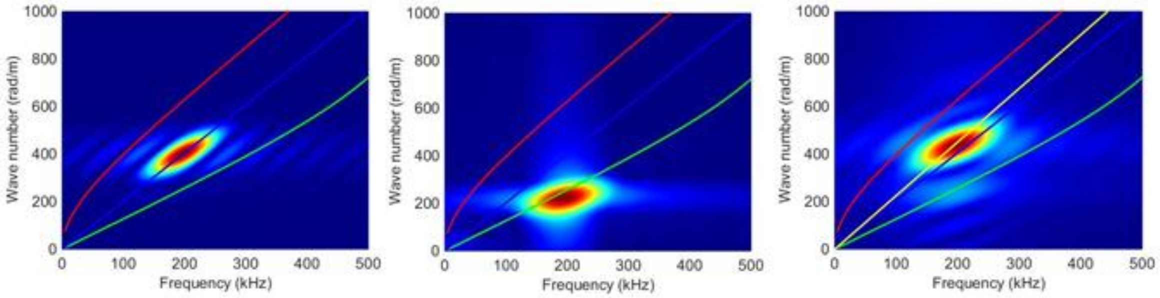

Figure 5.2.3: Plots of 2D FFT amplitude and dispersion curve indicating (a) (LEFT) a dominant SH0 wave in the θ component; (b) (MIDDLE) a dominant S0 wave in the r component; (c) (RIGHT) a circumferential edge wave along the hole circumference with wave speed close to the plane stress edge wave speed.

Figure 5.2.3 shows the Lamb wave dispersion curves indicating dominant S0 and SH0 modes in the radial, r, and angular, θ, components respectively. A 2D FFT is performed along the hole circumference to determine the circumferential edge wave wavelength as shown in Fig. 5.2.3(c)

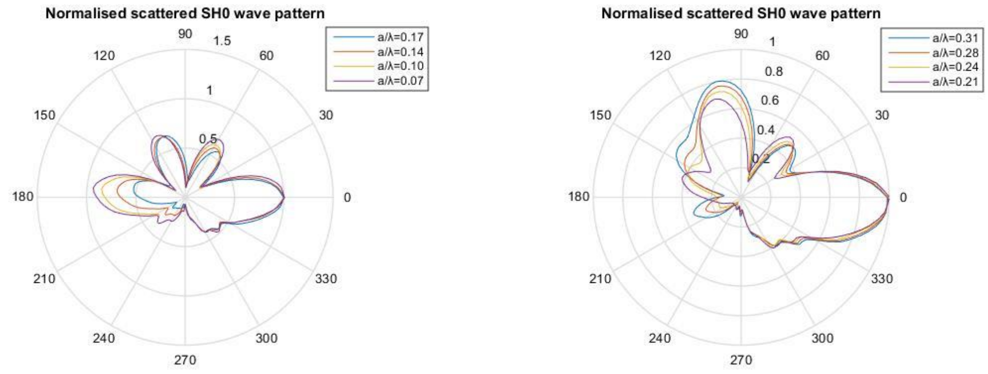

Figure 5.2.4: Normalised scattered wave polar plot of SH0 waves with respect to the incident wave maximum displacement. (a) 0.07≤a/λ≤0.17; (b) 0.21≤a/λ≤0.31

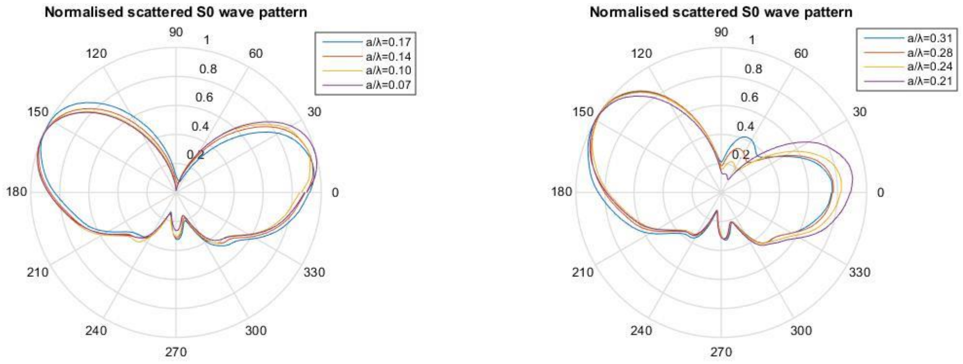

Figure 5.2.5: Normalised scattered wave polar plot of S0 waves with respect to the incident wave maximum displacement. (a) 0.07≤a/λ≤0.17; (b) 0.21≤a/λ≤0.31

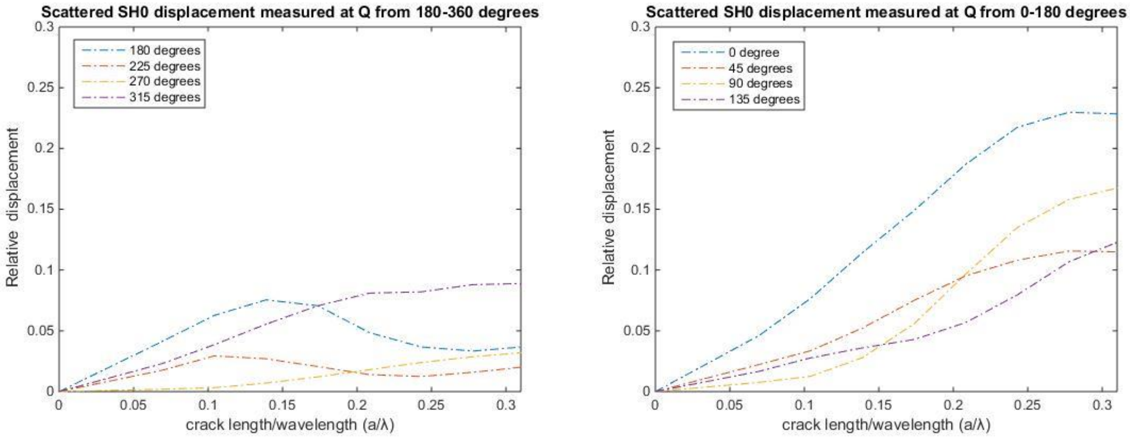

Figure 5.2.6: The scattered SH0 wave displacement for various a/λ in (a) 0˚-180˚ region and (b) 180˚-360˚ region with respect to the incident wave maximum displacement

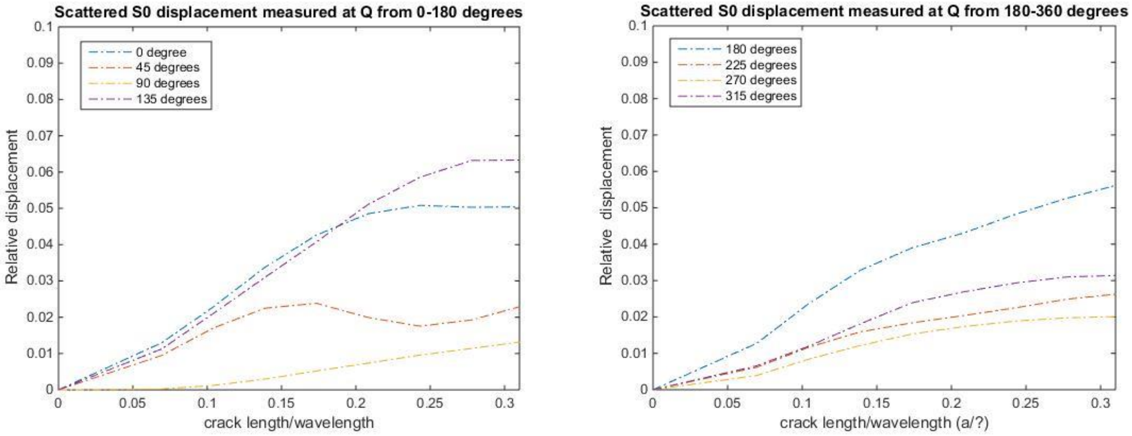

Figure 5.2.7: The scattered S0 wave displacement for various a/λ in (a) 0˚-180˚ region and (b) 180˚-360˚ region with respect to the incident wave maximum displacement

The scattered SH0 and S0 wave patterns are symmetrical along the 90˚ line and the pattern remains similar for *a/λ*<0.10 and *a/λ*<0.17, respectively, as seen in Fig. 5.2.4(a) and 5.2.5(a). As crack length increases, the SH0 lobes at 0˚ and at approximately 120˚ and S0 lobe at approximately 150˚ become relatively larger hence no longer retain a symmetrical pattern as shown in Fig. 5.2.4(b) and 5.2.5(b). Additionally, the SH0 lobe at 180˚ becomes relatively smaller. The scattered SH0 and S0 displacements have indicated in 0˚-180˚ degree regions increasing quadratically with respect to crack length until *a/λ*≈0.21 as shown in Fig. 5.2.6(a) and Fig. 5.2.7(a). As crack length increases further, the scattered displacement appears to stagnate. In 180˚-360˚ region, shown in Fig. 5.2.6(b), the scattered SH0 displacements increase with crack length until *a/λ*≈0.14. The scattered SH0 displacements trend is not apparent and amplitude is significantly weaker in this region. In Fig. 5.2.7(b), the scattered S0 displacements appear to plateau after *a/λ*≈0.14 in the 180˚-360˚ region.

The back-scatter and forward-scatter circumferential edge wave steadily increases with similar displacement until *a/λ*≈0.14 as shown in Fig. 5.2.9. Beyond this limit, the forward-scatter edge wave displacement dominants the back-scatter edge wave.

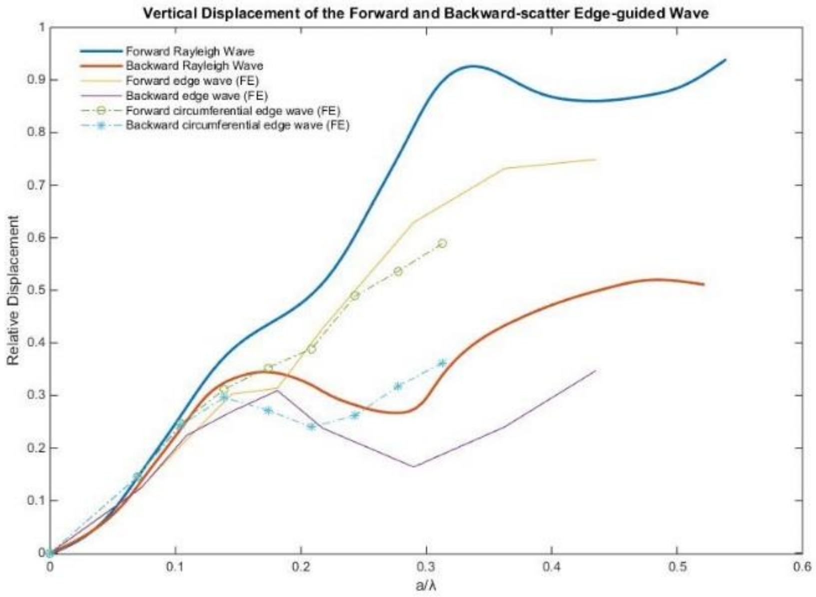

Figure 5.2.8: Relative displacements with respect to incident wave amplitude of analytical scattered Rayleigh wave displacement obtained from Mendelsohn [129], computational edge wave obtained from Vien et al [164] and computational circumferential edge wave.

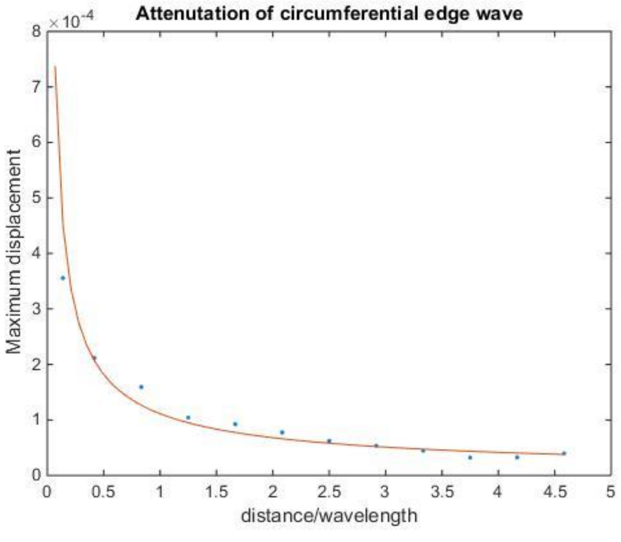

Figure 5.2.9: The attenuation of incident circumferential edge wave displacement over the circumference; (DOT) FE circumferential edge wave displacements, (LINE) data interpolation.

5.2.4 Discussion

The FE results showed that for small cracks $a/\lambda<0.10$, the scattered wave pattern is independent of crack lengths and the scattered amplitude increases with a^2. The small crack is equivalent to point source whose strength is proportional to the integral of the crack opening displacement, and thus gives a quadratic trend [119]. This suggests, under this cut-off limit, the small crack is equivalent to point source. Similarly to the edge crack investigation, the incident circumferential edge wave has a dominant σ_θ component and that the scattered wave pattern can be represented by a point source only consisting of a perpendicular forcing component.

The particular limit $a/\lambda\approx0.20$ is where the direction of particle rotation reverse for Rayleigh wave, similarly for symmetrical edge-guided waves, and where $\sigma_{r\theta}$ component becomes significantly dominant and σ_θ component is minimal. Since the stresses are no longer uniform, this resulted to an asymmetrical feature in wave pattern. Furthermore, representation for larger crack size can be achieved by applying opposite baseline stress profile as a function of depth on the crack faces.

The crack scattered a dominant circumferential edge-guided wave and a weak S0 wave. The scattered wave pattern trends; scattered lobes, similarly to the SH0 and S0 wave patterns for the edge crack case [164]. In Fig. 6.1.8(a), the reflected and transmitted circumferential edge wave trends similarly to the analytical results of Mendelsohn plane strain problem [129] and symmetrical edge wave with edge crack [164].

For $d/\lambda\approx2.8$, as the circumferential edge wave propagates, it has attenuated at a rate inversely proportional to a power of approximately 0.7 of propagating distance refer to Fig. 6.1.8(b). The rate of which the circumferential edge wave attenuates will also depend on the material property; Poisson’s ratio. For smaller d/λ, the edge wave should decay at a faster rate until at a critical ratio, the edge wave stops propagating along the circumferential and instead leaks to the medium. For larger d/λ, the wave should converge to the symmetrical edge wave speed similar to the plane strain case

[88]. Further study is required to analyse the circumferential edge wave dependence on *d/λ* and Poisson's ratio in detail.

5.2.5 Antisymmetric circumferential edge wave propagation around hole

The scattering of antisymmetric edge wave by edge crack on a straight boundary was also investigated. A pre-requisite attempt to investigate the antisymmetric edge wave propagating around a curved surface was conducted. The FE model configuration and analyse are the same as the symmetric circumferential edge problem, however the excitation involves an out-of-plane forcing component to generate antisymmetric wave modes.

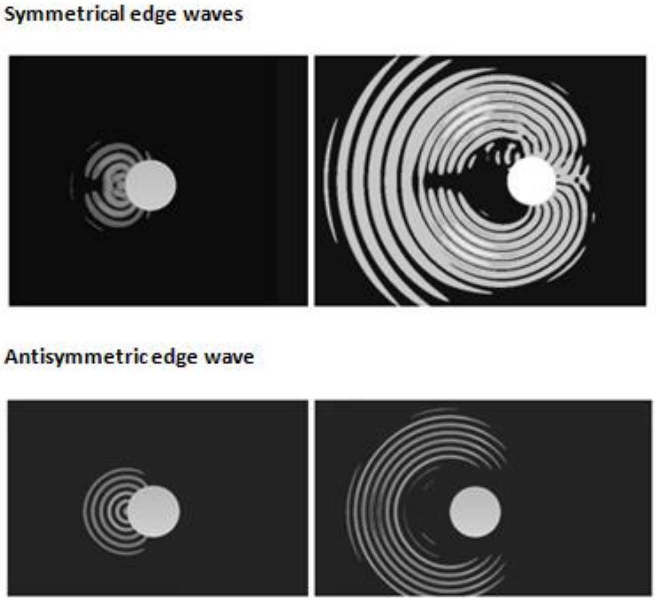

Figure 5.2.10 Time snapshot at 20μs and 40μs of edge waves propagating around the hole.

It was found that the antisymmetric edge wave immediately attenuates to the medium and decays much rapidly than symmetric edge wave propagating around the hole circumference, refer to Fig. 5.3.1. Although the diameter of the hole is 40mm, which is $d/\lambda > 1$, the attenuation cannot be quantified. This suggests the antisymmetric edge wave may not be ideal for curve boundary for shadow zone detection. Additional investigation analytical study is required to determine the behaviour of antisymmetric edge wave propagating around curve surface. The hole investigation proceeds to the scattering by symmetric Lamb wave mode instead.

5.3 Scattering of fundamental symmetric Lamb waves by an edge crack at a circular hole in an isotropic plate: Experimental and computational studies.

This study computationally and experimentally investigates the interaction of a symmetric edge-guided wave with a through-thickness crack emanating from a circular hole. This study is an extension to a previous small edge crack on a straight boundary problem [167]. The scattered wave amplitude and patterns dependencies on crack length are reported. It is expected that the scattered wave amplitude should increase quadratically with a/λ. This is a pre-requisite approach to determine the crack length dependence based on scattered wave measurements to facilitate the inverse problem of hidden crack detection.

5.3.1 Methodology

The scattered wave field associated with the small crack on hole is obtained via a baseline subtraction. This baseline subtraction procedure is illustrated in Fig. 5.3.1 using a visualisation of the computational results.

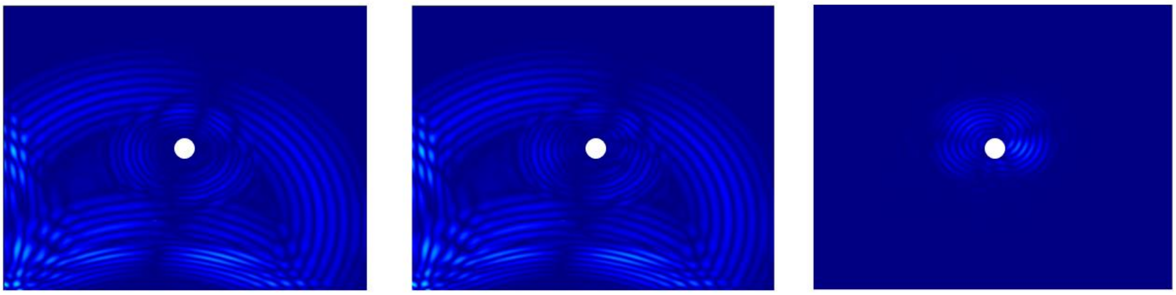

Figure 5.3.1: Illustration of the baseline subtraction procedure to obtain the scattered wave field due to the presence of a crack on hole

Edge waves can propagate around a hole, given the diameter is much larger than the wavelength. Unlike edge wave propagating along a straight boundary, these leaky circumferential edge waves decay with propagating distance, which is depended on d/λ and material property; Poisson's ratio. Beyond a critical diameter to wavelength ratio, these leaky edge waves attenuate to the medium and cease propagation on the curved surface.

A radial crack of length, a, emanating from a circular hole of diameter, d, is investigated. The crack length is assumed to be small compared to the incident wavelength λ and the hole diameter, such that $a/\lambda \ll 1$ and $a/d \ll 1$. Under these conditions, for small cracks, the scattered wave field should behave similarly to a point source consisting a particular combination of body-force doublets. This point source equivalence also suggests that the scattered wave pattern should be relatively independent of the crack size.

It is anticipated that the scattered wave patterns should have some features similar to the edge crack on a straight boundary [164, 167]. The scattered representation for larger crack size can be done by applying opposite baseline stress profile along the crack [20] as well. In this study, the SH0 and S0 scattered patterns and displacement trends with crack length are reported.

5.3.2 Computational Procedure

ANSYS 15.0 is used as the Finite Element (FE) computational analysis tool to simulate Lamb wave in an aluminium test specimen. An aluminium plate of 450mm x 450mm dimension and 3mm thickness (density 2700kg/m^2, Poisson ratio of 0.33 and Young modulus of 69 GPa) is modelled, refer to Fig. 5.3.2. A through-thickness hole with 20mm diameter is located at the centre of the plate. In this critical condition where $d/\lambda < 1$, circumferential edge wave cannot propagate along the hole boundary without rapidly attenuating into the medium. So, the incident wave is primarily S0 wave mode.

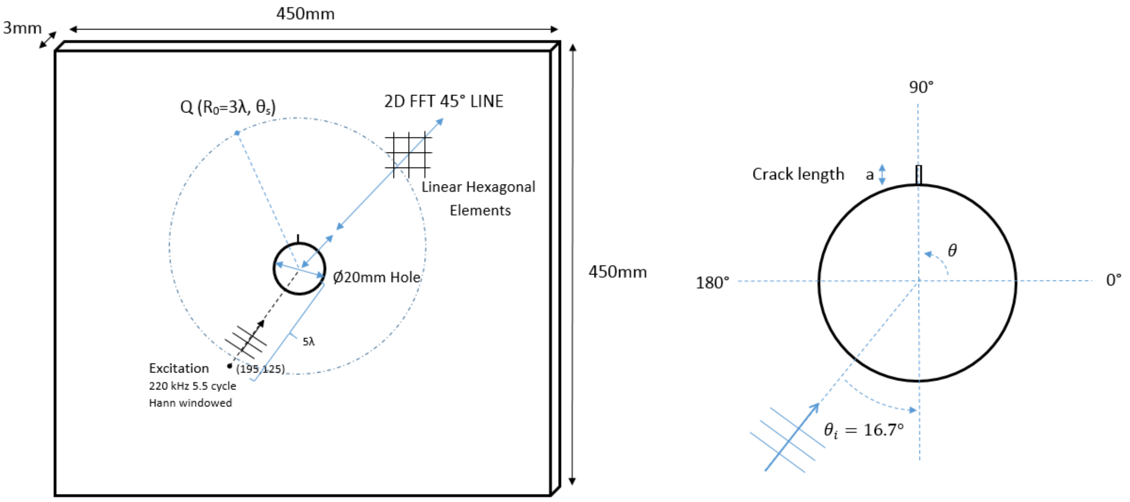

Figure 5.3.2: (LEFT) 450x450x3mm aluminium plate FE geometry showing the location of the crack, 45° 2D FFT scan line, scattered wave measurement; the excitation point and excitation point (RIGHT) Near hole diagram portraying the crack location and origin of the cylindrical coordinate system at centre of the hole.

The small crack modelled as a 0.5mm width notch emanate at the 12 o'clock position of the hole, with size 1mm to 4.5mm in 0.5mm increments as shown in Fig. 5.3.2. The plate specimen is discretised into 0.5mm, 8-node linear hexagonal elements, which satisfy the requirement of 10 elements per wavelength for accurate modelling [147]. The time step is 0.02 µs, which satisfies the standard stability criterion for Explicit Time Integration of being less than or equal to 0.8L/C, where L

denotes the smallest element length and *C* the fastest wave speed [148]. An applied force distribution that is symmetrical with respect to the plate's mid-plane can only generate purely symmetric modes. To generate only the S0 mode, equal and opposite point forces; *pinching forces*, are applied to nodes on opposite faces of the plate, with the forces acting in the direction normal to the plate surface. The S0 mode is excited at coordinate *(195, 125)* which is approximately 5λ away at incident 16.7˚, such that the crack is hidden along the illuminating path, as shown in Fig. 5.3.2. The force excitation signal is chosen to be a 5.5 cycle Hann-windowed tone burst with centre frequency 220 kHz. At this centre frequency, the wavelength of S0 and SH0 are 22.2mm and 14.0mm [33].

2D Fast Fourier transformation is performed along the 45˚ line from the centre of the hole as shown in Fig. 5.3.2. The 2D FFT results is used to create the dispersion curve for identifying the dominant Lamb Wave modes from DISPERSE [33]. The 2D FFT spatial distance is taken at least 3.5λ away from the crack base over approximately 5λ distance, with 1024 equidistant spatial sample and zero padding [147]. The maximum amplitude of the associated analytic signals was used as the measure of the scattered field amplitude. The maximum peak of Hilbert transformation over the time domain signals measured at point Q, at a distance approximately 4λ away was performed to obtain the maximum amplitude, refer to Fig. 5.3.2. The scattered wave displacements are analysed in two regions: from 0˚ to 180˚ and 180˚ to 360˚, refer to Fig. 5.3.2. The maximum scattered displacements are measured at 0˚, 45˚, 90˚, 180˚, 225˚ and 270˚.

The scattered wave amplitude results are normalised to account for the cylindrical wave decay and relative to the maximum incident S0 wave displacement at the location of the crack. For the purpose of analysing the scattered wave pattern dependence with crack size, the amplitude is normalised relative to the scattered wave field maximum amplitude. The scattered wave lobes locations and relative amplitudes with other lobes are used to determine whether the pattern is changing with crack length.

5.3.3 Experimental Procedure

The experimental specimen is a 5005H34 aluminium alloy plate with the same geometrical configuration as for the computational model. The in-plane velocity components of the propagating Lamb waves were recorded by Polytec CLV 3D automated laser vibrometry. A Polytec retro-reflective sheet is attached to the plate to significantly reduce the noise and improve the data quality. The specimen is secured on a XY positioning system and the experimental rig is mounted on a DAEIL system vibration isolation optical table to minimise vibration. The experimental setup is shown in Fig. 5.3.3. A PZ26 transducer of diameter 16mm and thickness 2mm was bonded on the aluminium plate to excite incident Lamb waves. Although, one can analyse the symmetric and antisymmetric modes in their dominant in-plane and out-of-plane component, respectively, refer to Fig. 5.3.4. However, weak signals of the other nondominant modes can still be detected. To achieve a clearer signal, the excitation distance being approximately 5λ ensures that the S0 Lamb wave cycle completely incident with the defect before the incident and reflected A0 waves from the boundaries.

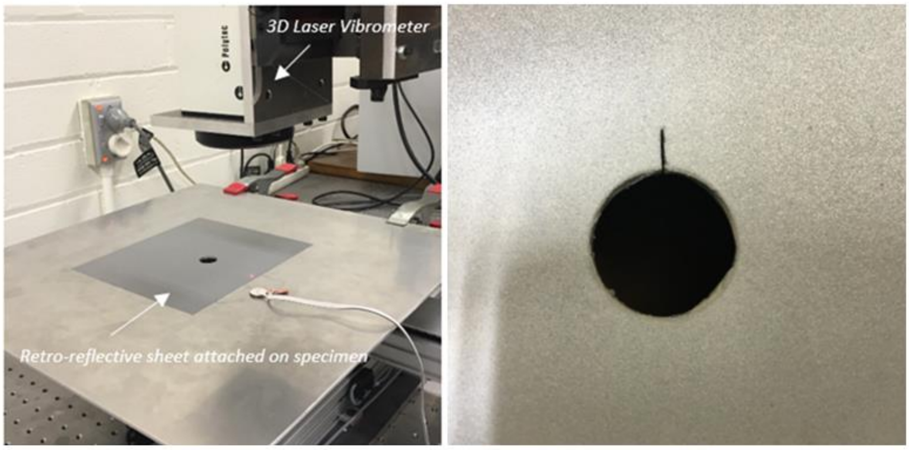

Figure 5.3.3: Experimental setup of 3D Laser Vibrometer and specimen and close-up image of the hole with crack attached with retro-reflective film

In the experimental investigation, a 0.4mm width notch is artificially created to prevent the surfaces of crack from contact. So, no waves can transmit through the crack surfaces as shown in Fig. 5.3.3.

The notch with lengths of 3.11mm, 3.58mm and 4.61mm are investigated. The post-processing of data is the same as that for the computational investigation.

5.3.4 Results and Discussion

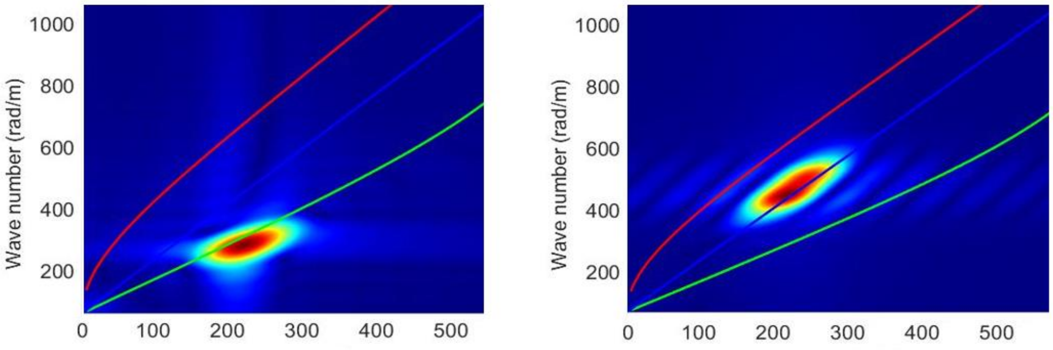

Figure 5.3.4: Plots of 2D FFT FE dispersion curve of the scattered wave field due to presence of crack indicating that (a) a dominant S0 wave in the r component;(b) a dominant SH0 wave in the θ component.

As crack size increases, the SH0 scattered wave pattern for $a/\lambda \approx 0.05$, as shown in Fig. 5.3.5, immediately becomes asymmetric. This is caused by the change in the distribution of normal and shear stress components along the location of the crack. For $a/\lambda < 0.11$, the lobes at 0˚, 60˚ and 120˚ remain relatively the same, whereas 180˚ lobe becomes relatively smaller when crack size increase, refer to Fig. 5.3.5. For $0.14 < a/\lambda < 0.20$, the 60˚ lobe becomes relatively smaller than the rest of the other lobes. The two lobes at 60˚ and 120˚ are similar to the scattered wave pattern for the edge crack problem [164, 167]. In Fig. 5.3.6, the S0 scattered wave patterns have two lobes at 30˚ and 150˚ and remain very similar and symmetrical about the 90° line.

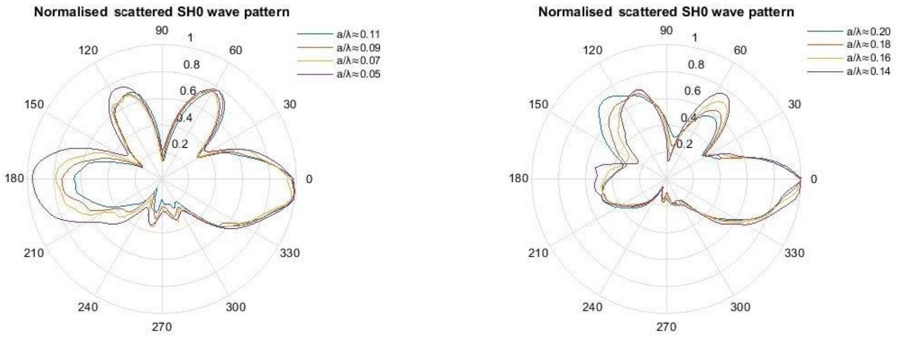

Figure 5.3.5: Normalised scattered wave polar plot of SH0 waves with respect to the incident wave maximum displacement. (a) 0.05≤a/λ≤0.11; (b) 0.14≤a/λ≤0.20

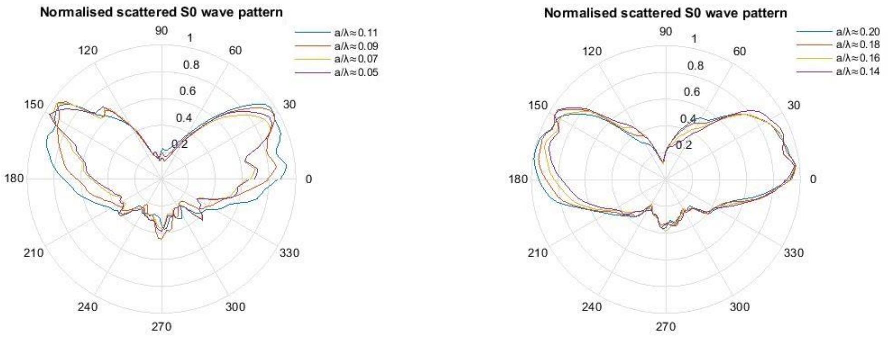

Figure 5.3.6: Normalised scattered wave polar plot of S0 waves with respect to the incident wave maximum displacement. (a) 0.05≤a/λ≤0.11; (b) 0.14≤a/λ≤0.20

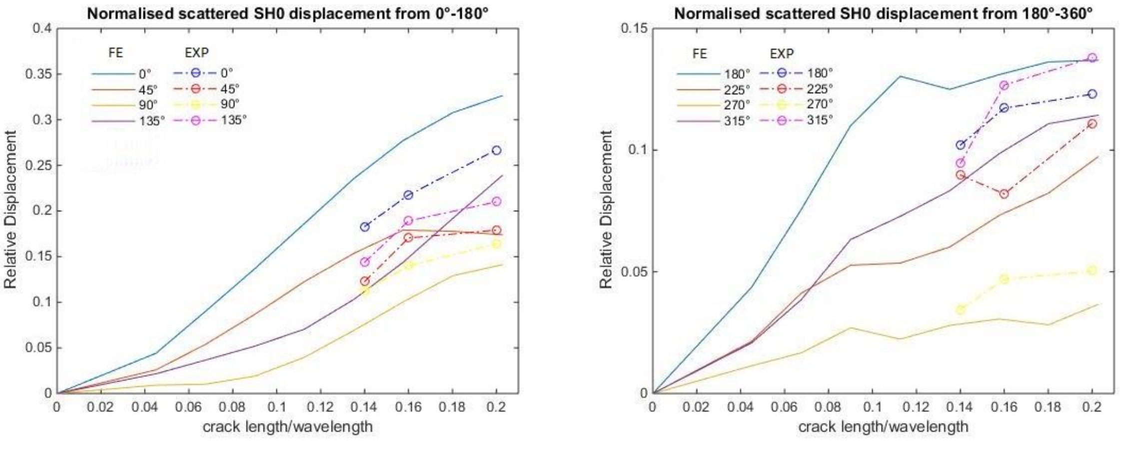

Figure 5.3.7: FE and experimental results: Normalised scattered SH0 wave displacement for various a/λ in (a) 0˚-180˚ region and (b) 180˚-360˚ region with respect to the incident wave maximum displacement.

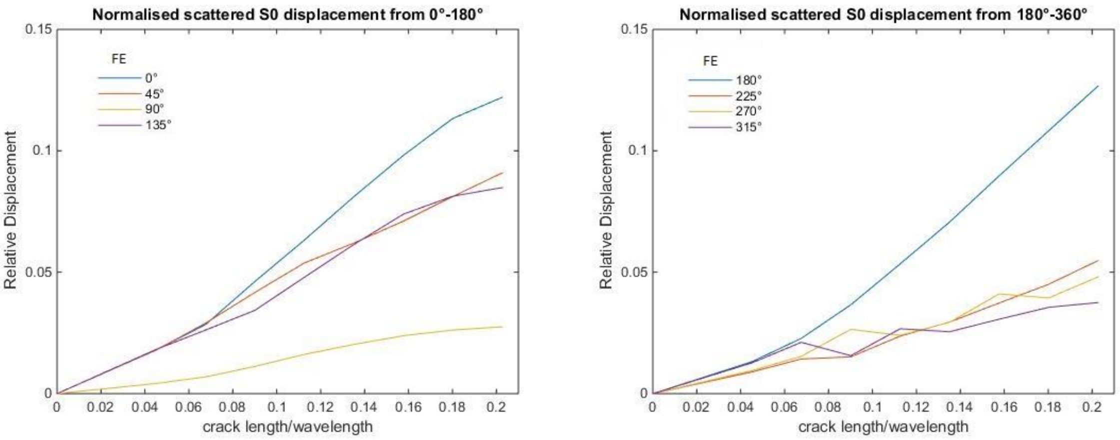

Figure 5.3.8: FE results: Normalised scattered S0 wave displacement for various a/λ in (a) 0˚-180˚ region and (b) 180˚-360˚ region with respect to the incident wave maximum displacement.

The scattered wave field shown in Fig. 5.3.7 are similar with the exception of the lobe at approximately 180˚ decreasing in relative amplitude as crack size increases. It is unsure why this particular lobe is relative smaller than the lobe at approximately 0˚ since it is expected minor different in pattern under this region. This may be an effect due to angle of incidence, however, future investigation is required to determine this discrepancy. The FE results suggest that the scattered wave field due to the presence of a small crack can be equivalent to a point source if the scattered wave pattern is independent of crack lengths and the scattered amplitude increases with a^2. The quadratic trend can be seen in the 0˚-180˚ regions in Fig. 5.3.7 and 5.3.8. Beyond $a/\lambda>0.10$, the increasing rate begins to stagnate. ‘

The experimental SH0 wave patterns indicated similar amplitude trend and features to the FE results, refer to Fig. 5.3.7. The experimental and computational SH0 wave patterns both showed weak scattering behind the hole between 240˚ and 330˚ and maximum scattered amplitude near 0˚. Two lobes at approximately 60˚ and 120˚ are apparent in FE and experimental wave patterns, refer to Fig. 5.3.9 and 5.3.10.

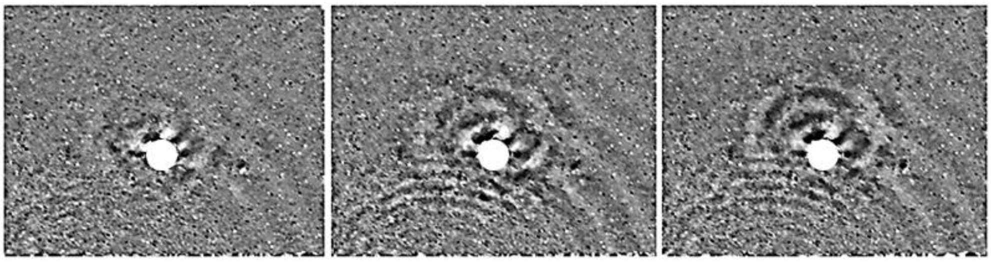

Figure 5.3.9: Snapshot of experimental scattered SH0 wave field at time 40μs for (a) a/λ≈0.14, (b) a/λ≈0.16 and (c) a/λ≈0.20.

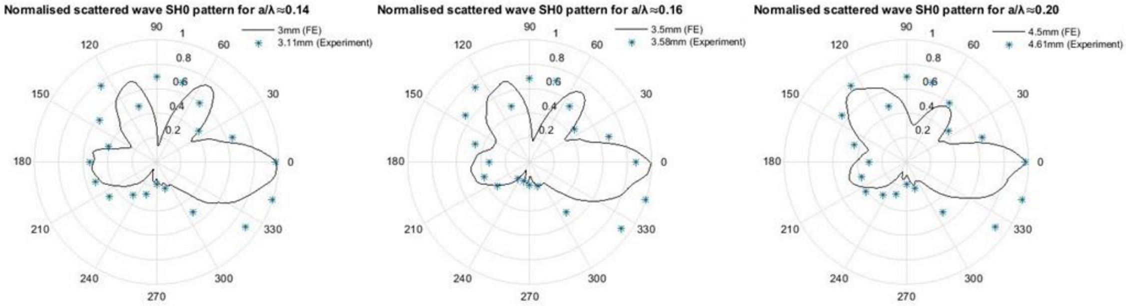

Figure 5.3.10: Experimental and computational comparison of the normalised scattered wave polar plot of SH0 waves with respect to the incident wave maximum displacement for (a) a/λ≈0.14, (b) a/λ≈0.16 and (c) a/λ≈0.20

In Fig. 5.3.10, there is a difference at the 90˚ between FE and experimental results. It is observed that the edge-guided wave leaks at the crack tip and propagating into the medium. This effect is similar to leaking Rayleigh wave observed by previous studies [32, 168], although it is considered a likely effect due to long crack lengths.

The crack scattered a dominant SH0 and a weak S0 wave. Experimental data in the radial component is particularly very weak compared the angular component. Consequentially, only the experimental scattered SH0 results were analysed and compared to the FE results.

The scattered leaky edge wave was also observed attenuating in the medium, similar to the Doherty and Chiu [13] scattering SH0 spiralling effect. The spiralling SH0 is the coalescing of the scattered SH0 wavefront from the crack and the leaky edge wave, resulting in the spiralling appearance [165].

Later, it evolves to resemble the wave pattern of a source located at the crack which is shown in this study. Further study is required to analyse the attenuation of circumferential edge wave and its dependences.

5.4 Conclusion

Three key studies are investigated in this chapter on the effect of a hole diameter, the scattering of fundamental S0 waves and symmetric edge-guided wave by the hidden crack.

The findings in the investigation of Lamb-wave (S0) scattering due to small notch on an open hole with different diameter are discussed. Provided the impinging wavelength is smaller than the hole diameter, creeping waves are perceptible, otherwise it will immediately leak to the medium. A 2D FFT analysis indicated the dominant presence of the SH0 mode in the scattered wave field. The SH0 spiralling effect has been explained as being due to SH0 source-like waves guided by leaky edge waves, and it has been shown to be strongly dependent on hole diameter relative to wavelength. The scattered field at first has the appearance of a spiralling SH0 wave, but later evolves to resemble the wave pattern of a source located at the notch tip. The guided edge waves can direct the scattered SH0 waves to an accessible region where damage detection can be conducted. These scattering phenomena suggest that the scattered SH0 waves can be utilised to characterise the defect.

The scattered wave field of a low frequency circumferential edge wave with a small crack on a hole in an isotropic plate has been reported. In study the hole was significantly large to allow edge-guided to creep around the hole to impinge with a hidden crack. It was shown for small crack length, $a/\lambda<0.10$, the scattered pattern is independent of crack size which suggest the scattered wave field can be represented as a point source consisting of a particular combination of force doublet at the location of the crack mouth. The scattered SH0 and S0 wave amplitude and reflected and transmitted amplitude for the circumferential edge guided wave are proportional to crack length squared a^2.

The scattered wave field of a fundamental symmetric Lamb wave mode with a small crack on a hole in an isotropic plate has been reported. In this particular study, the hole diameter is significantly small so that edge-guided wave cannot propagated around the hole boundary, so only incident S0 impinged with the hidden crack. It was shown for small crack length, $a/\lambda<0.10$, the scattered pattern is also independent of crack size and the scattered SH0 and S0 amplitude increases like a^2, when impinged by an incident S0 wave. This also suggests that the scattered wave field by incident S0 can be represented as a point source.

The findings in these hole studies, the scattering due to a small can is equivalent point source model when impinged by incident S0 or incident edge-guided wave. It is demonstrated that for hole diameter larger than the incident wave, waves can creep around the hole and propagates to the hard-to-inspect location. Furthermore, the studies have provided scattered wave measurements; amplitude and pattern, and its relationship with crack length which indicate the possibility to characterise the small crack on a hole as a simple source representation. This addresses the inverse problem of detecting and quantifying hidden cracks in hard-to-inspect location, based on scattered field measurements for an incident symmetric Lamb wave mode and edge-guided wave. In the next study, this research proceeds to a more complex geometry; rectangular slot, to show that edge-guided waves can be travel to hidden location and then

Chapter 6

The experimental and computational study on the scattering of fundamental edge-guided wave by a hidden crack on a rectangular curved slot

6.1 Introduction

This chapter reports on the investigation of scattering by a hidden crack on a rectangular curved slot with incident symmetric edge-guided waves. The study tackles on detecting and quantifying crack in a hard-to-inspect location by using the key findings from the previous chapters of the edge crack and hole. Both experimental and computational investigations were conducted to determine the scattered wave patterns and amplitudes due to the presence of small crack when impinged by symmetric edge-guided waves. This is done for quantitative inspection in structural health monitoring (SHM).

The objective of this study is to investigate the interaction of incident symmetric edge-guided wave in a plate with a small hidden crack (relative to the incident wavelength) in the shadow zone of the rectangular slot. It is highly advantageous to utilise edge-guided waves for SHM, since they do not decay with propagation distance on a straight boundary. However, edge-guided waves propagating around the curved surface will decay at a rate dependent on d/λ and Poisson’s ratio. The characteristic lengths in this problem are configured such that the edge-guided wave impinges with the crack at the upper surface of the rectangular curved slot. The scattered wave pattern and amplitude for crack length dependence will be reported on and compared to the previous findings of edge crack problem [164, 167] and hole problem.

In the case of bulk waves, it is known that scattering by an infinitesimal crack is equivalent to the wave field from a particular combination of body- force doublets [27]. The Lamb wave scattering by a small edge crack is expected to have similar force doublets equivalents [164, 166]. This point source equivalence indicates that the scattering pattern should be relatively independent of crack size and should increase quadratically with increasing *a/λ*. It is expected that a hidden crack on the rectangular slot can be represented as a point source on its boundary.

The study is a forward scattering problem of a known crack length and location. This is a necessary study before tackling the practical inverse problem of quantifying and detecting the crack size, based on scattered wave field measurements.

6.2 Methodology

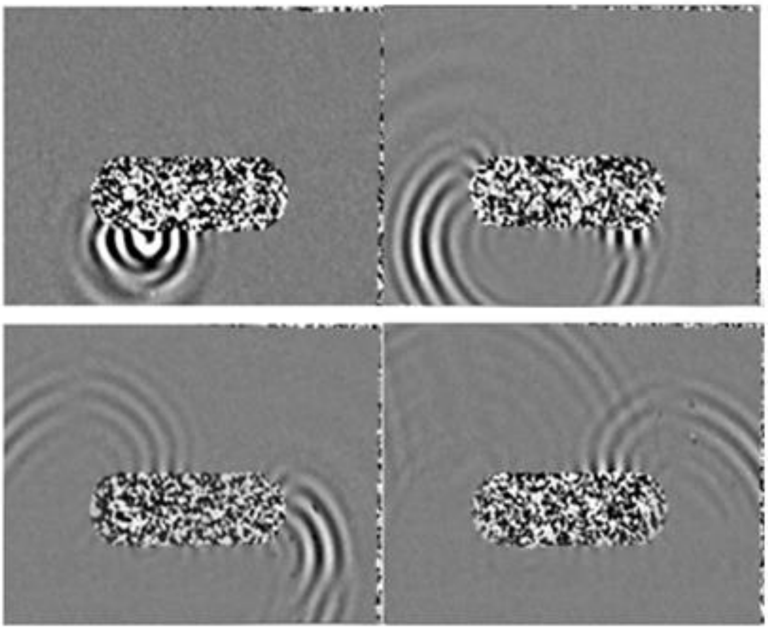

Figure 6.1: Time snapshot of the experimental wave field in the vertical component of the edge-guided wave propagating around the rectangular curved slot at 20, 40, 60 and 80μs

The excitation frequency is selected to be well below the cut-off of 1.53MHz-mm for the first order symmetrical Lamb wave mode SH1 for aluminium [33]. Hence, the only propagating Lamb waves are the fundamental modes S0, SHO and A0.

The symmetric modes can be generated by the application of force distributions that are symmetrical with respect to the plate's mid-plane. Likewise, a symmetric edge-guided wave can also be generated by mid-plane symmetric forces applied along a straight edge. This symmetric edge wave can be regarded as the plane stress analogue of the Rayleigh (surface) wave. The corresponding wave speed can therefore be obtained from the Rayleigh wave speed by using the familiar change of elastic constants to convert plane strain results to plane stress [18]. Symmetric edge wave can propagate on a curve surface as shown in Fig. 6.1. However, it will decay and travel with a wave speed slightly slower than the ones propagating along a straight boundary. At critical d/λ value, these leaky circumferential edge-guided waves cannot propagate on a curve surface without attenuating into the medium.

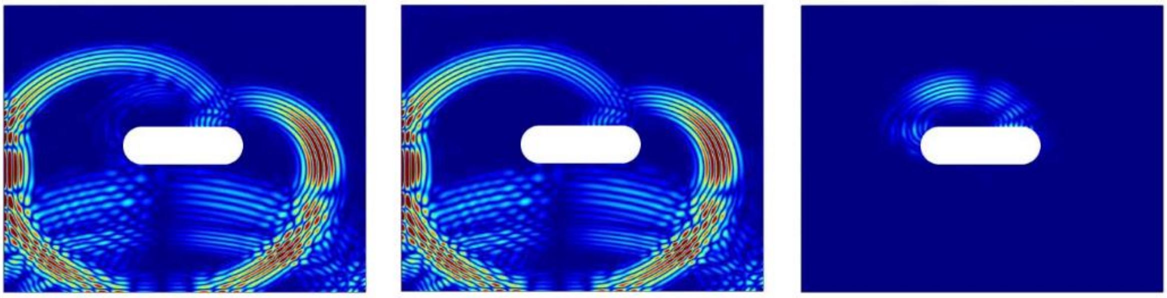

Figure 6.2: Baseline subtraction of total wave field with crack and original wave field without crack to obtain the scattered wave field due to the presence of a hidden crack

In order to analyse the scattered wave displacement field associated with the small hidden crack, a baseline subtraction is employed. The crack length a is assumed to be $a<<\lambda$, where λ the wavelength of the incident wave. For this crack size limitation, the incident field can be expected to consist primarily of the edge-guided wave. The contribution of the other propagating modes along the edge is negligible. For small cracks, the scattered field can be expected to be like that of a point source located at the crack tip and with the strength of the point source being proportional to some power of the crack length. This point source equivalence also suggests that the scattering pattern should be relatively independent of crack size. It is anticipated that the scattering of Lamb wave should share similar features to the previous study on a hole and edge crack problem [164, 166].

6.3 Computational Procedure

In the computational study, ANSYS 15.0 is used as the Finite Element (FE) computational analysis tool to simulate Lamb wave in a 450mm x 450mm aluminium plate of 3mm thickness (density 2700kg/m^2, Poisson ratio of 0.33 and Young modulus of 69 GPa), refer to Fig. 6.3. A through-thickness rectangular curved slot is located at the centre of the plate. The slot curves are modelled as semi-circles with 25mm radius, and the total length of the slot is 150mm, refer to Fig. 6.3.

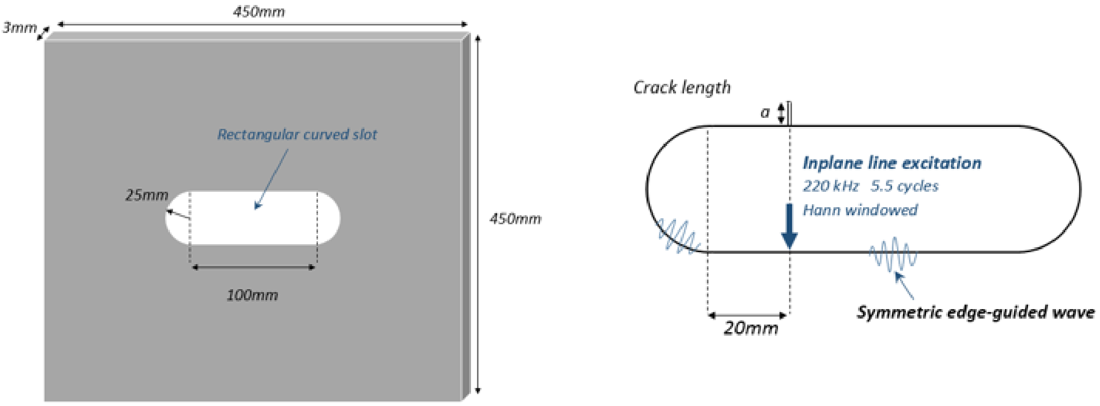

Figure 6.3: Model configuration of the rectangular curved slot centre in a 450 x 450 x 3 mm aluminium plate and close-up diagram of rectangular slot showing excitation and crack location.

The crack is located on the upper straight boundary of the slot, refer to Figure 6.3. The plate is discretised into 0.5mm 8-node linear hexagonal elements which satisfy the requirement of 10 elements per λ for accurate modelling [147]. The time step is set at 0.02 μs, which well satisfies the standard stability criterion for Explicit Time Integration of being less than or equal to $0.8L/C$, where L denotes the smallest element length and C is the fastest wave speed [148]. The defect is modelled as a 0.5mm width notch to avoid crack face contact. The dependence of scattered amplitude with crack length is investigated by varying the crack size, a, from 0.5mm to 4.5mm with 0.5mm increments. The incident edge-guided wave is generated approximately 8λ propagating distance away with the line force acting direction normal to the edge surface at (195, 200). To minimise dispersion, the line force excitation signal perpendicular to the slot straight edge (refer to Fig. 6.3) is chosen to be a 5.5 cycle Hann-windowed tone burst with a centre frequency of 220 kHz. At this centre frequency the wavelength of S0, SH0 and symmetric edge wave are 22.2mm, 14.0mm and 13.4mm, respectively [33]. It is noted that the wavelength of circumferential edge wave is slightly larger than the wavelength of symmetric edge waves travelling on a straight boundary; thus circumferential edge wave propagates relatively faster.

2D Fast Fourier Transformation is performed on the nodes along the straight boundary and along the line 45° from the crack base edge, as indicated in Fig. 4.1.2(b), to create the dispersion curve in order to identify the dominant Lamb wave mode from DISPERSE [33]. Another scan was performed along the boundaries of the rectangular slot to determine the leaky edge-guided wave modal content. The 2D FFT spatial distance is taken at least 3.5 wavelengths away from the crack base to avoid detection of higher non-propagating Lamb waves and approximately 10λ distances with 1024 equidistant spatial samples with zero padding [147].

The maximum amplitude of the associated signals was used to measure the scattered wave amplitude and to construct the scattering wave pattern in a polar plot. This is done by taking the maximum peak of Hilbert transformation over the time domain signals measured at point Q which is at a distance approximately 10λ away, refer to Fig. 6.4.

The scattered wave amplitude is analysed in the region from 0° to 180° centred at the crack base refer to Fig. 6.4 and the maximum scattered displacements were measured at 30°, 60°, 90°, 120° and 150° in radial (r) and angular (θ) components. The amplitudes of the back-scatter and forward-scatter edge waves were also analysed by taking the scattering displacements along the rectangular straight boundary.

The scattered S0 and SH0 wave pattern results are then normalised to account for the cylindrical wave decay, which is at a rate inversely proportional to the square root of propagating distance, and relative to the maximum incident edge wave displacement. For the purpose of analysing the wave pattern dependence with crack size, the amplitude is normalised relative to the maximum amplitude of the scattered wave field. This leaky edge wave attenuation over the curved boundary is measured, by taking the Hilbert transformation to obtain the maximum value, as a function of distance-to-wavelength ratio and briefly reported. This geometry decay is also accounted for in the normalisation process to analyse the scattered edge waves.

6.4 Experimental Procedure

A 5005H34 aluminium alloy plate with the same FE model configuration is considered as the test specimen for the experimental study. The plate is secured on a XY positioning system, as shown in Fig. 6.3 and the experimental rig is mounted on a DAEIL system vibration isolation optical table to minimise background vibration. The in-plane velocity components of the propagating Lamb waves were acquired by Polytec CLV 3D automated laser vibrometer. In order to enhance the data quality a Polytec retro-reflective sheet is attached to the aluminium plate. A PZ26 transducer of diameter 16mm and thickness 2mm was bonded to the straight edge of the rectangular slot to generate incident edge-guided waves refer to Fig. 6.4. This bond location is not applicable in real structures but significant in research to generate edge-guided waves. Since the plate thickness is smaller than the PZT diameter, it is difficult to bond the PZT on the edge of the plate. Furthermore, extreme care is need when handling the specimen since the PZT can be easily detached. The transducer was nominally placed symmetrically with respect to the plate’s midplane, in an attempt to generate only the symmetric modes. However, it was found to be difficult in practice to avoid some asymmetry, which results in the generation of weak antisymmetric modes as well. There is no mode coupling due to the scattering process because the crack geometry is symmetrical with respect to the plate’s midplane. This means an incident symmetric wave generates only symmetric scattered modes and vice versa for the antisymmetric wave. The symmetric wave modes can be analysed in their dominant in-plane components. However, since the scattered S0 signal is particularly weak, only the SH0 scattered wave amplitude and patterns are analysed in the experimental study. It should be noted that the weak signal of non-dominant modes can still be detected due to the nature of Lamb waves.

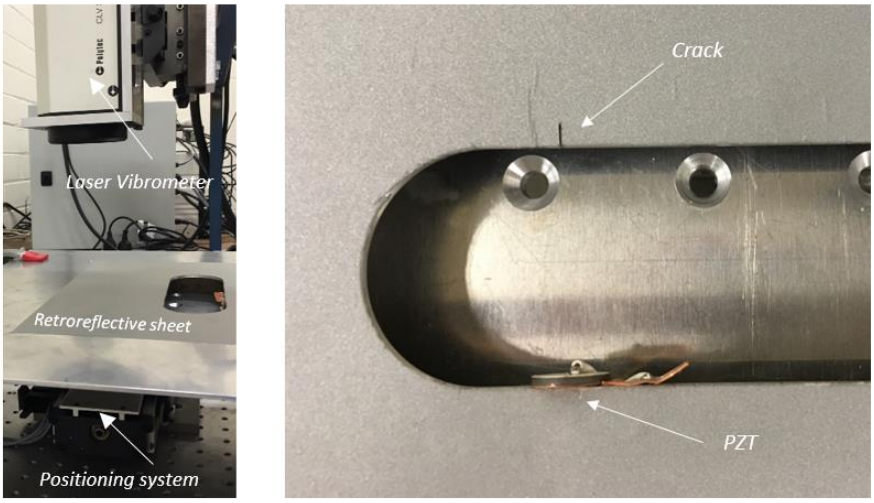

Figure 6.4: (LEFT) Laser vibrometry setup showing 450 x *450 mm aluminium plate with retroreflective sheet mounted on the positioning system (RIGHT) Close-up image of crack and PZT bonded on the rectangular slot edge.*

In the experimental investigation, 0.4mm width notches are artificially created to prevent wave transmission through the crack surface as shown in Figure 6.4. The notch of lengths 2.59mm, 3.49mm, and 4.64mm scattered wave patterns are investigated. The post-processing of data is the same in both computational and experimental investigations.

6.5 Results

A 2D FFT processing was used to identify the dominant wave modes in conjunction with Lamb-wave dispersion curves from DISPERSE, as shown in Fig. 6.5. The scans taken along the 45° line from the crack base have indicated a dominant scattering S0 and SH0 wave in the radial and angular components, respectively. Thus, the scattered S0 and SH0 wave amplitudes and patterns are analysed in their respective dominant cylindrical components. The 2D FFT scan along the straight boundary of the slot indicated a propagating symmetric edge-guided wave whose speed is similar to the Rayleigh wave speed. The scattered edge wave amplitude does not decay as it propagates on the straight boundaries. However, as the edge wave travels along the curve boundaries it leaks energy into the medium at a rate inversely proportional to a power of 0.55 over propagating distance for *d/λ≈3.7*, refer to Fig. 6.6. The FE and experimental scattered edge-guided wave results were normalised to account for this decay and compared with the analytical Rayleigh wave case.

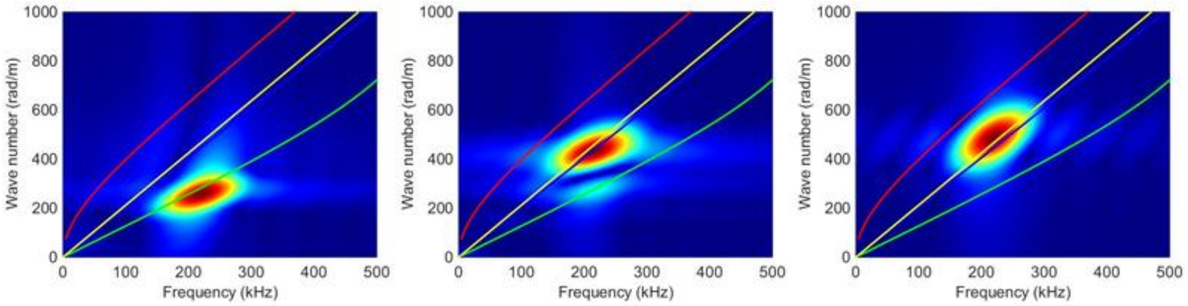

Figure 6.5: (a) Plots of 2D FFT FE dispersion curve indicating (a) a dominant S0 wave in the r component; (b) a dominant SH0 wave in the θ component; (c) a symmetric edge-guided wave along the straight boundary.

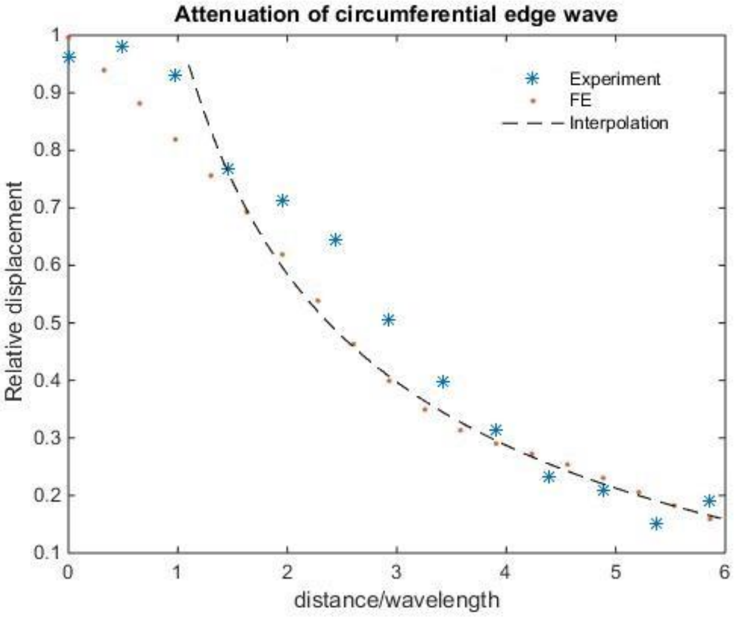

Figure 6.6: The experimental and FE attenuation of incident circumferential edge wave displacement over the circumference. Interpolation line indicates a rate of inversely proportional to power of 0.55 over distance/wavelength.

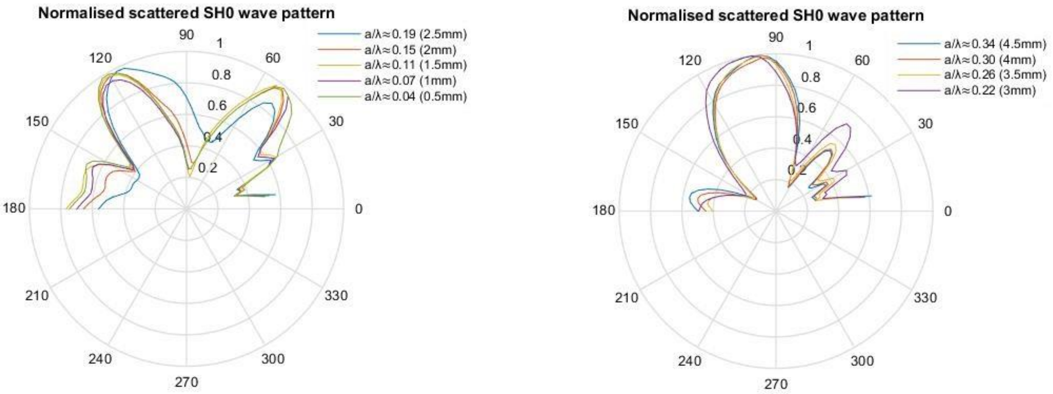

Figure 6.7: FE normalised scattered wave polar plot of SH0 waves with respect to the incident wave maximum displacement. (a) 0.04≤a/λ≤0.19; (b) 0.22≤a/λ≤0.34.

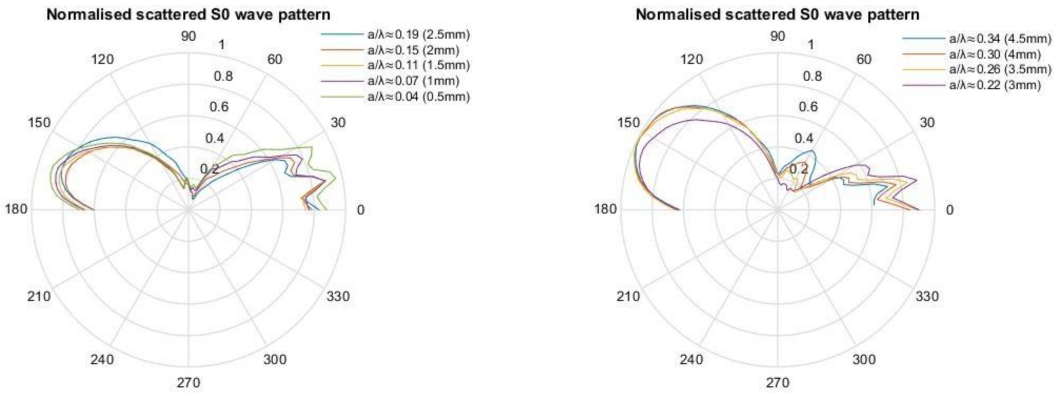

Figure 6.8: FE normalised scattered wave polar plot of S0 waves with respect to the incident wave maximum displacement. (a) 0.04≤a/λ≤0.19; (b) 0.22≤a/λ≤0.34.

Figure 6.7 portrays the scattering pattern for SH0 mode for various crack lengths. For *a/λ≤0.19,* the SH0 wave pattern remains symmetrical along the 90˚ line. However, as crack length increase beyond this limit, the wave pattern is asymmetrical and has a relatively larger back-scatter lobe, which is approximately twice as large than the forward-scatter lobe. The *a/λ≈0.19, 0.26,* and *0.34* experimental scattered wave pattern results indicated a strong bias back-scatter lobe as well and have shown good correlations with the computational results, refer to Fig. 6.9. There is also an additional contribution of the leaky edge-guided wave in the scattered SH0 wave pattern as shown in Fig. 6.7 in the 150˚-180˚ region.

Fig. 6.8 shows the scattering pattern for S0 wave for various crack lengths. Similarly to the SH0 waves, the S0 wave pattern remains the independent of crack length for *a/λ≤0.19*. As crack increases, the back-scatter S0 lobe becomes relatively larger than the forward-scatter lobe and hence, no longer retains its symmetrical pattern. The S0 and SH0 scattered wave pattern results are very similar to a previous edge crack problem investigation.

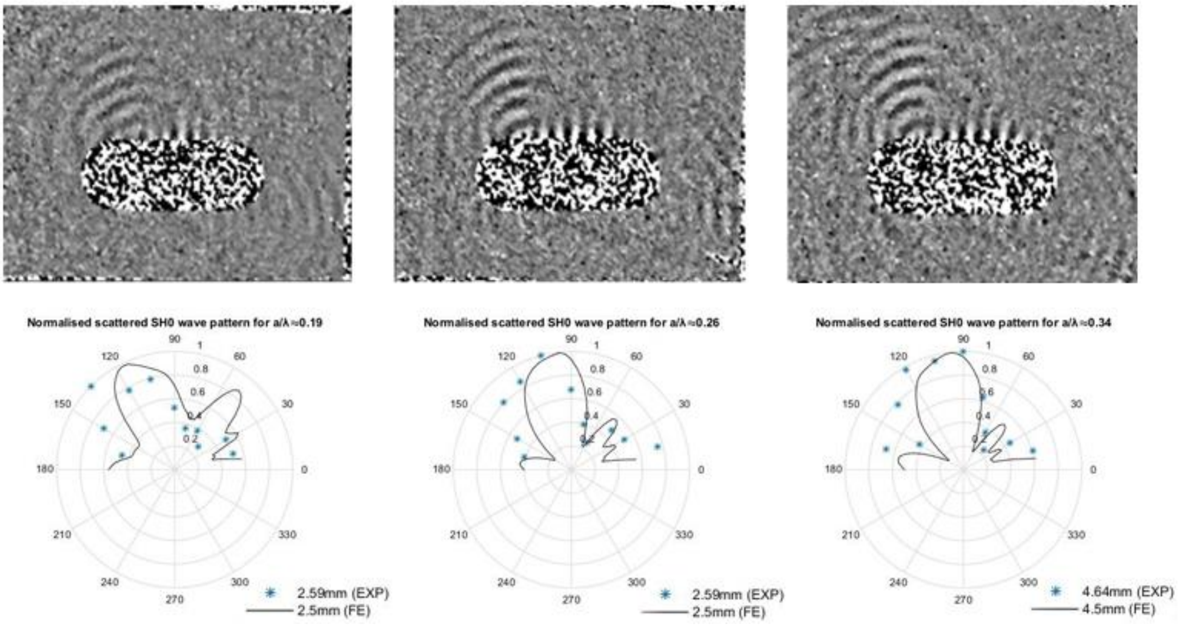

Figure 6.9: (TOP) Snapshot of experimental in the angular cylindrical component showing a dominant scattered SH0 wave field at time 70μs and (BOTTOM) Experimental and FE normalised scattered SH0 wave patterns for (a) a/λ≈0.19, (b) a/λ≈0.26 and (c) a/λ≈0.34

The S0 and SH0 scattered wave displacements have indicated increasing quadratic trend with respect to crack length until approximately *a/λ≈0.19* as shown in Fig. 6.10. As crack length increases beyond *a/λ>0.19*, the scattered wave displacement no longer increases with crack length. The forward and backward scattered edge wave maximum displacements are of similar magnitude and increases as a function of a^2 until *a/λ≈0.11*, refer to Fig. 6.11. The forward scattered edge wave becomes dominant as crack length increases. The experimental scattered wave displacement trends are similar to the computational wave displacement.

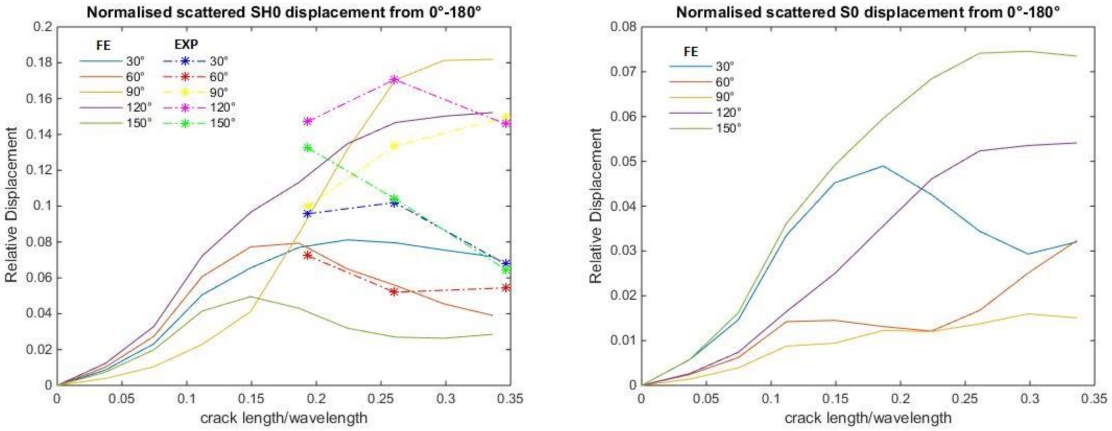

Figure 6.10: FE and experimental results: Normalised scattered SH0 wave displacement for various a/λ and (b) FE results: Normalised scattered S0 wave displacement for various a/λ with respect to the incident wave maximum displacement

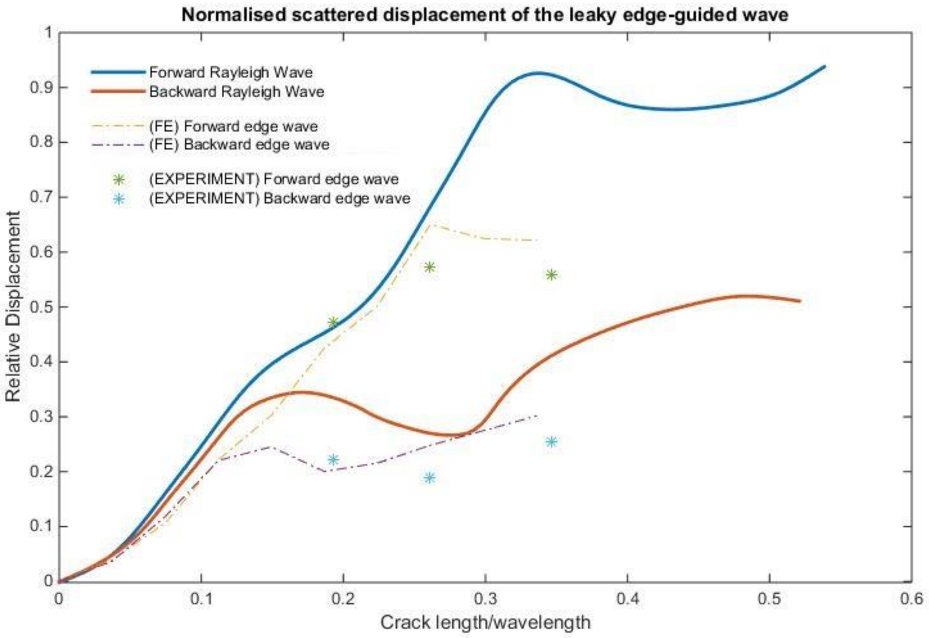

Figure 6.11: Experimental and computational comparison of the normalised scattered wave displacement of the edge-guided waves with respect to the incident wave maximum displacement, compared with analytical Rayleigh wave case[129]

6.6 Discussion

The FE results indicated that for relatively small crack *$a/\lambda \approx 0.19$*, the scattered S0 and SH0 wave patterns are independent of crack length, and the scattered wave displacement increases with crack length squared. This suggests that the scattered wave pattern due to a crack with length *$a/\lambda < 0.19$* is equivalent to the radiation field produced by a point source.

At approximately 0.2 depths to wavelength ratio, the Rayleigh wave retrograding particle motion and stress reverse. This is similar to symmetric edge-guided wave particle displacement and stress. Under *$a/\lambda < 0.19$*, the incident edge wave has a dominant normal stress component σ_{xx}, and minimal shear stress component σ_{xy}, as shown in Fig. 6.12.

The normal stress gives rise to a mode I crack opening whereas the shear stress gives rise to a mode II crack opening. For small, relative to incident wavelength, the mode I crack opening generate a scattered field that is the as that of a force doublet as shown in Fig. 6.13. This field is symmetrical with respect to θ = 90°. The mode II crack opening generates a scattered field that is the same as that for the force doublet. However, this field is asymmetric with respect to θ = 90°. Therefore, under the cut-off limit *$a/\lambda < 0.19$*, the point source representation consists of a primarily perpendicular forcing component for a small crack impinged with an incident symmetric edge-guided wave.

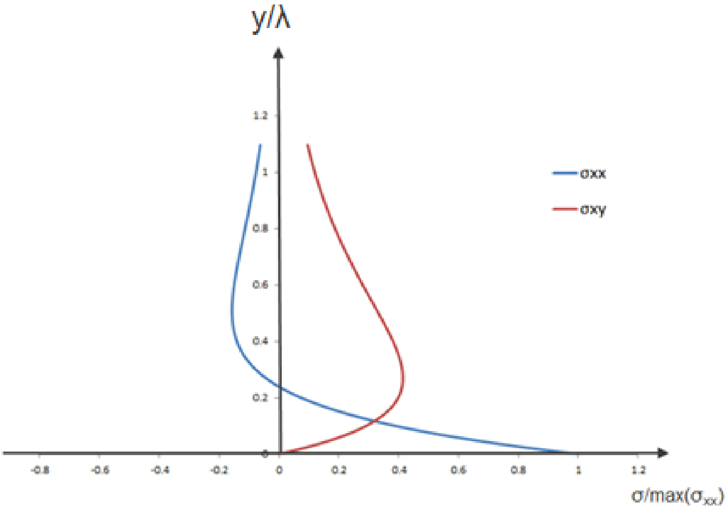

Figure 6.12: Stress variations associated with the incident edge wave, as a function of depth y from the edge

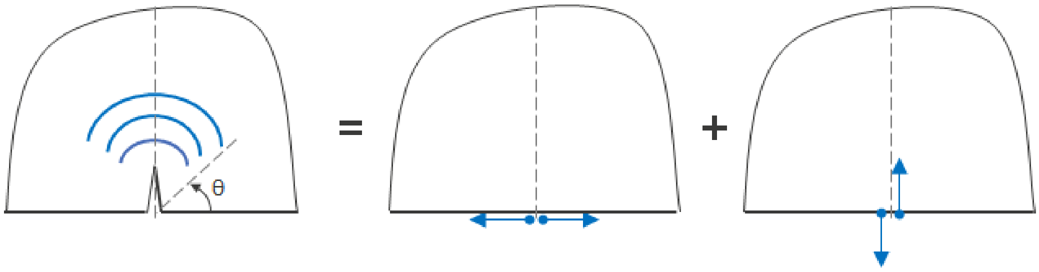

Figure 6.13: Scattered wave field representation due to the contribution of force-doublets associated with the mode I and mode II crack opening displacements

The scattered symmetric edge-guided amplitude has a similar trend to the analytical result of Mendelsohn et al. [129] for the corresponding plane strain problem as shown in Fig. 6.11. It can be seen that there is a reasonably good agreement for approximately $a/\lambda \approx 0.11$. The inaccuracy for larger crack size is because the FE and experimental results of the incident wave include some contribution from the bulk wave modes, whereas the incident wave for the analytical results is purely Rayleigh wave. Thus, this difference also applies for the scattered wave.

The results showed that the scattering amplitude appears to increase quadratically, which is in agreement with the theoretical expectation [119]. In a previous edge crack problem [164], a linear trend was observed for $0.07 < a/\lambda < 0.22$. The normal and shear stress variation within $0.07 < a/\lambda < 0.22$ (refer to Fig. 6.12) are the reason for the linear increase of scattering amplitude with crack size. In this hidden crack study, a smaller crack length $a/\lambda \approx 0.04$ was also investigated. Hence, a more obvious quadratic trend is observed for the values $a/\lambda < 0.19$.

Beyond the cut-off limit, the point source representation is no longer valid as the stress profiles and crack opening displacements vary rapidly, refer to Fig. 6.12. It can be seen that the normal stress is a maximum at the surface and decays to zero for $y/\lambda \approx 0.2$, and it is negative after that. On the other hand, the shear stress increases to a maximum at $y/\lambda \approx 0.2$. This maximum value is less than half the maximum value of the normal stress. These characteristic of the stress distribution serve to explain the feature of the asymmetry wave pattern results.

For $a/\lambda<0.19$, the normal stress is much larger than the shear stress, and accordingly the mode I contribution dominates the scattered wave field. This explains why the scattering pattern is symmetrical for small crack but becomes asymmetrical as crack length increases beyond this value due to the dominant contribution of shear stress, refer to Fig. 6.7 and 6.8.

Based on the principle of superposition [20], the scattered wave pattern can be produced by applying opposite baseline stress profile as a function of depth on the crack face for a crack size larger than $a/\lambda\approx0.19$.

For potential crack detection, it is observed that the scattered edge-guided wave coalescing with the scattered SH0 wave can redirect back to the location of the PZT. This suggest if edge-guided waves can be generated on the slots edge, which can also be done by mode conversion with incident symmetric wave modes, a hidden crack can be detected. The relationship scattered wave measurements; amplitude and pattern, and crack length can be exploited to characterised small crack. The scattering S0 wave is found to be significantly weaker than SH0 mode and was difficult to detect experimentally. It will be more beneficial to use all fundamental symmetric Lamb wave measurements to assess the crack, thus enhance techniques to detect the weaker S0 wave should further be investigated in future.

Smaller crack lengths were also investigated, however only experimental scattered wave measurements of crack lengths larger than 2.59mm were detected, hence was not reported in this study. This is a noteworthy limitation as it requires high performance transducers to detect and integrated into complex structures if implemented for SHM systems.

The possible crack characterisation strategy, based on these research findings, is explained as follows. The strategy consists of excitation of Lamb waves at different low frequencies to impinge with the hidden defect. A specific frequency is recorded when scattered wave pattern starts to be crack length dependent and scattered wave pattern stop varying quadratically with crack length. At that particular frequency, we can characterise the crack length based on point source equivalence cut-off limit i.e. $a/\lambda\approx0.19$. This can be repeated by using scattered S0, SH0 and edge-guided waves for confidence and accuracy. This particular strategy will involve accurately acquiring scattered wave patterns. The range of frequency for this strategy is determine by SH1 cut-off and minimum frequency needed so the full scattered wave trains can be measured. Based on this studies aluminium plate geometry, it is estimated that frequency range of 100 kHz to 500 kHz can be excited to predict crack size of approximately 1mm-7mm.

6.7 Conclusion

The findings of the previous hole and straight edge problems established the configuration and technique to detect a hard-to-inspect crack on a rectangular slot. The rectangular slot problem is an extension to the previous problems by combining the two previous problem unique features; curve and straight boundary, to form a complex application.

It has been shown that incident symmetric edge-guided waves can propagate along the rectangular slot boundary and impinge on small hidden crack. The ability for symmetric edge-guided waves to propagate on a curve boundary strongly depends on the diameter to incident wavelength ratio. Thus, the symmetric edge-guided wave serves as an essential incident propagating wave to detect and quantify cracks in hard-to-inspect location for SHM.

It has been shown in this study that for a small crack, in the range of $a/\lambda<0.19$, the scattering wave pattern is independent of crack size and the scattering amplitude increases quadratically with the crack size. In particular, the FE scattered wave directivity and scattered amplitude variation with crack size were investigated and are in good agreement with the experimental findings. The scattered wave amplitudes and patterns are very similar to the results found in the previous hole and straight edge investigations.

The study has shown a potential technique to propagate waves in the shadow zone and interaction with a small crack on a complex geometric shape. The scattered wave amplitudes and patterns vary with crack size and, thus, serve as a key measurement tool for crack detection and quantification. A strategy is reported by using sequence of multiple frequencies to determine when the scattered wave measurements cease to be a point source model. The research established a fundamental groundwork before tackling the inverse problem of detecting and quantifying hidden crack, based on the scattered wave field measurements.

Chapter 7

Summary

The aim of this thesis was to develop new knowledge that will enable the scattering Lamb wave measurements based structural health monitoring techniques to be successfully applied to complex and unitised components. Over the past few decades, Lamb wave propagation has been a very active field of research for non-destructive evaluation purposes in ideal and complex structures. Although the advanced unitised components significantly improve the aircraft performances, the conventional methods for structural health monitoring are not optimal for these components. Hence, the new manufacturing design and technology pose a significant challenge for SHM. Therefore, there is a lack of development in diagnosis methods to address the anticipated challenging problems of damage detection and quantification in hard-to-inspects in future structures.

The thesis presents a systematic study to investigate the pre-requisite problems of edge crack and hole before extending the research to a hard-to-inspect rectangular slot problem. The approach was to conduct the studies as a forward scatter problem of known crack geometry and location but an unknown scattering wave field. This will give comprehensive insight into the inverse problem of crack characterisation based on scattering wave measurements.

The experimental and computational investigations primarily explored the scattered wave pattern and amplitude variations due to varying crack length. The findings have shown for small crack size (relative to incident wavelength) the scattered wave field can be represented as the field produced by a point source. This was anticipated for Lamb wave scattering since it is already known that bulk wave at an infinitesimal small crack is equivalent to point source consisting of a particular combination of body-force doublets. The point source representation suggests that the scattered wave pattern is independent of crack size and the scattered wave amplitude increases proportionally to the integral of the crack opening displacement. The results indeed indicated that the Lamb wave scattering is of point source equivalence.

7.1 Scattering of symmetric waves by edge crack in isotropic plate

The first topic chapter involves a computational investigation to study the scattering of symmetric Lamb waves by edge crack on a straight boundary in an aluminium plate. The S0 and SH0 scattered wave patterns and amplitudes change as crack length and incident angle increase. The scattered wave pattern remains symmetrical and independent until $a/\lambda \approx 0.23$, where the pattern becomes asymmetrical. Stresses beyond this limit change rapidly resulting in asymmetrical wave pattern. Under this cut-off limit, the variation of stresses is simple and thus, the small crack is equivalent to a point source.

A second set of investigations has shown that by applying the opposite baseline stresses as traction on the crack faces, very similar wave patterns to the scattered wave fields due to the presence of a small crack are produced. The results indicated that for small cracks, a scattered wave field could be modelled as body-forces. The combination and strength of the body forces relate to the normal and shear baselines stresses. For example, at lower incident angle, the normal stress is much larger than the shear stress, and accordingly, the perpendicular forcing dominates the scattered field. It is noted that the normal stress corresponds to a mode I crack opening displacement and shear stress gives rise to a mode II crack opening displacement.

The first study established the fundamental understanding of scattering due to a small crack impinged by an incident symmetric Lamb wave. For a given cut-off limit, the existence of small crack can be modelled as point source approximation, whose body-force strength depends on the incident angle and crack length. Furthermore, the study indicated that scattered wave directivity and amplitude could be utilised to locate and quantify crack.

7.2 Scattering of edge-guided waves by edge crack in isotropic plate

The second topic chapter investigates the scattering of symmetric and antisymmetric edge-guided wave by edge crack on a straight boundary in an aluminium plate. Edge-guided waves travelling on straight boundary has no geometric decay over propagating distance, which makes them highly advantageous for SHM. Since the model configuration and force excitation are symmetrical with respect to the midplane of the plate, only symmetric waves mode scatter symmetric waves mode and only antisymmetric waves mode scatter antisymmetric waves mode.

For the incident symmetric edge-guided wave, the S0 and SH0 scattered wave patterns remain symmetrical and independent of crack length until $a/\lambda \approx 0.22$ before becoming asymmetrical. This asymmetrical feature is due to the additional contribution of the shear stress component. For the incident antisymmetric edge-guided wave, the A0 scattered wave pattern remains symmetrical throughout all investigated crack lengths. Both experimental and computational wave pattern and amplitude results have shown in good agreement.

At approximately 0.2 depths to wavelength ratio, the Rayleigh wave and edge-guided wave particle motions and stresses reverse direction. Under this cut-off limit, the symmetric edge-guided wave normal stress is dominant than the shear stress component and thus, the small crack is equivalent to a simple point source consisting primarily of perpendicular forcing components. Similarly, for the antisymmetric edge wave incidence, the small crack is equivalent to a point source consisting of a combination of body-forces, which corresponds to the mode II and mode III crack opening displacements. The shear stresses, σ_{xy} and σ_{xz}, give rise to mode II and mode III cracking, respectively.

For crack size $a/\lambda<0.22$, the scattered wave amplitudes for the symmetric edge guided wave have shown similar trends to the analytical Rayleigh wave scattering. Furthermore, the scattering amplitudes for the scattered wave into the plate are observed to increase linearly with the crack length a. For the antisymmetric edge-guided wave, the quadratic trend is more apparent within the range of

$a/\lambda<0.2$. The scattered wave fields by edge crack were investigated and had shown informative scattering behaviour for potential crack quantification. The point source model can be used for characterising small crack severity when propagating edge-guided waves for non-destructive wide area inspection.

7.3 Scattering of fundamental Lamb wave mode by an edge crack at circular hole in isotropic plate

The third topic chapter investigates the scattering of symmetric Lamb wave by an edge crack at a through-thickness circular hole in an aluminium plate. If the impinging wavelength is smaller than the hole diameter, edge waves can creep around the hole boundary. This circumferential edge wave also leaks energy to the medium as it propagates along a curved surface at a decay rate depending on diameter to wavelength ratio and Poisson’s ratio. The wave speed, which is similar to the Rayleigh wave speed, also depends on these parameters.

A scattered SH0 source-like wave guided by leaky edge portrayed a SH0 spiralling effect. The SH0 scattered wave has the appearance of a spiralling SH0. But later in the far-field, it resembles a point like source located at the crack tip. This spiralling effect is perceptible for a particular range of diameter to wavelength ratio.

An investigation was mode for an incident leaky circumferential edge-guided wave, which was excited to impinge on a small crack on the hole. This study is an extension to the edge crack on straight boundary problem with an impinging edge-guided wave. Thus, the results found in this investigation are similar to the previous edge crack problem.

The investigation proceeds to an incident symmetric Lamb wave mode and the geometry was configured such that the crack is in the shadow zone of the incident wave. The configuration of the model has limits such that the edge-guided wave cannot propagate along the curve boundary but instead attenuates to the medium. So, the primarily incident wave is the fundamental symmetric Lamb wave mode. However, the scattered waves produced by the incident symmetric wave mode are weaker than the one produced by edge-guided wave incidence. Furthermore, both experimental and computational results have shown good correlation with the scattered wave pattern and amplitude.

For both incident symmetric edge-guided wave and incident symmetric wave mode, the S0 and SH0 scattered wave pattern and amplitude results acquired are very similar. For $a/\lambda<0.10$, the scattered pattern is independent of crack size and the scattered wave amplitude are proportional to crack length squared a^2. This suggests that the scattered wave field can be represented as a point source, which consists of a particular combination of force doublets at the location of the hole boundary.

7.4 Scattering of edge-guided wave with a hidden crack on a rectangular curved slot in isotropic plate

The last topic chapter tackles on detection of a hidden crack on a rectangular curved slot in an aluminium plate. The previous findings aid the configuration to construct this hidden crack problem.

The symmetric edge-guided wave is excited on the bottom straight boundary of the rectangular slot. The incident wave leaks energy as it propagates around the curved surface and then impinges on a hidden crack on the top straight boundary of the slot. It is expected and shown that the scattering field of the crack will give similar results to the previous edge crack problem. Experimental results of the scattered wave pattern and amplitude are in good agreement with the findings from the computational investigation. Since a smaller crack size was investigated in this study, an obvious quadratic trend was perceivable for the scattered wave amplitude variation with crack dependence in the limit $a/\lambda<0.19$ for point source equivalence.

The guided edge waves can propagate to the hard-to-inspect areas and scattered waves to an accessible region where damage evaluation is possible. Furthermore, the scattered wave measurements can be utilised to characterise the defect in hard-to-inspect location for SHM.

7.5 Implication for crack detection and quantification

The research focuses on the forward scattering problem to determine the scattering phenomena, based on known crack geometry. The study primarily investigated scattered wave field with the crack length dependence for crack on the straight boundary and hole, as well as hidden cracks. The scattered wave field also depends on the incident angle of an impinging symmetric Lamb wave mode.

It is shown that for small crack size (relative to the incident wavelength) can be approximated as a point source for the Lamb wave case. The feature of scattered wave pattern independence and scattered wave amplitude increases as a function of crack length squared, suggesting a point source representation. Additionally, the edge-guided wave propagation has shown the ability to interact with hidden crack. This implies the effectiveness of edge-guided waves to direct waves to hard-to-inspect areas.

The study provided insights that both scattered wave pattern directivity and amplitude variation can be employed for non-destructive crack evaluation. Furthermore, the point source approximation of a small crack can be applied to characterise cracks before critical size is reached.

The fundamental sciences are explored on the scattering phenomena of a crack in this thesis. The thesis provided understanding in the area of Lamb wave and engineering knowledge to provide the basis for innovative inspection technique. Further studies can develop from this basis to address the other possible complexities of extending the use of Lamb wave scattering for structural integrity management.

7.6 Future work

This research showed findings on the most basic levels of configuration to allow future studies to develop. In this study, it was demonstrated that edge-guided waves were able to propagate around to the blind of sight location. It would be useful to analytically investigate the attenuation of leaky edge waves propagating around the curve surfaces for both symmetric and antisymmetric edge-guided waves.

An investigation on a partial-thickness edge crack is also worth studying. Due to the defect asymmetry about the midplane, it is expected that the modes will be coupled in the scattering process. One may also apply a more practical idea of generating a fatigue crack, or model a closed crack with different orientations for research.

Lamb waves have been studied in metallic structures, however, extensive studies have been increasingly published on Lamb wave propagation to characterise delamination in composite materials [169-172]. This is a resulted because the use of composite materials has significantly increased in the majority of industries, such as aerospace, automotive and civil due to their advantageous properties which include their light weight and high specific stiffness characteristic. However, most studies on Lamb wave in composite relies on computational simulation since analytical models of Lamb wave scattering at defect do not exist for composite. Thus, studies commonly investigate composite by first attempting and comparing to the equivalent isotropic model [169]. This research approach is to investigate simple analytical models for quantifying small defects in an isotropic plate which can be later incorporated into composites materials. It should be noted defect in a composite, such as delamination, is entirely different study and should be considered as a part of future work.

Although, in practice, the researchers favour a method in which the signals are simple as possible, studies on the second harmonic generation of elastic waves propagating in a nonlinear and dispersive medium have shown to be more effective in monitoring fatigue crack before crack initiation. Nonlinear Lamb wave propagation is subjected to considerable attention because the non-linear parameters are much more sensitive to defect than the linear parameters [173-176]. The acoustic nonlinearity parameter is an intrinsic material parameter which is obtained from the magnitude of the second order harmonic. In contrast to linear ultrasonic methods, nonlinear ultrasonic wave methods showed more potential to quantitatively assess early damage, especially for fatigue crack which is caused by plastic deformation. It is expected future studies will revolve around nonlinear wave propagating for effective crack detection due to nonlinear guided waves are much more suited for real crack. However, it is known that nonlinear Lamb wave propagations are significantly more difficult to solve analytically. There is a lack of a novel analytical solution in complex problems such as composite and non-linear wave propagation which needs to be addressed.

A multiple frequencies strategy, as explained previously, to determine the point source limit by using scattered wave measurement should be considered. An attempt on the inverse problem of crack characterisation will be a good extension to this study as well. The behaviour of the scattering wave field in this study focused only on the low frequency-thickness regime. Thus, further understanding of the scattering phenomena due to the presence of edge crack with higher order Lamb wave modes should be considered. More investigations are required to demonstrate whether the point source model can be included in high frequency excitation, nonlinear propagation, and composite materials.

Bibliography

1. Groneck, D. and Harmon, D., *Design Development of Unitized Titanium Structure.* Journal of Engineering for Gas Turbines and Power, 2002. **125**(1): p. 252-256.
2. Deo, R.B., Starnes Jr, J.H., and Holzwarth, R.C., *Low-cost composite materials and structures for aircraft applications.* 2003.
3. Renton, W.J., Olcott, D., Roeseler, W., Batzer, R., Baron, W., and Velicki, A., *Future of Flight Vehicle Structures (2000 to 2023).* Journal of Aircraft, 2004. **41**(5): p. 986-998.
4. Ware, L., Xidas, K., Clark, P., and Thomsen, M., *Development of an inspectable repair for A-10 fuel vent hole cracking in integrally stiffened wing skins and extruded spar caps*, in *USAF Aircraft Structural Integrity Conference*. 2005: Ogden, Utah.
5. Rose, J.L., *A baseline and vision of ultrasonic guided wave inspection potential.* Journal of pressure vessel technology, 2002. **124**(3): p. 273-282.
6. Fiedler, C.J., *Laser based ultrasound technology assessment.* Review of Progress in QNDE, 2001. **20**: p. 308-315.
7. Nagy, P., Blodgett, M., and Golis, M., *Weep hole inspection by circumferential creeping waves.* NDT & E international, 1994. **27**(3): p. 131-142.
8. Ihn, J.-B. and Chang, F.-K., *Pitch-catch Active Sensing Methods in Structural Health Monitoring for Aircraft Structures.* Structural Health Monitoring, 2008. **7**(1): p. 5-19.
9. Jeong-Beom, I. and Fu-Kuo, C., *Detection and monitoring of hidden fatigue crack growth using a built-in piezoelectric sensor/actuator network: I. Diagnostics.* Smart Materials and Structures, 2004. **13**(3): p. 609.
10. Achenbach, J.D., *Modeling for quantitative non-destructive evaluation.* Ultrasonics, 2002. **40**(1–8): p. 1-10.
11. Blodgett, M., Nagy, P.B., and Golis, M., *Weep hole inspection for radial fatigue cracks by circumferential creeping waves*, in *Review of Progress in Quantitative Nondestructive Evaluation*. 1995, Springer. p. 1963-1970.
12. Moreu De Leon, P., González-Prida Díaz, V., Barberá Martínez, L., and Crespo Márquez, A., *A practical method for the maintainability assessment in industrial devices using indicators and specific attributes.* Reliability Engineering & System Safety, 2012. **100**: p. 84-92.
13. Doherty, C. and Chiu, W., *Scattering of ultrasonic-guided waves for health monitoring of fuel weep holes.* Structural Health Monitoring, 2012. **11**(1): p. 27-42.
14. Doherty, C. and Chiu, W.K., *Guided wave mode selection for health monitoring of sub-surface hidden defects on fuel weep holes.* The Journal of the Acoustical Society of America, 2013. **133**(6): p. 3863-3874.
15. Doherty, C.C. and Chiu, W.K., *Three-dimensional finite element modelling of ultrasonic-guided wave scattering from fuel weep holes.* Structural Health Monitoring, 2012. **11**(4): p. 442-451.
16. Lamb, H., *On the Propagation of Tremors over the Surface of an Elastic Solid.* Philosophical Transactions of the Royal Society of London. Series A, Containing Papers of a Mathematical or Physical Character, 1904. **203**(359-371): p. 1-42.
17. Worlton, D.C., *Ultrasonic testing with Lamb waves. Non-Destructuive Testing*, 1957. **15**: p. 218-222.
18. Graff, K.F., *Wave Motion in Elastic Solids*. Dover Publications.
19. Achenbach, J.D., *Wave Propagation in Elastic Solids*. 1975, Amsterdam: Elsevier.
20. Auld, B.A., *Acoustic fields and waves in solids*. 1973: Рипол Классик.
21. Alleyne, D.N. and Cawley, P., *The interaction of Lamb waves with defects.* IEEE Transactions on Ultrasonics, Ferroelectrics, and Frequency Control, 1992. **39**(3): p. 381-397.
22. Giurgiutiu, V., *Structural Health Monitoring with Piezoelectric Wafer Active Sensors (2nd Edition)*. Elsevier.

23. Lee, B. and Staszewski, W., *Modelling of Lamb waves for damage detection in metallic structures: Part II. Wave interactions with damage.* Smart Materials and Structures, 2003. **12**(5): p. 815.
24. Staszewski, W.J., Lee, B.C., and Traynor, R., *Fatigue crack detection in metallic structures with Lamb waves and 3D laser vibrometry.* Measurement Science and Technology, 2007. **18**(3): p. 727.
25. Wilcox, P., Lowe, M., and Cawley, P. *Lamb and SH wave transducer arrays for the inspection of large areas of thick plates*. in *Review of Progress in Quantitative Nondestructive Evaluation: Volume 19*. 2000. AIP Publishing.
26. Su, Z.Q. and Ye, L., *Identification of damage using Lamb waves: From fundmentals to application*. Lecture Notes in Applied and Computational Mechanics. Vol. 48. 2009: Springer.
27. Aki, K. and Richards, P.G., *Quantitative seismology*. Vol. 1. 2002.
28. Diligent, O., Grahn, T., Boström, A., Cawley, P., and Lowe, M.J.S., *The low-frequency reflection and scattering of the S0 Lamb mode from a circular through-thickness hole in a plate: Finite Element, analytical and experimental studies.* The Journal of the Acoustical Society of America, 2002. **112**(6): p. 2589-2601.
29. Lowe, M.J.S., Cawley, P., Kao, J.-Y., and Diligent, O., *The low frequency reflection characteristics of the fundamental antisymmetric Lamb wave a0 from a rectangular notch in a plate.* The Journal of the Acoustical Society of America, 2002. **112**(6): p. 2612-2622.
30. Lowe, M.J.S. and Diligent, O., *Low-frequency reflection characteristics of the s0 Lamb wave from a rectangular notch in a plate.* The Journal of the Acoustical Society of America, 2002. **111**(1): p. 64-74.
31. Rajagopal, P. and Lowe, M.J.S., *Short range scattering of the fundamental shear horizontal guided wave mode normally incident at a through-thickness crack in an isotropic plate.* The Journal of the Acoustical Society of America, 2007. **122**(3): p. 1527-1538.
32. Ratassepp, M., Lowe, M.J.S., Cawley, P., and Klauson, A., *Scattering of the fundamental shear horizontal mode in a plate when incident at a through crack aligned in the propagation direction of the mode.* The Journal of the Acoustical Society of America, 2008. **124**(5): p. 2873-2882.
33. Pavlakovic, B., Lowe, M.J.S., Alleyne, D., and Cawley, P., eds. *Disperse: A General Purpose Program for Creating Dispersion Curves*. *Review of Progress in Quantitative Nondestructive Evaluation*, ed. D. Thompson and D. Chimenti. 1997, Springer: US. 185-192.
34. Ghosh, T., Kundu, T., and Karpur, P., *Efficient use of Lamb modes for detecting defects in large plates.* Ultrasonics, 1998. **36**(7): p. 791-801.
35. Ng, C.-T. and Veidt, M., *Scattering of the fundamental anti-symmetric Lamb wave at delaminations in composite laminates.* The Journal of the Acoustical Society of America, 2011. **129**(3): p. 1288-1296.
36. Veidt, M. and Ng, C.-T., *Influence of stacking sequence on scattering characteristics of the fundamental anti-symmetric Lamb wave at through holes in composite laminates.* The Journal of the Acoustical Society of America, 2011. **129**(3): p. 1280-1287.
37. Fromme, P., Wilcox, P., Lowe, M., and Cawley, P., *On the Scattering and Mode Conversion of the A0 Lamb Wave Mode at Circular Defects in Plates.* AIP Conference Proceedings, 2004. **700**(1): p. 142-149.
38. Niri, E.D. and Salamone, S., *A probabilistic framework for acoustic emission source localization in plate-like structures.* Smart Materials and Structures, 2012. **21**(3): p. 035009.
39. Wang, D., Ye, L., and Lu, Y., *A Probabilistic Diagnostic Algorithm for Identification of Multiple Notches Using Digital Damage Fingerprints (DDFs).* Journal of Intelligent Material Systems and Structures, 2009. **20**(12): p. 1439-1450.
40. Wang, D., Ye, L., Su, Z., Lu, Y., Li, F., and Meng, G., *Probabilistic Damage Identification Based on Correlation Analysis Using Guided Wave Signals in Aluminum Plates.* Structural Health Monitoring, 2010. **9**(2): p. 133-144.

41. Dongyue, G., Zhanjun, W., Lei, Y., and Yuebin, Z., *Guide waves-based multi-damage identification using a local probability-based diagnostic imaging method.* Smart Materials and Structures, 2016. **25**(4): p. 045009.
42. A., B., A., A., and N., K., *Reference-Free Damage Identification in Plate-Like Structures Using Lamb-Wave Propagation with Embedded Piezoelectric Sensors.* Journal of Aerospace Engineering, 2016. **29**(6).
43. Bagheri, A., Li, K., and Rizzo, P., *Reference-free damage detection by means of wavelet transform and empirical mode decomposition applied to Lamb waves.* Journal of Intelligent Material Systems and Structures, 2013. **24**(2): p. 194-208.
44. Kim, M.K., Kim, E.J., An, Y.K., Park, H.W., and Sohn, H., *Reference-free impedance-based crack detection in plates.* Journal of Sound and Vibration, 2011. **330**(24): p. 5949-5962.
45. Gangadharan, R., Murthy, C.R.L., Gopalakrishnan, S., and Bhat, M.R., *Time reversal technique for health monitoring of metallic structure using Lamb waves.* Ultrasonics, 2009. **49**(8): p. 696-705.
46. Ing, R.K. and Fink, M., *Time-reversed Lamb waves.* IEEE Transactions on Ultrasonics, Ferroelectrics, and Frequency Control, 1998. **45**(4): p. 1032-1043.
47. Park, H.W., Kim, S.B., and Sohn, H., *Understanding a time reversal process in Lamb wave propagation.* Wave Motion, 2009. **46**(7): p. 451-467.
48. Watkins, R. and Jha, R., *A modified time reversal method for Lamb wave based diagnostics of composite structures.* Mechanical Systems and Signal Processing, 2012. **31**: p. 345-354.
49. Jeong, H., Lee, J.-S., and Bae, S.-M., *Defect detection and localization in plates using a lamb wave time reversal technique.* International Journal of Precision Engineering and Manufacturing, 2011. **12**(3): p. 427-434.
50. Rajic, N. and Rosalie, S., *A feasibility study into the active smart patch concept for composite bonded repairs*. 2008, DTIC Document.
51. Lowe, M., Alleyne, D., and Cawley, P., *The mode conversion of a guided wave by a part-circumferential notch in a pipe.* Journal of Applied mechanics, 1998. **65**(3): p. 649-656.
52. Alleyne, D., Lowe, M., and Cawley, P., *The reflection of guided waves from circumferential notches in pipes.* Journal of Applied mechanics, 1998. **65**(3): p. 635-641.
53. Diligent, O., Lowe, M.J.S., Cawley, P., and Wilcox, P., *Reflection of the S0 Lamb Mode from a Part-Depth Circular Defect in a Plate, When the Incident Wave is Created by a Small Source.* AIP Conference Proceedings, 2003. **657**(1): p. 197-204.
54. Chang, Z. and Mal, A., *Scattering of Lamb waves from a rivet hole with edge cracks.* Mechanics of Materials, 1999. **31**(3): p. 197-204.
55. Fromme, P. and Sayir, M.B., *Measurement of the scattering of a Lamb wave by a through hole in a plate.* The Journal of the Acoustical Society of America, 2002. **111**(3): p. 1165-1170.
56. Grahn, T., *Lamb wave scattering from a circular partly through-thickness hole in a plate.* Wave Motion, 2003. **37**(1): p. 63-80.
57. Mallet, L., Lee, B.C., Staszewski, W.J., and Scarpa, F., *Structural health monitoring using scanning laser vibrometry: II. Lamb waves for damage detection.* Smart Materials and Structures, 2004. **13**(2): p. 261.
58. Lu, Y., Ye, L., Su, Z., and Yang, C., *Quantitative assessment of through-thickness crack size based on Lamb wave scattering in aluminium plates.* NDT & E International, 2008. **41**(1): p. 59-68.
59. Yu, L. and Leckey, C.A., *Lamb wave–based quantitative crack detection using a focusing array algorithm.* Journal of Intelligent Material Systems and Structures, 2013. **24**(9): p. 1138-1152.
60. Hongchen, M., Qiang, H., and Faxin, L., *Excitation and reception of pure shear horizontal waves by using face-shear d 24 mode piezoelectric wafers.* Smart Materials and Structures, 2016. **25**(11): p. 11LT01.
61. Wang, W., Zhou, W., Wang, P., Wang, C., and Li, H. *In-plane shear piezoelectric wafer active sensor phased arrays for structural health monitoring*. 2016.

62. Miao, H., Dong, S., and Li, F., *Excitation of fundamental shear horizontal wave by using face-shear (d36) piezoelectric ceramics.* Journal of Applied Physics, 2016. **119**(17): p. 174101.
63. Wang, W., Lynch, J.P., and Li, H., *Damage Detection in Metallic Plates using d36 Piezoelectric Phased Arrays.* composite structures. **9**: p. 12.
64. Seung, H.M., Park, C.I., and Kim, Y.Y., *An omnidirectional shear-horizontal guided wave EMAT for a metallic plate.* Ultrasonics, 2016. **69**: p. 58-66.
65. Ogilvy, J.A. and Temple, J.A.G., *Diffraction of elastic waves by cracks: application to time-of-flight inspection.* Ultrasonics, 1983. **21**(6): p. 259-269.
66. Scruby, C.B., Jones, K.R., and Antoniazzi, L., *Diffraction of elastic waves by defects in plates: Calculated arrival strengths for point force and thermoelastic sources of ultrasound.* Journal of Nondestructive Evaluation, 1986. **5**(3): p. 145-156.
67. McKeon, J.C.P. and Hinders, M.K., *Lamb wave scattering from a through hole.* Journal of Sound and Vibration, 1999. **224**(5): p. 843-862.
68. Wilcox, P., Lowe, M., and Cawley, P., *The effect of dispersion on long-range inspection using ultrasonic guided waves.* NDT & E International, 2001. **34**(1): p. 1-9.
69. Mira, M. and Gopalakrishnan, S., *Guided wave based structural health monitoring: A review.* Smart Materials and Structures, 2016. **25**(5): p. 053001.
70. Frank Pai, P., Deng, H., and Sundaresan, M.J., *Time-frequency characterization of lamb waves for material evaluation and damage inspection of plates.* Mechanical Systems and Signal Processing, 2015. **62–63**: p. 183-206.
71. Lingyu, Y., Cara, A.C.L., and Zhenhua, T., *Study on crack scattering in aluminum plates with Lamb wave frequency–wavenumber analysis.* Smart Materials and Structures, 2013. **22**(6): p. 065019.
72. Masserey, B. and Mazza, E., *Ultrasonic sizing of short surface cracks.* Ultrasonics, 2007. **46**(3): p. 195-204.
73. Tian, Z. and Yu, L., *Lamb wave frequency–wavenumber analysis and decomposition.* Journal of Intelligent Material Systems and Structures, 2014. **25**(9): p. 1107-1123.
74. J., S.W., C., L.B., and R., T., *Fatigue crack detection in metallic structures with Lamb waves and 3D laser vibrometry.* Measur. Sci. Technol., 2007. **18**: p. 727.
75. Leong, W.H., Staszewski, W.J., Lee, B.C., and Scarpa, F., *Structural health monitoring using scanning laser vibrometry: III. Lamb waves for fatigue crack detection.* Smart Materials and Structures, 2005. **14**(6): p. 1387.
76. Staszewski, W.J., Lee, B.C., Mallet, L., and Scarpa, F., *Structural health monitoring using scanning laser vibrometry: I. Lamb wave sensing.* Smart Materials and Structures, 2004. **13**(2): p. 251.
77. Love, A.E.H., *A treatise on the mathematical theory of elasticity*. 1944: In Dover Publications.
78. Viktorov, I.A., *Rayleigh and Lamb waves : physical theory and applications.* 1967, New York: Plenum Press.
79. Konenkov, Y.K., *A Rayleigh-type flexural wave.* Sov. Phys. Acoust, 1960. **6**: p. 122-123.
80. Norris, A.N., Krylov, V.V., and Abrahams, I.D., *Flexural edge waves and Comments on "A new bending wave solution for the classical plate equation" [J. Acoust. Soc. Am. 104, 2220–2222 (1998)]*. The Journal of the Acoustical Society of America, 2000. **107**(3): p. 1781-1784.
81. Norris, A.N. and Rebinsky, D.A., *Membrane and Flexural Waves on Thin Shells.* Journal of Vibration and Acoustics, 1994. **116**(4): p. 457-467.
82. Thurston, R.N. and Mckenna, J., *Flexural Acoustic Waves Along the Edge of a Plate.* IEEE Transactions on Sonics and Ultrasonics, 1974. **21**(4): p. 296-297.
83. Zakharov, D.D., *Analysis of the acoustical edge flexural mode in a plate using refined asymptotics.* The Journal of the Acoustical Society of America, 2004. **116**(2): p. 872-878.
84. Galinde, A., Koochakzadeh, M., and Abbaspour-Tamijani, A., *Elastic Modes of an Anisotropic Ridge Waveguide.* Advances in Acoustics and Vibration, 2012. **2012**.
85. Krushynska, A.A., *Flexural edge waves in semi-infinite elastic plates.* Journal of Sound and Vibration, 2011. **330**(9): p. 1964-1976.

86. Lagasse, P.E. and Oliner, A.A., *Acoustic flexural mode on a ridge of semi-infinite height.* Electronics Letters, 1976. **12**(1): p. 11-13.
87. Zernov, V. and Kaplunov, J. *Three-dimensional edge waves in plates*. in *Proceedings of the Royal Society of London A: Mathematical, Physical and Engineering Sciences*. 2008. The Royal Society.
88. Rulf, B., *Rayleigh Waves on Curved Surfaces.* The Journal of the Acoustical Society of America, 1969. **45**(2): p. 493-499.
89. Ewing, M., Jardetzky, W., and Press, F., *Elastic Waves in Layered Media*. McGraw-Hill Series in the Geological Science, ed. R.R. Shrocks. 1957, New York: McGraw-Hill Book Company.
90. Wang, X.-M. and Ying, C.F., *Scattering of Lamb waves by a circular cylinder.* The Journal of the Acoustical Society of America, 2001. **110**(4): p. 1752-1763.
91. Diligent, O. and Lowe, M.J.S., *Reflection of the s0 Lamb mode from a flat bottom circular hole.* The Journal of the Acoustical Society of America, 2005. **118**(5): p. 2869-2879.
92. Jin, F., Wang, Z., and Kishimoto, K., *Basic properties of Rayleigh surface wave propagation along curved surfaces.* International Journal of Engineering Science, 2005. **43**(3–4): p. 250-261.
93. Ying, C.F., Zhang, S.Y., and Shen, J.Z., *Scattering of ultrasound in solids as visualized by the photoelastic technique.* Journal of Nondestructive Evaluation, 1984. **4**(2): p. 65-73.
94. Hurst, D.P. and Temple, J.A.G., *Calculation of the velocity of creeping waves and their application to non-destructive testing.* International Journal of Pressure Vessels and Piping, 1982. **10**(6): p. 451-464.
95. Hassan, W. and Nagy, P.B., *Circumferential creeping waves around a fluid-filled cylindrical cavity in an elastic medium.* The Journal of the Acoustical Society of America, 1997. **101**(5): p. 2496-2503.
96. Aldrin, J.C. and Achenbach, J.D., *Model and methodology for crack detection on a cylindrical hole containing an elastic insert.* AIP Conference Proceedings, 2002. **615**(1): p. 181-188.
97. Hassan, W. and Nagy, P.B., *On the anomalously low attenuation of the leaky Rayleigh wave in a fluid-filled cylindrical cavity.* The Journal of the Acoustical Society of America, 1998. **104**(3): p. 1246-1255.
98. Vasudevan, N. and Mal, A.K., *Response of an Elastic Plate to Localized Transient Sources.* Journal of Applied Mechanics, 1985. **52**(2): p. 356-362.
99. Halabe, U.B. and Reynold, F., *Detection of flaws in structural members using spectral analysis of ultrasonic signals.* Nondestructive Testing and Evaluation, 1998. **15**(3-4): p. 215-236.
100. Halabe, U.B. and Franklin, R., *Fatigue Crack Detection in Metallic Members Using Spectral Analysis of Ultrasonic Rayleigh Waves*, in *Review of Progress in Quantitative Nondestructive Evaluation*. 1999, Springer. p. 1771-1777.
101. Gubernatis, J., *Elastic Wave Scattering Methods: Assessments and Suggestions*, in *Review of Progress in Quantitative Nondestructive Evaluation*. 1986, Springer. p. 21-33.
102. Kraut, E.A., *Review of Theories of Scattering of Elastic Waves by Cracks.* IEEE Transactions on Sonics and Ultrasonics, 1976. **23**(3): p. 162-167.
103. Thompson, D., *Purpose and progress of quantitative NDE.* 1979.
104. Ang, D. and Knopoff, L., *Diffraction of vector elastic waves by a finite crack.* Proceedings of the National Academy of Sciences, 1964. **52**(4): p. 1075-1081.
105. Ang, D. and Knopoff, L., *Diffraction of scalar elastic waves by a finite crack.* Proceedings of the National Academy of Sciences, 1964. **51**(4): p. 593-598.
106. Robertson, I.A. *Diffraction of a plane longitudinal wave by a penny-shaped crack.* in *Mathematical Proceedings of the Cambridge Philosophical Society*. 1967. Cambridge Univ Press.
107. Mal, A., *Dynamic stress intensity factor for a non-axisymmetric loading of the penny shaped crack.* International Journal of Engineering Science, 1968. **6**(12): p. 725-733.

108. Mal, A., *Dynamic stress intensity factor for an axisymmetric loading of the penny shaped crack.* International Journal of Engineering Science, 1968. **6**(11): p. 623-629.
109. Mal, A., *Interaction of elastic waves with a penny-shaped crack.* International Journal of Engineering Science, 1970. **8**(5): p. 381-388.
110. Mal, A.K., *Interaction of elastic waves with a Griffith crack.* International Journal of Engineering Science, 1970. **8**(9): p. 763-776.
111. Achenbach, J., Sotiropoulos, D., and Zhu, H., *Characterization of cracks from ultrasonic scattering data.* Journal of applied mechanics, 1987. **54**(4): p. 754-760.
112. Sotiropoulos, D. and Achenbach, J., *Crack characterization by an inverse scattering method.* International journal of solids and structures, 1988. **24**(2): p. 165-175.
113. Achenbach, J.D., Gautesen, A.K., and McMaken, H., *Ray Methods for Waves in Elastic Solids- With Applications to Scattering by Cracks*. 1982, Boston: Pitman.
114. Gubernatis, J. and Domany, E., *Rayleigh scattering of elastic waves from cracks.* Journal of Applied Physics, 1979. **50**(2): p. 818-824.
115. Sih, G.C. and Loeber, J.F., *Wave propagating in an elastic solid with a line discontinuity of finite crack.* Quarterly of Applied Mathematics, 1969. **27**(2): p. 193-213.
116. Sih, G.C. and Loeber, J.F., *Normal Compression and Radial Shear Waves Scattering at a Penny-Shaped Crack in an Elastic Solid.* The Journal of the Acoustical Society of America, 1969. **46**(3B): p. 711-721.
117. Teitel, S., *Determination of crack characteristics from the quasistatic approximation for the scattering of elastic waves.* Journal of Applied Physics, 1978. **49**(12): p. 5763-5767.
118. Rose, J. and Krumhansl, J., *A technique for determining flaw characteristics from ultrasonic scattering amplitudes.* 1979.
119. Resch, M., Shyne, J., Kino, G., and Nelson, D., *Long wavelength Rayleigh wave scattering from microscopic surface fatigue cracks.* Review of Progress in Quantitative Nondestructive Evaluation, 1982. **1**: p. 573-578.
120. Resch, M.T. and Nelson, D.V., *An ultrasonic method for measurement of size and opening behavior of small fatigue cracks,* in *Small-crack test methods*. 1992, ASTM International.
121. Babich, V. and Ivanov, M., *Long-wavelength approximation in scattering of elastic waves.* Journal of Soviet Mathematics, 1990. **50**(4): p. 1685-1693.
122. Visscher, W.M., *Elastic wave scattering by a surface-breaking or subsurface planar crack.* Journal of applied physics, 1984. **56**(3): p. 713-725.
123. Visscher, W.M., *Elastic wave scattering by a surface-breaking or subsurface planar crack. II. Three-dimensional geometry.* Journal of applied physics, 1985. **57**(5): p. 1538-1550.
124. Gubernatis, J., Krumhansl, J., and Thomson, R., *Interpretation of elastic-wave scattering theory for analysis and design of flaw-characterization experiments: The long-wavelength limit.* Journal of Applied Physics, 1979. **50**(5): p. 3338-3345.
125. Kohn, W. and Rice, J., *Scattering of long-wavelength elastic waves from localized defects in solids.* Journal of Applied Physics, 1979. **50**(5): p. 3346-3353.
126. Tittmann, B., Morris, W., and Richardson, J., *Elastic wave scattering at long wavelengths.* Applied Physics Letters, 1980. **36**(3): p. 199-201.
127. Cook, D. and Berthelot, Y., *Detection of small surface-breaking fatigue cracks in steel using scattering of Rayleigh waves.* NDT & E International, 2001. **34**(7): p. 483-492.
128. Hevin, G., Abraham, O., Pedersen, H., and Campillo, M., *Characterization of surface cracks with Rayleigh waves: a numerical model.* NDT & E International, 1998. **31**(4): p. 289-297.
129. Mendelsohn, D., Achenbach, J., and Keer, L., *Scattering of elastic waves by a surface-breaking crack.* Wave motion, 1980. **2**(3): p. 277-292.
130. Achenbach, J. and Brind, R., *Scattering of surface waves by a sub-surface crack.* Journal of sound and vibration, 1981. **76**(1): p. 43-56.
131. Achenbach, J.D., Keer, L.M., and Mendelsohn, D.A., *Elastodynamic Analysis of an Edge Crack.* Journal of Applied Mechanics, 1980. **47**(3): p. 551-556.

132. Harumi, K. and Uchida, M., *Computer simulation of ultrasonics and its applications.* Journal of nondestructive evaluation, 1990. **9**(2-3): p. 81-99.
133. Liu, S.-W., Sung, J.-C., and Chang, C.-S., *Transient scattering of SH waves by surface-breaking and sub-surface cracks.* International journal of solids and structures, 1997. **34**(30): p. 4019-4035.
134. Scandrett, C. and Achenbach, J., *Time-domain finite difference calculations for interaction of an ultrasonic wave with a surface-breaking crack.* Wave Motion, 1987. **9**(2): p. 171-190.
135. Stone, S., Ghosh, M., and Mal, A., *Diffraction of antiplane shear waves by an edge crack.* Journal of Applied Mechanics, 1980. **47**(2): p. 359-362.
136. Sesma, F.J.S. and Viveros, U.I., *Scattering and diffraction of SH waves by a finite crack: an analytical solution.* Geophysical Journal International, 2001. **145**(3): p. 749-758.
137. Gunawan, A. and Hirose, S., *Reflection of obliquely incident guided waves by an edge of a plate.* Materials transactions, 2007. **48**(6): p. 1236-1243.
138. Burridge, R. and Knopoff, L., *Body force equivalents for seismic dislocations.* Bulletin of the Seismological Society of America, 1964. **54**(6A): p. 1875-1888.
139. Lee, J. and Mal, A.K., *A volume integral equation technique for multiple scattering problems in elastodynamics.* Applied Mathematics and Computation, 1995. **67**(1): p. 135-159.
140. Mal, A., *Rayleigh waves from a moving thrust fault.* Bulletin of the Seismological Society of America, 1972. **62**(3): p. 751-762.
141. Zhang, H. and Achenbach, J.D., *Use of equivalent body forces for acoustic emission from a crack in a plate.* Mechanics Research Communications, 2015. **68**: p. 105-108.
142. Lee, B. and Staszewski, W., *Modelling of Lamb waves for damage detection in metallic structures: Part I. Wave propagation.* Smart Materials and Structures, 2003. **12**(5): p. 804.
143. Willberg, C., Duczek, S., Vivar-Perez, J.M., and Ahmad, Z.A.B., *Simulation Methods for Guided Wave-Based Structural Health Monitoring: A Review.* Applied Mechanics Reviews, 2015. **67**(1): p. 010803-010803-20.
144. Marburg, S., *Discretization requirements: How many elements per wavelength are necessary?*, in *Computational Acoustics of Noise Propagation in Fluids-Finite and Boundary Element Methods*. 2008, Springer. p. 309-332.
145. Mace, B.R. and Manconi, E., *Modelling wave propagation in two-dimensional structures using finite element analysis.* Journal of Sound and Vibration, 2008. **318**(4): p. 884-902.
146. Moser, F., Jacobs, L.J., and Qu, J., *Modeling elastic wave propagation in waveguides with the finite element method.* Ndt & E International, 1999. **32**(4): p. 225-234.
147. Alleyne, D. and Cawley, P., *A two-dimensional Fourier transform method for the measurement of propagating multimode signals.* The Journal of the Acoustical Society of America, 1991. **89**(3): p. 1159-1168.
148. Bathe, K.-J., *Finite element procedures*. 2006: Klaus-Jurgen Bathe.
149. *LS-DYNA Support.*
150. Dokainish, M. and Subbaraj, K., *A survey of direct time-integration methods in computational structural dynamics—I. Explicit methods.* Computers & Structures, 1989. **32**(6): p. 1371-1386.
151. Plešek, J., Kolman, R., and Gabriel, D., *Estimation of the critical time step for explicit integration.* Engineering Mechanics, 2012: p. 292.
152. Nagy, P.B., Simonetti, F., and Instanes, G., *Corrosion and erosion monitoring in plates and pipes using constant group velocity Lamb wave inspection.* Ultrasonics, 2014. **54**(7): p. 1832-1841.
153. Hora, P. and Červená, O., *Determination of Lamb wave dispersion curves by means of Fourier transform.* 2012.
154. Ge, L., Wang, X., and Jin, C., *Numerical modeling of PZT-induced Lamb wave-based crack detection in plate-like structures.* Wave Motion, 2014. **51**(6): p. 867-885.
155. Luyao, G., Xinwei, W., and Feng, W., *Accurate modeling of PZT-induced Lamb wave propagation in structures by using a novel spectral finite element method.* Smart Materials and Structures, 2014. **23**(9): p. 095018.

156. Moreau, L. and Castaings, M., *The use of an orthogonality relation for reducing the size of finite element models for 3D guided waves scattering problems.* Ultrasonics, 2008. **48**(5): p. 357-366.

157. Rose, J.L., *Ultrasonic waves in solid media*. 2004: Cambridge university press.

158. Owen, D.R.J. and Fawkes, A., *Engineering fracture mechanics: numerical methods and applications.* Pineridge Press Ltd, 91 West Cross Lane, West Cross, Swansea, UK, 1983. 305, 1983.

159. Aliabadi, M., *The boundary element method: Applications in solids and structures, vol. 2.* Chicester: Wiley, 2002.

160. Chopra, I., *Review of State of Art of Smart Structures and Integrated Systems.* AIAA Journal, 2002. **40**(11): p. 2145-2187.

161. Lanzara, G., Yoon, Y., Kim, Y., and Chang, F.-K., *Influence of interface degradation on the performance of piezoelectric actuators.* Journal of Intelligent Material Systems and Structures, 2009. **20**(14): p. 1699-1710.

162. Kusaka, T. and Qing, X.P., *Characterization of loading effects on the performance of smart layer embedded or surface-mounted on structures.* Structural Health Monitoring 2003: From Diagnostics & Prognostics to Structural Health Management: Proceedings of the 4th International Workshop on Structural Health Monitoring, 2003.

163. Qing, X.P., Beard, S.J., Kumar, A., Sullivan, K., Aguilar, R., Merchant, M., and Taniguchi, M., *The performance of a piezoelectric-sensor-based SHM system under a combined cryogenic temperature and vibration environment.* Smart Materials and Structures, 2008. **17**(5): p. 055010.

164. VIEN, B., Nadarajah, N., ROSE, L., and CHIU, W., *Scattering of the Symmetrical Edge-guided Wave by a Small Edge Crack in an Isotropic Plate.* Structural Health Monitoring 2015, 2015.

165. Vien, B.S., Nadarajah, N., Chiu, W.K., and Rose, L. *Scattering of the Fundamental Symmetric Wave Mode Incident at a Defect on the Blind Side of a Weep Hole in an Isotropic Plate*. in *Advanced Materials Research*. 2014. Trans Tech Publ.

166. Vien, B.S., Chiu, W.K., and Rose, L.F., *An experimental study on the scattering of edge guided waves by a small edge crack in an isotropic plate*, in *EWSHM 2016*. 2016: Spain, Bilbao.

167. Vien, B.S., Nadarajah, N., Chiu, W.K., and Rose, L.F., *Scattering of the Fundamental Symmetrical Lamb Wave Mode by a Small Edge Crack in an Isotropic Plate.* JMEA, 2015. **5**(4): p. 210-219.

168. Schröder, C.T. and Jr., W.R.S., *On the complex conjugate roots of the Rayleigh equation: The leaky surface wave.* The Journal of the Acoustical Society of America, 2001. **110**(6): p. 2867-2877.

169. Ng, C.T., Veidt, M., Rose, L.R.F., and Wang, C.H., *Analytical and finite element prediction of Lamb wave scattering at delaminations in quasi-isotropic composite laminates.* Journal of Sound and Vibration, 2012. **331**(22): p. 4870-4883.

170. Qiu, L., Liu, B., Yuan, S., and Su, Z., *Impact imaging of aircraft composite structure based on a model-independent spatial-wavenumber filter.* Ultrasonics, 2016. **64**: p. 10-24.

171. Sause, M.G.R., Hamstad, M.A., and Horn, S., *Finite element modeling of lamb wave propagation in anisotropic hybrid materials.* Composites Part B: Engineering, 2013. **53**: p. 249-257.

172. Tian, Z., Yu, L., and Leckey, C., *Delamination detection and quantification on laminated composite structures with Lamb waves and wavenumber analysis.* Journal of Intelligent Material Systems and Structures, 2015. **26**(13): p. 1723-1738.

173. Cantrell, J.H. and Yost, W.T., *Nonlinear ultrasonic characterization of fatigue microstructures.* International Journal of Fatigue, 2001. **23, 1**: p. 487-490.

174. Christoph, P., Jin-Yeon, K., Jianmin, Q., and Laurence, J.J., *Evaluation of fatigue damage using nonlinear guided waves.* Smart Materials and Structures, 2009. **18**(3): p. 035003.

175. Rauter, N. and Lammering, R., *Impact Damage Detection in Composite Structures Considering Nonlinear Lamb Wave Propagation.* Mechanics of Advanced Materials and Structures, 2015. **22**(1-2): p. 44-51.

176. Zuo, P., Zhou, Y., and Fan, Z., *Numerical and experimental investigation of nonlinear ultrasonic Lamb waves at low frequency.* Applied Physics Letters, 2016. **109**(2): p. 021902.
177. Masserey, B. and Fromme, P., *On the reflection of coupled Rayleigh-like waves at surface defects in plates.* The Journal of the Acoustical Society of America, 2008. **123**(1): p. 88-98.
178. Guo, N. and Cawley, P., *The interaction of Lamb waves with delaminations in composite laminates.* The Journal of the Acoustical Society of America, 1993. **94**(4): p. 2240-2246.

APPENDIX A

A.1 Elastic waves in infinite medium

The governing equation of motion (d'Alembert's principle) for a homogeneous isotropic elastic solid, in Cartesian tensor notation is given by:

$$\tau_{ij,j} + \rho f_i = \rho \ddot{u}_i \tag{A1.1.1}$$

where, τ_{ij} is the stress tensor; symmetric, at a point u_i is the displacement vector of a point. The density is ρ and body force per unit mass acting on the medium is f_i.

Constitutive equation of stress tensor and strain tensor relationship is

$$\sigma_{ij} = c_{ijkl}\epsilon_{kl} \tag{A1.1.2}$$

Where, c_{ijkl} is stiffness matrix.

For an isotropic material, the stiffness matrix is expressed as

$$c_{ijkl} = \lambda\delta_{ij}\delta_{kl} + \mu(\delta_{ik}\delta_{jl} + \delta_{il}\delta_{jk}) \tag{A1.1.3}$$

The elastic constants for material is λ and Lamé constant is μ.

Where, δ_{ij} is the Kronecker delta tensor, $\delta_{ij} = \begin{cases} 1 & \text{if i = j} \\ 0 & \text{if i} \neq \text{j} \end{cases}$

Furthermore, the relationships are

$$\sigma_{ij} = \lambda\epsilon_{kk}\delta_{ij} + 2\mu\epsilon_{ij}$$

$$\epsilon_{ij} = \frac{1}{2}\left(u_{i,j} + u_{j,i}\right)$$

$$\omega_{ij} = \frac{1}{2}(u_{i,j} - u_{j,i}) \qquad \text{(A1.1.4)}$$

Here, the strain tensor is ε_{ij} and the rotational tensor is ω_{ij}.

By substituting into the stress-strain relations Eqn. (A1.1.3) and (A1.1.4) into the equation of motion Eqn. (A1.1.1), this reconfigure to the Navier's equation,

$$(\lambda + \mu)u_{j,ji} + \mu u_{i,ji} + \rho f_i = \rho\ddot{u}_i$$

And in vector form,

$$(\lambda + \mu)\nabla(\nabla.\mathbf{u}) + \mu\nabla^2\boldsymbol{u} + \rho\boldsymbol{f} = \rho\ddot{\boldsymbol{u}} \qquad \text{(A1.1.5)}$$

An approach to uncouple the equation is by considering *Helmholtz Decomposition Theorem*. The above equation (A1.1.5) can be express in terms of scalar and vector potentials.

$$\boldsymbol{u} = \nabla\varphi + \nabla \times \psi \;\text{ given } \nabla.\psi = 0$$

$$u_i = \varphi_{i,i} + \psi_{k,j} - \psi_{j,k} \qquad \text{(A1.1.6)}$$

Again, we know,

$$\boldsymbol{f} = \nabla \mathrm{f} + \nabla \times \Pi \text{ given } \nabla.\Pi = 0 \qquad \text{(A1.1.7)}$$

Considering no body forces f and $\Pi = 0$, Helmholtz decomposition of $\boldsymbol{u}$ can provide the scalar and vector wave equations of velocity c_1 and c_2.

$$(\lambda + \mu)\nabla\nabla.(\nabla\varphi + \nabla \times \psi) + \mu\nabla^2(\nabla\varphi + \nabla \times \psi) = \rho\frac{\partial^2}{\partial t^2}\left(\nabla\varphi + \ddot{\nabla} \times \psi\right) \tag{A1.1.8}$$

Since $\nabla.\nabla\varphi = \nabla^2\varphi$ and $\nabla.\nabla \times \psi = 0$

$$\nabla((\lambda + 2\mu)\nabla^2\varphi - \rho\frac{\partial^2}{\partial t^2}\varphi) + \nabla \times (\mu\nabla^2\psi - \rho\frac{\partial^2}{\partial t^2}\psi) = 0 \tag{A1.1.9}$$

Considering the scalar field component, we have,

$$\nabla^2\varphi = \frac{1}{c_1^2}\frac{\partial^2\varphi}{\partial t^2} \tag{A1.1.10}$$

And for the vector field component,

$$\nabla^2\psi = \frac{1}{c_2^2}\frac{\partial^2\psi}{\partial t^2} \tag{A1.1.11}$$

Further investigation will lead to the wave equation of dilatational and distortional waves. The propagating wave velocities are, respectively,

$$c_1 = \sqrt{\frac{(\lambda+2\mu)}{\rho}} = \sqrt{\frac{E(1-v)}{\rho(1+v)(1-2v)}} \quad and \quad c_2 = \sqrt{\frac{\mu}{\rho}} \tag{A1.1.12}$$

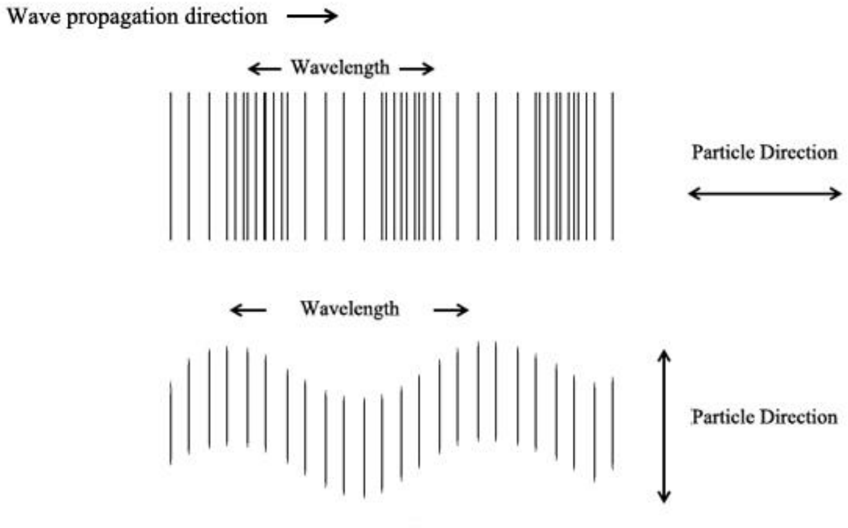

Figure A.1: (TOP) Longitudinal wave and (BOTTOM) Transverse wave and their particle oscillation direction

c_1 is the wave speed of dilatational waves, which are also called longitudinal, volumetric, irrotational and primary (P) waves. c_2 is the wave speed of rotational waves, which are also called transverse, shear, equi-voluminal, distortional and secondary (SV) waves, as illustrated in Fig. A.1. Given the condition $0 \leq \ v \leq \frac{1}{2}$, longitudinal velocity is always greater than shear velocity $c_1 > c_2$.

The ratio of the two wave speeds, k, is expressed as

$$k = \frac{c_1}{c_2} = \sqrt{\frac{(\lambda+2\mu)}{\mu}} = \sqrt{\frac{2-2v}{1-2v}} \tag{A1.1.13}$$

A.2 Elastic waves in semi-infinite medium

Considering semi-infinite medium, where the motion is invariant with respect to z direction, the problem can be resolved into plane strain and anti-plane strain components. By applying boundary conditions and considering Snell's law, the possible mode conversion from a single wave incident can be deduced. Furthermore, the relationship between the ratio of longitudinal speed and transverse speed is only depended on the Poisson's ratio and the relationship depends on only the angle of incident and Poisson's Ratio as well.

In a situation where the motion is invariant with respect to z direction, if the wave normal is in vertical in the plane, the governing equations become:

$$u_x = \varphi_x + \psi_{z,y}$$

$$u_y = \varphi_y - \psi_{z,x}$$

$$u_z = -\psi_{x,y} + \psi_{y,x}$$

$$\psi_{x,x} + \psi_{y,y} = 0$$

$$\nabla^2 \varphi = \frac{1}{c_1^2}\frac{\partial^2 \varphi}{\partial t^2}$$

$$\nabla^2 \psi = \frac{1}{c_2^2}\frac{\partial^2 \psi}{\partial t^2} \tag{A1.2.1}$$

The stress-displacement expression are given by,

$$\tau_{xx} = (\lambda + 2\mu)(u_{x,x} + u_{y,y}) - 2\mu u_{y,y}$$

$$\tau_{yy} = (\lambda + 2\mu)(u_{x,x} + u_{y,y}) - 2\mu u_{x,x}$$

$$\tau_{zz} = \frac{\lambda}{2(\lambda + \mu)}(\tau_{xx} + \tau_{yy}) = \lambda(u_{x,x} + u_{y,y})$$

$$\tau_{xy} = \mu(u_{x,y} + u_{y,x})$$

$$\tau_{yz} = \mu u_{z,y}$$

$$\tau_{xz} = \mu u_{z,x} \tag{A1.2.2}$$

The above stress equations are expressed in terms of potential as:

$$\tau_{xx} = (\lambda + 2\mu)\left(\varphi_{xx} + \varphi_{yy}\right) - 2\mu\left(\varphi_{yy} - \psi_{z,yx}\right)$$

$$\tau_{yy} = (\lambda + 2\mu)\left(\varphi_{xx} + \varphi_{yy}\right) - 2\mu\left(\varphi_{xx} + \psi_{z,xy}\right)$$

$$\tau_{zz} = \lambda\left(\varphi_{xx} + \varphi_{yy}\right)$$

$$\tau_{xy} = \mu\left(2\varphi_{xy} + \psi_{z,yy} - \psi_{z,xx}\right)$$

$$\tau_{yz} = \mu(\psi_{y,xy} - \psi_{x,yy})$$

$$\tau_{xz} = \mu(\psi_{y,xx} - \psi_{x,xy}) \qquad \text{(A1.2.3)}$$

The displacement components u_x and u_y are depended on φ and ψ_z, since $\tau_{xx}, \tau_{yy}\ and\ \tau_{zz}$ are depended only on these components, they are also dependent on φ and ψ_z. Component u_z is depended only on ψ_x and ψ_y and so does τ_{yz} and τ_{xz}. Hence the problem can be dealt as two uncoupled wave motions equation. The problem can be resolve into two parts; plane strain and shear horizontal (SH; anti-plane).

The boundary conditions are given by,

$$\tau_{yy} = \tau_{xy} = \tau_{yz} = 0 \text{ at } y = 0 \qquad \text{(A1.2.4)}$$

In plane strain motion, the conditions are:

$$u_z = \frac{\partial}{\partial z} = 0$$

$$u_y\ and\ u_x \neq 0 \qquad \tau_{yy} = \tau_{xy} = 0 \qquad \text{(A1.2.5)}$$

And in SH wave motion, the conditions are:

$$u_x = u_y = \frac{\partial}{\partial z} = 0$$

$$u_z \neq 0 \ \tau_{yz} = 0 \text{ at } y = 0 \tag{A1.2.6}$$

Considering the solution of plane strain motion,

$$\varphi = f(y)e^{i(\xi x - \omega t)}$$

$$\psi_z = h_z(y)e^{i(\xi x - \omega t)} \tag{A1.2.7}$$

Substituting the potential wave equation,

$$\frac{d^2 f}{dy^2} + \alpha^2 f = 0$$

$$\frac{d^2 h_z}{dy^2} + \beta^2 h_z = 0 \tag{A1.2.8}$$

Where,

$$\alpha^2 = \frac{\omega^2}{c_1^2} - \xi^2$$

$$\beta^2 = \frac{\omega^2}{c_2^2} - \zeta^2 \tag{A1.2.9}$$

Thus the solution for the plane wave,

$$\varphi = A_1 e^{i(\xi x - \alpha y - \omega t)} + A_2 e^{i(\xi x + \alpha y - \omega t)}$$

$$\psi_z = B_1 e^{i(\zeta x - \beta y - \omega t)} + B_2 e^{i(\zeta x + \beta y - \omega t)} \tag{A1.2.10}$$

It may be written as,

$$\xi = \gamma_1 \sin\theta_1, \qquad \alpha = \gamma_1 \cos\theta_1$$

$$\zeta = \gamma_2 \sin\theta_2, \qquad \beta = \gamma_2 \cos\theta_1 \tag{A1.2.11}$$

θ_1 and $\theta_2$between the normal of the boundary and the wave normal of the longitudinal and transverse waves. γ_1 and γ_2 are the wave numbers along the respective waves.

$$\varphi = A_1 e^{i(\gamma_1 \sin\theta_1 x - \gamma_1 \cos\theta_1 y - \gamma_1 c_1 t)} + A_2 e^{i(\gamma_1 \sin\theta_1 x + \gamma_1 \cos\theta_1 y - \gamma_1 c_1 t)}$$

$$\psi_z = B_1 e^{i(\gamma_2 \sin\theta_2 x - \gamma_2 \cos\theta_1 y - \gamma_2 c_2 t)} + B_2 e^{i(\gamma_2 \sin\theta_2 x + \gamma_2 \cos\theta_1 y - \gamma_2 c_2 t)} \tag{A1.2.12}$$

Now, applying the boundary conditions for plane strain wave, $\tau_{yy} = \tau_{xy} = 0$ at $y = 0$, we get,

$$\left(\tau_{yy}\right)_{y=0} = \gamma_1^2 (2\sin\theta_1 - k^2)(A_1 + A_2) e^{i\gamma_1(\sin\theta_1 x - c_1 t)} - \gamma_2^2 \sin 2\theta_2 \,(B_1 - B_2) e^{i\gamma_2(\sin\theta_2 x - c_2 t)} = 0$$

$$\left(\tau_{xy}\right)_{y=0} = \gamma_1^2 \sin 2\theta_1 \,(A_1 - A_2) e^{i\gamma_1(\sin\theta_1 x - c_1 t)} - \gamma_2^2 \cos 2\theta_2 \,(B_1 + B_2) e^{i\gamma_2(\sin\theta_2 x - c_2 t)} = 0$$

$$\tag{A1.2.13}$$

In optical and acoustic waves, waves are reflected and transmitted as it encounters a boundary between two media as illustrated in Fig. A.2. For the case of elastic waves, wave energy is reflected and transmitted from and across the boundary, respectively. The elastic wave will also undergo mode conversion as it encounters a boundary. An incident wave is converted into two waves on reflection; longitudinal and transverse wave. In addition, surface waves may also propagate in a semi-infinite media.

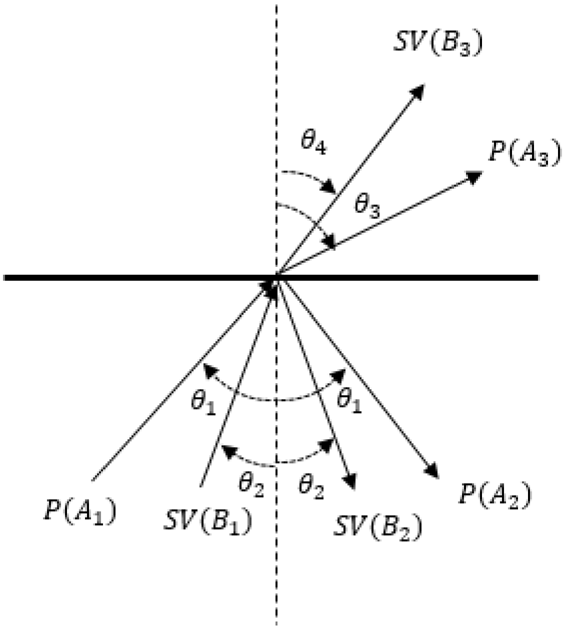

Figure A.2: Reflection, transmission and mode conversion of incident longitude wave at an angle

When incident wave propagates and meets an interface at an angle normal to the boundary, the angle of reflection and oblique transmission (refraction) are determined by Snell's Law. This is illustrated in Fig. A.2, where the subscript 1 denotes incident; subscript 2 denotes reflected wave; and subscript 3 denotes transmitted wave.

$$\frac{\sin(\theta_1)}{V_{P(A_1)}} = \frac{\sin(\theta_2)}{V_{SV(B_2)}} = \frac{\sin(\theta_3)}{V_{P(A_3)}} = \frac{\sin(\theta_4)}{V_{SV(B_3)}} \tag{A1.2.14}$$

Furthermore, since

$$\frac{\sin\theta_1}{\sin\theta_2} = \frac{c_1}{c_2} = \frac{\gamma_2}{\gamma_1} = k \tag{A1.2.15}$$

The boundary stress condition equations (A1.2.5) reduce to:

$$\left(\tau_{yy}\right)_{y=0} = \gamma_1^2(2\sin\theta_1 - k^2)(A_1 + A_2) - \gamma_2^2 \sin 2\theta_2\,(B_1 - B_2) = 0$$

$$\left(\tau_{xy}\right)_{y=0} = \gamma_1^2 \sin 2\theta_1\,(A_1 - A_2) - \gamma_2^2 \cos 2\theta_2\,(B_1 + B_2) = 0 \tag{A1.2.16}$$

These equations govern the reflection of plane waves in half space.

i) Reflection of SH waves

The reflection of the plane shear horizontal (SH) waves is an anti-plane strain problem. SH-wave is the simplest wave mode to study due to the one directional vector restriction and no mode conversation. The SH-wave upon reflection must satisfy the boundary condition of traction free surface with no out-of-plane displacement at the surface.

Consider the solutions in this case

$$\psi_x = h_x(y)e^{i(\xi x-\omega t)}$$

$$\psi_y = h_y(y)e^{i(\xi x-\omega t)} \tag{A1.2.17}$$

Hence through substitution to potential wave equations

$$\frac{d^2h_x}{dy^2} + \eta^2 h_x = 0$$

$$\frac{d^2h_y}{dy^2} + \eta^2 h_y = 0 \tag{A1.2.18}$$

Where,

$$\eta^2 = \frac{\omega^2}{c_2^2} - \xi^2 \tag{A1.2.19}$$

Hence the solutions

$$\psi_x = C_1 e^{i(\xi x-\eta y-\omega t)} + C_2 e^{i(\xi x+\eta y-\omega t)}$$

$$\psi_y = D_1 e^{i(\xi x-\eta y-\omega t)} + D_2 e^{i(\xi x+\eta y-\omega t)} \tag{A1.2.20}$$

Apply this equation to the divergence of vector potential

$$i\xi\left(C_1 e^{-i\eta y} + C_2 e^{i\eta y}\right) + i\eta\left(-D_1 e^{-i\eta y} + D_2 e^{-i\eta y}\right) = 0$$

$$\left(\xi C_1 e^{-i\eta y} - \eta D_1 e^{-i\eta y}\right) + \left(\xi C_2 e^{i\eta y} + \eta D_2 e^{-i\eta y}\right) = 0 \qquad \text{(A1.2.21)}$$

Therefore,

$$D_1 = \frac{\xi}{\eta} C_1$$

$$D_2 = -\frac{\xi}{\eta} C_2 \qquad \text{(A1.2.22)}$$

So the solutions simplify to,

$$\psi_x = C_1 e^{i(\xi x - \eta y - \omega t)} + C_2 e^{i(\xi x + \eta y - \omega t)}$$

$$\psi_y = \frac{\xi}{\eta} C_1 e^{i(\xi x - \eta y - \omega t)} - \frac{\xi}{\eta} C_2 e^{i(\xi x + \eta y - \omega t)} \qquad \text{(A1.2.23)}$$

Under boundary conditions, $\tau_{yz} = 0$ at $y = 0$

$$\left(\tau_{yz}\right)_{y=0} = \eta^2 (C_1 + C_2) + \xi^2 (C_1 + C_2) = 0 \qquad \text{(A1.2.24)}$$

The above equations govern the reflection of SH waves.

For incident SH wave case for reflection from equation (A1.2.21),

$$(\eta^2 + \xi^2)(C_1 + C_2) = 0$$

$$\eta^2 (C_1 + C_2) + \xi^2 (C_1 + C_2) = 0 \qquad \text{(A1.2.25)}$$

Thus, $C_2 = -C_1$

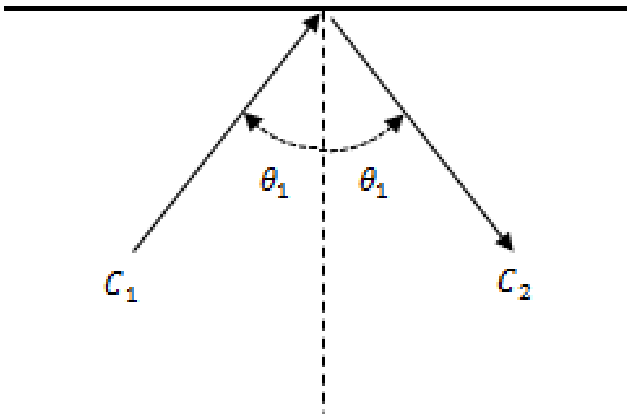

Figure A.3: Ray representation of reflection of SH-wave from a free boundary

Hence the reflection angle is the same as the incident angle. The SH wave reflects itself with no mode conversion in Fig. A.3.

ii) Reflection of longitudinal waves

Unlike SH-waves, the reflection of P waves is more complex. The free and fixed boundary condition of longitudinal waves are considered, where traction is zero and displacement at the surface is constrained.

An incident P wave will reflect P wave and mode convert SV wave. The reflected P wave at the free surface satisfies traction free boundary. A condition that has to be met is that wavelength along the common boundary has to equal for all reflected and mode converted waves. Therefore the reflected SV wave will always have a lower angle of refection compared to the P waves, which obeys Snell's law as illustrated in Fig. 1.7.

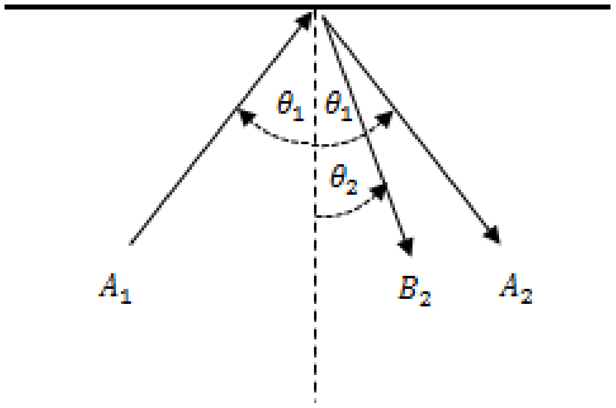

Figure A.4: Ray representation of the reflection of P-wave from a free boundary

Hence, for longitudinal waves, $B_1 = 0$ in the expressions (A1.2.16). Therefore, the amplitude ratios are,

$$\frac{A_2}{A_1} = \frac{\sin 2\theta_1 \sin 2\theta_2 - k^2 \cos 2\theta_2}{\sin 2\theta_1 \sin 2\theta_2 + k^2 \cos 2\theta_2}$$

$$\frac{B_2}{A_1} = \frac{2\sin 2\theta_1 \cos 2\theta_2}{\sin 2\theta_1 \sin 2\theta_2 + k^2 \cos 2\theta_2}$$

(A1.2.26)

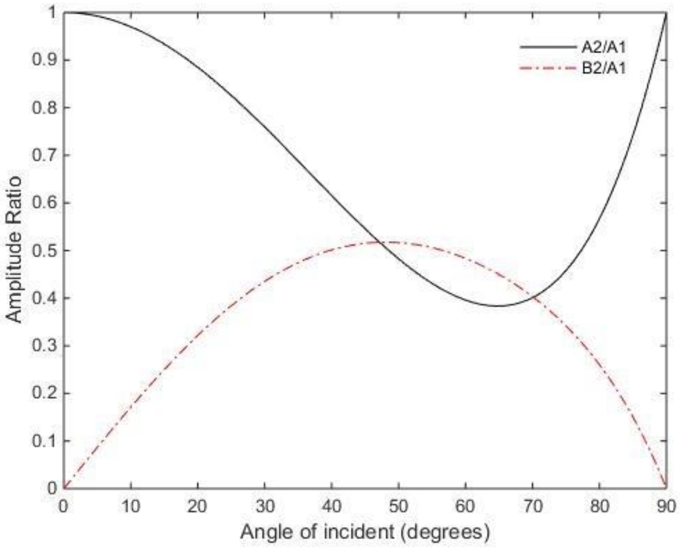

Figure A.5: Amplitude ratios A_2/A_1 and B_2/A_1 for incident P wave for Poisson's ratio ν=1/3

The other special case $\frac{A_2}{A_1} = 0$ implies that there will be no reflected P waves as the critical angle is achieved.

iii) Reflection of SV waves

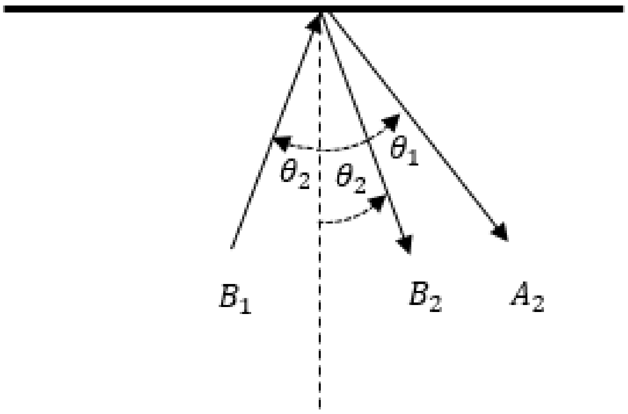

Figure A.6: Ray representation of the reflection of SV-wave from a free boundary

For incident SV waves, in this case $A_1 = 0$ in the expressions (A1.2.16). The amplitude ratios are

$$\frac{B_2}{B_1} = \frac{\sin 2\theta_1 \sin 2\theta_2 - k^2 \cos 2\theta_2}{\sin 2\theta_1 \sin 2\theta_2 + k^2 \cos 2\theta_2}$$

$$\frac{A_2}{B_1} = \frac{-\mathrm{k}^2 2\sin 2\theta_2 \cos 2\theta_2}{\sin 2\theta_1 \sin 2\theta_2 + k^2 \cos 2\theta_2}$$

(A1.2.27)

We see for P and SV waves, the amplitudes are depended only on incident angle and Poisson’s Ratio.

Similar to P waves, incident SV wave undergoes mode conversion. For the special case where $\frac{A_2}{B_1} = 0$ and $\frac{B_2}{B_1} = -1$, as of normal incidence when $\theta_2 = 0°$. The case where $\theta_2 = 45°$ where $\frac{A_2}{B_1} = 0$ and $\frac{B_2}{B_1} = 1$ has applications in plate theory. Only P reflection occurs, when $B_2 = 0$ due to only an incident SV wave. This occurs when,

$$\sin 2\theta_1 \sin 2\theta_2 = k^2 \cos^2 2\theta_2 \tag{A1.2.28}$$

For critical angle such that P wave is tangential to the surface,

$$\sin \theta_1 = \mathrm{k} \sin \theta_2 = 1 \tag{A1.2.29}$$

Where $k > 0$

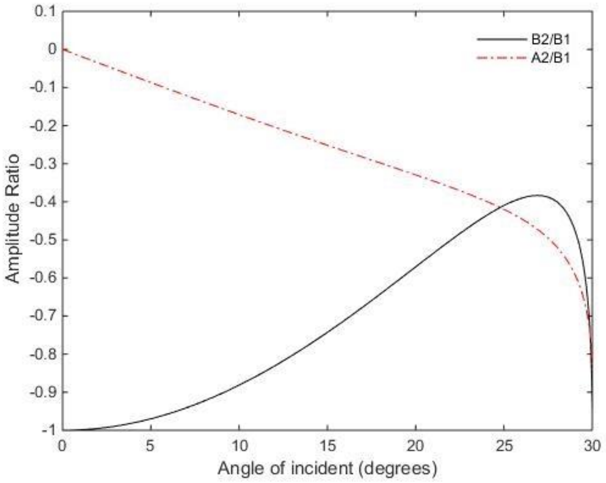

Figure A.7: Amplitude ratios A_2/B_1 and B_2/B_1 for incident SV wave for Poisson's ratio v=1/3

If the shear wave of arbitrary polarisation impinges on a free surface, the SV portion of the wave will lose a portion of its energy to P wave. However, the SH portion of the amplitude and energy will reflect a change in phase.

A.3 Surface waves (Rayleigh waves)

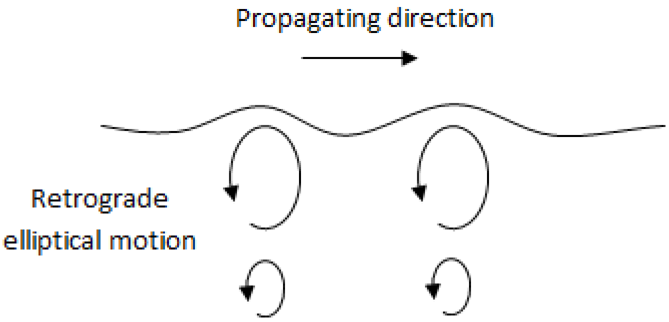

Figure A.8: Rayleigh wave propagation

Where there is a boundary, in a half-space problem, a surface wave may exist. First investigated by Lord Rayleigh, surface waves effectively decrease with depth. The velocity of propagation of surface waves are smaller than body waves as illustrated in Fig. A.8. These waves are known as Rayleigh waves and have been used extensively in non-destructive evaluation [72, 78, 100, 114, 119, 127, 177]. The energy associated with this wave suggest that the energy dissipates less rapidly than P and SV waves, though this could only be accounted for by assuming it was essentially confined to the surface. The Rayleigh wave's displacement field can be decomposed into scalar and vector potential by using Helmholtz theorem.

From equation (A1.2.8), consider the potential equations are now given by

$$\frac{d^2 f}{dy^2} - \bar{\alpha}^2 f = 0$$

$$\frac{d^2 h_z}{dy^2} - \bar{\beta}^2 h_z = 0 \qquad \text{(A1.3.1)}$$

Note that,

$$\bar{\alpha}^2 = -\alpha^2 = \xi^2 - \frac{\omega^2}{c_1^2}$$

$$\bar{\beta}^2 = -\beta^2 = \xi^2 - \frac{\omega^2}{c_2^2}$$

$$\omega = \xi c_R \tag{A1.3.2}$$

This study of incident SV wave extends beyond the critical angle such that the angle at which P-waves are reflected tangential to the free surface. The solutions give waves with exponentially increasing and decreasing parts. Ignoring the increasing term, we have

$$\varphi = Ae^{-\bar{\alpha}y}e^{i\xi(x-c_R t)}$$

$$\psi_z = Be^{-\bar{\beta}y}e^{i\xi(x-c_R t)} \tag{A1.3.3}$$

Therefore the expression for displacement and stresses are,

$$u_x = (i\xi Ae^{-\bar{\alpha}y} - \bar{\beta}Be^{-\bar{\beta}y})e^{i\xi(x-c_R t)}$$

$$u_y = -(\bar{\alpha}Ae^{-\bar{\alpha}y} + i\xi Be^{-\bar{\beta}y})e^{i\xi(x-c_R t)}$$

$$\tau_{xx} = \mu\left(\left(\bar{\beta}^2 - \xi^2 - 2\bar{\alpha}^2\right)Ae^{-\bar{\alpha}y} - 2i\bar{\beta}\xi Be^{-\bar{\beta}y}\right)e^{i\xi(x-c_R t)}$$

$$\tau_{yy} = \mu\left(\left(\bar{\beta}^2 + \xi^2\right)Ae^{-\bar{\alpha}y} + 2i\bar{\beta}\xi Be^{-\bar{\beta}y}\right)e^{i\xi(x-c_R t)}$$

$$\tau_{xy} = \mu\left(-2i\bar{\alpha}\xi Ae^{-\bar{\alpha}y} + \left(\bar{\beta}^2 + \xi^2\right)Be^{-\bar{\beta}y}\right)e^{i\xi(x-c_R t)} \tag{A1.3.4}$$

At the free surface $\tau_{xy} = \tau_{yy} = 0$ at $y = 0$ and it will reduce to

$$\left(\bar{\beta}^2 + \xi^2\right)A + 2i\bar{\beta}\xi B = 0$$

$$-2i\bar{\alpha}\xi A + \left(\bar{\beta}^2 + \xi^2\right)B = 0 \tag{A1.3.5}$$

Hence the amplitude ratio,

$$\frac{A}{B} = -\frac{2i\bar{\beta}\xi}{\bar{\beta}^2+\xi^2} = \frac{\bar{\beta}^2+\xi^2}{2i\bar{\alpha}\xi} \tag{A1.3.6}$$

And the frequency of the surface wave,

$$\left(\bar{\beta}^2 + \xi^2\right)^2 - 4\bar{\alpha}\bar{\beta}\xi^2 = 0 \tag{1.3.7}$$

Resulting in,

$$\frac{c_R^2}{c_2^2}\left(\left(\frac{c_R}{c_2}\right)^6 - 8\left(\frac{c_R}{c_2}\right)^4 + (24 - 16k^{-2})\left(\frac{c_R}{c_2}\right)^2 - 16(1 - k^{-2})\right) = 0 \tag{A1.3.8}$$

Further investigation indicates that the roots of the equation are depended on the Poisson's ratio given by equation (A1.1.12). The resulting surface wave propagating with the velocity form equation above is called Rayleigh surface wave.

The particle motion from the equation and using the amplitude ratio at $y = 0$

$$u_z = Ai\left(\gamma - \frac{\bar{\beta}^2+\gamma^2}{2\gamma}\right)e^{i\xi(x-c_R t)}$$

$$u_y = A\left(-\bar{\alpha} + \frac{\bar{\beta}^2+\gamma^2}{2\bar{\beta}}\right)e^{i\xi(x-c_R t)} \tag{A1.3.9}$$

The propagation Rayleigh velocity is independent of frequency indicates that a surface propagates non-dispersive and velocity less than the shear velocity. An approximate expression for Rayleigh velocity is graphed in Fig. A.9,

$$\frac{c_R}{c_2} = \frac{0.87+1.12v}{1+v} \tag{A1.3.10}$$

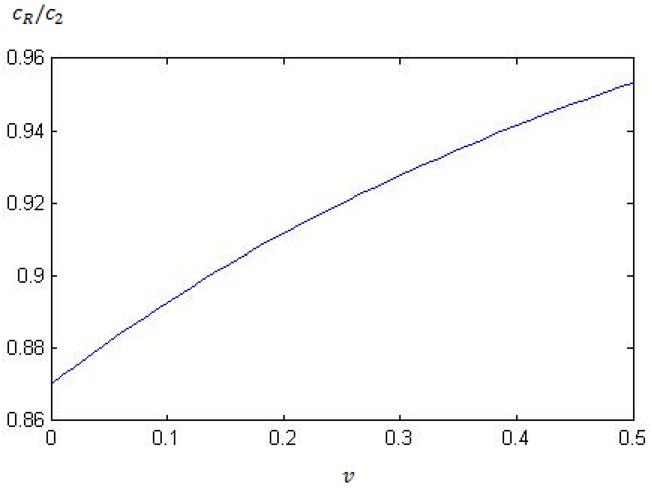

Figure A.9: Rayleigh wave speed as a function of Poisson's Ratio using the approximation expression

Rayleigh wave has no geometric decay with propagating distance, which makes it a good choice for long-range non-destructive evaluation. The particle motion is elliptical and retrograde with the direction of travel as illustrated in Fig. A.8. The vertical displacement component is greater than the horizontal component at the surface and the motion decreases exponentially in depth. At approximately 0.192 wavelengths in depth, the direction of the particle motion as well as the normal stress is reversed, as illustrated in Fig. A.10.

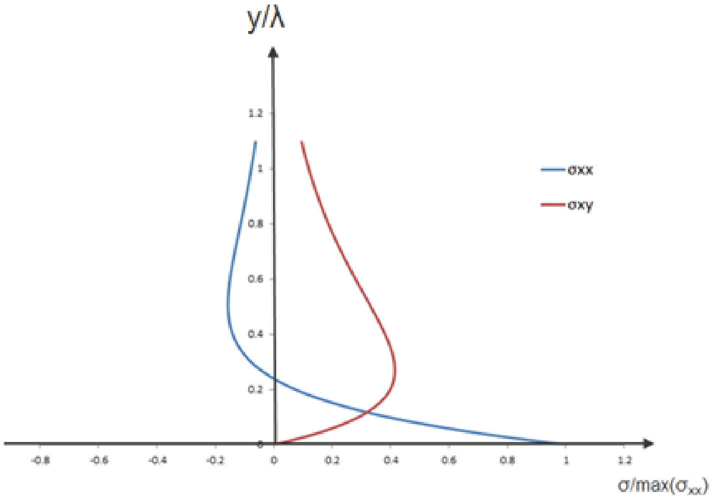

Figure A.10: Relative normal and shear stresses of Rayleigh wave as a function of depth/wavelength

A.4 Wave propagation in plates

The early developments of wave propagation in solid plates were concerned with bulk waves, which are also known as Lamb waves. This chapter introduces the solution of Lamb waves in isotropic plates. In addition to the expressions from bulk waves for plates, the boundary conditions now have two traction free surfaces to guide the wave, refer to Fig. A.11.

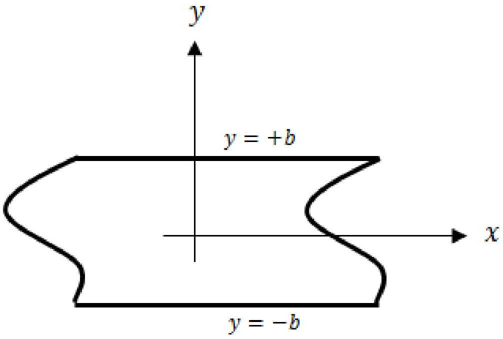

Figure A.11: Boundary conditions at $y=\pm b$ *on isotropic plate for Lamb wave propagation*

Consider a plate with two boundary surfaces with thickness *2b* in the x-y plane. Two concerns of complexity arise: first the multiple reflections of waves between boundary surface, and second the mode conversion of P and SV waves. Since we are considering only SH wave case, the second complication is removed. Hence, we restrict our attention to the first area of concern.

First, we consider the simplest case, SH wave.

The governing equation is

$$\nabla^2 u_z = \frac{1}{c_2^2}\frac{\partial^2 u_z}{\partial t^2} \qquad \text{(A1.4.1)}$$

Such that $u_z = u(x, y, t)$

Immediately, the general solution of the wave equation is,

$$u_z = h(y)e^{i(\xi x - \omega t)} \tag{A1.4.2}$$

By substituting in the wave equation gives,

$$\frac{d^2h}{dy^2} + \beta^2 h = 0$$

$$\beta^2 = \frac{\omega^2}{c_2^2} - \xi^2 \tag{A1.4.3}$$

Thus the solution becomes,

$$u_z = (A_1 \sin\beta y + A_2 \cos\beta y)e^{i(\xi x - \omega t)}$$

$$u_z = A_1' e^{i(\xi x - \beta y - \omega t)} + A_2' e^{i(\xi x + \beta y - \omega t)} \tag{A1.4.4}$$

Considering the boundary conditions,

$$y = \pm b, \tau_{yy} = \tau_{xy} = \tau_{zy} = 0 \tag{A1.4.5}$$

Since SH wave restriction has restriction on τ_{zy} and given that

$$\frac{\partial u_z}{\partial y} = 0 \text{ where, } y = \pm b \tag{A1.4.6}$$

Applying these conditions to the solutions,

$$A_1 \sin\beta b - A_2 \cos\beta b = 0$$

$$A_1 \sin\beta b + A_2 \cos\beta b = 0 \tag{A1.4.7}$$

Resulting in,

$$\cos\beta b \sin\beta b = 0$$

$$\beta b = \frac{n\pi}{2} \text{ given } n = 0, 1, 2, 3, \dots \tag{A1.4.8}$$

Under these results, the harmonic SH wave may propagate only under special conditions. Consider the displacement solution with respect to the $y = 0$, the motion involves symmetric (S) and antisymmetric (A) mode, denoted in the equation by A_2 and A_1, respectively.

Suppose the frequency satisfies $\cos\beta b = 0$ where $A_2 = 0$. Then the motion is antisymmetric,

$$u_z = (A_1 \sin\beta_n y)e^{i(\xi x - \omega t)} \tag{A1.4.9}$$

Where $n = 1, 3, 5, \dots$

Similarly, if $\sin\beta b = 0$ where $A_1 = 0$. Then the motion is symmetric,

$$u_z = (A_2 \cos\beta_n y)e^{i(\xi x - \omega t)} \tag{A1.4.10}$$

Where $n = 0, 2, 4, \dots$

For the longitudinal and transverse waves propagating in a plate, we consider plate geometry and if conditions of plane strain hold in the z-direction we have

$$u_z = 0 \frac{\partial}{\partial z} = 0$$

$$u_x = u_x(x, y, t) = \varphi_x + \psi_{z,y}$$

$$u_y = u_y(x, y, t) = \varphi_y - \psi_{z,x}$$

$$\nabla^2\varphi = \frac{1}{c_1^2}\frac{\partial^2\varphi}{\partial t^2}$$

$$\nabla^2\psi = \frac{1}{c_2^2}\frac{\partial^2\psi}{\partial t^2}$$

(A1.4.11)

In the P and S wave boundary conditions are,

$$u_y = \tau_{xy} = \tau_{zy} = 0 \text{ at } y = \pm b \tag{A1.4.12}$$

Hence, the solutions to the wave equation are,

$$\varphi = f(y)e^{i(\xi x - \omega t)}$$

$$\psi_z = ih_z(y)e^{i(\xi x - \omega t)} \tag{A1.4.13}$$

Note: factor of i has been insert for later convenience.

Substituting the potential wave equation:

$$\frac{d^2 f}{dy^2} + \alpha^2 f = 0$$

$$\frac{d^2 h_z}{dy^2} + \beta^2 h_z = 0$$

Where,

$$\alpha^2 = \frac{\omega^2}{c_1^2} - \xi^2$$

$$\beta^2 = \frac{\omega^2}{c_2^2} - \xi^2$$

$$f = A\sin\alpha y + B\cos\alpha y$$

$$h_z = C\sin\beta y + D\cos\beta y \tag{A1.4.14}$$

The resulting potentials and displacements are:

$$\varphi = (A\sin\alpha y + B\cos\alpha y\,)e^{i(\xi x - \omega t)}$$

$$\psi_z = i(C\sin\beta y + D\cos\beta y)e^{i(\xi x - \omega t)}$$

$$u_x = i\big(\xi(A\sin\alpha y + B\cos\alpha y) + \beta(C\cos\beta y - D\sin\beta y)\big)e^{i(\xi x - \omega t)}$$

$$u_y = \big(\alpha(A\cos\alpha y - B\sin\alpha y) + \xi(C\sin\beta y + D\cos\beta y)\big)e^{i(\xi x - \omega t)} \qquad \text{(A1.4.15)}$$

Consider the stress potentials, provided previously, the stress is in terms of the potentials.

So,

$$\tau_{xx} = \mu\left(\big(2\alpha^2 - k^2(\xi^2 + \alpha^2)\big)(A\sin\alpha y + B\cos\alpha y) - 2\xi\beta(C\cos\beta y - D\sin\beta y)\right)e^{i(\xi x - \omega t)}$$

$$\tau_{yy} = \mu\left(\big(2\xi^2 - k^2(\xi^2 + \alpha^2)\big)(A\sin\alpha y + B\cos\alpha y) + 2\xi\beta(C\cos\beta y - D\sin\beta y)\right)e^{i(\xi x - \omega t)}$$

$$\tau_{xy} = i\mu\big(2\xi\alpha(A\cos\alpha y - B\sin\alpha y) - (\beta^2 - \xi^2)(C\sin\beta y + D\cos\beta y)\big)e^{i(\xi x - \omega t)} \qquad \text{(A1.4.16)}$$

τ_{zz} is obtained from τ_{xx} and τ_{yy}, while $\tau_{xz} = \tau_{zy} = 0$

Applying solutions for u_y and τ_{xy} to boundary conditions to obtain

$$\alpha(A\cos\alpha b - B\sin\alpha b) + \xi(C\sin\beta b + D\cos\beta b) = 0$$

$$\alpha(A\cos\alpha b + B\sin\alpha b) - \xi(C\sin\beta b - D\cos\beta y) = 0$$

$$2\xi\alpha(A\cos\alpha b - B\sin\alpha b) - (\beta^2 - \xi^2)(C\sin\beta b + D\cos\beta b) = 0$$

$$2\xi\alpha(A\cos\alpha b + B\sin\alpha b) + (\beta^2 - \xi^2)(C\sin\beta b - D\cos\beta b) = 0 \qquad \text{(A1.4.17)}$$

Simplifying further,

$$\alpha A\cos\alpha b + \xi D\cos\beta b = 0$$

$$\alpha B\sin\alpha b - \xi C\sin\beta b = 0$$

$$2\xi\alpha A\cos\alpha b - (\beta^2 - \xi^2)D\cos\beta b = 0$$

$$2\xi\alpha B\sin\alpha b + (\beta^2 - \xi^2)C\sin\beta b = 0 \tag{A1.4.18}$$

Hence,

$$\begin{bmatrix} \alpha\cos\alpha b & \xi\cos\beta b \\ 2\xi\alpha\cos\alpha b & -(\beta^2-\xi^2)\cos\beta b \end{bmatrix}\begin{bmatrix} A \\ D \end{bmatrix} = 0$$

$$\begin{bmatrix} \alpha\sin\alpha b & -\xi\sin\beta b \\ 2\xi\alpha\sin\alpha b & (\beta^2-\xi^2)\sin\beta b \end{bmatrix}\begin{bmatrix} B \\ C \end{bmatrix} = 0 \tag{A1.4.19}$$

Before continue further investigation, it should be noted that the displacement in equation, u_x and u_y contain symmetric and antisymmetric mode.

The term B and C gives symmetric displacement with respect to $y = 0$, whereas A and D terms gives antisymmetric displacement in u_x and u_y.

Continuing with the determinants for the antisymmetric mode,

$$\alpha(\beta^2 + \xi^2)\cos\alpha b\cos\beta b = 0 \tag{A1.4.20}$$

This frequency equation will be satisfied by

$$\alpha = 0, \qquad \alpha b = \frac{m\pi}{2}, \qquad \beta b = \frac{n\pi}{2}, \qquad \text{where } m, n = 1, 3, 5, \ldots \tag{A1.4.21}$$

If $\alpha = 0$ or $\alpha b = \frac{m\pi}{2}$ such that $D = 0$, so, antisymmetric P mode,

$$u_x = i\xi A \sin \alpha_m y \, e^{i(\xi x - \omega t)}$$

$$u_y = \alpha_m A \cos \alpha_m y \, e^{i(\xi x - \omega t)} \tag{A1.4.22}$$

If $\beta b = \frac{n\pi}{2}$ such that $A = 0$, antisymmetric SV mode,

$$u_x = -i\beta D \sin \beta_m y \; e^{i(\xi x - \omega t)}$$

$$u_y = \xi D \cos \beta_m y \, e^{i(\xi x - \omega t)} \tag{A1.4.23}$$

It is possible for these modes to be uncoupled from one another due to the boundary condition. Recall the study of the half-space, where it is was found that P and SV reflect without mode conversion from mixed boundary constraints of the present type.

Similarly, for symmetric mode,

$$\alpha(\beta^2 + \xi^2) \sin \alpha b \sin \beta b = 0$$

This frequency equation will be satisfied by,

$$\alpha = 0, \qquad \alpha b = m\pi, \qquad \beta b = n\pi, \qquad \text{where } m, n = 1, 2, 3, \ldots \tag{A1.4.24}$$

If $\alpha b = m\pi$ such that $C = 0$, then, for symmetric P mode,

$$u_x = i\xi B \cos \alpha_m y \, e^{i(\xi x - \omega t)}$$

$$u_y = -\alpha_m B \sin \alpha_m y \, e^{i(\xi x - \omega t)} \tag{A1.4.25}$$

For $m = 0$

$$u_x = i\xi B e^{i(\xi x - \omega t)}$$

$$u_y = 0 \tag{A1.4.26}$$

If $\beta b = n\pi$ such that $B = 0$, symmetric SV mode,

$$u_x = i\beta C \cos \beta_m y \ e^{i(\xi x - \omega t)}$$

$$u_y = \xi C \sin \beta_m y \, e^{i(\xi x - \omega t)} \tag{A1.4.27}$$

A.5 The Rayleigh-Lamb frequency equation for the plate

Again, consider waves of plane strain propagating in the x-direction in a plate of thickness *2b* with traction-free boundaries. The displacements, potential functions and stresses governing equations, again, still holds and the boundary conditions are given by,

$$\tau_{yy} = \tau_{xy} = \tau_{zy} = 0, \text{ at } y = \pm b \tag{A1.5.1}$$

Resolving for antisymmetric wave,

$$u_x = i(A\xi \sin \alpha y - D\beta \sin \beta y)e^{i\Psi}$$

$$u_y = (\alpha A \cos \alpha y + D\xi \cos \beta y)e^{i\Psi} \tag{A1.5.2}$$

Where,

$$\Psi = \xi x - \omega t$$

Ψ is called the phase factor.

Since, for antisymmetrical case, $B = C = 0$. Thus, applying boundary conditions, we obtain

$$\pm((\xi^2-\beta^2)A\sin\alpha b-2\xi\beta B\sin\beta b)=0$$

$$2\xi\alpha A\cos\alpha b-D(\beta^2-\xi^2)\cos\beta b=0 \qquad \text{(A1.5.3)}$$

Thus, the Rayleigh-Lamb frequency equation for antisymmetric waves and amplitude ratios are

$$\frac{\tan(\beta b)}{\tan(\alpha b)}=-\frac{(\xi^2-\beta^2)^2}{4\alpha\beta\xi^2}$$

$$\frac{A}{D}=\frac{2\xi\beta\sin\beta b}{(\xi^2-\beta^2)\sin\alpha b}=-\frac{(\xi^2-\beta^2)\cos\beta b}{2\xi\alpha\cos\alpha b} \qquad \text{(A1.5.4)}$$

Now, resolving in symmetric wave,

$$u_x=i(B\xi\cos\alpha y+\ C\beta\cos\beta y\,)e^{i\Psi}$$

$$u_y=(-\alpha B\sin\alpha y+\ C\xi\sin\beta y\,)e^{i\Psi} \qquad \text{(A1.5.5)}$$

Since, for symmetrical case, $A=D=0$. Hence, applying boundary conditions, we obtain,

$$(\xi^2-\beta^2)B\cos\alpha b+2\xi\beta C\cos\beta b=0$$

$$\pm i(2\xi\alpha B\sin\alpha b+C(\xi^2-\beta^2)\sin\beta b)=0 \qquad \text{(A1.5.6)}$$

With the boundary conditions and equating the determinant of coefficient to zero, frequency equation and amplitude ratio are produced.

In summary, the Rayleigh-Lamb frequency equation for the plate,

$$\frac{\tan(\beta b)}{\tan(\alpha b)}=-\left\{\frac{4\alpha\beta\xi^2}{(\xi^2-\beta^2)^2}\right\}^{\pm1}\begin{cases}+1=symmetric\\-1=antisymmetric\end{cases}$$

Recall that,

$$\alpha^2 = \frac{\omega^2}{c_1^2} - \xi^2 \text{ and } \beta^2 = \frac{\omega^2}{c_2^2} - \xi^2 \text{ and wavenumber } \xi = \frac{\omega}{c} \qquad \text{(A1.5.7)}$$

The real roots of the Rayleigh-Lamb frequency Eqn. (A.1.5.7) corresponds to the propagating symmetric and antisymmetric wave modes. The roots can be obtained by using numerical root solution methods [157]. It is found that there exist an infinite number of solutions for infinite number of modes to the Rayleigh-Lamb frequency equation. The program DISPERSE [33] is used to obtain the solution to dispersion equations of Lamb waves, as illustrated in Fig. A.12.

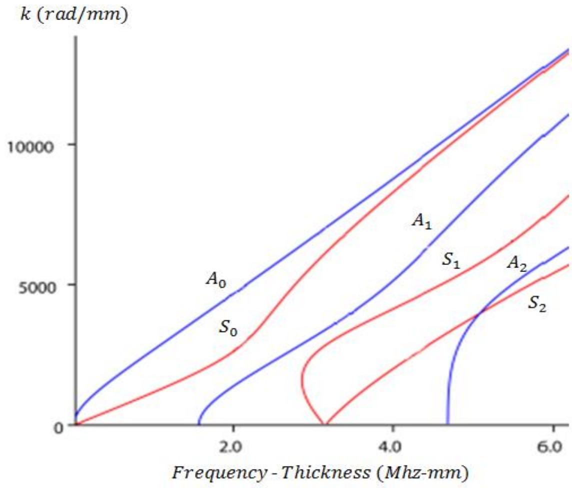

Figure A.12: Dispersion curve for the symmetric and antisymmetric modes in a 3mm aluminium plate

Furthermore, the symmetric and antisymmetric waves have different mode shapes. The dominant displacements for symmetric modes are the in-plane components, and for antisymmetric modes are the out-of-plane components.

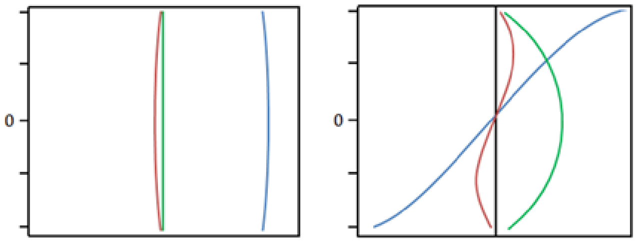

Figure A.13: Stress through thickness profile of mode shape (LEFT) S_0 mode and (RIGHT) A_0 mode in a 3mm aluminium plate at 200 kHz frequency (BLUE) in-plane stress (RED) out-of-plane stress and (GREEN) shear stress

In Fig A.13, the S_0 mode has a strong in-plane stress component and the normal σ_{xx} is almost uniform throughout thickness. However, the A_0 mode stresses are more complex and have a dominant shear stress distribution through thickness. Due to the A_0 stress profile, the antisymmetric wave is highly advantageous than the symmetric wave when detecting laminar type defect such as delamination [178].

The dispersion can be expressed in terms of phase velocity, c_p. One can obtain the phase velocity by using,

$$c_p = \frac{\omega}{k} \tag{A1.5.8}$$

Fig A.14 shows the dispersion curve in terms of phase velocity and group velocity. At low frequency-thickness regime, the S_0 mode is essentially non-dispersive, and the group velocity is independent of frequency. This makes S_0 highly favourable for wide area scanning for SHM. The phase velocity of all modes converges to Rayleigh wave speed at higher frequency.

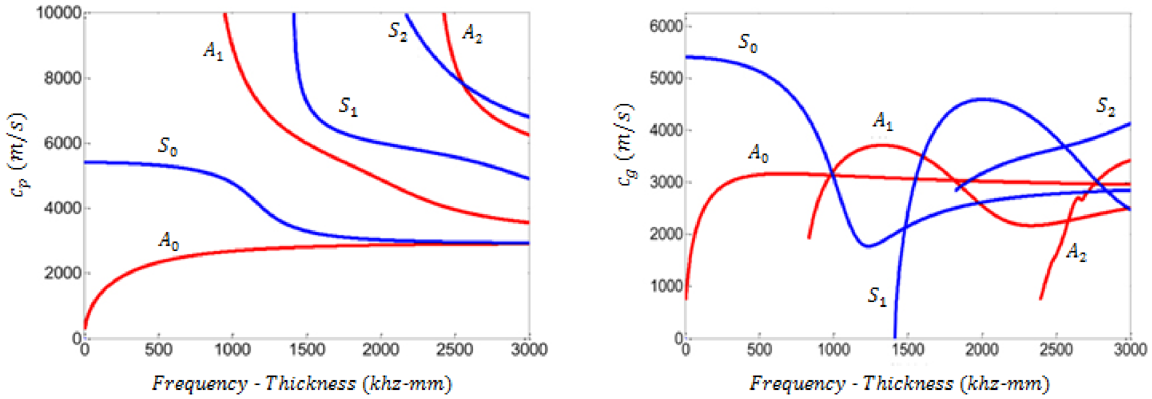

Figure A.14: (LEFT) Dispersion curve in terms of phase velocity. (RIGHT) Dispersion curve in terms of group velocity

When exciting Lamb waves, usually a number of cycles of wave train are generated to minimise dispersion. One may consider group velocity of the wave packet, c_g, which describes the speed at which the energy is travelling through the medium The group velocity can be obtained by using,

$$c_g = \frac{d\omega}{dk} \tag{A1.5.9}$$